Quantitative analysis of *in situ* time-resolved RHEED during growth of self-catalysed GaAs nanowires

Zur Erlangung des akademischen Grades eines
DOKTORS DER NATURWISSENSCHAFTEN (Dr. rer. nat.)

von der KIT-Fakultät für Physik des
Karlsruher Instituts für Technologie (KIT)
genehmigte

DISSERTATION

von

M. Sc. Julian Benjamin Jakob

Tag der mündlichen Prüfung: 26. Juni 2020

Referent: Prof. Dr. Tilo Baumbach
Korreferent: Prof. Dr. Ullrich Pietsch

Kurzfassung

Die morphologischen und kristallographischen Eigenschaften vertikaler, freistehender Nanodrähte, welche mittels der Dampf-Flüssigkeits-Feststoff-Methode (VLS) gezüchtet werden, sind durch ein kompliziertes Wechselspiel der Wachstumsparameter während des Herstellungsprozesses beeinflusst. Das Verständnis und die Kontrolle dieser dynamischen Prozesse sind folglich Voraussetzung für die Herstellung von Nanodrähten mit maßgeschneiderten Eigenschaften. Zeitaufgelöste *in situ* Charakterisierungsmethoden ermöglichen die direkte Beobachtung und Analyse solcher dynamischen Prozesse, sowie deren Wechselwirkung.
Die *in situ* Beugung hochenergetischer Elektronen unter streifendem Einfall (RHEED) spielt in der gegenwärtigen Nanodrahtforschung unter den kristallographischen *in situ* Charakterisierungsmethoden, aufgrund der bisherigen Beschränkung auf rein *qualitative* Analysen, eine untergeordnete Rolle, obwohl eine umfassende Verfügbarkeit der Methode an fast allen Molekularstrahlepitaxie-Anlagen besteht.
In der vorliegenden Arbeit wird ein Ansatz zur *quantitativen* Auswertung von zeitaufgelösten Intensitätsverläufen der *in situ* gemessenen RHEED Beugungsbildern entwickelt, welche während des Wachstums von vertikaler, freistehender Nanodrähte in Transmissionsgeometrie gemessen werden. Auf dieser Basis werden methodische Einschränkungen der *qualitativen* Analyse überwunden. Über die Intensitätsverläufe charakteristischer Beugungsreflexe der verschiedenen Kristallphasen erlaubt RHEED die *quantitative* Untersuchung von in III-V Nanodrähten auftretenden strukturellen Polytypismus. In der Arbeit wird dazu ein Simulationsprogramm entwickelt, welches sowohl die Wechselwirkungen der Elektronen mit einzelnen Nanodrähten als auch den Einfluss des gesamten Nanodrahtensembles auf die gebeugten Intensitäten abschätzt, sowie deren Dynamik während der Nanodrahtherstellung berücksichtigt.
Mittels Simulationen werden Einflüsse morphologischer und kristallographischer Veränderungen während des Wachstums auf die resultierenden Intensitätsverläufe der Beugungsreflexe untersucht und deren Ursache diskutiert. Die wichtigsten Herausforderungen, Möglichkeiten und Einschränkungen der Methode für *in situ* RHEED Studien des Nanodrahtwachstums werden dabei identifiziert. Darüber hinaus wird gezeigt, dass die bei RHEED an Nanodrähten durch Elektronenabsorption verursachte Elektronenschattenbildung, zu einem auf die Nanodrahtspitze reduzierten Informationsvolumen führt, was RHEED unempfindlich für die untere, abgeschattete Nanodrahtregion macht.

Die erhöhte höhenselektive Sensitivität von *in situ* RHEED gegenüber der Nanodrahtspitze eignet sich insbesondere dazu, komplementäre Informationen zu den etablierten *in situ* Charakterisierungsmethoden, wie *in situ* Röntgenbeugung (XRD), zu erhalten. Simultan durchgeführte *in situ* RHEED und *in situ* XRD Experimente während der Herstellung von selbstkatalysierten GaAs Nanodrähten erlaubten es, diese Komplementarität auszunutzen. Während *in situ* RHEED vorrangig Informationen über die Kristallstruktur an der Nanodrahtspitze liefert, untersucht *in situ* XRD das gesamte Nanodrahtvolumen. Zusammen mit abschließender *ex situ* Rasterelektronenmikroskopie (REM), erhält man umfassende und repräsentative Informationen über die morphologische und kristallographische Entwicklung großer Nanodrahtensembles während des Wachstums. Darüber hinaus wird *in situ* RHEED als laborbasierte, eigenständige Methode etabliert. Es wird gezeigt, dass *in situ* RHEED untersetzt mit angemessenem *a priori* Wissen, eine leistungsfähige Charakterisierungstechnik der Nanodraht-Kristallstruktur ist und sich daher auch für grundlegende Nanodraht-Wachstumsstudien mit gängigen Molekularstrahlepitaxie-Anlagen eignet. Mit Hilfe der hier vorgestellten Datenanalyseprozeduren konnte allein mittels laborbasierter *in situ* RHEED- und REM-Analytik ein kürzlich publiziertes theoretisches VLS-Wachstumsmodell an großen Nanodrahtensembles *quantitativ* verifiziert werden.
Zusammenfassend ebnen die in dieser Arbeit vorgestellten Ergebnisse den Weg für die Verwendung von *quantitativem in situ* RHEED während des Nanodrahtwachstums, sowohl als eigenständige, laborbasierte, wie auch als komplementär zu anderen Charakterisierungsmethoden einsetzbare *in situ* Analysemethode der Kristallstruktur.

Abstract

The final morphological and structural properties of vertical free-standing nanowires, grown by the vapour-liquid-solid (VLS) mode, are affected by a complicated interplay of the growth parameters during the fabrication process. The understanding and control of these dynamical processes are consequently prerequisite for the production of nanowires with dedicated properties. Time-resolved *in situ* characterization methods allow direct observation and analysis of these dynamical processes and their interplay.
In the portfolio of *in situ* structural characterization methods, *in situ* reflection high-energy electron diffraction (RHEED) plays a minor role in current nanowire research due to the restriction to *qualitative* analysis to date, although it is broadly available at nearly all molecular-beam epitaxy systems.
In the present thesis, we overcome these limitations of *qualitative* analysis by developing an approach for the *quantitative* evaluation of time-resolved *in situ* RHEED intensity patterns measured during the growth of vertical, free-standing nanowires in transmission geometry. Via the intensity evolution of characteristic diffraction spots of the different crystal phases, RHEED is suitable for the investigation of the structural polytypism occurring in e.g. III-V nanowires. We present a simulation model which estimates the interaction of the electrons with the individual nanowires and with the whole nanowire ensemble, as well as the dynamics of both during nanowire fabrication. We discuss by means of the simulation model, the impact of morphological and structural variations during growth in the resulting diffraction spot intensity evolution. Moreover, we demonstrate that the electron shadowing occurring in RHEED, which is caused by electron absorption, results in a reduced information volume at the nanowire apex and thus makes RHEED sensitive to this upper region. We identify the main challenges, possibilities and limitations of *in situ* RHEED studies during nanowire growth.
The increased sensitivity of *in situ* RHEED to the nanowire apex makes it especially suitable to obtain complementary information to the established *in situ* structural characterization techniques, such as X-ray diffraction (XRD). We will show that simultaneous *in situ* RHEED and *in situ* XRD experiments during the growth of self-catalysed GaAs nanowires allows their complementarity to be exploited. While RHEED provides structural information at the nanowire tip, XRD probes the whole nanowires giving volume information. In combination with post-growth scanning electron microscopy (SEM), we

obtain comprehensive information about the mean morphological and structural evolution of a large nanowire ensemble during growth.
Moreover, we establish *in situ* RHEED as a laboratory-based stand-alone method. We demonstrate that with adequate *a priori* knowledge, *in situ* RHEED is likewise a powerful structural characterization technique and can be applied for fundamental growth studies in common molecular-beam epitaxy chambers. By means of the laboratory-based *in situ* RHEED and post-growth SEM analysis, we verify a recently published theoretical VLS growth model applied to large nanowire ensembles.
All results presented in this thesis pave the way for using *in situ* RHEED during nanowire growth as a laboratory-based *quantitative* analysis method of the crystal structure but also to complement other characterization techniques.

Contents

1. Introduction

The digital revolution has had an enormous impact on our society, the broad availability of smartphones, laptops and other digital devices changed the nature of our private and working lives. The technological development leading to the high availability of these digital devices was mainly driven by the permanent reduction of the dimensions of transistors, and thus their number per area in integrated circuits, known as *Moore's law*. More than 50 years ago, Moore postulated that the complexity of integrated circuits doubles every year at minimum costs,[1] later modified to a doubling every two years. For several decades it was the benchmark of the semiconductor industry caused by the opportunity to exploit quantum effects associated with the size reduction.

However, during the last years it has become evident that the technological development can no longer follow Moore's law and has slowed down. This was mainly caused by the approach at the physical limits of the manufacturing processes and the associated expensive economic aspects of the technological development related to the further miniaturization of the integrated circuits. Thus, future developments demand a paradigm shift, instead of only relying on the miniaturization of components. This is known by the catch phrase *More than Moore*.

Among different routes to proceed with the technological development in the *More than Moore* era, the integration of III-V semiconductors in the standard silicon platform has found to be attractive. By combining both material systems, the cost-effective and mature silicon platform can be combined with the III-V semiconductors offering high electron mobilities and direct band-gaps to increase the performance of the devices. Furthermore, this approach allows the direct integration of optoelectronics with the complementary-metal-oxide-semiconductor (CMOS) technology, e.g. for on-chip optical communication.[2]

Monolithic integration of both material systems is essential and can be realized by vertical nanowires of III-V semiconductors. Nanowires are defined as small crystalline objects, of which two dimensions are below 200 nm and the third dimension can be much larger, ranging up to several micrometer in length.[3] The small interface between nanowires and silicon in the vertical arrangement allows for defect-free integration, because the induced stress caused by the lattice mismatch of both material systems can elastically relax. The fabrication of these vertical nanowires can be realized by techniques based on the self-assembly of atoms which involve complex dynamical processes. Industrial nanowire applications require defect-free structures with high structural quality. Consequently, their production

afford a high degree of control over different interacting parameters influencing the growth process.

In contrast to the bulk III-V semiconductors, where only one crystal structure is stable, in vertical III-V nanowires different crystal structures can be present, even within one single nanowire, which is called polytypism. Polytypism may have negative impact on the performance of nanowires devices,[4,5] however it may also be used to switch the polytypes in nanowires intentionally to exploit their different band structure.[6,7]

In this context, *in situ* techniques for the characterization of the crystal structure during nanowire fabrication give valuable insight into fundamental growth processes such as the formation of polytypes, as well as their dynamics. Moreover, they enable a direct feedback, resulting in a high degree of control over the fabrication processes and the resulting crystal quality. In contrast, *ex situ* characterization techniques allow only insight into the nanowire final state. For dynamical conclusions, sample series are required which mimic the dynamics of the processes.

Most of the established *in situ* characterization techniques are limited to special equipment, which is not broadly available in laboratories, such as *in situ* transmission electron microscopy (TEM) or *in situ* X-ray diffraction (XRD). In contrast, Reflection high-energy electron diffraction (RHEED) is part of most nanowire epitaxy chambers and thus easy accessible, however RHEED is currently restricted to only qualitative analysis.

The aim of this work is the development of a quantitative method for the analysis of the crystal structure of vertical nanowires by time-resolved *in situ* RHEED. We will consider the essential interactions of electrons and nanowires to obtain an understanding of the important aspects determining the RHEED intensity formation. We will show that time-resolved *in situ* RHEED during nanowire growth is particular suitable for the characterization of the polytypism near the axial growth front of vertical nanowires. The characteristics of *in situ* RHEED make it further suitable as a complementary analysis method to other techniques, such as XRD.

In chapter 2, we give the main principles of the growth of self-catalysed GaAs nanowires and discuss the different crystal structures which are present in these nanowires, as well as the aspects resulting in the structural polytypism. We will further introduce X-ray and electron scattering, which we will use for the subsequent characterization of the polytypism. We will present the portable molecular-beam epitaxy chamber, which is used to grow and to *in situ* characterize the nanowire structures in chapter 3.

In chapter 4, we introduce the basic principles of *in situ* RHEED and develop a quantitative analysis method to characterize the polytypism in vertical nanowires. Therefore, we will discuss the interactions of electrons with the individual nanowires, with the nanowire ensemble and their temporal development during growth. All these findings are incorporated into a simulation programme which models the intensity evolution of diffraction spots in RHEED patterns, sensitive to certain crystal phases. By means of the simulation we will

discuss the characteristics, possibilities and limitations of *in situ* RHEED and we elucidate the impact of certain sample properties on the RHEED intensity evolution. Parts of this chapter are published in publication I (see appendix A).
In chapter 5, we use the quantitative *in situ* RHEED analysis for the characterization of self-catalysed GaAs nanowires. In combination with simultaneous time-resolved *in situ* XRD experiments during nanowire growth, we firstly validate the developed RHEED model and secondly use the complementarity of both techniques for a comprehensive investigation of the evolution of the mean shape and mean crystal structure in nanowire ensembles. We show that *in situ* RHEED is particularly suited for studying the crystal structure at the axial growth front of the nanowires, while XRD probes the whole nanowire volume and thus is sensitive to changes inside the electron shadows of RHEED. Further, we will use the simultaneous time-resolved *in situ* XRD and *in situ* RHEED approach for the investigation of the nucleation phase of self-catalysed GaAs nanowires. By studying different scenarios of initiating the nanowire growth, we show that the way of initiating the growth has a direct impact on the extend of the polytypism at the nanowire-substrate interface.
For further analysis of the nucleation phase, we employ *in situ* RHEED as a stand-alone laboratory-based characterization technique of the crystal structure in chapter 6. Combined with scanning electron microscopy (SEM) analysis, we use the high sensitivity and shadowing-effects of *in situ* RHEED to correlate the nucleation probabilities of the different polytypes with the shape of the catalyst particle responsible for the axial growth. We set our results in the context of a previously published theoretical model explaining the polytypism in self-catalysed GaAs nanowires. Our results demonstrate the significance of *in situ* RHEED analysis as a laboratory-based characterization technique of the crystal structure gaining the mean structural properties of large nanowire ensembles in common growth chambers. The results of chapter 5 and 6 will be published in publication II (see appendix A).
Finally, in chapter 7 we will conclude the results and we will give an outlook.

2. Basic principles

2.1. Fabrication of self-catalysed GaAs nanowires

The miniaturisation of integrated circuits in semiconductor technology is one of the driving forces for research in nanowire technology.[3,8] The nearly one-dimensional appearance of nanowires not only allows for a high packing factor for devices on microchips,[9] but more importantly the reduced size in two directions leads to a modification of the density of state of the electrons and phonons and thus quantum effects become dominant,[10,11] leading to enhanced properties which make them very interesting for potential new technological aspects.[12]

The high aspect ratio leads to a large proportion of surface atoms, and thus surface effects cannot be neglected.[13,14] Moreover, the high surface ratio makes nanowires interesting for functional parts in electronical and optoelectronical devices which are realized by semiconductor heterostructures. These heterostructures are characterized by layers of materials with different band-gaps. The band-gap variation can be achieved by doping of the intrinsic semiconductor or by a combination of material systems with different lattice parameters. Typically this induces stress at the respective interface, however in the case of nanowires, due to the small size, the induced stress can relax elastically without defects.[3,14] This is different to planar thin film growth, where the stress relaxes typically via misfit dislocations.[15] The integration of different material systems can be realized in radial as well as in axial direction. Consequently, nanowires find application in many devices, like e.g. transistors,[16–18] light-emitting diodes (LEDs),[19–21] solar cells,[22–24] lasers,[25–27] thermoelectrics[28–30] or sensors,[14,31,32] integrating such demands of properties.

Two general approaches for fabrication of nanowires exist, one is called 'top-down', and the second 'bottom-up' approach. The 'top-down' approach uses bulk material as basis on which the nano structures are designed by lithographic methods, followed by an etching step to cut out the structures themselves. This method has dominated the material processing over the last decades.[33] The 'bottom-up' approach is based on self-assembly of atoms and is often realized by the vapour-liquid-solid growth (VLS),[34] where a liquid metal catalyst particle sits on top of the nanowires. This metal droplet acts as catalyst particle for the crystal growth. The growth species which are supplied by the vapour phase dissolve therein until supersaturation is reached, followed by the formation of a new layer of the crystalline

material at the liquid-solid interface. The nanowire grows and pushes the catalyst droplet upwards.

One big advantage of the 'bottom-up' approach is the opportunity to combine materials with dissimilar lattice parameters of substrate and nanowires, since the induced stress can relax along the growth axis.[15] This is highly interesting for integrating direct band-gap materials systems, like III-V semiconductors with their superior electrical and optical properties, with the standard semiconductor platform which is silicon. Compared to silicon, on which the industrial processing is optimised, many of the source materials of III-V semiconductors are rare and thus expensive.[35] Thus effective use of the III-V semiconductors is essential for economic reasons. However, the integration of both material systems promises many advantages and allows e.g. for on-chip optical communication[2,36] or high-performance devices, like high electron mobility transistors.[37,38]

The 'bottom-up' synthesis of nanowires can be carried out with several techniques, the most common ones are molecular-beam epitaxy (MBE) and metalorganic chemical vapor deposition (MOCVD). In MOCVD, which is typically used for industrial purposes, the source material is supplied by chemical compounds in a carrier gas flowing through the reactor, in which the substrate is located. By this technique, high crystal growth rates can be achieved and the crystal growth itself occurs under moderate vacuum. MBE allows for high purity crystals with only few contaminations, since the crystal growth is done under ultra-high vacuum conditions inside the growth reactor. The material flux is generated by evaporating high purity solid state source materials resulting in a molecular-beam interacting with the substrate. MBE is a versatile tool for investigating fundamental growth phenomena because the related processes can be precisely controlled, enabling e.g. the deposition of only one single atomic monolayer.

Over many years Au has been the best choice as catalyst particle material because it does not oxidise and is still stable at the desired small droplet sizes.[39] Besides that Au has been shown to be a versatile catalyst particle for nanowire growth in many different material systems like Si,[34,40] other group IV elements,[41] the III-V,[18,36] or the II-VI[42,43] compound semiconductors.

The typical growth of Au-catalysed III-V nanowires starts with the deposition of a thin Au film on the substrate, followed by an annealing step to melt the film and form small Au droplets. Afterwards, the growth species are introduced into the reactor, dissolving in the liquid Au droplet until supersaturation is reached, followed by formation of a solid crystal resulting in a growing nanowire.

For the future integration of III-V nanowires with the standard complementary metal-oxide-semiconductor (CMOS) technology based on Si, the VLS process with Au as catalyst particle has however several drawbacks. Au is a forbidden element in the standard CMOS technology, since it forms deep level traps in the band-gap of Si and has a high diffusivity contaminating large areas.[44] Furthermore it is difficult to remove Au from contaminated

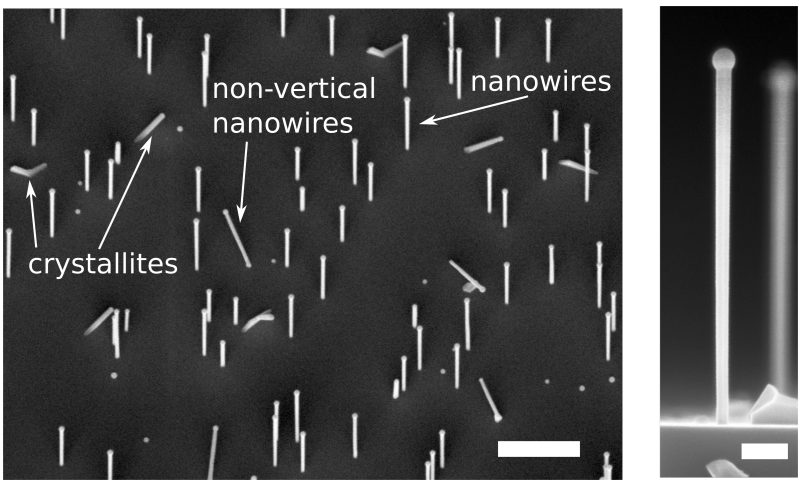

Figure 2.1.: Scanning electron micrograph of GaAs nanowires. Left image: 30° tilted view of vertical and non-vertical nanowires. Besides the nanowires, GaAs crystallites grow directly on the substrate. The scale bar is 1 µm. Right image: side view of vertical GaAs nanowire with the Ga catalyst droplet at the apex. The scale bar is 200 nm.

fabrication equipment.[45]

The present thesis focuses on the growth of GaAs nanowires (compare figure 2.1), which is seen as the prototype for III-V semiconductors. However, other III-V semiconductor nanowires have been demonstrated already on Si substrates, such as GaP,[46] GaN,[47] InAs,[48] InP,[49] as well as some of their alloys.

The growth temperatures of Au-catalysed GaAs nanowires are typically around 350 °C to 500 °C.[50,51] Although the literature agrees that Au becomes incorporated into nanowires,[52–55] the reports on the effect of Au on the nanowire themselves are contradictory. Tambe *et al.* demonstrated that the electrical properties worsen by Au incorporation,[53] which is in accordance with the observation of Breuer *et al.*, who could identify a much smaller carrier lifetime in Au-catalysed GaAs nanowires, compared to the latter described Ga-catalysed.[54] However, other authors could reach carrier lifetimes comparable to those of the Ga-catalysed GaAs nanowires presented by Breuer *et al.* by simply optimising the growth conditions.[56,57] Nevertheless, to reduce the risk of a negative influence on those properties, Au should be best avoided and there are several approaches to circumvent Au as catalyst. An obvious one is to simply replace Au with other elements, like e.g. Pd,[58] Cu[59] or Ag,[60] however, there still exists the possibility of incorporation into the nanowire material. By replacing the foreign element by the group III compound metal as catalyst during the VLS growth any contamination can be avoided, this technique is called self-catalysed or III-assisted VLS growth. Contaminations can be also avoided by fabrication methods without any catalyst particle, like the catalyst-free selective area growth.[61] In this work, the self-catalysed VLS growth is of importance and thus it will be discussed in the following. For other approaches information can be found in Ref.[45]

The self-catalysed growth of III-V nanowires will be now discussed at the model system of GaAs nanowires grown on Si(111) substrates covered with a native Si oxide layer. As shortly described before, the main idea is the substitution of the Au particle by the III element, which is Ga in the case of GaAs nanowires. The growth conditions need to be carefully chosen in order to allow the liquid Ga droplet to be in equilibrium with the solid GaAs, which is fulfilled close to the congruent temperature $T_C = 630\,^{\circ}\mathrm{C}$.[62] The processing temperature for GaAs nanowires close to the congruent temperature is not yet fully compatible with standard CMOS processing,[3] thus current effort is made to fabricate nanowires at lower substrate temperatures.[63] The substrate temperature close to T_C allows for Ga rich conditions which is prerequisite for the VLS growth. On the other hand, this means that the As flux limits the axial growth rate.[64] This is oppositional to the 2D layer-by-layer growth. Furthermore, the flux ratio of the group III and group V materials needs to be chosen carefully since they are essential to maintain the axial growth and determine the shape of the nanowire.[64] In the following chapters, we simply call the ratio between the fluxes "V/III - ratio". The liquid Ga droplet at the apex is a key property of the growing nanowire itself, it influences the diameter as well as the crystal structure as we will show in section 2.2.

For successful nanowire fabrication there are additional requirements on the substrate. The substrate's surface should have non-wetting properties, which can be achieved with GaAs or Si substrates covered with a thin oxide layer.[39] Characteristics such as thickness, roughness and chemical composition have a direct impact on the nucleation behaviour of the nanowires, because they determine e.g. the diffusion of the growth species on the substrate and the ability of forming liquid nano-droplets with suitable wetting angles close to 90° which is essential to increase the nanowire yield.[65–67]

GaAs nanowires grow usually along the [111] crystal direction, by choosing substrates with an identical crystal orientation, the resulting nanowires are vertical and free-standing objects with respect to the substrate, as shown in figure 2.1. The cross sections of the vertical nanowires are hexagonal with {110}-facet family in case of self-catalysed GaAs nanowires on Si(111), which is different to the Au-catalysed GaAs nanowires on Si(111), where the side facets are of {112}-type.[50] Besides the intended nanowires, there can exist other GaAs objects on the substrate, which grow together with the nanowires, as shown in figure 2.1. These unintentionally grown objects can be divided into non-vertical nanowires, which grow along the other {111} - directions, and bulky VLS growth nucleating along the substrate's surface or vapour-solid (VS) deposition grown directly on the substrate. These crystallites have typically many grain boundaries. All these objects, non-vertical nanowires and crystallites, are called parasitic intergrowth in the following.

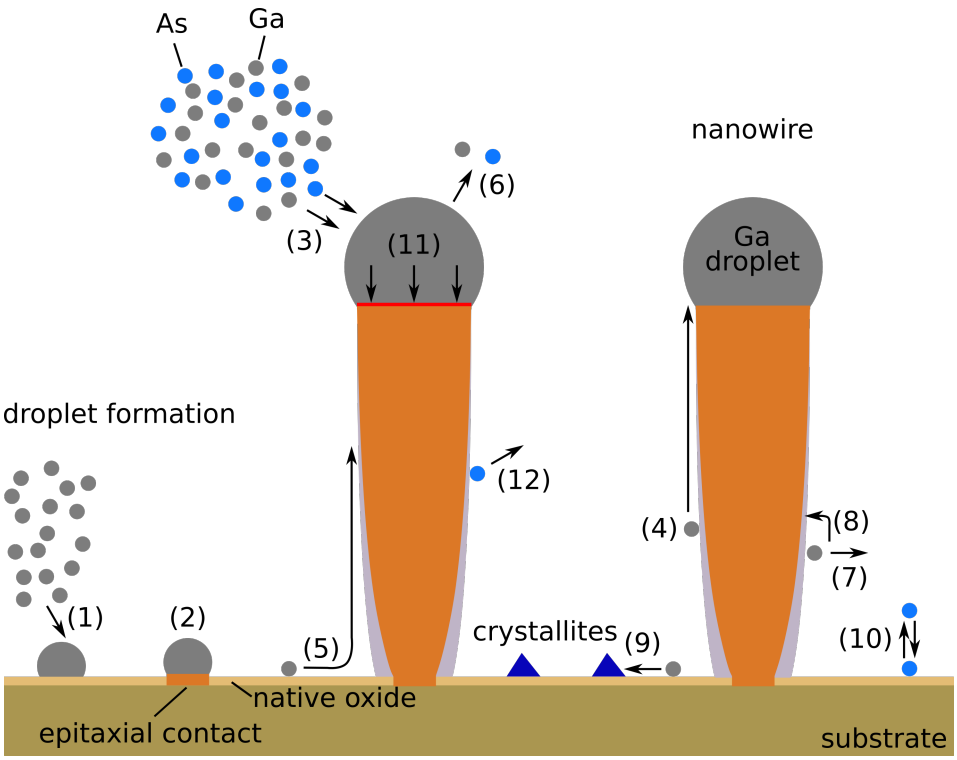

Figure 2.2.: Diagram of processes involved in self-catalysed GaAs nanowire growth. Adapted from Ref.[68] Details on the numbered processes are in the text.

In this section, we discuss in detail the growth of self-catalysed GaAs nanowires and processes involved. In figure 2.2, adapted from Ref.,[68] a diagram of the nanowire growth and the process paths involved in such a VLS growth are depicted. For a successful nucleation of the nanowires, the impinging Ga atoms need to conglomerate on the blank substrate surface to small droplets (1) which then are able to etch the oxide layer and create contact to the underlying Si substrate (2). After the formation of Ga droplets and the established contact to the Si, the As atoms arriving dissolve into the droplet until supersaturation is reached, followed by the onset of nanowire growth with epitaxial contact.[69] During the growth, the Ga and As adatoms are provided by the gas phase. Ga adatoms may be incorporated into the droplet by direct impingement (3), by diffusion of Ga adatoms which have impinged directly at the nanowire side walls (4) and by diffusion of Ga adatoms from the substrate's surface via the side walls (5). The effective influx into the catalyst particle is determined by the desorption of adatoms from the droplet (6). The adatoms which do not reach the droplets can either evaporate on their way to the droplet (7) or they can be incorporated at the side walls (8), which result in side wall or facet growth (indicated in grey). However, if they do not reach any nanowires, they can form other GaAs objects like crystallites (9). The sticking coefficient of As is small compared to that of Ga, resulting in a direct re-evaporation of As from the substrate (10) and an

As dominated atmosphere close to the substrate. If the As adatoms impinge directly at the droplet (3), they can dissolve in the liquid and the concentration increases until both species, Ga and As, are incorporated in the nanowires in a layer-by-layer manner indicated in red (11). Growth species evaporating from the surface or side walls return to the vapour phase and can be collected by nearby nanowires (12). Adatoms which dissolve in the droplet contribute to the axial VLS growth (3,4,5), the VS facet growth is determined by the processes (7,8,12). For more detailed information on GaAs nanowire growth, we refer to the reviews in Ref.[13,39,64,70]

Until now we considered the fundamental aspects of self-catalysed GaAs nanowire growth. Technological applications require, however, controlling and tuning of the nanowires' number density on the substrate, this can be realized by combining 'top-down' and 'bottom-up' techniques. Using this combination, a thick spacing layer, like e.g SiO_x, is deposited onto the substrate which prevents nanowire nucleation. Afterwards, the substrate is patterned by lithographic processes, usually with electron beam lithography, to define the nucleation sites of the nanowires. After an additional etching step, the substrate's surface is only bare again in the patterned holes, allowing epitaxial contact only there. Nanowires grown by this technique achieve a high control of number density and location.[71–73] Although this lithography patterning is widely used, the fabrication involves many steps being complex and optimised separately. Consequently, lithography-free approaches to tune the nanowire number density promise simplified fabrication protocols, for purposes where defined locations of nanowires are not important. Typically, these approaches contain additional deposition steps directly in the growth reactor before the actual nanowire growth.[74–78] Moreover, Tauchnitz *et al.* could achieve an extreme narrow length distribution in the nanowire ensemble by simply applying a lithography-free growth protocol.[79] However, these techniques have in common that only the nanowires' number density can be tuned without any control over their actual location.

2.2. Crystal structure and polytypism in GaAs nanowires

In several III-V compound nanowires structural polytypism naturally occurs, which is the coexistence of different crystal phases within one single nanowire. For example in InAs,[80] GaP,[81] InP[82] or GaAs[73] extended segments of the cubic zinc blende and the hexagonal wurtzite lattice were observed. In this section, the crystal structure of self-catalysed GaAs nanowires is discussed, based on Ref.[83] Furthermore, we extent the discussion to those properties which cause and influence the polytypism in nanowires.

In figure 2.3 the unit cells of both crystal structures, zinc blende (ZB) and wurtzite (WZ), are illustrated. The zinc blende unit cell is similar to the diamond structure, in which e.g. Si crystallizes. Both structures can be described by a face-centred cubic (fcc) crystal of lattice parameter a_c, with an additional second fcc crystal shifted by (1/4, 1/4, 1/4) a_c.

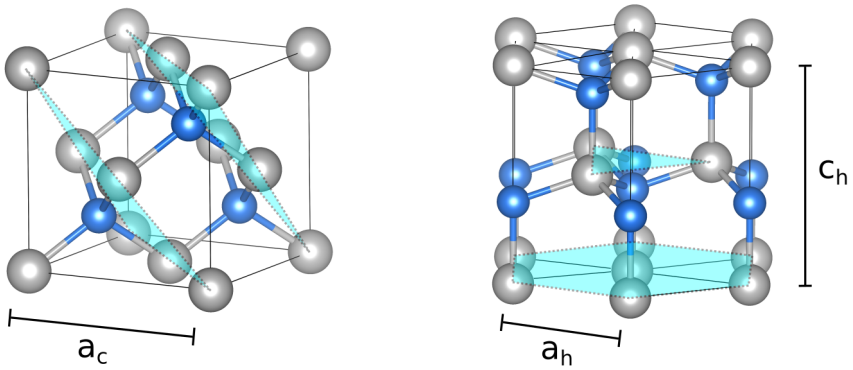

(a) Crystal structure of ZB with lattice parameter a_c.[84]

(b) Crystal structure of WZ with lattice parameters a_h and c_h.[84]

Figure 2.3.: Zinc blende and wurtzite unit cells of GaAs. The Ga atoms are shown in grey and the As atoms in blue. The monolayers perpendicular to the [111] = [00.2] directions are indicated with cyan planes.

In case of the diamond structure, all atoms are of the same species, in case of GaAs zinc blende, however, the fcc lattice at (0, 0, 0) a_c is only occupied by Ga atoms (grey spheres) and the second fcc lattice at positions (1/4, 1/4, 1/4) a_c is only occupied by As atoms (blue spheres) shown in figure 2.3(a). The relative positions for the different atom species in the unit cell are summarized in table 2.1. Viewing along the [111]-direction of the zinc blende unit cell, monolayers with a hexagonal closed package orientation are discernible, indicted by cyan planes in figure 2.3(a). Each of these monolayers is composed of two sub-monolayers of Ga, respectively As atoms, only. Figure 2.3(b) in contrast depicts the wurtzite unit cell, the hexagonal lattice is characterised by two different lattice parameters a_h and c_h. The monolayers are orientated differently in this unit cell, displayed again with cyan planes. This difference in the orientation of the monolayers, which are perpendicular to the VLS growth direction, results in different stacking sequences along the growth axis. In figure 2.4, we are now considering an extended crystal of both phases, which allows us to discuss their differences. In figure 2.4(a) a zinc blende crystal with viewing direction along the [111]-direction (top) and along the [1$\bar{1}$0]-direction (bottom) is depicted. The atoms are located at three possible relative positions in each monolayer which are named 'A' (grey), 'B' (red) and 'C' (green). For a direct comparison, in figure 2.4(b) a wurtzite crystal with the same viewing directions is presented. The viewing directions in the hexagonal lattice are along the [00.2]-direction (top) and along the [$\bar{1}$2.0]-direction (bottom). In contrast to the three possible positions of the zinc blende structure, only two are discernible in the wurtzite crystal. Consequently, the zinc blende structure can be characterised by a monolayer stacking sequence of 'ABC', whereas the wurtzite crystal structure show an 'ABA' behaviour. As previously introduced in section 2.1, the growth of nanowires occurs in a layer-by-layer manner. Thus, stacking faults can be included easily and depending on

Table 2.1.: Relative atomic positions in the unit cells.

atom species	zinc blende unit cell	wurtzite unit cell
Ga atoms	$(0\ 0\ 0)$ $\left(\frac{1}{2}\ \frac{1}{2}\ 0\right)$ $\left(0\ \frac{1}{2}\ \frac{1}{2}\right)$ $\left(\frac{1}{2}\ 0\ \frac{1}{2}\right)$	$(0\ 0\ 0)$ $\left(\frac{2}{3}\ \frac{1}{3}\ \frac{1}{2}\right)$
As atoms	$\left(\frac{1}{4}\ \frac{1}{4}\ \frac{1}{4}\right)$ $\left(\frac{3}{4}\ \frac{3}{4}\ \frac{1}{4}\right)$ $\left(\frac{1}{4}\ \frac{3}{4}\ \frac{3}{4}\right)$ $\left(\frac{3}{4}\ \frac{1}{4}\ \frac{3}{4}\right)$	$\left(0\ 0\ \frac{3}{8}\right)$ $\left(\frac{2}{3}\ \frac{1}{3}\ \frac{7}{8}\right)$

their frequency, switching of the polytypes is possible and leads to extended segments along the nanowire. A stacking fault can lead to a transition from the zinc blende to the wurtzite phase stacking or vice versa, but it is also possible that the stacking sequence of the zinc blende gets reversed to 'CBA'. This stacking is called twinned zinc blende (TZB), which is a 180° rotation of the crystal around the growth axis of the original zinc blende orientation. Such a twin boundary is indicated as a black line in figure 2.4(a). The substrate orientation acts as reference and defines the zinc blende stacking order.

An important property of crystals is the distance between two lattice planes, especially regarding the characterization by X-ray and electron diffraction, which we will discuss in sections 2.3 and 2.4. The distance between two crystal planes for the cubic zinc blende crystal structures can be determined by:[10]

$$d_{hkl} = \frac{a_c}{\sqrt{h^2 + k^2 + l^2}} \tag{2.1}$$

and for the hexagonal wurtzite crystal structure by[10]

$$d_{hk.l} = \frac{a_h}{\sqrt{\frac{4}{3}(h^2 + k^2 + hk) + \left(\frac{a_h}{c_h}\right)^2 l^2}}, \tag{2.2}$$

where h,k and l are the Miller indices.

The polytypes of GaAs have a slightly different vertical spacing of the monolayers along the [111]=[00.2] direction. However, in literature there exists a wide range of possible values for $(d_{wz} - d_{zb}/d_{zb})$ even with different sign (Ref.[68,83,85] and Ref. therein). In this work, we orientate ourselves on the work of Köhl *et al.*, who determined the difference of spacing of the lattice planes by 0.66 % ± 0.02 % measured by *ex situ* X-ray diffraction,[86] which is in good agreement with the results of Biermanns *et al.*[87,88]

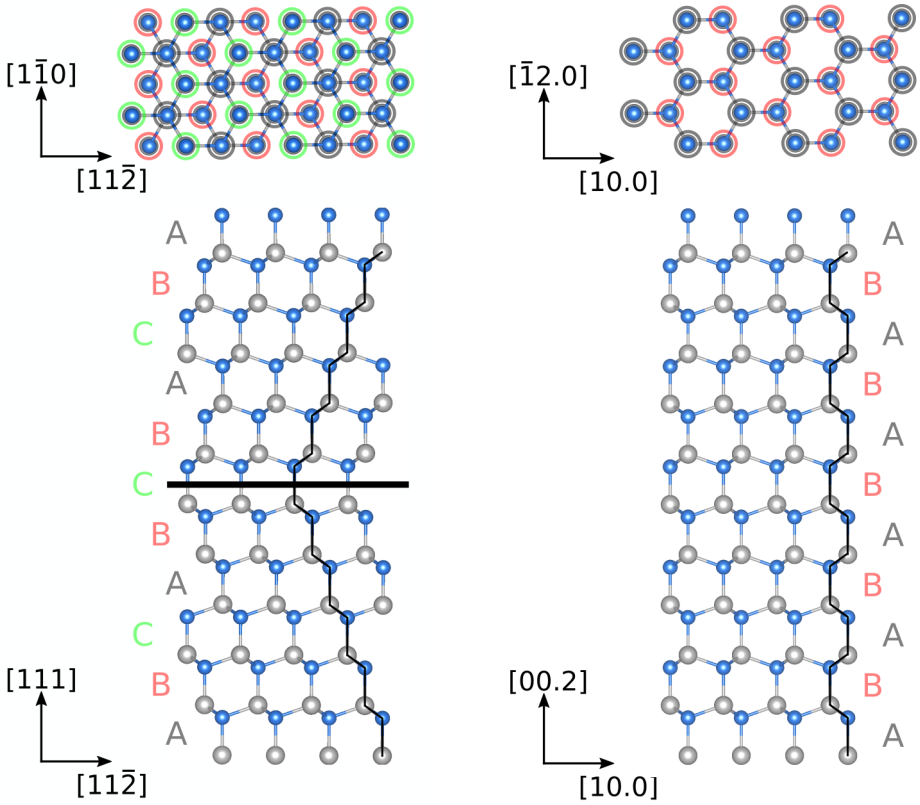

(a) Stacking sequence of zinc blende. Top: viewing direction is along [111]. Bottom: viewing direction is along [1$\bar{1}$0]. The three colours mark different relative positions of atoms in the monolayer.[84]

(b) Stacking sequence of wurtzite. Top: viewing direction is along [00.2]. Bottom: viewing direction is along [$\bar{1}$2.0]. The two colours mark different relative positions of atoms in the monolayer.[84]

Figure 2.4.: Stacking sequence of zinc blende (a) is periodic with '...ABC...'. At a twin boundary, indicated by the black line, the sequence gets reversed to '...CBA...' which is called twinned zinc blende structure. The wurtzite crystal (b) is characterised by a '...ABAB...' stacking sequence.

The possibility of different polytypes in nanowires, as well as the factors determining their nucleation at the growth front are controversially discussed in the literature. In the following, we give an overview and the current understanding of the occurrence of the zinc blende/wurtzite polytypism in self-catalysed GaAs nanowires.

In bulk material most III-V semiconductors form the zinc blende crystal structure, an exception are here the III-nitrides which usually form the wurtzite structure. The cohesive energy between wurtzite and zinc blende $\Delta E = E_{WZ}$ - E_{ZB} explains this observation because for III-nitrides ΔE is negative, whereas for the other III-V compound semiconductors ΔE is positive, e.g. for GaAs $\Delta E = 24\,\mathrm{meV\,per\,III-V\,pair}$.[89]

The earliest attempts to explain the observation of wurtzite in nanowires, which should nominally crystallizes in zinc blende structure only, is related to the possible lower surface

energy at the side walls of wurtzite facets.[90] However, according to this, wurtzite is only stable in very thin nanowires far below the typical nanowire diameters in the range of 50 nm to 100 nm. Glas *et al.* demonstrated that wurtzite can form in nanowires with larger diameter, if the top facet is flat and the nucleation sites are at the triple phase line (TPL) between the vapour, the liquid catalyst particle and the solid nanowire.[91] However, subsequent works showed that the formation of the crystal structure is influenced by many other aspects like the supersaturation[92–94] and the shape of the catalyst particle[95,96] or the geometry of the involved top facet.[97]

A first direct observation of the nucleation of different polytypes was presented by Jacobsson *et al.* by *in situ* transmission electron microscopy (TEM) during MOVPE growth of Au-catalysed GaAs nanowires. The authors saw that the dominating effect is the wetting angle of the liquid droplet determining the polytype. They claim that the supersaturation only affects the droplet shape and thus is an indirect parameter. A small wetting angle around 100° leads to wurtzite structure and a wetting angle larger than 120° results in zinc blende structure. Additionally, according to them the top facet is truncated during zinc blende nucleation, whereas it is flat while wurtzite is nucleating.[98]

The wetting conditions of the catalyst droplet on top of the nanowires are consequently important to understand the occurrence of polytypism in self-catalysed III-V nanowires. Therefore, we now discuss the related fundamental aspects of this phenomena in detail.

The wetting conditions of a droplet depend on the surface energies involved in the phase boundaries. The surface energy G of a droplet with a base radius R and the contact angle β located on a flat surface, where the contact area between droplet and surface is S_0, can be written as:[15]

$$G = \gamma_{LV}\frac{2\pi R^2}{1+\cos\beta} + \gamma_{SL}\pi R^2 + \gamma_{SV}(S_0 - \pi R^2), \tag{2.3}$$

with the liquid-vapour, solid-liquid and solid-vapour surface energies γ_{LV}, γ_{SL} and γ_{SV}. The differential surface energy dG at constant droplet volume V follows as

$$dG_{V=const} = (\gamma_{SL} - \gamma_{SV} + \gamma_{LV}\cos\beta)2\pi R dR. \tag{2.4}$$

The equilibrium value for G is reached when dG is minimal and satisfies the Young's equation

$$\gamma_{SV} = \gamma_{SL} + \gamma_{LV}\cos\beta. \tag{2.5}$$

In case of self-catalysed III-V nanowires theoretical works first predicted only one stable wetting angle during crystal growth which is independent of the volume and only governed by the growth conditions. In this model, the nanowire reacts to changing material fluxes with an increase or decrease of its diameter at the top directly below the droplet to get to steady state conditions with an equilibrium diameter.[99,100] This change of diameter during VLS growth is called tapering. Schroth *et al.* extended the model and modulated a

changing wetting angle with a Fermi function transition approach.[101]
Recent reports give a more explicit explanation for the wetting angle configuration and the resulting nucleation of different polytypes. All are based on the framework of the mononuclear VLS growth regime, where one new monolayer is instantaneously removed from the droplet.[102] Following Ref.,[103] there exist four scenarios for the wetting conditions of droplets on nanowires, which are nonwetting (n) and wetting (w) conditions on vertical (0), respectively inclined facets with an angle θ (tapering). The formation energy for creating a monolayer of height h for the different growth scenarios are:

$$\Delta G_{\theta}^{n} = 2\pi Rh \cdot \left(\frac{\gamma_{\theta V}}{\cos\theta} - \gamma_{LV} \frac{\Omega_L}{\Omega_S} \sin\beta - (\gamma_{SL} + \gamma_{LV}\cos\beta)\tan\theta \right), \tag{2.6}$$

$$\Delta G_{0}^{n} = 2\pi Rh \cdot \left(\gamma_{0V} - \gamma_{LV} \frac{\Omega_L}{\Omega_S} \sin\beta \right), \tag{2.7}$$

$$\Delta G_{\theta}^{w} = 2\pi Rh \cdot \left(\frac{\gamma_{\theta L}}{\cos\theta} - \gamma_{LV} \left(\frac{\Omega_L}{\Omega_S} - 1 \right) \sin\beta - \gamma_{SL}\tan\theta \right), \tag{2.8}$$

$$\Delta G_{0}^{w} = 2\pi Rh \cdot \left(\gamma_{0L} - \gamma_{LV} \left(\frac{\Omega_L}{\Omega_S} - 1 \right) \sin\beta \right), \tag{2.9}$$

where Ω_L and Ω_S are the elementary volumes per atom or pair in the liquid and solid phase, $\gamma_{\theta V}$, γ_{0V}, $\gamma_{\theta L}$, γ_{0L} the surface energies of the vapour-solid respectively liquid-solid interface for vertical facets and tapered facets with angle θ.
In contrast to Tersoff,[99] who predicts only one stable wetting angle, Kim *et al.* suggest two stable wetting angles β_{min} and β_{max},[104] motivated by experimental results. The author and co-workers determine the equilibrium wetting angles β_{min} and β_{max} by finding the transition from non-tapered to tapered nanowire growth. Mathematically this is the difference of surface energies of forming non-wetted inclined facets and non-wetted vertical facets, which is expressed by the difference of equations (2.6) and (2.7). The authors used for the unknown surface energies such values that both stable wetting angles fit to their experimental observations of approximately 90° and approximately 130°,[104] meaning that the absolute values can be however different. Furthermore, they determined the angle at which the flat top facet becomes truncated and vice versa by the difference of surface energies of forming wetted truncated facets and non-wetted vertical facets, expressed by the difference of equations (2.8) and (2.7).[104]
In a subsequent study, these theoretical considerations are expanded by Panciera *et al.* to include the different polytypes.[105] According to their experimental results obtained by *in situ* TEM during molecular-beam epitaxial growth of self-catalysed GaAs nanowires, they changed the interpretation of β_{min} and β_{max}. Both angles are identified as the transition angles when switching from one polytype to the other. The authors modified the vapour-solid surface energies γ_{0V}^{k} and $\gamma_{\theta V}^{k}$ in the equations (2.6) and (2.9) to be either ZB or WZ, $k \in \{\text{ZB,WZ}\}$. Consequently, the equation for widening or narrowing of the

nanowire diameter (tapering) is:

$$\begin{aligned}\Delta F^{k}_{tapered}(\theta,\beta) &= \Delta G^{n}_{\theta} - \Delta G^{n}_{0} \\ &= 2\pi Rh \cdot \left(\frac{\gamma^{k}_{\theta V}}{\cos\theta} - \gamma^{k}_{0V} - (\gamma_{SL} + \gamma_{LV}\cos\beta)\tan\theta \right). \end{aligned} \tag{2.10}$$

The angle at which the flat top facet becomes truncated and vice versa follows as:

$$\begin{aligned}\Delta F^{k}_{truncated}(\alpha,\beta) &= \Delta G^{w}_{\alpha} - \Delta G^{n}_{0} \\ &= 2\pi Rh \cdot \left(\frac{\gamma_{\alpha L}}{\cos\alpha} - \gamma^{k}_{0V} - \gamma_{SL}\tan\alpha + \gamma_{LV}\sin\beta \right), \end{aligned} \tag{2.11}$$

where α gives the angle of the truncated top facet, as illustrated in figure 2.6(d).

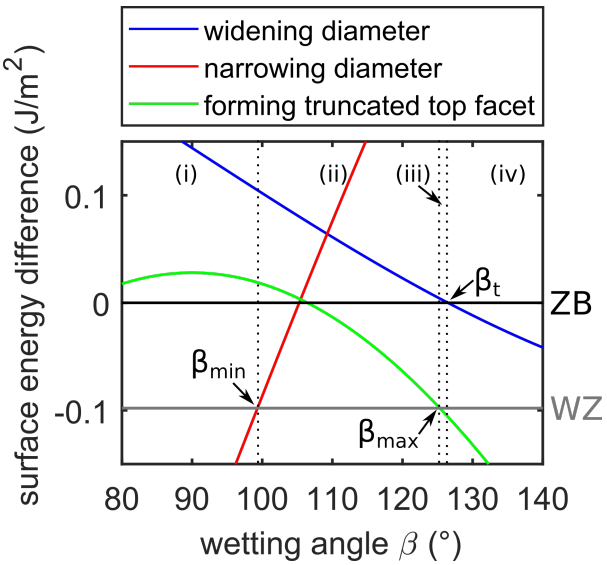

Figure 2.5.: Results of equations (2.10) and (2.11). The black zero level corresponds to the energy level of vertical (110) ZB side facets and the grey level to vertical $(1\bar{1}00)$ WZ facets. The diagram show the transition from positive tapered ZB nanowires at small wetting angles (i) to WZ nanowires with vertical side facets (ii) to again ZB nanowires with vertical side facets in (iii) and inversely tapered ZB nanowires at larger wetting angles in (iv) as a function of β. At β_{max} the flat top facet becomes truncated or vice versa, the transition to tapered nanowires is at β_{min} and to inversely tapered nanowires is at β_t. The regions (i)-(iv) are identical to figure 2.6.

In figure 2.5 the surface energy differences of equation (2.10) and (2.11) are plotted versus the wetting angle β by using the values of Panciera *et al.* in Ref.[105] The authors used for the unknown surface energies such values that both transition angles fit to their experimental observations during *in situ* TEM analysis of $\beta_{min} \approx 100°$ and $\beta_{max} \approx 125°$, meaning that the absolute values can still be different. Between β_{min} and β_{max} WZ nucleates with a flat top facet, whereas at lower and higher wetting angles ZB nucleates. Furthermore very

close to β_{max} it is more favourable to widen the side facets leading to negative tapering at the angle $\beta_t \approx 127°$.

These recent results, in combination with the self-stabilizing process of the diameter of self-catalysed nanowires[99,100] give now a comprehensive picture of nanowire growth in the self-catalysed VLS mode. There exist now four distinguishable regions for a distinct set of growth parameters and nanowire diameter, which are shown in figure 2.5 and 2.6.[104,106] In region (i), the wetting angle is below β_{min} resulting in ZB nucleation. The nanowire diameter reacts by narrowing and consequently with a positive tapered shape to a high V/III - ratio of the material fluxes (figure 2.6(a)). Region (ii) is between β_{min} and β_{max} (figure 2.6(b)), here the droplets sits on top of the vertical top facet and new monolayers nucleate at the TPL. The nanowires are consequently of WZ crystal structure and non-tapered with vertical side facets. At β_{max} the shape of the top facet changes from vertical to an inclined top facet, which result again in ZB nanowires. Region (iii) is between β_{max} and β_t, which is the angle where the widening of the nanowire diameter begins. In region (iii), however the side facets are still vertical and new monolayers adopt the ZB crystal structure, as shown in figure 2.6(c). In the last region shown in figure 2.6(d), the wetting angles are larger than β_t resulting in negative tapered ZB nanowires (region (iv)). The similar shape of the top facet while being truncated and positively tapered gives evidence that the ZB phase always emerges in the presence of inclined top facets.[105]

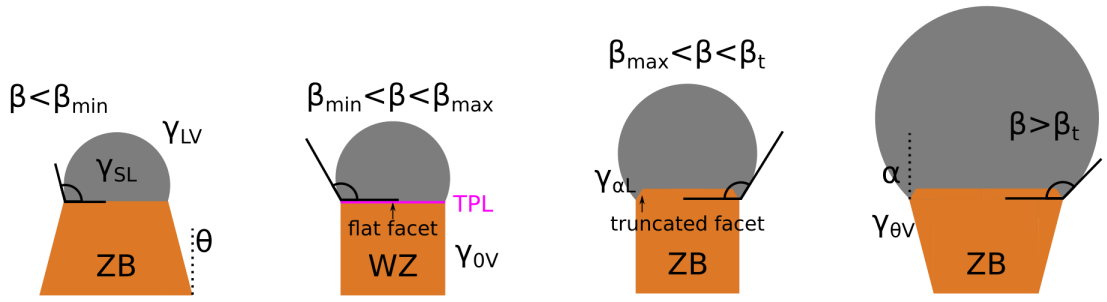

(a) Wetting condition (i). (b) Wetting condition (ii). (c) Wetting condition (iii). (d) Wetting condition (iv).

Figure 2.6.: The four configurations of droplet wetting angle and nanowire top facet and the resulting crystal structure. (a) wetting angle below β_{min}: new monolayers adapt the ZB crystal structure and the small wetting angle causes positive tapered nanowires. (b) wetting angles between β_{min} and β_{max}: new monolayers adapt the WZ structure and nucleate at the TPL at the flat top facet. The nanowires exhibit vertical side facets. (c) wetting angles between β_{max} and β_t: at β_{max} the flat top facet changes to an inclined one with angle α, resulting in ZB nucleation. The side facets remain vertical. (d) wetting angles larger than β_t: the nanowire diameter increases resulting in negative tapered nanowires. New monolayers adapt the ZB crystal structure.

2.3. X-ray diffraction

X-ray diffraction has been established as a versatile method for the characterization of polytypism,[48,101,107–110] because it offers certain advantages, such as the non-destructive nature of X-rays and the resulting compatibility for *in situ* characterization during the fabrication processes. In chapter 5, we use X-rays for the characterization of the nanowires' crystal structure, therefore we give a short introduction to X-ray scattering of nanostructures.
In all our experiments, we assume elastic scattering, where energy conservation is fulfilled, and $\mid \vec{k}_i \mid = \mid \vec{k}_f \mid = \frac{2\pi}{\lambda} = k$, with $\vec{k}_{i,f}$ the incident and the outgoing wave-vector of the wave and λ the corresponding wavelength. For the interpretation of the experimental results in chapter 5, we assume the kinematical approximation to be valid because the extinction length is much larger than the size of our nanostructures. In the kinematical approximation a X-ray photon only scatters once in the structure and multiple scattering is neglected. The typical dimensions of nanowires in the µm range are much smaller than the first Fresnel zone $\sqrt{\lambda R}$, because the distance R from sample to the detector is in the meter range, consequently the far-field or 'Fraunhofer' approximation applies.
Considering, all these assumptions, the scattering amplitude in the Fraunhofer approximation follows as:[107]

$$E_{sc}(\vec{R}) \propto -E_0 C r_0 \frac{e^{ikR}}{R} \int \rho(\vec{r}) e^{-i\vec{Q}\cdot\vec{r}} d\vec{r}, \tag{2.12}$$

with the polarisation factor C, the electron radius r_0 and the scattering vector $\vec{Q} = \vec{k}_f - \vec{k}_i$. In equation (2.12), we directly see that the scattering amplitude is proportional to the Fourier transform of the electron density $\rho(\vec{r})$ of the scattering object.
For a hypothetical infinite, perfect crystal the equation would lead to non-zero values only, if $\vec{Q}$ is equal to a reciprocal lattice vector $\vec{G}_{hkl}$, with the Miller indices h,k and l. The diffraction condition $\vec{Q} = \vec{G}_{hkl}$ is equal to Bragg's law:

$$n\lambda = 2d_{hkl} \sin\theta_B, \tag{2.13}$$

where d_{hkl} is the distance between two lattice planes and θ_B is the Bragg angle.
For X-rays the scattering centres $\vec{r}$ are mainly the electrons inside the atomic shell, the interaction with the atomic core is much weaker and thus can be neglected (which is not true in the case of electrons, as discussed in section 2.4). For a small crystal of finite size, such as nanowires, one can introduce a shape function $\Omega(\vec{r})$, which is one inside and zero outside the crystal. The electron density $\rho(\vec{r})$ for such a small crystal can be expressed as

$$\rho(\vec{r}) = \Omega(\vec{r})\rho_\infty(\vec{r}) = \Omega(\vec{r})\rho_{lattice}(\vec{r}) \otimes \rho_{uc}(\vec{r}), \tag{2.14}$$

where $\rho_{lattice}$ gives the periodicity of the electron density in the crystal and ρ_{uc} gives the

electron density inside a unit cell. The Fourier transform follows as

$$\rho^{FT}(\vec{Q}) = \frac{1}{(2\pi)^3}\Omega^{FT}(\vec{Q}) * \rho^{FT}_{lattice}(\vec{Q})\rho^{FT}_{uc}(\vec{Q}). \tag{2.15}$$

Thus, the scattering amplitude for a small crystal is proportional to

$$E_{sc}(\vec{R}) \propto \underbrace{\sum_{hkl} \Omega^{FT}(\vec{Q} - \vec{G}_{hkl})}_{\text{geometrical factor } \Gamma(\vec{Q})} \cdot \underbrace{\int_{V_{uc}} \rho_{uc}(\vec{r}) e^{-i\vec{Q}\cdot\vec{r}} d\vec{r}}_{\text{structure factor } F_{hkl}(\vec{Q})}, \tag{2.16}$$

The first term in equation (2.16) is called geometrical factor $\Gamma(\vec{Q})$. For finite crystals, it is expressed by the convolution of the Fourier transformed of the shape function and the crystal lattice. The second term in equation (2.16) is the well-known structure factor $F_{hkl}(\vec{Q})$, it gives the intensity of certain Bragg reflections and is determined by considering the relative positions of all atoms a in a unit cell:

$$F_{hkl}(\vec{Q}) = \sum_a f_a(\vec{Q}) e^{i\vec{Q}\cdot\vec{r}_a}, \tag{2.17}$$

where f_a is the atomic form factor. The atomic form factors can be found in Ref.[111] In experiments we are measuring the intensity distribution around Bragg peaks, the maximum intensity I_{hkl} of the Bragg peak is proportional to the square of the crystal volume V:

$$I_{hkl}(\vec{G}_{hkl}) = |E_{sc}(\vec{G}_{hkl})|^2 \propto |F_{hkl}(\vec{G}_{hkl})|^2 \ |V|^2. \tag{2.18}$$

The integrated intensity $\hat{I}_{hkl}$, however, is proportional to the crystal volume V and follows as:

$$\hat{I}_{hkl} = \int I_{hkl}(\vec{q}) \ d\vec{q} \propto |F_{hkl}|^2 \int |\Omega^{FT}(\vec{q})|^2 \ d\vec{q} \propto |F_{hkl}|^2 \ 8\pi^3 \ V, \tag{2.19}$$

with $\vec{q}$ = $\vec{Q}$ - $\vec{G}_{hkl}$. From these equations we directly see, that the intensity of the reflections is determined by the structure factor F_{hkl}, which is again determined by the relative positions of the different atoms inside a unit cell. In section 2.2, we showed that for the different polytypes in GaAs the relative positions of the atoms in the unit cells vary. For cubic zinc blende, F_{hkl} simplifies to:

$$F_{hkl} = (1 + e^{i\pi(h+k)} + e^{i\pi(h+l)} + e^{i\pi(k+l)}) \cdot (f_{As} + f_{Ga} + e^{i\frac{\pi}{2}(h+k+l)}), \tag{2.20}$$

with the solutions

$$F_{hkl} = 4 \cdot \begin{cases} f_{As} + f_{Ga}, & \text{if } h,k,l \text{ even and } h+k+l = 4n; n \in \mathbb{Z} \\ f_{As} - f_{Ga}, & \text{if } h,k,l \text{ even and } h+k+l \neq 4n; n \in \mathbb{Z} \\ f_{As} \pm i f_{Ga}, & \text{if } h,k,l \text{ odd} \\ 0, & \text{else} \end{cases} \tag{2.21}$$

and for the hexagonal wurtzite reflections $(hk.l)$ the structure factor is:

$$F_{hk.l} = (f_{As} \cdot (1 + e^{-2\pi i\left(\frac{h+2k}{3} + \frac{1}{2}l\right)}) + f_{Ga} \cdot (e^{-2\pi i\left(\frac{3}{8}l\right)}) + e^{-2\pi i\left(\frac{h+2k}{3} + \frac{7}{8}l\right)}). \tag{2.22}$$

A detailed list of the important GaAs Bragg reflections in this work and their structure factors can be found in Ref.[83]

2.4. Electron diffraction

In the chapters 4, 5 and 6, we will use RHEED for the characterization of the crystal structure of nanowires. Therefore, we give a short introduction to electron scattering which is the basis of RHEED. This differs from X-ray diffraction significantly, due to the stronger interaction of electrons with matter, which is related to the nature of the electrons as charged particles. We assume again elastic scattering and due to the high scattering cross section of electrons compared to X-rays, already for thin crystals the assumption of kinematical scattering cannot be upheld. Instead, dynamical processes need to be considered in the description of electron scattering processes. For a full and detailed description of the electron scattering, a n-beam dynamical theory is used. However, in some cases the quite complex description can be simplified to a two beam approximation, where only the incidence beam and one diffracted beam are assumed to be intense.
In the following paragraph, we derive the intensities of the forward-transmitted and the diffracted beam after passing a crystal with thickness d. This section is based on the book of Cowely[112] and details can be found therein. Please note that in this section, we follow the definitions of Ref.,[112] where k is defined as $k = \frac{1}{\lambda}$.
In the two beam approximation the solution for the two Bloch waves of the time-independent Schrödinger equation is:

$$\begin{pmatrix} \kappa^2 - k_0^2 & \nu_{0h} \\ \nu_{h0} & \kappa^2 - k_h^2 \end{pmatrix} \begin{pmatrix} \Psi_0 \\ \Psi_h \end{pmatrix} = 0, \tag{2.23}$$

where κ is the wave vector of the incidence beam inside the crystal and ν are the Fourier coefficients of the periodic crystal potential.

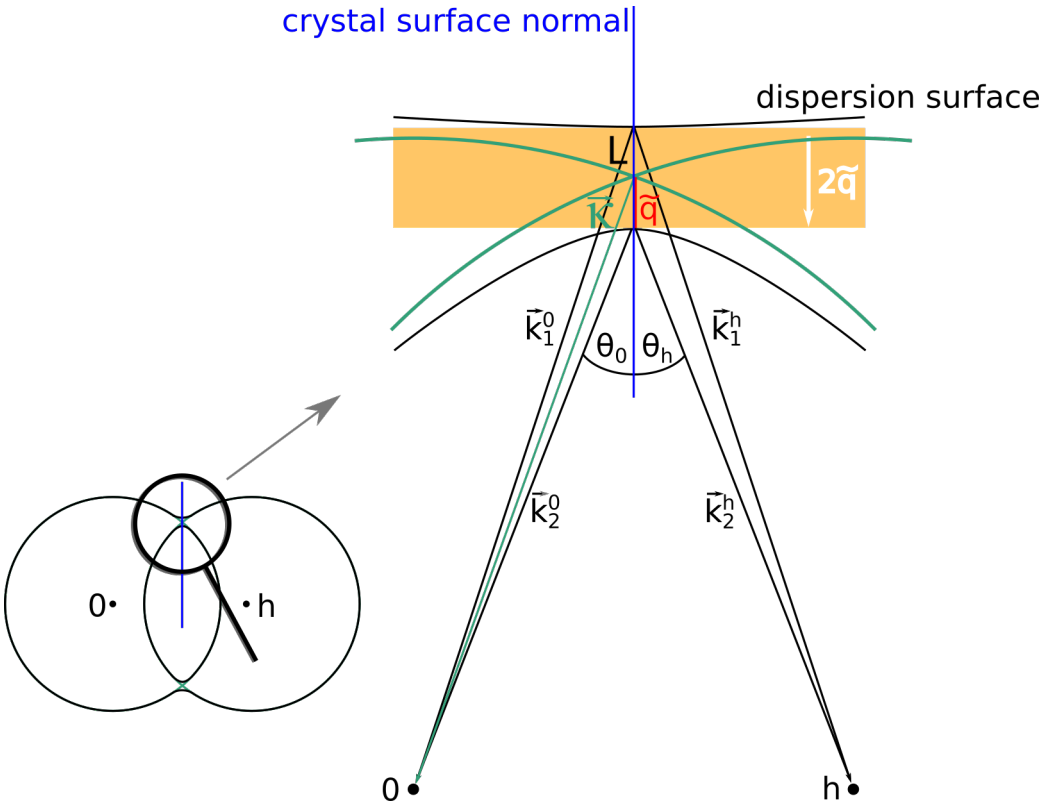

Figure 2.7.: Dispersion surfaces in the two-beam case close to the Lorentz point L. The crystal surface in Laue geometry is depicted in blue. The wave vector inside the crystal $\vec{\kappa}$ is shown in green and the wave vectors $\vec{k}_i^0$ and $\vec{k}_i^h$ (with i=1,2) from the branches 1 and 2 to the reciprocal lattice points 0 and h are illustrated in black.

Figure 2.7 illustrates the dispersion surfaces at the intersection of both Ewald spheres in the two-beam case. In blue the normal of the crystal surface is depicted, which is in our case in Laue geometry. From figure 2.7 follows the relation

$$k_i^{0,h} = \kappa - \tilde{q}\cos\theta_{0,h} \text{ with } i = 1,2, \tag{2.24}$$

where $k_i^{0,h}$ are the wave vectors resulting from the splitting of the dispersion surface into two branches. In case of a thin parallel-sided plate with no back scattering, equation (2.23) modifies to:

$$\begin{pmatrix} 2k\tilde{q}\cos\theta_t & \nu_{0h} \\ \nu_{h0} & 2k\tilde{q}\cos\theta_h \end{pmatrix} \begin{pmatrix} \Psi_t \\ \Psi_h \end{pmatrix} = 0 \tag{2.25}$$

and the total wave in the crystal follows as the sum of the two Bloch waves:

$$\Psi(\vec{r}) = \sum_{i=1,2} \alpha_i e^{2\pi i \vec{k}_i^0 \cdot \vec{r}} + C_i e^{2\pi i \vec{k}_i^h \cdot \vec{r}}, \tag{2.26}$$

where $\alpha_{1,2}$ are the amplitudes of the wave and $C_{1,2}$ are the reflection coefficients.

By finding the correct boundary conditions at the surfaces and by applying the small angle approximation, which is common in transmission electron diffraction, the intensities of the forward-transmitted and the diffracted beams I_t and I_h in the diffraction maximum can be written as

$$I_t = \cos^2\left(\frac{\pi d}{\xi_h}\right) \tag{2.27}$$

and

$$I_h = \sin^2\left(\frac{\pi d}{\xi_h}\right), \tag{2.28}$$

where we considered the relations $|(\vec{k}_2^{0,h} - \vec{k}_1^{0,h})| = 2\ \tilde{q}$ and $\xi_h = 1/2\tilde{q}$, with the extinction distance ξ_h.
If we now introduce the absorption, which means that k is described by a complex number, equation (2.27) and (2.28) are modified to

$$I_t = \frac{1}{2}\mathrm{e}^{-\mu_0 d}\left(\cosh(\mu_h d) + \cos\left(\frac{2\pi d}{\xi_h}\right)\right) \tag{2.29}$$

and

$$I_h = \frac{1}{2}\mathrm{e}^{-\mu_0 d}\left(\cosh(\mu_h d) - \cos\left(\frac{2\pi d}{\xi_h}\right)\right). \tag{2.30}$$

Equation (2.29) and (2.30) describe the intensities of the forwards-transmitted and the diffracted beam after passing a crystal with thickness d in the two-beam approximation with absorption. Both equation are mutually connected by the cosines, giving rise to thickness dependent oscillating intensities, known as 'pendellösung' fringes.
The electron diffraction structure factors are different from those of X-ray diffraction. However, the structure factors can be determined with equations (2.21) and (2.22) and by the atomic form factors of the electron diffraction given in Ref.[111] In table 2.2 the structure factors for the important diffraction spots in this work are summarized.

Table 2.2.: List of structure factors F_{hkl} of the diffraction spots which are important at the RHEED experiments in chapters 4 - 6.

(hkl)	(111)	(220)	(311)	(10.3)
F_{hkl}	14.9	12.1	16.9	8.6

3. The portable molecular-beam epitaxy system

The nanowire growth experiments, which are part of this work, are performed in a special MBE system which is dedicated for *in situ* characterization and growth experiments. The system enables simultaneous *in situ* RHEED and *in situ* XRD experiments at synchrotron beamlines.[113] The so called portable MBE (pMBE) system is a compact custom-designed device which was developed in a collaboration of the Institute for Photon Science and Synchrotron Radiation at the Karlsruhe Institute of Technology and the company Createc. The compact design is required to be compatible with the infrastructure at different synchrotron beamlines, such as the load and the dimension restrictions of the available heavy load-goniometer. Besides the compact design, it features two Be windows which are transparent for X-rays and allow diffraction experiments during nanowire growth with an angular range of ± 23°.

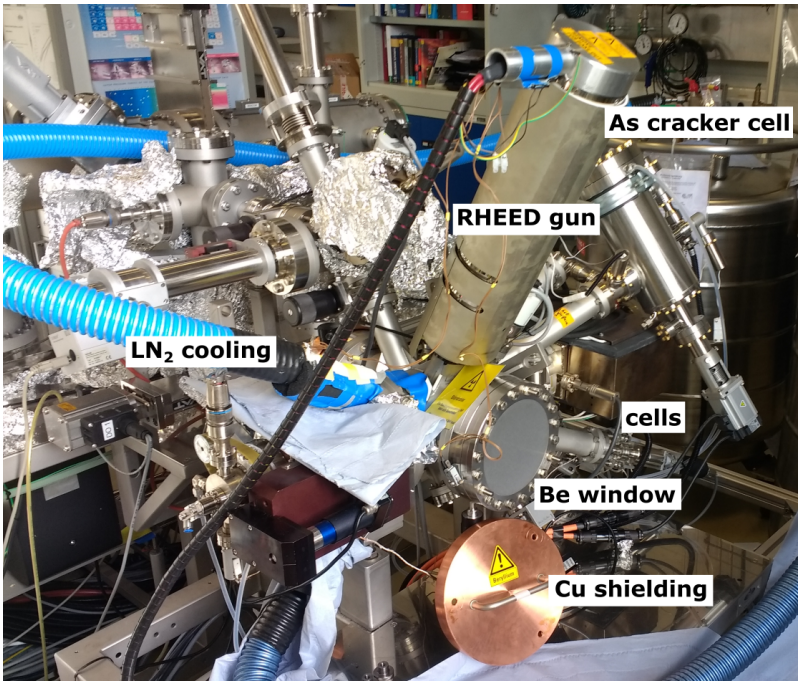

Figure 3.1.: The portable molecular-beam epitaxy system.

An obvious difference to common MBE systems, however, is the changed arrangement of the whole system, as shown in figures 3.1 and 3.2. The substrate is turned by 90° resulting in a vertical orientation of the substrate's surface, whereas at standard MBE systems it is in horizontal orientation facing downwards. Thus, the arrangement of all other attachments are also turned by 90°. Although the arrangement differs from other system, the obtained growth results of common systems and the pMBE system are similar, as demonstrated in Ref.[68] As solid source materials, the pMBE offers elementary Ga, In and Al in three Knudsen evaporation cells, further elementary As is supplied by an Arsenic valved cracker cell (manufactured by Veeco), see figure 3.1. The Arsenic valved cracker cell allows a fast and precise control over the As_4 flux and thus a good control over the nanowire growth. The growth chamber is equipped with a cryoshroud, cooled by liquid nitrogen (LN_2), to improve the vacuum.
The substrate heater holds substrates up to the size of a quarter two inch wafer. As an *in situ* characterization technique it is equipped with a RHEED setup consisting of an electron gun and a fluorescence screen. Additionally, the pMBE has a small storage chamber directly connected to the main growth chamber, in which four samples can be stored. This is essential during *in situ* XRD experiments of nanowire growth, where the system is separated from the load lock. The portable MBE concept has been successfully operated at different synchrotron facilities like the ESRF, the KIT synchrotron KARA and PETRA III at DESY.[101,110,113–115]

3.1. The RHEED setup

The RHEED setup at the pMBE consists of a SPECS RHD-30 electron gun with a tungsten hairpin filament as source for the electron beam. It generates beam energies from 1 to 30 keV with an energy spread of approximately 0.9 eV, which is given by the temperature of the filament. The distance of the electron gun is approximately 20 cm to the substrate and the beam spot size on the sample is below 100 µm at ideal conditions with a maximal divergence of the electron beam below 2°. In standard laboratory use of the pMBE, Cu shielding are placed over the Be windows to protect the environment from any X-ray radiation generated by impinging of the electron beam inside the growth chamber (figure 3.1). To ensure the safety during a growth experiment, the RHEED system is equipped with an interlock system allowing to accelerate electrons only if the shielding is closed. At the synchrotron beamlines, however, the RHEED setup needs to be run while the Cu shielding is removed. Therefore, the RHEED interlock system can be integrated into the beamline interlock system to ensure all safety regulations.

The electron diffraction pattern is visualized on a fluorescent screen with a sample to screen distance of 18 cm. The images are taken with a PCO.pixelfly CCD camera. The camera has a 14 bit dynamic range and a low readout noise. The collection of the CCD data as well as the export of the video frames for further processing are done with Safire, a software provided by CreaTec.

3.2. The portable MBE system integrated at the synchrotron beamline

The results presented in chapter 5 are obtained during experiments at a synchrotron beamline, therefore we are now describing the beamline setup of the pMBE in the following section. In figure 3.2(a), we show an image of the pMBE installed at the Resonant Scattering and Diffraction beamline P09[116] at the PETRA III synchrotron at DESY in Hamburg. In the centre of the image, the pMBE is mounted on the heavy-load diffractometer of the beamline, with the cells facing to the front of the image. The RHEED gun is visible at the top of the pMBE, indicating the RHEED geometry to be from the top left to the bottom right at the image. The X-ray beam enters the pMBE from the right, as marked by the red arrow, and hits the detector at the left (see figure 3.2(b)).

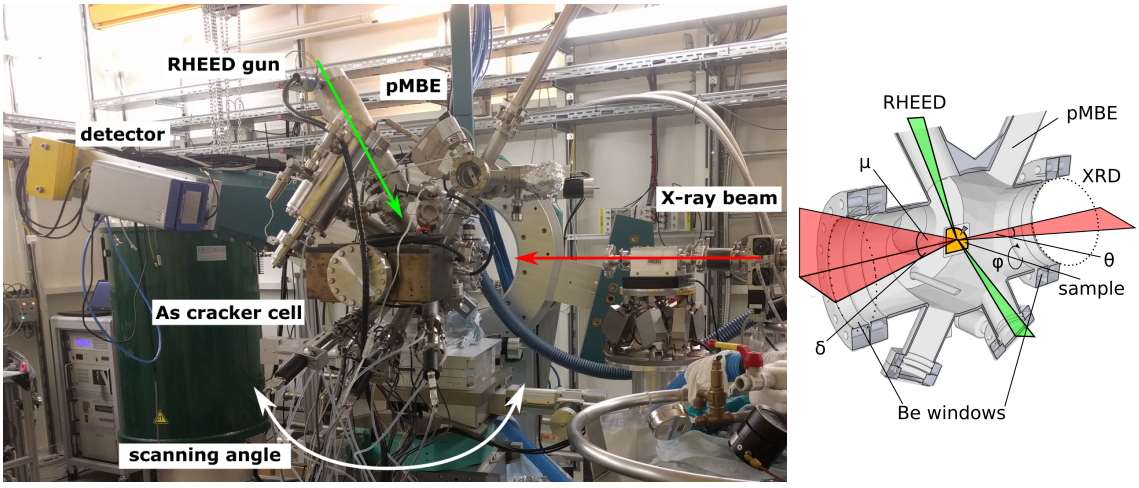

(a) (b)

Figure 3.2.: (a) the portable MBE setup at the Resonant Scattering and Diffraction beamline P09 at DESY. (b) diagram of the portable MBE with RHEED and XRD geometries.

The RHEED setup is directly connected to the pMBE, thus it can be used independently from the XRD experiment. Different XRD Bragg reflections are excited by moving the whole chamber on the goniometer in Bragg condition, including the RHEED setup. This

Table 3.1.: Diffraction angles of asymmetric skew X-ray diffraction geometry at fixed incidence angle of $\theta = 15.5°$ at a X-ray beam energy of 15 keV. The definition of the angles follows figure 3.2(b).

	GaAs			Si	
Reflection	(220)	(10.3)	(311)	(220)	(311)
Bragg angle	11.93°	12.90°	14.03°	12.43°	14.62°
relative azimuthal angle φ	0°	2.33°	4.85°	0.80°	5.85°
μ	13.85°	13.84°	13.97°	14.23°	14.59°
δ	14.42°	15.21°	16.51°	15.23°	17.57°

separation enables parallel RHEED and XRD experiments with reduced interference between both methods.

For the X-ray diffraction experiments, we are using an asymmetric skew X-ray diffraction geometry at fixed incidence angle,[117] which allows to scan the reciprocal space in the desired region by only one motor movement. The scanning angle in this geometry is an azimuthal rotation around the sample normal, realized by a movement of the whole chamber, indicated in figure 3.2(a) by the white arrow. Furthermore, the fixed incidence angle maintains the information depth for the different Bragg reflections. Details on the geometry can be found in Ref.[117] We also follow the authors in the definition of the angles, which are additionally depicted in figure 3.2(b). For the used X-ray beam energy of 15 keV and the fixed incidence angle of $\theta = 15.5°$ the diffraction angles of the important Bragg reflections in this thesis are summarized in table 3.1.

3.3. Typical growth protocols of the portable MBE system

In the following section, we present the standard growth protocol used for the growth of all nanowire samples fabricated in the pMBE chamber during this work. The pMBE was successfully commissioned for nanowire growth in a previous work by Philipp Schroth and a detailed study of the nanowire growth window can be found in his PhD thesis.[68]

The material flux and temperature calibration is important in order to find the correct growth window and to compare the obtained results. The temperature of the substrate heater is calibrated by the desorption temperature of the natural oxide on GaAs substrates. Therefore, epi-ready GaAs substrates are loaded in the growth chamber, followed by a stepwise increase of the substrate temperature, in parallel to the heating the surface reconstruction is analysed by means of RHEED. At the desorption temperature of the oxide, the reconstruction changes and the typical (2x4) respectively the (4x2) reconstruction is discernible, depending on the azimuthal orientation of the substrate with respect to the RHEED beam.

The calibration of the material fluxes is achieved by measuring the intensity oscillations of the specular spot in RHEED while growing 2D - layers of GaAs on GaAs substrates. Close to equivalent fluxes of Ga and As_4 the reconstruction of the pattern changes from (2x4) to (4x2) or vice versa.

The GaAs nanowires were grown by the self-catalysed VLS mode on n-doped Si(111) substrates covered by a native oxide layer. The substrates are provided by Sil'tronix. The oxide layer is a crucial parameter during the growth of self-catalysed GaAs nanowires (compare section 2.1), because on a too thin layer, the Ga droplets cannot form suitable wetting angle necessary to initiate the growth, and a too thick oxide layer prevents the epitaxial connection to the underlying Si. In our case, we used two different batches of substrates with an oxide thickness of 1.8 nm and 2.4 nm measured by optical ellipsometry.

Before loading the substrates into the pMBE, we first perform a chemical cleaning procedure to remove any organic residuals on the substrates' surface. The chemical cleaning consists of typically two cycles of cleaning in Acetone, followed by isopropanol and by deionised water, each step is done in an ultrasound cleaner for 5 min.

Afterwards, the substrates are loaded in the load lock, where they are degassed for 35 min at approximately $T = 300\,°C$ to evaporate possible contaminations and to keep the main growth chamber as clean as possible (the pressure in the load lock after degassing is below 5.0×10^{-8} mbar). The substrates are transferred under UHV conditions to the growth chamber with a base pressure of approximately 3×10^{-9} mbar to 9×10^{-9} mbar.

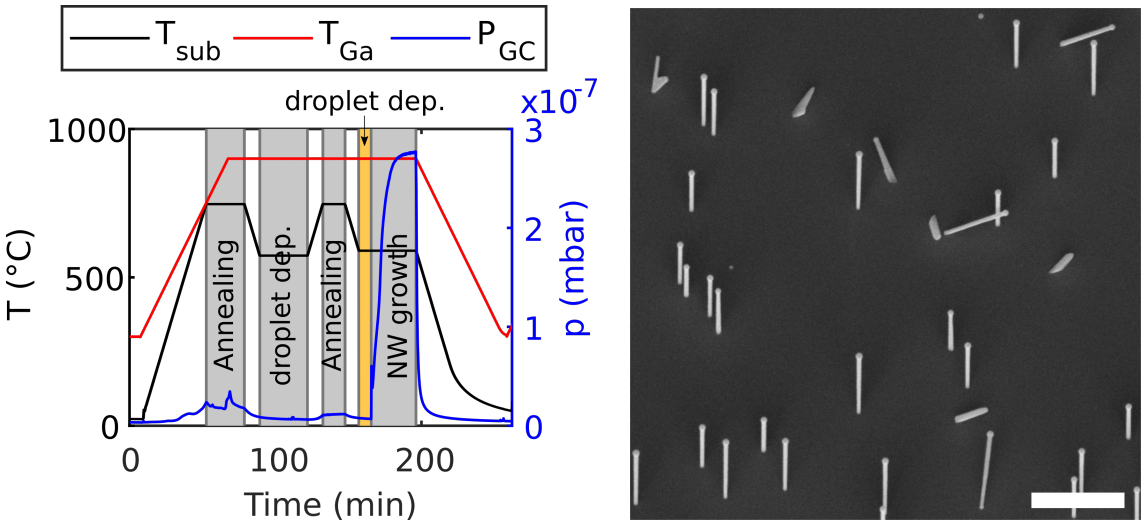

(a) (b)

Figure 3.3.: Example of a typical nanowire growth run in the pMBE system. (a) different steps during nanowire fabrication with temperatures of substrate heater T_{sub} and Ga cell T_{Ga} and the pressure in the growth chamber P_{GC}. (b) Scanning electron micrograph of final nanowires. The scale bar is 1 µm.

The nanowire growth, if not explicitly stated otherwise, is performed according to the so called 'surface modification procedure' (SMP) presented in Ref.,[77] enabling a good control over the nanowire density on the substrate. A typical growth run is shown in figure 3.3(a), where the background pressure in the growth chamber (P_{GC}) as well as the temperature of the Ga cell (T_{Ga}) and of the substrate (T_{sub}) are depicted during the full process.
The growth protocol starts with thermal annealing of the substrate at approximately T_{sub} = 750 °C for 25 min. This first step is important to condition the oxide layer by creating pinholes in the oxide, where later the Ga droplets can accumulate. Furthermore, remaining contaminations on the substrate evaporate, as discernible by the pressure increase in figure 3.3(a). After the first annealing step, T_{sub} is reduced, the temperature during this step determines the number density of nanowires. The lower T_{sub}, the higher the number density. Once the desired substrate temperature (here T_{sub} = 570 °C) is reached, Ga is deposited on the substrate forming small droplets at the pinholes. In our example the amount of Ga equals 8 ML (monolayers) of a 2D layer of GaAs. The third step is again annealing at T_{sub} = 750 °C for 15 min, during this step the Ga reacts with the oxygen of the substrate's native oxide layer and defines the nucleation sites on the substrate by an etching process. At the elevated temperature, the Ga and GaO, which was created by the reaction of the Ga and the oxygen of the substrate's oxide layer, evaporates again and leaves the nucleation site for the nanowires.
After these three steps, the actual nanowire growth takes place at the growth temperature of T_{sub} = 590 °C, at this point we deviate from the presented method in Ref.[77] Instead, we introduce a Ga pre-deposition step, where we again deposit a certain amount of pure Ga, to fill the nucleation sites with Ga droplets (marked in yellow in figure 3.3(a)). In our example, we deposit Ga corresponding 8 ML of GaAs. Immediately after this pre-deposition, we start the supply of As_4 by opening the valve of the cracker cell which initiates the nanowire growth. At this moment, we see in figure 3.3(a), that the background pressure rises quickly above the 1×10^{-7} mbar range, the atmosphere in the chamber is dominated by the As_4. In our example the nanowire growth is performed at an equivalent 2D layer growth of GaAs of 0.08 ML/s and a V/III - ratio of approximately 2.6. After 30 min of growth, the Ga and As_4 supply is stopped. The closing of the As_4 valve results in a fast decrease of the pressure in the growth chamber. A scanning electron micrograph of the resulting nanowires is shown in figure 3.3(b).

4. *In situ* RHEED during growth of vertical nanowires - quantitative analysis

In this chapter we will develop an approach of simulating the intensity evolution of phase-sensitive diffraction spots in RHEED patterns of vertical nanowires. The quantitative analysis of time-resolved *in situ* RHEED diffraction spot intensities opens up new routes for the characterization of structural polytypism in vertical nanowires. The broad availability of RHEED in common nanowire growth equipment and the low barrier for capturing suitable RHEED data is a main benefit of this characterization method. However, the interpretation of RHEED intensities is quite complex. We will introduce a model which allows an estimation of the diffraction spot intensities and by comparison of simulation and experiment it enables quantitative conclusions on structural properties of the nanowires. In particular, it allows to characterize the mean generation probability of the polytypes at the axial growth front in large nanowire ensembles.
In section 4.1 we will introduce *in situ* RHEED of vertical nanowires, explain features which are present in typical RHEED patterns, correlate these features to properties of the samples and we will explain the dependence of the pattern to azimuthal changes of the substrate. In section 4.2 we begin with the fundamental interactions of the electron beam with the nanowires. We will focus on the interaction of the electrons with the single nanowires, with the whole nanowire ensemble and on their temporal changes because we are dealing with *in situ* RHEED during nanowire growth. Afterwards, we will condense these findings with appropriate assumptions into a simulation model in section 4.3 and we will discuss its important parameters and their impact on typical intensity evolution of RHEED diffraction spots. Furthermore, the possibilities and restrictions of the developed model will be discussed. Finally, in section 4.4 we will present the experimental determination of setup parameters, which are needed for the simulations. Parts of this chapter are published in publication I.[118]

4.1. Introduction to RHEED of vertical nanowires

Generally, the main purpose of RHEED is the characterization of thin films during and after growth. During growth, *in situ* RHEED gives direct feedback on the crystal structure and surface quality of the thin film and allows control of the growth conditions.[119,120] For non-planar structures the RHEED pattern changes from reflection geometry to transmission geometry,[120] where the electrons diffract while transmitting the nanostructures. Exemplary RHEED patterns for these geometries are shown in figures 4.1 and 4.2. The reflection geometry features typically streaky RHEED patterns, as shown in figure 4.1, whereas in transmission geometry distinct diffraction spots are present caused by the diffraction of the electrons during transmitting the nanostructures, as shown in figure 4.2.

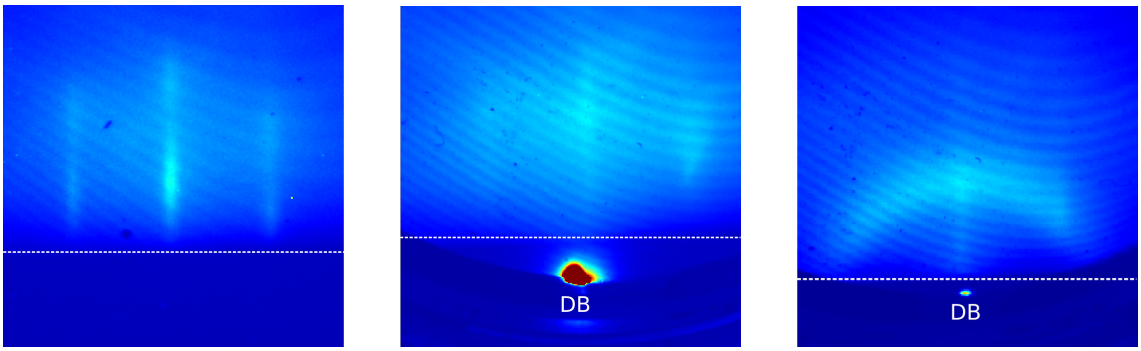

(a) Thin native oxide layer. The surface reconstruction is still visible underneath the polycrystalline SiO_x layer.

(b) Thicker native oxide layer. The surface reconstruction is barely visible underneath the polycrystalline SiO_x layer, instead a diffuse intensity distribution is discernible.

(c) Deposition of Ga before the nanowire growth: liquid Ga on substrate gives rise to a circular intensity distribution.

Figure 4.1.: Experimental RHEED patterns of Si(111) substrates covered with a native oxide layer before the nanowire growth. The dashed lines indicate the horizon and DB the direct beam.

At the onset of each nanowire fabrication, the reflection geometry is always given because RHEED is probing only the surface of the planar substrate, which is in our case a Si(111) substrate covered with a thin native oxide layer. Already at this stage RHEED gives valuable information for the subsequent nanowire growth. In section 2.1, we discussed the importance of the oxide layer covering the substrate in the context of nanowire nucleation. The surface sensitivity of RHEED in reflection geometry, which is a result of the small vertical penetration depth of the electrons into the substrate, allows direct estimation of the quality of the native oxide layer. In figure 4.1(a) a RHEED pattern of a Si(111) surface covered with a comparable thin SiO_x layer is shown, in contrast figure 4.1(b) shows a Si(111) surface covered with a thicker SiO_x layer. While for the thinner oxide layer the reconstruction of the underlying Si is still visible, it is barely discernible for the substrate

with the thicker oxide layer. The electrons cannot penetrate deep enough to probe the underlying bulk Si and the pattern consists mainly of a diffuse intensity distribution originating from the polycrystalline SiO_x. During the further steps of nanowire growth, typically Ga is deposited on the substrate. This can be either to create and control the amount of nucleation sites on the substrate or to initiate the nanowire growth. Again, RHEED allows us to monitor these deposition steps. Due to the deposited liquid Ga on the substrate, a circular intensity distribution arises as shown in figure 4.1(c). It originates from the mean interatomic distance in the liquid without preferential orientation, which is also known from powder diffraction experiments. From the intensity of the ring one can conclude on the amount of the deposited Ga.
The main focus of this work, however, is RHEED during nanowire growth. Therefore, we will now focus on the transmission geometry of RHEED, which is given during the growth of vertical free-standing nanowires. In this section, we explain the typical RHEED patterns of GaAs nanowires in transmission geometry and discuss the origin of the diffraction spots in these patterns. The Ewald sphere for high energy electrons is large and intersects the reciprocal lattice nearly perpendicular in forward direction, thus several reciprocal lattice points (RLP) can be excited at the same time. The positions and relative intensities depend on the crystal structure and the material system (compare sections 2.2 - 2.4). In figure 4.2 exemplary RHEED patterns of self-catalysed GaAs nanowires along different azimuthal orientations of the substrate with respect to the incident electron beam are depicted. The left images show the experimental RHEED pattern with the diffraction spots located at different positions, the Miller indices of these spots are presented in the middle figure and the relative orientation of nanowires and electron beam is indicated on the right side. Parts of the diffraction pattern can be shadowed by either the sample itself or by other parts inside the growth chamber, for example by the frame of the fluorescence screen. We mark these shadow borders by dashed lines in the images. Due to the size of the electron beam and the grazing incident angle, a part of the electron beam might pass the sample without interaction, thus it can be detected as well on the fluorescence screen, indicated by (DB).

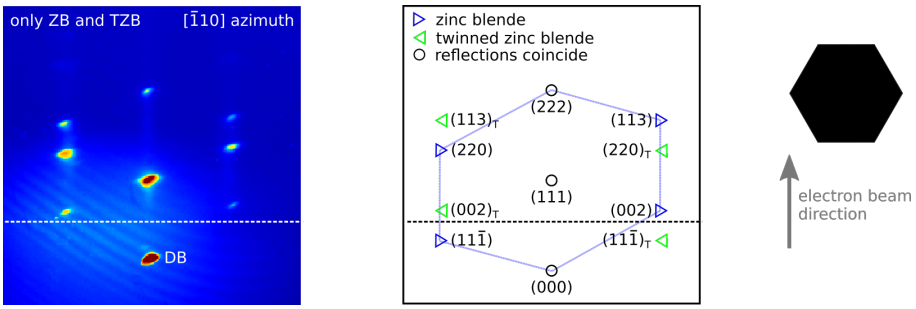

(a) RHEED pattern of nanowires with ZB and TZB crystal structures in the [1̄10] azimuth.

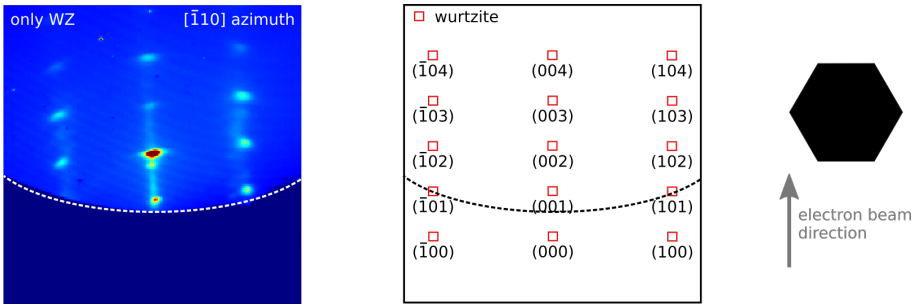

(b) RHEED pattern of nanowires with WZ crystal structure in the [1̄10] azimuth.

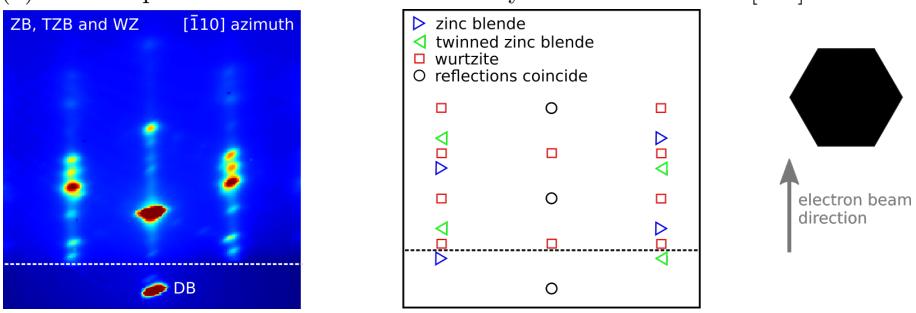

(c) RHEED pattern of nanowires with ZB, TZB and WZ crystal structures in the [1̄10] azimuth.

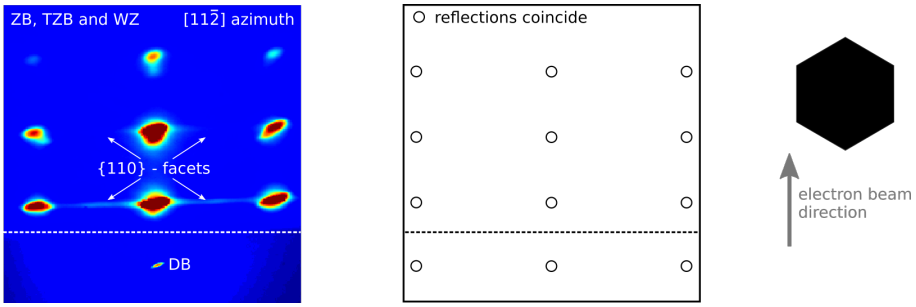

(d) RHEED pattern of nanowires with ZB, TZB and WZ crystal structures in the [11̄2] azimuth.

Figure 4.2.: Experimental RHEED patterns of vertical GaAs nanowires in different azimuthal orientations (left) and the corresponding indices of the reflections (hkl) (center) with the relative orientation of nanowire cross section and electron beam (right). The dashed lines indicate the horizon and DB the direct beam.

The most important azimuthal orientation of the substrate and thus the nanowires with respect to the electron beam is along the $[\bar{1}10]$ azimuth. In this orientation, we can identify Bragg reflections which are characteristic for different crystal phases occurring in the nanowires, which we introduced in section 2.2. In figure 4.2(a), a RHEED pattern of nanowires composed of only ZB and TZB is depicted. The pattern has the characteristic appearance of a distorted hexagon. The central symmetric reflections are insensitive to any crystal phase, because at this position both the ZB and the TZB reflections coincide (marked by a black circle). The asymmetric reflections, however, split for the different polytypes, as can be seen in the figure in the centre. Here the diffraction spots are labelled with (hkl) indices for the reflections in the orientation of the substrate and $(\mathrm{hkl})_\mathrm{T}$ for the reflections of the rotational twin. The diffraction pattern of the wurtzite crystal structure is clearly distinguishable and has a rectangular appearance. The experimental RHEED pattern as well as the indices of the reflections for purely WZ nanowires are shown in figure 4.2(b). However, in typical GaAs nanowires all three polytypes are present, consequently the diffraction pattern consists of all respective diffraction spots. Such a case is shown in figure 4.2(c). For the later analysis in chapters 5 and 6, the most important reflections are the three intense spots on the left and right side in the experimental pattern, labelled as (220), (113) and (103). These reflections are phase-sensitive, do not coincide with other reflections and have comparable diffraction angles.

By changing the azimuthal orientation of the nanowires, the diffraction pattern changes and becomes phase-insensitive. In the $[11\bar{2}]$ azimuth the diffraction spots for the different crystal phases overlap and consequently a characterization of the polytypism is not possible (figure 4.2(d)). However, in this azimuth the electron beam is parallel to the facets of the hexagonal cross section of the nanowires, resulting in intensity streaks which elongate the symmetric reflections. The occurrence of these streaks enables us to conclude on the successful growth of nanowires on the substrate already during growth before further characterization e.g. by SEM.

In some cases, the RHEED pattern can become even more complicated and one observes additional spots and features in the pattern, which cannot be explained purely by the reciprocal lattice of the different polytypes in the nanowires. However, we want to emphasize that the following features in the RHEED patterns are at the same time limiting factors for the analysis and the applicability of the model which will be presented later in this chapter.

In figure 4.3(a), we observe beside the already known diffraction peaks of the polytypic nanowires, a circular intensity distribution. As indicated in the figure below the experimental RHEED pattern, the circle intersect only the ZB and TZB peaks. We attribute this feature to small crystalline objects, which are not epitaxially connected to the Si substrate and thus have a random orientation giving rise to this intensity distribution.

In contrast, figure 4.3(b) shows additional spots between the symmetrical reflections,

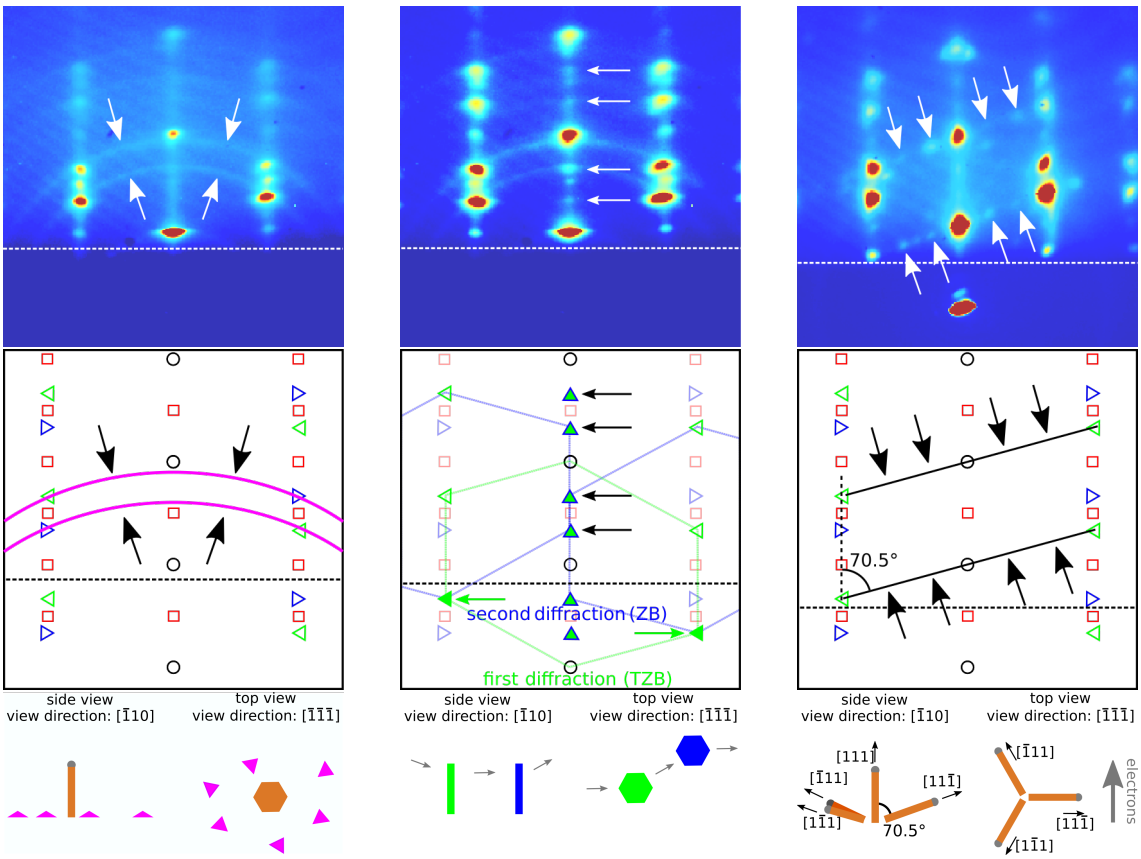

(a) RHEED pattern with intensity contribution due to non-epitaxial GaAs on the substrate.

(b) RHEED pattern with additional diffraction spots due to multiple diffraction in ZB and TZB segments.

(c) RHEED pattern of nanowires grown in different {111} - directions.

Figure 4.3.: Experimental RHEED patterns of vertical nanowires with features, which cannot be explained purely by the reciprocal lattice of the polytypes. The dashed lines indicate the horizon. The arrows mark the additional features which are explained in the text.

marked with arrows. These spots can be explained by electrons which first scatter in a TZB segment of the nanowire and afterwards a second time in a ZB segment or vice versa. In the figure, we illustrate these features by the ZB reciprocal lattice introduced before, where we saw that the ZB and TZB reciprocal lattices have the appearance of distorted hexagons. The first diffraction event gives rise to the reciprocal lattice points marked with green solid triangles (TZB). In the second diffraction event, these green solid triangles act as origin for a second reciprocal lattice, but this time the diffraction happens in a ZB segment, indicated by the blue distorted hexagon. The resulting intensity spots are depicted as green triangles with a blue frame. However, we emphasize that we could observe these RHEED patterns only for thin nanowires. The last example illustrates the case where not all nanowires are vertically aligned but some of them growing in equivalent

{111} - directions on the substrate. Then additional diffractions spots appear, as shown in figure 4.3(c). Since the electron beam is orientated along $[\bar{1}10]$ azimuth, only one of the three possible {111} - directions is perpendicular to the electron beam and thus can be excited, in our case it is the $[11\bar{1}]$ - direction. The angle between the nanowires along [111] and those along $[11\bar{1}]$ is 70.5° and consequently the indicated spots are simply the reciprocal lattice tilted by this angle. At the bottom of figure 4.3(c), the different {111} - directions are depicted from top and from side view.

The variety of RHEED patterns reflects the possible applications of RHEED, consequently in literature *in situ* RHEED during nanowire growth is used to analyse many different aspect of their fabrication. It is used to identify and determine the nucleation time of nanowires on the substrate by measuring the time from starting the supply of the material fluxes to the appearance of the diffraction spots,[121–123] or to identify the transformation from a 2D to 3D growth by following the characteristic changes in the diffraction patterns.[122–124] Cheze *et al.* could identify even small tilts of the nanowires during growth by carefully analysing the splitting of the diffraction spots in the pattern.[125] A different characteristic of *in situ* RHEED was used by Somaschini *et al.*: during the consumption of the catalyst particle in the VLS growth, they monitored and characterized the formation of flat top facets on the nanowires by the onset of an elongation of the RHEED spots perpendicular to the substrate's surface.[126]

By analysing the phase-sensitive reflections of *in situ* RHEED during the VLS growth of self-catalysed GaAs nanowires, Cirlin *et al.* could conclude that in their case the nanowires are mainly composed of ZB and TZB, while at the end of growth, when the liquid catalyst particle was consumed, WZ forms as evidenced by the occurrence of additional WZ peaks. They confirmed this by TEM.[127] A similar approach was suggested by Jo *et al.*, where they combined *in situ* RHEED with *ex situ* TEM to get a comprehensive picture of the crystal structure during growth of InAs nanowires.[128]

More advanced studies interpret the intensity evolution of certain diffraction spots. Rudolph *et al.* could conclude on different growth modes (vapour-solid and vapour-liquid-solid) during the synthesis of GaAs nanowires by following the intensity evolution of only one diffraction spot in the RHEED pattern.[129] By tracking the intensities of phase-sensitive diffraction spots in the RHEED pattern of Au-catalyzed GaAs nanowires, Breuer *et al.* could discriminate between the scattering contributions of nanowires and crystallites.[130]

A very promising application of *in situ* RHEED was proposed by Dursap *et al.*, where they used it to monitor the crystal structure and optimised the material fluxes in such a way that they could grow extended wurtzite segments in GaAs nanowires and switch intentionally from one polytype to another,[131] however without a structural characterization directly by RHEED.

All these reports demonstrate the wide variety of *in situ* RHEED applications, however they also show a current drawback of *in situ* RHEED, which is the limitation to only qualitative

observations. The last-mentioned publications, in particular, track the intensity evolution of diffraction spots, but without any quantified interpretation of the measured intensities or conclusion on the evolving crystal volume. Until now, to our knowledge, no approach exist to obtain quantitative information about the crystal structure by *in situ* RHEED during nanowire growth.
The ability to follow quantitatively the evolution of the crystal structure would give deeper insight into the formation of polytypism in nanowires or of nucleation processes and thus increase the control over nanowire growth. The quantitative analysis of RHEED intensities would be a great progress to establish a laboratory based and relatively easy accessible *in situ* characterization technique for the crystal structure of vertical nanowires.

4.2. Quantitative analysis of the polytypism by time-resolved *in situ* RHEED during growth of vertical nanowires

In this section, we discuss the essential interactions of electrons with the nanowires and estimate their effects on the diffraction process. Our aim is to develop an understanding of their influences on the intensity evolution. Afterwards, we condense these findings into a model which is capable of simulating the intensity evolution of phase-sensitive RHEED diffraction spots of polytypic vertical nanowires during growth.
For the development of a better quantitative interpretation of time-resolved RHEED patterns, we include the estimations of (1) the interaction of high-energy electrons with the individual nanowires in dependence on their crystal structures, mean radius and shape, (2) the mean interaction with the nanowire ensemble as a function of the nanowire density, the positional distribution and on instrumental parameters, and (3) the temporal development of these factors as a function of the growth dynamics.
We will show that in the transmission geometry of RHEED, where the electrons impinge nearly perpendicular to the nanowire growth axis, the electron absorption in the nanowires lead to shadowing of the incidence electron beam. In particular, the slightly inclined incidence direction of the electron beam with respect to the mean substrate surface has the effect that not the full nanowire height uniformly contributes to the scattering signal. Usually, there remains a non-shadowed part next to the apex of the nanowires, which will always be fully illuminated. Aiming towards height-selective information of polytypism, we will make targeted use of electron shadowing effects, which were observed in literature before, though without any discussion.[128–131]

4.2.1. Electron beam diffraction by a single nanowire

We start our discussion with the interaction of the electron beam and the individual nanowires. For the description of the diffraction of high-energy electrons by the quite perfect crystalline nanowires we need to consider the influences of absorption and multiple scattering. We saw in section 2.4 that in the dynamical diffraction theory in the conventional two-beam Laue case, the intensities of the forward-transmitted and diffracted beams of a crystal of thickness d, can be written in the diffraction maximum as[112]

$$I_t = \frac{1}{2}\mathrm{e}^{-\frac{d}{\Lambda_0}}\left(\cosh\left(\frac{d}{\Lambda_h}\right) + \cos\left(\frac{2\pi d}{\xi_h}\right)\right), \tag{4.1}$$

$$I_h = \frac{1}{2}\mathrm{e}^{-\frac{d}{\Lambda_0}}\left(\cosh\left(\frac{d}{\Lambda_h}\right) - \cos\left(\frac{2\pi d}{\xi_h}\right)\right), \tag{4.2}$$

where we substitute the absorption coefficient μ_0 and μ_h with the mean free path length Λ_0 and Λ_h, respectively (compare to the equations (2.29) and (2.30)). Λ_0 corresponds to the mean free path length of electrons, Λ_h to the influence of the imaginary part of the crystal structure factor giving rise to anomalous absorption (so-called Borrmann-effect) and ξ_h is the Pendellösung length or extinction length due to multiple diffraction. The forward-transmitted and diffracted beam intensities I_t and I_h are mutually connected by the Pendellösung phenomenon, giving rise to thickness dependent oscillating intensities, known as Pendellösung fringes.

In figure 4.4 different nanowire cross sections are depicted: a hexagonal cross section with two different orientations with respect to the electron beam, as well as a circular nanowire cross section. In the hexagonal case, with electron incidences *perpendicular* to the facets, the diffraction can be modelled by two wedge-shaped side pieces enclosing a central cuboid part of constant thickness. In the complementary case of electron incidence *parallel* to the facets, it can be modelled by an arrangement of wedges with cut tips. As a consequence of equations (4.1) and (4.2) and of the varying electron path lengths within the cross sections, both the forward-transmitted and the diffracted intensities I_t and I_h oscillate along the x-axis, whereby their Pendellösung fringes are mutually phase shifted, as shown in the bottom panel. The additionally shown non-oscillating mean centre curve in blue is obtained by omitting the Pendellösung terms in equations (4.1) and (4.2), thus it only considers attenuation by ordinary and anomalous absorption. The colour code in the top panel illustrates the mean diffraction contribution according to the mean centre curves of the bottom panel.

In the further discussion we limit ourselves to the case of a hexagonal nanowire cross section, where the electron beam is *perpendicular* to the facets. In this arrangement, the phase-sensitive diffraction spots of vertical GaAs nanowires are present (compare to figure 4.2). Therefore, the nanowire becomes increasingly opaque towards the central cuboid

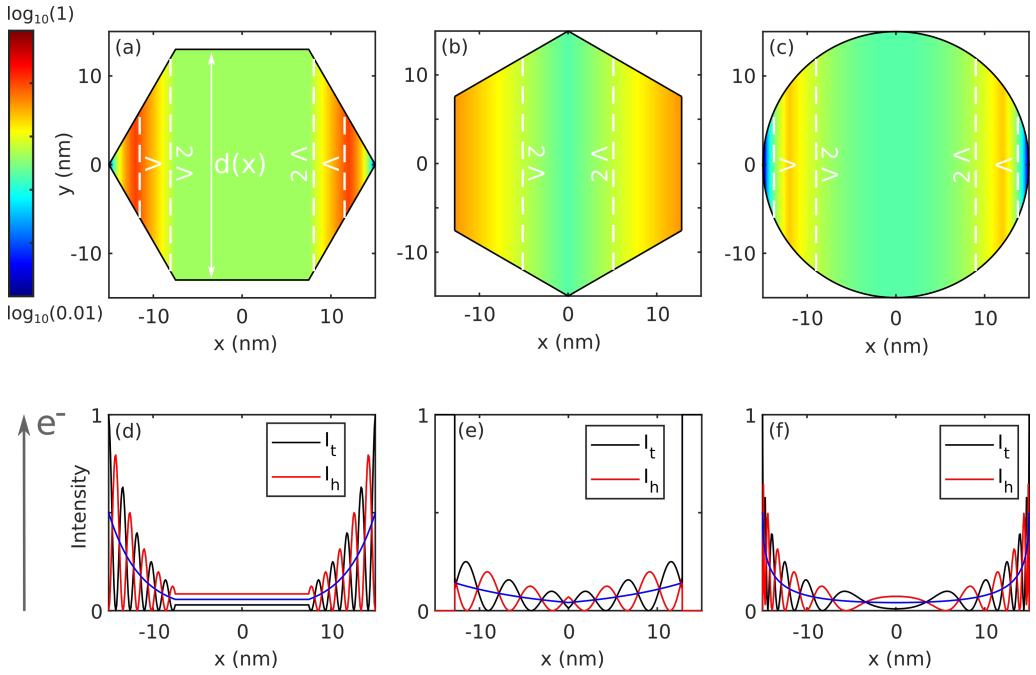

Figure 4.4.: Illustration of electron beam diffraction by a nanowire in dependence of the cross section (beam direction along y direction). Top panel: nanowire cross sections for $D_c = 30\,\text{nm}$, the thickness d in beam direction varies as a function of x. The positions where d=Λ and d=2Λ for Λ=12 nm are marked. The colour code illustrates the mean diffraction contribution according to the centre curve of (d) - (f). Bottom panel: forward-transmitted and diffracted intensities I_t and I_h as a function of x (perpendicular to the beam direction) for $\Lambda_0 = 12\,\text{nm}$, $\xi_h = 5.6\,\text{nm}$, $\Lambda_0/\Lambda_h \approx 0.1$. The mean center curve, plotted in blue is obtained by omitting the Pendellösung terms.

region for both the diffracted and the forward-transmitted beam contributions, or, *vice versa*, increasingly transparent towards the two wedge tips.

If we now integrate the forward-transmitted and the diffracted intensity curves in the bottom panel of figure 4.4 along x over the complete circumference diameter D_c of the nanowire hexagon as a function of D_c, one obtains the curves in figure 4.5(a), where for comparison the intensity curves and their mean centre curves for two different electron mean free path lengths Λ are drawn. Roughly speaking, the internal absorption leads to a so-called *self-shadowing* of the diffracted and forward-transmitted beam contributions by the nanowire.

For small nanowire diameters, the mean centre curves first increase with D_c and pass through a Λ-dependent maximum, before converging to a Λ-dependent constant value. This value corresponds to the diffraction contribution arising exclusively from the semi-transparent wedge tip regions.

If we allow for tapering effects of the nanowires, the additional variation of the nanowire diameter over the examined nanowire height results in further damping of the Pendellösung

fringes, which is shown as red curve in figure 4.5(a). However, tapering does not have a significant influence on the mean diffracted intensity contribution of the whole nanowire, which essentially depends on the mean diameter averaged over the illuminated nanowire height.

To summarize our findings, the behaviour of the forward-transmitted and the diffracted intensities averaged over a single nanowire essentially depends on the energy dependent mean free electron path length Λ, on the shape and size of the nanowire cross section and on the orientation of the cross section with respect to the incident electron beam. [132]

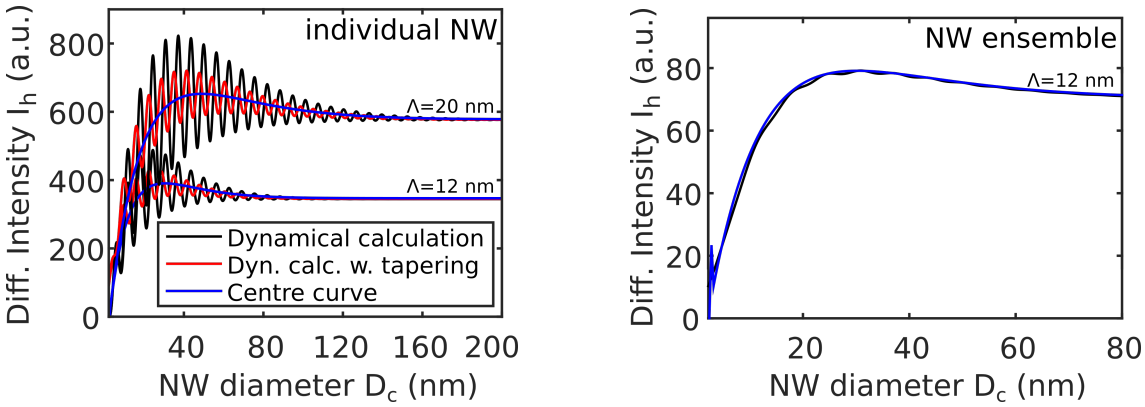

(a) (b)

Figure 4.5.: Diffracted intensity integrated along x over D_c as a function of D_c: (a) of a single nanowire for two mean free path lengths Λ without tapering (black) and with tapering (red). The mean centre curve is shown in blue. (b) mean centre curve (blue) and mean diffracted intensity (black) integrated over the nanowire cross section and averaged over several thousand nanowires with small diameter variation, responsible for the attenuation of the Pendellösung fringes. A Gaussian distribution of the nanowire radius with a standard deviation of 2 nm is used.

4.2.2. RHEED by stationary nanowire ensembles

The typical dimension of the electron beam in RHEED is such that several thousand individual nanowires are probed at the same time. Considering all nanowires of the ensemble to contribute incoherently to the diffracted signal, the diffracted intensity of the ensemble is equal to the sum of all individual intensity contributions. If we assume a statistically homogeneous ensemble with a slight fluctuation of nanowire diameters this also results in rapidly vanishing 'Pendellösung' oscillations so that practically only the first part in the parenthesis of equations (4.1) and (4.2) remains to be considered. In figure 4.5(b), the overall intensity of the diffracted beam of such a nanowire ensemble is plotted together with the mean centre curve. The overall intensity is calculated by the complete equations (4.1) and (4.2) and an exemplary Gaussian radius distribution with a standard deviation

of 2 nm, which is justified for all our samples in this work. Moreover, quantitative RHEED analysis employs the intensity integrated over the whole RHEED spot of a given reciprocal lattice point. This corresponds to integration over the angular divergence and the energy spread of the electron beam, further attenuating the Pendellösung fringes. Performing purely radial growth experiments we have found no evidence for radius dependent intensity fluctuations even for small nanowire diameters. On the basis of these arguments we omit the Pendellösung terms in the following discussion.
For the precise consideration of multiple scattering, we need exact values for Λ_0 and Λ_h, which are not available in our case. Instead, we approximate an effective Λ, which can be determined experimentally as will be shown in section 4.4.2. For the typical dimensions of the nanowires, this approximation deviates only moderately from the considerations with normal and anomalous absorption effects, as illustrated in figure 4.6. There we plot the intensity decay without anomalous absorption in black, which we will use later as the effective Λ, and for specific Λ_0/Λ_h – ratios in blue, red and green. The ratios are derived from typical values known by TEM. From figure 4.6, we conclude that for the typical dimensions of nanowires, as indicated by the dotted line, the variation of the graphs are moderate. Thus, in the following we proceed with an effective Λ in our model.

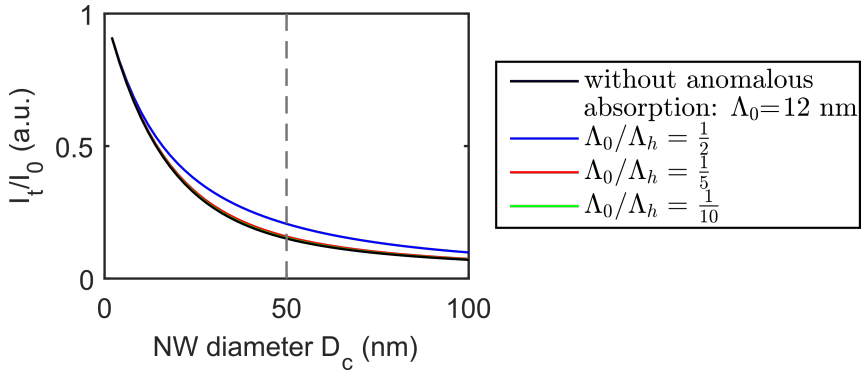

Figure 4.6.: Relative forward-transmitted intensity I_t/I_0 as a function of D_c for different Λ_0/Λ_h – ratios. The variation for realistic Λ_0/Λ_h – ratios is low within the diameter of typical nanowires (indicated by the dashed line), thus we can approximate an effective Λ.

In the figures 4.7(a) and 4.7(b) the diffracted and forward-transmitted intensities for the three introduced cross sections and by omitting the Pendellösung terms and applying an effective Λ are shown. For the three cross sections, the diffracted intensity I_h shows different graphs as a functions of the nanowire diameter D_c, depicted in figure 4.7(a). For the hexagonal cross section with facets perpendicular to the beam direction, the diffracted intensity stabilizes at a high intensity level, as discussed before. This is opposite to the other cross sections, where I_h converges to nearly zero at large nanowire diameters. The mean free path length Λ determines the level of the diffracted intensity, as well as the diameter at which the maximum occurs.

In Figure 4.7(b) we illustrate the averaged attenuation of the electron flux due to absorption during transmission in GaAs nanowires for the different cross sections and different values of the electron mean free path length Λ. For beam energies of 20 keV - 30 keV in GaAs, we expect Λ values of approx. 10 nm - 25 nm.[133,134] For these Λ values on average 15 % respectively 30 % of the incident intensity hitting one single nanowire remains in the forward-transmitted beam, assuming hexagonal nanowires with circumference diameters of 50 nm, which may then hit a subsequent nanowire on its path, but with a strongly reduced mean flux density.

The forward-transmitted intensities are normalized to the incident intensity and both are integrated along the nanowire. Therefore, the relative intensity always decreases with increasing nanowire diameter D_c. Even in the case of electron incidence *perpendicular* to the facets, the absolute diffracted and forward-transmitted intensity integrated over the nanowire converges to finite, non-zero minimum intensity values, arising from the outermost wedge regions, which always remain semi-transparent.

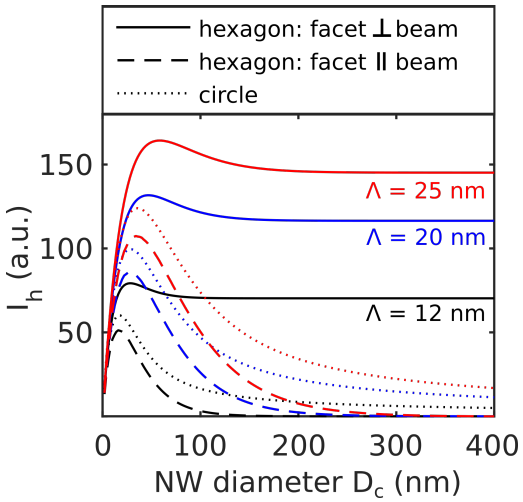

(a) Diffracted intensity I_h passes through a Λ-depended maximum and converges afterwards to an again Λ-depended value.

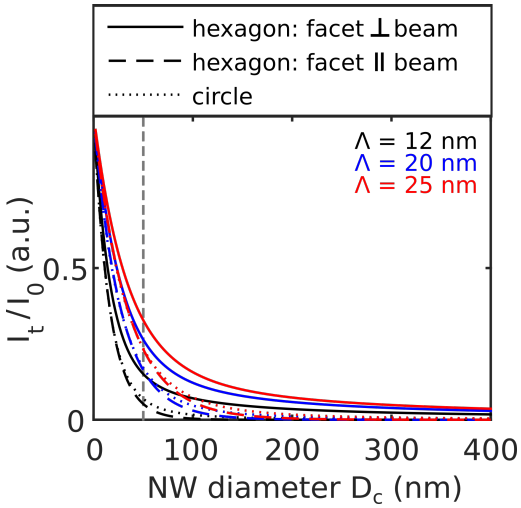

(b) Relative forward-transmitted intensity I_t/I_0 drops quickly within the dimension of a typical nanowire, which is around 50 nm.

Figure 4.7.: Diffracted intensity I_h and relative forward-transmitted intensity I_t/I_0 integrated along the nanowire for different nanowire cross sections and different mean free path lengths Λ.

In other words, beside the *self-shadowing effect* described in section 4.2.1, which limits the diffraction contribution of a single nanowire, each individual nanowire additionally causes a shadow on the geometrical electron beam path behind the nanowire. The precise shadowing conditions behind the nanowire depend again, aside from D_c on the shape and the azimuthal nanowire orientation. Within reasonable precision, this situation can be accounted for by introducing an *effective shadow diameter* D_{shad}, which takes the related

local variation of transmission sufficiently into account. In such a way the incomplete shadowing of a nanowire of given D_c, shape and orientation (e.g., due to the remaining transmission at the wedge tips) equals a complete electron shadow corresponding to an effective diameter D_{shad}.
The inclined angle of incidence of the electron beam α with respect to the substrate surface results in a decreasing height of the nanowire shadow h_S as a function of the distance from the nanowires, as shown in figure 4.11. The lower part of a nanowire may become shadowed while the top part will still remain illuminated by the full primary flux density. In the following, the height of this fully illuminated upper part will be called *illumination height* λ, and the mutual shadowing of the nanowires *ensemble-shadowing*.

4.2.3. Structure dynamics during nanowire growth

The previous two sections dealt with the general aspects of electron beam - nanowire interaction. However, in order to reach conclusions on temporal changes of the crystalline properties of the nanowire ensemble from quantitative RHEED, the underlying RHEED simulation model needs to relate the dynamics of the signals to suitable growth models. This would allow simulation of the evolution of the individual nanowires or crystallites during growth and estimation of the evolution of the intensities from the complete nanowire and crystallite ensembles.

Table 4.1.: Determination of growth rates.

nanowires	
$m_{axial}^{NW} = \frac{h_f^{NW}}{t_f}$	axial growth rate
$m_{facet} = \frac{r_{f,b}^{NW} - r_0^{NW}}{t_f}$	facet growth rate
$m_{tapering} = \frac{r_{f,t}^{NW} - r_{f,b}^{NW}}{t_f}$	tapering growth rate
crystallites	
$m_{axial}^{cry} = \frac{h_f^{cry} - h_0^{cry}}{t_f}$	axial growth rate
$m_{radial} = \frac{r_f^{cry} - r_0^{cry}}{t_f}$	radial growth rate

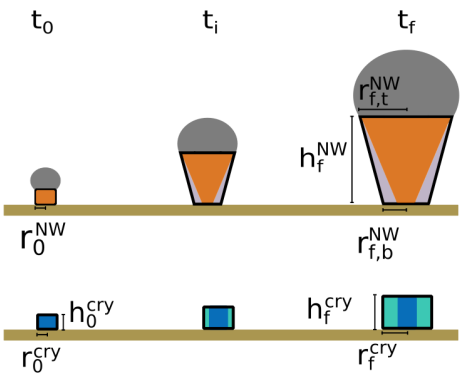

Figure 4.8.: Growth model of nanowires and crystallites. Illustrated parameters are used to determine the growth rates.

In section 2.1, we introduced different contributions of crystal growth which lead to variation of height, shape or crystal structure of the nanowires. These contributions result in a temporal evolution of size, shape and crystal structure of nanowires and crystallites which can be described by axial and radial growth rates, whereby the latter distinguishes tapering and facet growth in case of nanowires. The increase in height of nanowires and

crystallites is characterized by their respective axial growth rate $m_{axial}(t)$ averaged over the ensembles and their radial size with the corresponding radial growth rates ($m_{radial}(t)$). For the nanowires, the radial growth rates split in $m_{facet}(t)$ and $m_{tapering}(t)$.
If these growth rates can be supposed to be linear, such a linear model manages with a few parameters only, namely the growth time t_f, the initial object shape, and three constant growth rates, or equivalently, with the initial and final object shapes. The growth rates used in our simulation model can be found in table 4.1. Figure 4.8 illustrates the main structure parameters used in our model. The intensity evolution of the RHEED patterns of our samples could already be modelled sufficiently precise with this simple model. However, the RHEED simulation model could be easily extended to incorporate more accurate growth models, as presented elsewhere.[76,99,101,135]

4.2.4. Dynamics of ensemble-shadowing

During nanowire growth, self-shadowing and ensemble-shadowing are not constant and their dynamics depends on the evolution of the nanowire shape. For the ensemble-shadowing besides the mean height and the averaged size of the nanowire ensemble, its number density and positional distribution, as well as instrumental parameters like the illumination geometry of the RHEED setup play an important role.
We account for the positional distribution of the nanowire ensemble by Monte Carlo simulations and assume uniformly distributed random nanowire positions over the substrate, but also other appropriate statistical distributions can be easily implemented into Monte Carlo simulation procedures. The employed distribution is motivated by an experimental analysis of the mean nanowire next neighbour distance at our samples, analysed by SEM. A histogram of the next neighbour distance of the Monte Carlo simulation and of the SEM analysis is presented in figure 4.9. The random distribution fits well to the observation, however at very small nanowire-to-nanowire distances the Monte Carlo simulation seems to overestimate the number of neighbouring nanowires.
In the subsequent section, we will discuss the determination of the ensemble-shadowing within the simulation model. Therefore, a total number N of nanowires is positioned randomly at the positions (x_n,y_n), $n \in [1,N]$ inside an area A (of size X_S in beam direction times Y_S perpendicular to the beam) leading to a mean number density ρ_{NW}, as shown in figure 4.10(a). Examples of the nanowire positions for different ρ_{NW}, created by the Monte Carlo simulation, are shown in figure 4.10(b) - (d).
An individual nanowire casts a shadow with a footprint on the substrate surface of $D_{shad} \cdot l_S(t)$, with the shadow length $l_S(t)$

$$l_S(t) = \frac{h^{NW}(t)}{\tan(\alpha)}, \tag{4.3}$$

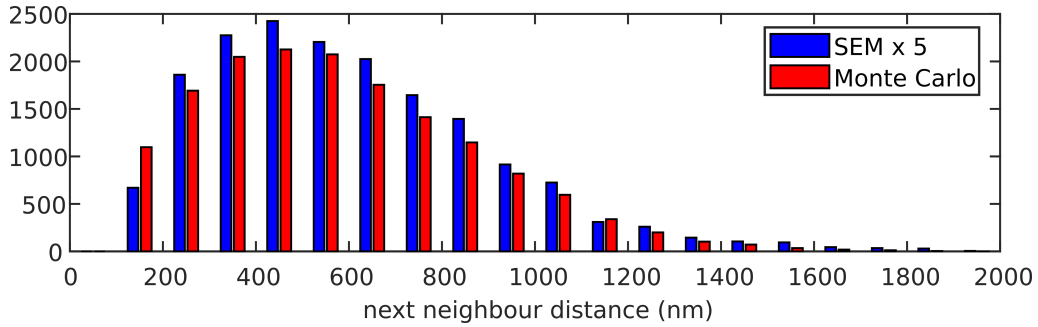

Figure 4.9.: Histogram of the nanowire next neighbour distance determined experimentally by SEM and by the Monte Carlo simulation using uniformly distributed nanowire positions. For a better comparison we multiplied the SEM results by 5. The number density ρ_{NW} is $0.8\,\mu m^{-2}$.

where α is the incidence angle of the electron beam. To prevent misinterpretation of the shadowing conditions, which might occur because of the non-shadowed nanowires close to the border of A, we consider additional nanowires with identical ρ_{NW} located the distance $l_S(t_f)$ upstream the beam direction (compare figure 4.10 (a)), with t_f being the final growth time.

Since with increasing growth time each nanowire casts a growing shadow $l_S(t)$, more and more nanowires will become increasingly shadowed. Their individual shadowed height $h_S^{(n)}(x_n,y_n,t)$, $n \in N$, changes as a function of their relative position and distance with respect to the surrounding shadowing nanowires and the mean axial nanowire growth dynamics of $h^{NW}(t)$ of the ensemble.

In figure 4.11, we illustrate the situation for three different times during one growth run. In order to reduce the computing time we make the following simplification: all nanowires are assumed to have similar shape and are vertically aligned. We also neglect tapering for the shadow calculations, instead we use the mean effective shadow diameter $\overline{D}_{shad}$ averaged over the ensemble. In principle, tapering can easily be included into the treatment of ensemble-shadowing, but such more thorough calculations would only give a difference of a few % of the shadowed area for realistic tapering of the nanowires, which is here 2% for $r_{f,t}^{NW}/r_{f,b}^{NW} = 1.2$.

Thus, the nanowires, in this approximation, cast rectangular and total shadows on the surface, the width of the shadows along y equals $\overline{D}_{shad}$ originating at the nanowire position $(y_n \pm \overline{D}_{shad}/2)$, the length along x follows equation (4.3). The related shadowing height at a given position and growth time is

$$h_S(x,t) = h^{NW}(t)\frac{(x_n - x + l_S(t))}{l_S(t)}. \tag{4.4}$$

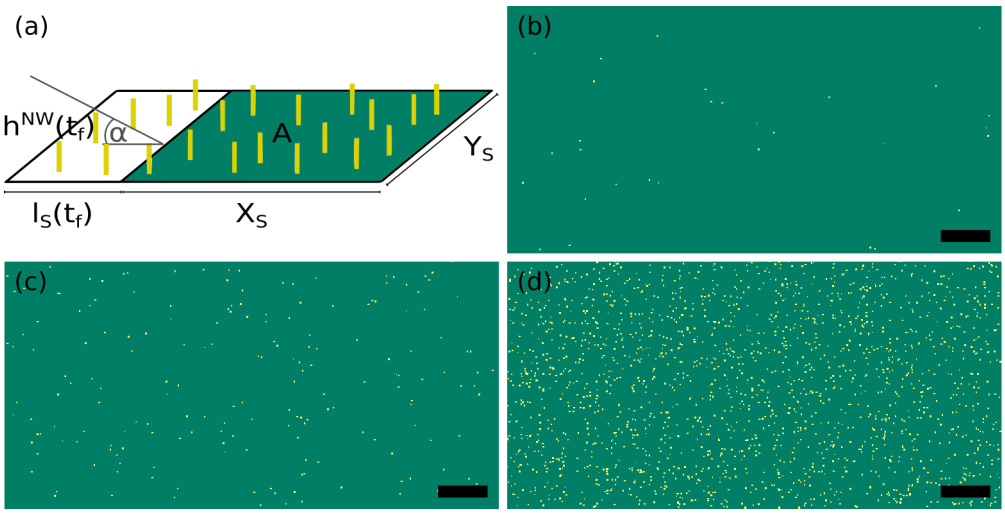

Figure 4.10.: (a) illustration of nanowire positioning inside $A = X_S \cdot Y_S$. For a correct determination of the shadowing at the border of A, additional nanowires with the maximal distance $l_S(t_f)$ from the border of A are considered. (b) - (d) exemplarily simulated nanowire positions for different nanowire densities ρ_{NW} with $\rho_{NW} = 0.1\,\mu m^{-2}$ in (b), $\rho_{NW} = 1\,\mu m^{-2}$ in (c) and $\rho_{NW} = 10\,\mu m^{-2}$ in (d). The scale bar is 2 µm.

At any point (x,y) inside A the shadows of nanowires contribute with different shadow heights as a function of their relative positions. Accordingly, each individual nanowire localized at position (x_m,y_m), $m \in N$ becomes shadowed by the nanowire ensemble, up to the shadowed height $h_S^{(m)}(x_m,y_m,t)$ being the maximum value of all shadows of the surrounding nanowires evaluated by equation (4.4).

As a further reasonable approximation, the nanowire m is assumed to be shadowed from the bottom up to $h_S^{(m)}$ over its whole cross section. Evaluating $h_S^{(m)}(t)$ for all N nanowires inside A, we can determine the ensemble fraction $s(h,t)$ of wires which are shadowed up to a certain height $h(t)$. Unintentional statistical fluctuations in the results from Monte Carlo simulations decrease for larger ρ_{NW}. Aiming to simulate statistically homogeneous ensembles, the Monte Carlo simulations might be repeated j times depending on A and ρ_{NW}, which is in our case in the order of 1-10 times. Similarly, we can determine the individual illumination heights for all nanowires, $\lambda^{(m)}(x_m,y_m,t) = h(t) - h_S^{(m)}(x_m,y_m,t)$, and for any height and time, the corresponding ensemble-fraction of wires being completely illuminated from the top down to this height, $(1 - s(h,t))$. Further, we determine the mean shadowed height $\overline{h_S(t)}$ and the corresponding mean illumination height $\overline{\lambda(t)} = h^{NW}(t) - \overline{h_S(t)}$, by averaging over all $h_S^{(m)}$ or respectively $\lambda^{(m)}$ of the whole ensemble.

The specific dependence of $\overline{\lambda}$ as a function of the nanowire height $h^{NW}(t)$ and therefore of the axial growth rate and time is illustrated in figure 4.12 for three different nanowire number densities of the ensemble ρ_{NW} and constant nanowire radius. During the initial phase of growth almost no shadowing occurs, since the shadows mostly do not reach

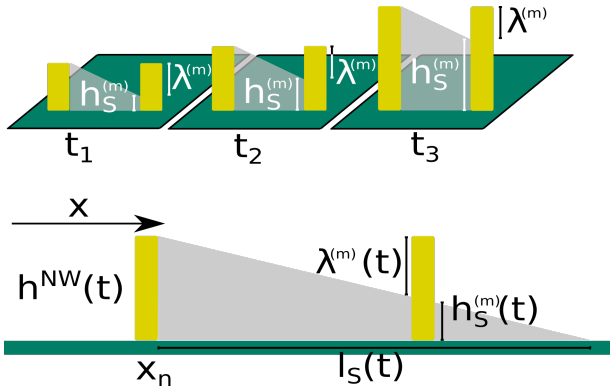

Figure 4.11.: The diffraction intensity origins from the illuminated part of the nanowires with the illumination height $\lambda^{(m)}(t)$. Top panel: $h_S^{(m)}(t)$ changes during growth, as illustrated by the three growth times. Bottom panel: model for the determination of the ensemble-shadowing dynamics.

the neighbouring nanowires. Consequently, $\overline{\lambda(t)}$ increases nearly linearly with $h^{NW}(t)$ until the first critical time t_{c1}. Afterwards, the shadowing increases moderately because more and more nanowires become shadowed, till at the second critical time t_{c2}, when the nanowires become sufficiently long all shadows reach to the next nanowires. The mean ensemble illumination height reaches a critical value $\overline{\lambda}(t_{c2}) = \overline{\lambda}_{crit}$, which during further growth remains constant, since the further increase in nanowire height $h^{NW}(t)$ results in a proportional increase in the mean ensemble shadow height $\overline{h_S(t)}$. The exact value of $\overline{\lambda}_{crit}$ strongly depends, beside the angle of electron incidence, on D_{shad} and the nanowire number density.

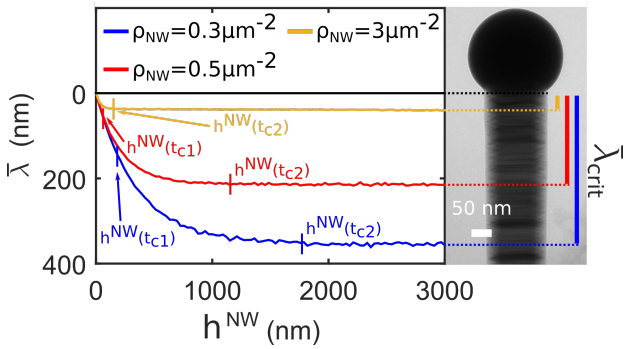

Figure 4.12.: Illustration of the dynamics of the mean illumination height $\overline{\lambda}(h^{NW}(t))$ with growing nanowire height $h^{NW}(t)$ for different ρ_{NW} and constant $D_{shad} = 50$ nm. The incidence angle is $\alpha = 0.6°$. $\overline{\lambda}(h^{NW}(t))$ increases linearly until $h^{NW}(t_{c1})$, followed by a signal saturation which gets constant at $h^{NW}(t_{c2})$. The constant illumination height is defined as $\overline{\lambda}(h^{NW}(t_{c2})) = \overline{\lambda}_{crit}$. For higher ρ_{NW}, $\overline{\lambda}_{crit}$ is smaller which increases the height-selectivity, as illustrated in the TEM images at the right side.

The dependence of $\overline{\lambda}_{crit}$ as function of ρ_{NW}, $r^{NW} \propto D_{shad}$ and α are depicted in figure 4.13. Figure 4.13(a) shows the dependence on ρ_{NW} and r^{NW} at constant $\alpha = 0.6°$ and figure 4.13(b) shows $\overline{\lambda}_{crit}$ as a function of ρ_{NW} and α for constant $r^{NW} = 25\,\text{nm}$.
Both figures indicate that ρ_{NW} is the dominating parameter for $\overline{\lambda}_{crit}$, because with increasing number density, the distance between nanowires decreases and thus the electron shadow covers more of the nanowires. In contrast, the nanowire radius r^{NW} has a small impact on $\overline{\lambda}_{crit}$. As described in section 4.2.2, the nanowire radius affects the mean shadow footprint by increasing $\overline{D}_{shad}$ and thus the shadowed volume per nanowire. Together with the number density of wires it leads to an increasing mean shadow coverage of the nanowire ensemble. The incidence angle α of the electron beam has an intermediate influence. For given mean nanowire density the shadow coverage reduces by increasing incidence angles and consequently a larger upper part of the nanowires $\overline{\lambda(t)}$ becomes illuminated, corresponding to a reduction of $\overline{h_S(t)}$, as described by equations (4.3) and (4.4). Furthermore, the shadowed ensemble fraction $s(h,t)$ undergoes for larger nanowire density a sharper height transition Δh from a complete shadowed bottom part (with $s(h,t) = 1$) to a completely illuminated top part (with $s(h + \Delta h,t) = 0$).
A general expression for $\overline{\lambda}_{crit}$ in nm can be estimated by fitting the functions in figures 4.13(a), and 4.13(b) with power law functions. Equation (4.5) is an empirical function of the illumination height $\overline{\lambda}_{crit}$ of α, r^{NW} and ρ_{NW}:

$$\overline{\lambda}_{crit} = \frac{c_1}{\rho_{NW}} \exp\left((c_2 \cdot \alpha)^{c_3} - (c_4 \cdot r^{NW})^{c_5}\right), \tag{4.5}$$

where α is given in rad, r^{NW} in nm and ρ_{NW} in nm^{-2}. The coefficients are $c_1 = 1 \times 10^{-6}\,\text{nm}^{-1}$, $c_2 = 2.8304 \times 10^6$, $c_3 = 0.1686$, $c_4 = 0.0574\,\text{nm}^{-1}$ and $c_5 = 0.4002$.

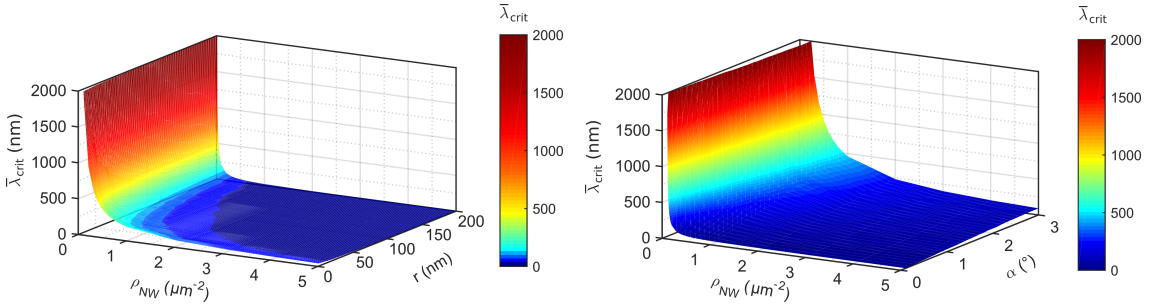

(a) (b)

Figure 4.13.: Function of the mean illumination height $\overline{\lambda}_{crit}$ from sample parameters: (a) illumination height $\overline{\lambda}_{crit}$ as a function of ρ_{NW} and $r^{NW} \propto \overline{D}_{shad}$ at fixed $\alpha = 0.6°$ and (b) illumination height $\overline{\lambda}_{crit}$ as a function of ρ_{NW} and α at fixed $r^{NW} = 25\,\text{nm}$.

Concluding, similarly to planar RHEED, also RHEED in transmission geometry can become extremely sensitive towards changes in the crystal structure at the growth front, due to the reduced mean illumination height $\overline{\lambda}_{crit}$ at the nanowire apex.

4.2.5. The effective scattering cross section $\Omega(r(h,t),\Lambda)$

In the previous section, we presented the determination of the ensemble-shadowing in the RHEED simulation model. As next step, we now present the calculation of the self-shadowing effect in the model. Our interpretation of the magnitude of forward-transmitted and the diffracted beam intensities bases on the three aspects: nanowire radius, nanowire cross section and electron mean free path length. We include all these aspects in a so-called *effective scattering cross section* $\Omega(r(h,t),\Lambda)$, which can be seen as the nanowire's geometrical cross section weighted by the absorption of the electron beam inside the material. The effective cross section is a function of the nanowire radius at a given height and growth time $r(h,t)$ and of the mean free path length Λ. In this section, we will obtain general expressions for $\Omega(r(h,t),\Lambda)$ for the different nanowire cross sections introduced in section 4.2.1.

We integrate the path distances of the electron beam in the nanowire $\gamma(x,h,t)$, equal to $d(x)$ in figure 4.4, along the nanowire diameter and consider additionally the attenuation of the electron beam intensity while passing $\gamma(x,h,t)$.

We start the discussion with the important case in this work: the hexagonal nanowire cross section where the electron beam is perpendicular to a side facet. We recall that this is the arrangement for self-catalysed GaAs nanowires measured along the $[\bar{1}10]$ azimuth. We write for $\gamma(x,h,t)$:

$$\gamma(x,h,t) = \begin{cases} \sqrt{3}(r(h,t)+x), & \text{for } -r < x < -\frac{r}{2}. \\ \frac{\sqrt{3}}{2}r(h,t), & \text{for } -\frac{r}{2} \leq x \leq \frac{r}{2}. \\ \sqrt{3}(r(h,t)-x), & \text{for } \frac{r}{2} < x < r. \end{cases} \tag{4.6}$$

The effective scattering cross section $\Omega(r(h,t),\Lambda)$ follows by integration along x and by consideration of the attenuation of the electron beam intensity due to absorption:

$$\Omega(r(h,t),\Lambda) = \int_{-r(h,t)}^{r(h,t)} \int_{0}^{\gamma(x,h,t)} \mathrm{e}^{-\frac{2\gamma(x,h,t)}{\Lambda}} \,\mathrm{dy}\,\mathrm{dx} \tag{4.7}$$

$$= \frac{\Lambda^2}{\sqrt{3}} - \frac{1}{3}\mathrm{e}^{-\frac{\sqrt{3}\cdot r(h,t)}{\Lambda}} \cdot \left(-3\sqrt{3}\cdot r(h,t)^2 + 3r(h,t)\Lambda + \sqrt{3}\Lambda^2\right), \tag{4.8}$$

With equation (4.8), we have now an expression for the self-shadowing in self-catalysed GaAs nanowires. Consequently, we use this equation in the simulation model in section 4.2.6.

For the sake of completeness, we now determine $\Omega(r(h,t),\Lambda)$ for a hexagon, where the electron beam is parallel to a side facet. Here $\gamma(x,h,t)$ is:

$$\gamma(x,h,t) = \begin{cases} \frac{1}{\sqrt{3}}x + r(h,t), & \text{for } -\frac{\sqrt{3}}{2}r \leq x \leq 0. \\ -\frac{1}{\sqrt{3}}x + r(h,t), & \text{for } 0 < x \leq \frac{\sqrt{3}}{2}r. \end{cases} \tag{4.9}$$

and $\Omega(r(h,t),\Lambda)$ is consequently

$$\Omega(r(h,t),\Lambda) = \int_{-\frac{\sqrt{3}}{2}r(h,t)}^{\frac{\sqrt{3}}{2}r(h,t)} \int_0^{\gamma(x,h,t)} \mathrm{e}^{-\frac{2\gamma(x,h,t)}{\Lambda}} \,\mathrm{dy}\,\mathrm{dx} \tag{4.10}$$

$$= \sqrt{3}\mathrm{e}^{-\frac{2r(h,t)}{\Lambda}}\Lambda(-2r(h,t) - \Lambda + \mathrm{e}^{\frac{r(h,t)}{\Lambda}}(r(h,t) + \Lambda)). \tag{4.11}$$

The final case is a circular nanowire cross section, here $\gamma(x,h,t)$ and $\Omega(r(h,t),\Lambda)$ are:

$$\gamma(x,h,t) = \sqrt{r^2(h,t) - x^2} \tag{4.12}$$

$$\Omega(r(h,t),\Lambda) = \int_{-r(h,t)}^{r(h,t)} \int_0^{\gamma(x,h,t)} \mathrm{e}^{-\frac{2\gamma(x,h,t)}{\Lambda}} \,\mathrm{dy}\,\mathrm{dx} \tag{4.13}$$

$$= \int_{-r(h,t)}^{r(h,t)} 2\mathrm{e}^{-\frac{2\sqrt{r(h,t)^2 - y^2}}{\Lambda}} \sqrt{(r^2(h,t) - x^2)}\,\mathrm{dx}. \tag{4.14}$$

For circular cross sections, an analytical formula cannot be given. For further nanowire cross sections, $\Omega(r(h,t),\Lambda)$ should be determined accordingly.

4.2.6. RHEED intensity evolution for dynamical statistical ensembles

Finally, all our considerations and results achieved until now, allow us to simulate the RHEED intensity evolution during growth of the two statistical ensembles of nanowires and crystallites. We assume homogeneous growth conditions meaning that all objects show a more or less identical structure evolution. A slight variation of nanowire or crystallite diameters around their respective mean ensemble values is allowed and indirectly considered by omitting the Pendellösung terms, as we discussed in section 4.2.2, but all objects of a respective ensemble are treated to have the same height $h^{obj}(t) = m_{axial}^{obj} \cdot t$, $obj \in \{NW,cry\}$. As illustrated in figure 4.14, the objects can be subdivided along the axial growth axis into $K^{obj}(t) = \lfloor (m_{axial}^{obj} \cdot t/\Delta h^{obj}) \rfloor$ slices of even thicknesses Δh^{obj}.

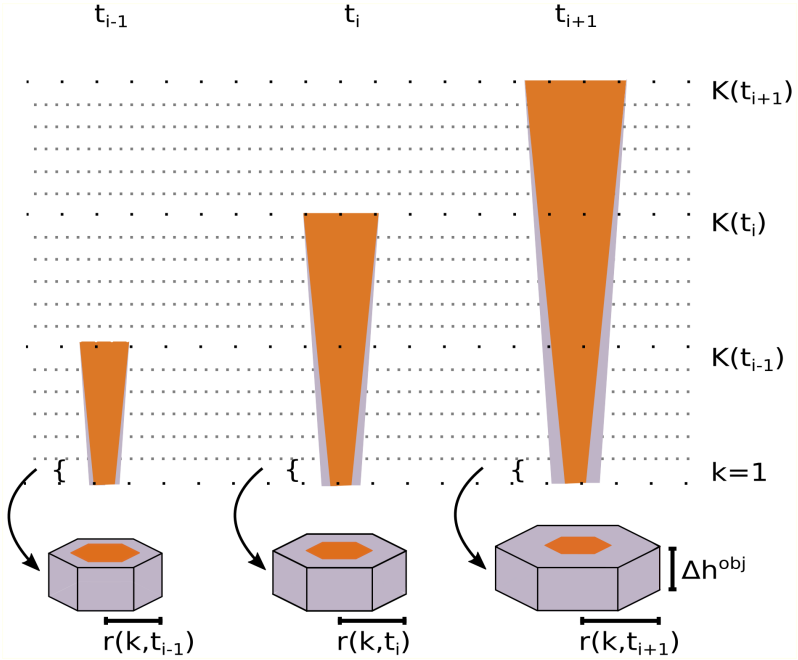

Figure 4.14.: Schematic illustration of the nanowire growth model underlying the RHEED simulation. At each observation time t_i, the nanowires can be subdivided into $K^{NW}(t_i)$ slices with thickness Δh^{obj} and circumference radius $r(k,t_i)$ allowing to define the corresponding effective scattering cross sections $\Omega(r(k,t_i),\Lambda)$. The number of slices increases due to axial growth, the scattering cross section of a slice k is influenced by tapering (orange) and changes with time as a function of additional facet growth (shown in grey).

Starting with an initial slice $k = 1$ at the object bottom determined by its shape and the initial circumference radius r_0, the model generates the objects by stacking slice per slice with growing number index k on top of another. The objects are finalized by one last slice $k = K^{obj}(t) + 1$ with thickness $\Delta h_{k=K^{obj}(t)+1} = m^{obj}_{axial} \cdot t - (K^{obj}(t) \cdot \Delta h^{obj})$ to fit the total height of the stack to the total object height $h^{obj}(t)$, but this last slice does not play any significant role for sufficiently small Δh^{obj}.
Each object slice k is characterized by its radius $r^{obj}(k,t)$, temporally developing as a function of the radial facet and tapering growth rates, and has the time-dependent effective scattering cross section $\Omega(r(k,t),\Lambda)$:

$$\Omega(r(k,t),\Lambda) = \frac{\Lambda^2}{\sqrt{3}} - \frac{1}{3} e^{-\frac{\sqrt{3}\cdot r(k,t)}{\Lambda}} \cdot \left(-3\sqrt{3} \cdot r(k,t)^2 + 3r(k,t)\Lambda + \sqrt{3}\Lambda^2\right), \tag{4.15}$$

where we substitute the height h by the slice k in equation (4.8). The model calculates the object intensities by summing incoherently the diffraction contributions of all slices. In order to deal with polytypism in the nanowire ensemble, we may introduce for each slice k the ensemble averaged fraction of polytypes $f_p(k)$. The resulting ensemble averaged

relative intensity contribution of one phase to the overall signal of one *hkl* reflection can be estimated by

$$I^{obj}_{hkl,p}(t) = F_{hkl,p} \cdot C^{obj} \cdot \sum_{k=1}^{K^{obj}(t)} f_p(k) \cdot \Omega(r(k,t),\Lambda) \cdot (1 - s(k,t)), \tag{4.16}$$

where $F_{hkl,p}$ is the structure factor of electron diffraction listed in table 2.2, $s(k,t)$ is the shadowed fraction of slices k at t, determined by the Monte Carlo approach in section 4.2.4, and $(1-s(k,t))$ is the complementary illuminated fraction. The constant C^{obj} considers the different number densities for nanowire and crystallite ensembles, C^{NW}=1 and $C^{cry}=\frac{\rho_{cry}}{\rho_{NW}}$, where ρ_{cry} is the number density of crystallites. The total integrated diffraction intensity of a RHEED spot becomes

$$I^{total}_{hkl}(t) = \sum_p I^{NW}_{hkl,p}(t) + I^{cry}_{hkl,p}(t). \tag{4.17}$$

In the experimental examples we study ensembles of GaAs nanowires, with polytypism of WZ, ZB and TZB. However, ZB and TZB occur equally frequent, and thus we distinguish between the cubic (ZB and TZB $\coloneqq \Sigma$ ZB) and the hexagonal WZ phases and the respective phase fractions are f_{ZB} and f_{WZ}. The crystallites are considered to grow only in zinc blende phase.[83]

4.3. Simulation of RHEED intensity evolution

We incorporate the results of section 4.2 into a simulation programme, which uses input parameters describing the nanowire and crystallite shape and crystal structure, and parameters describing the characteristics of the setup to determine the temporal evolution of RHEED diffraction spot intensities. Details on the programme can be found in appendix B. In the following, we are discussing the characteristics, possibilities and the limitations of the developed simulation model. A diagram illustrating the important parts of the versatile simulation programme is shown in figure 4.15. The green marked area determines the nanowire and crystallite shape evolution. The yellow part calculates the ensemble-shadowing which is used in the red part, together with the results of the self-shadowing, to determine the intensity evolution of certain diffraction spots. These simulated intensities are then compared to real experiments. The large parameter space which is needed to describe the complex growth and thus to run the simulation is listed in table 4.2.

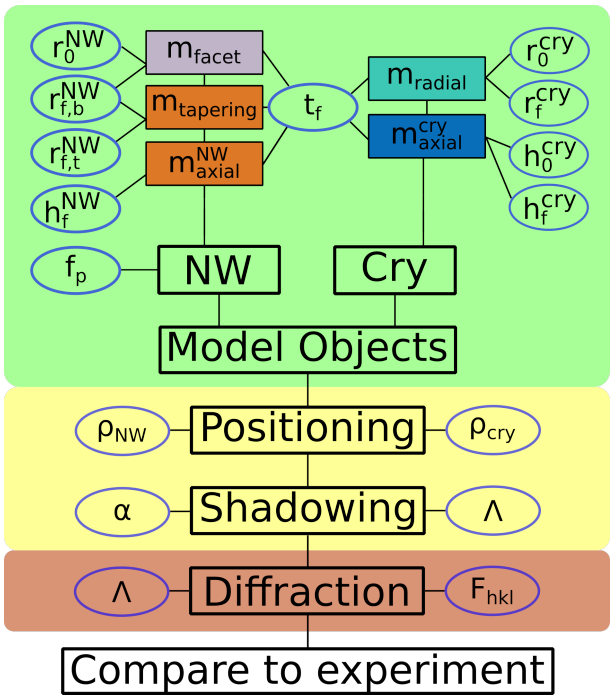

Figure 4.15.: The essential parameters for the simulation software defining the growth (green), the Monte-Carlo simulation for positioning and ensemble-shadowing (yellow), and the determination of the nanowire diffraction signals including self-shadowing (red).

The model needs, in total, two parameters to describe the characteristics of the setup and eleven parameters for the shape evolution of nanowires and crystallites. An additional parameter space giving the time-resolved polytype distribution in the nanowires is required to determine the impact of the crystal structure on the signal. The temporal sampling of the polytypism distribution can be individually chosen, the input is used as so-called

Table 4.2.: Parameters and their abbreviations necessary to run the simulation programme.

t_f	growth time	α	incidence angle electron beam
r_0^{NW}	initial nanowire radius at substrate	Λ	mean free path length electrons
$r_{f,b}^{NW}$	final nanowire radius at substrate	ρ_{NW}	nanowire number density
$r_{f,t}^{NW}$	final nanowire radius at tip	ρ_{cry}	crystallite number density
h_f^{NW}	final nanowire height	$m_{axial}^{NW}=\frac{h_f^{NW}}{t_f}$	nanowire axial growth rate
r_0^{cry}	initial crystallite radius	$m_{facet}=\frac{r_{f,b}^{NW}-r_0^{NW}}{t_f}$	nanowire facet growth rate
r_f^{cry}	final crystallite radius	$m_{tapering}=\frac{r_{f,t}^{NW}-r_{f,b}^{NW}}{t_f}$	nanowire tapering growth rate
h_0^{cry}	initial crystallite height	$m_{axial}^{cry}=\frac{h_f^{cry}-h_0^{cry}}{t_f}$	crystallite axial growth rate
h_f^{cry}	final crystallite height	$m_{radial}=\frac{r_f^{cry}-r_0^{cry}}{t_f}$	crystallite radial growth rate

anchor values of the polytype fraction at certain growth times. In order to allocate each slice k a distinct value of $f_p(k)$, the given sampling of the anchor values are interpolated to a suitable higher sampling.
Next, we develop an understanding of the characteristic features observable in the intensity evolution of RHEED diffraction spots and relate these features to properties of the nanowire or crystallite ensembles and to the properties of the setup.

4.3.1. Setup properties: electron beam energy and incidence angle

The setup properties, namely the acceleration voltage of the electrons and the RHEED geometry, affect two parameters in the simulation model. The acceleration voltage has an impact on the mean free path length Λ and the incidence angle α as parameter is determined by the RHEED geometry. To get a better understanding of their influence, we simulate the RHEED intensities and keep all parameters constant except one. By varying only a single parameter, we are able to discuss its impact on the intensity evolution. We first focus on the mean free path length Λ at three different ρ_{NW}.
In figure 4.16 each graph illustrates the temporal intensity evolution for different nanowire number densities. We simulate phase pure nanowires (no polytypism is considered so far) which have an axial and a radial growth component, meaning that the nanowires grow in height and also increase in diameter. We restrict the simulations to only nanowire ensembles, without intensity contribution from crystallites. The constant simulation parameter are listed in the table in figure 4.16.
From equation (4.16), we see directly that Λ dominates the self-shadowing in the nanowires. Consequently, for low ρ_{NW}, where the ensemble-shadowing plays a minor role, as in figure 4.16(a) with $\rho_{NW} = 0.01\,\mu\text{m}^{-2}$, Λ affects only the slope of the intensity evolution.

For large mean free path lengths, the nanowire volume contributing to the diffraction process increases faster due to the competition of radial growth and absorption. Once the ensemble-shadowing plays a significant role in the diffraction process, as in figures 4.16(b) and 4.16(c), Λ has an influence on the transition time, when the intensity starts to saturate. For small Λ, stable self-shadowing conditions are reached earlier, resulting in a faster saturation of the overall intensity. In our case the stable self-shadowing conditions are not yet reached for the black and red curve in figure 4.16(b), with $\rho_{NW} = 0.1\,\mu m^{-2}$, leading to an intensity rise due to the remaining radial growth. In the last case, which is shown in figure 4.16(c), where a high ensemble-shadowing is present at $\rho_{NW} = 1\,\mu m^{-2}$, Λ can even lead to a decrease of the intensity because the competition of radial growth and absorption changes in favour of the absorption for the small mean free path length values. In our examples this is discernible for the blue, cyan and magenta curves starting from $t \approx 15\,min$.

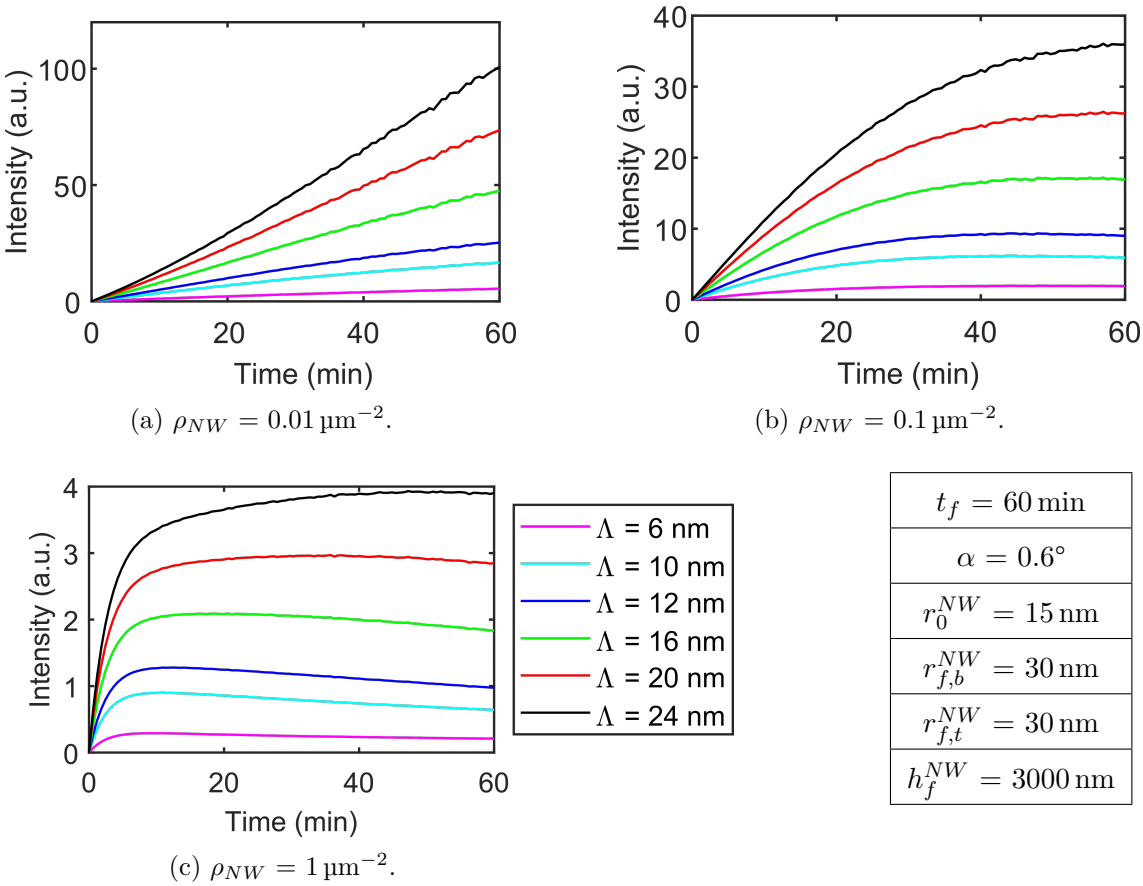

(a) $\rho_{NW} = 0.01\,\mu m^{-2}$.

(b) $\rho_{NW} = 0.1\,\mu m^{-2}$.

(c) $\rho_{NW} = 1\,\mu m^{-2}$.

Figure 4.16.: Simulated RHEED intensity evolutions for different mean free path lengths Λ and nanowire number densities ρ_{NW} ((a) - (c)). The further constant parameters are listed in the table. Λ affects mainly the magnitude of the diffracted intensity.

For illustrating the impact of the electron incidence angle α on the intensity evolution, we again simulate different nanowire number densities ρ_{NW} and incidence angles α of the electron beam under otherwise constant parameters. We still restrict the simulation to phase pure nanowires without the presence of crystallites. Figure 4.17 demonstrates that α essentially affects the ensemble-shadowing. Depending on ρ_{NW}, changing α results in different final values of intensity saturation. A second influence is discernible in the transition region from the non-shadowed nanowire ensemble to the fully shadowed one. The smaller α, the smaller the transition interval and the intensity evolution appears more like a step-function. Of course, this transition region depends also on the distribution of the nanowires in the ensemble, however, in the current examples the distribution functions are identical.

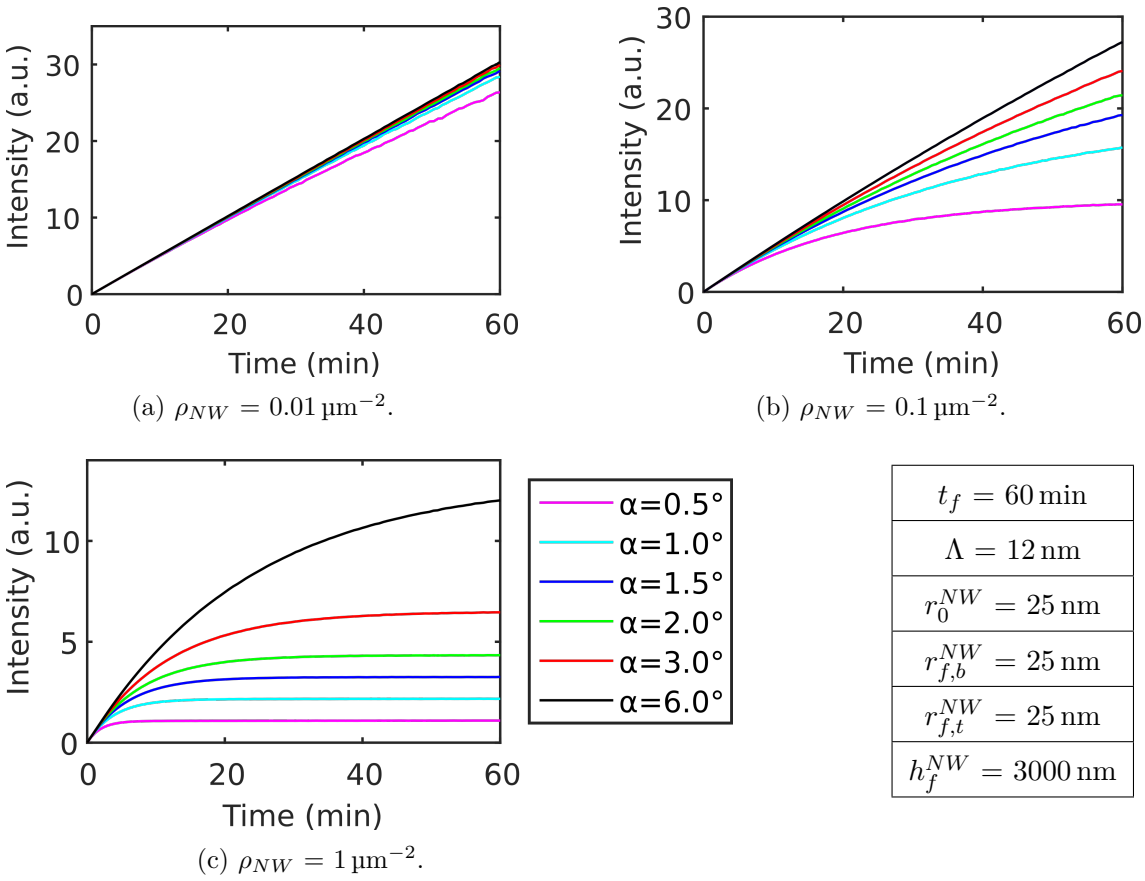

(a) $\rho_{NW} = 0.01\,\mu\mathrm{m}^{-2}$.

(b) $\rho_{NW} = 0.1\,\mu\mathrm{m}^{-2}$.

(c) $\rho_{NW} = 1\,\mu\mathrm{m}^{-2}$.

Figure 4.17.: Simulated RHEED intensity evolutions for different electron incidence angles α and nanowire number densities ρ_{NW} ((a) - (c)). The further constant parameters are listed in the table. α determines the strength of the ensemble-shadowing and thus the time, when the intensity saturation starts and constant values are reached.

4.3.2. Ensemble properties and growth dynamics: nanowire and crystallite number density and nanowire axial and radial growth rates

In this section we discuss and illustrate the peculiarities of the different growth contributions to the RHEED intensities. First, we start with the influence of the nanowire number density on the signal, followed by a discussion on the axial and radial growth rates of the nanowire ensemble and finally we deal with the impact of the crystallites on the signal. Again, we restrict ourselves to phase pure nanowires without the contribution of crystallites. They are only considered in the final case.

In section 4.2.4 we saw already that the nanowire number density ρ_{NW} has a direct impact on the mean illumination height $\overline{\lambda}_{crit}$ and thus we expect the same for the intensity evolution. In figure 4.18, we plot the intensity evolution for different ρ_{NW} as a function of growth time, the other parameters are kept constant and are listed in the table. The intensity first rises linear until a saturation sets in. The onset and the final saturation level are ρ_{NW} dependent. In figure 4.18 this saturation is discernible in the cyan, blue and green curves. We see that the onset of saturation starts earlier and the intensity level decreases with higher ρ_{NW}. We can correlate this observation directly with figure 4.12, because the mean illumination height $\overline{\lambda}_{crit}$ influences the diffracted intensity of the nanowires, and thus both are proportional at constant diameters.

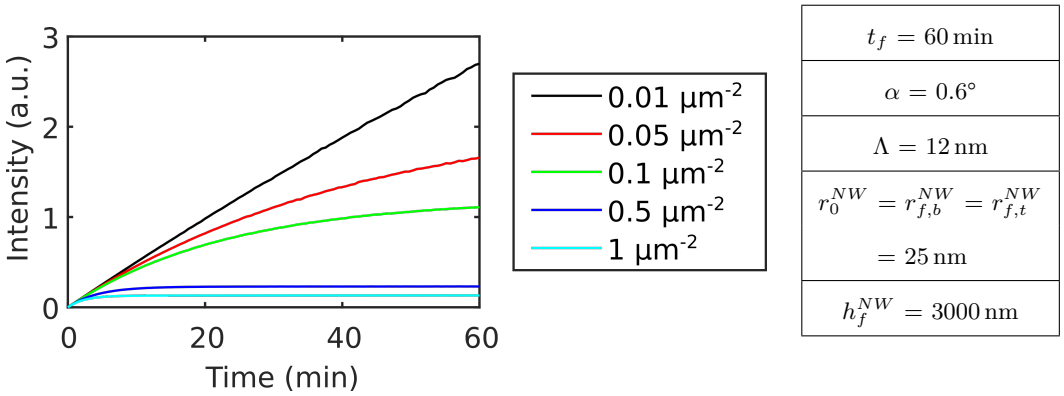

Figure 4.18.: Simulated RHEED intensity evolutions for different number densities ρ_{NW}. The further constant parameters are summarized in the table. ρ_{NW} determines the strength of the ensemble-shadowing and thus the time, when the intensity saturation starts and gets to the constant value.

In the next case studies, we investigate the effects of axial and radial growth on the RHEED signal. Collecting *in situ* RHEED data during growth results in a time-resolved data set. However, the actual ensemble-shadowing conditions are determined by the mean nanowire height at constant number density ρ_{NW} and electron incidence angle α. The nanowire height again is given by the axial growth rate of the nanowire ensemble m_{axial}^{NW}.

Consequently the onset of the ensemble-shadowing depends on m_{axial}^{NW} for otherwise constant parameters. As a result, the shape of the time-resolved intensity evolution is influenced by the axial growth rate m_{axial}^{NW}.

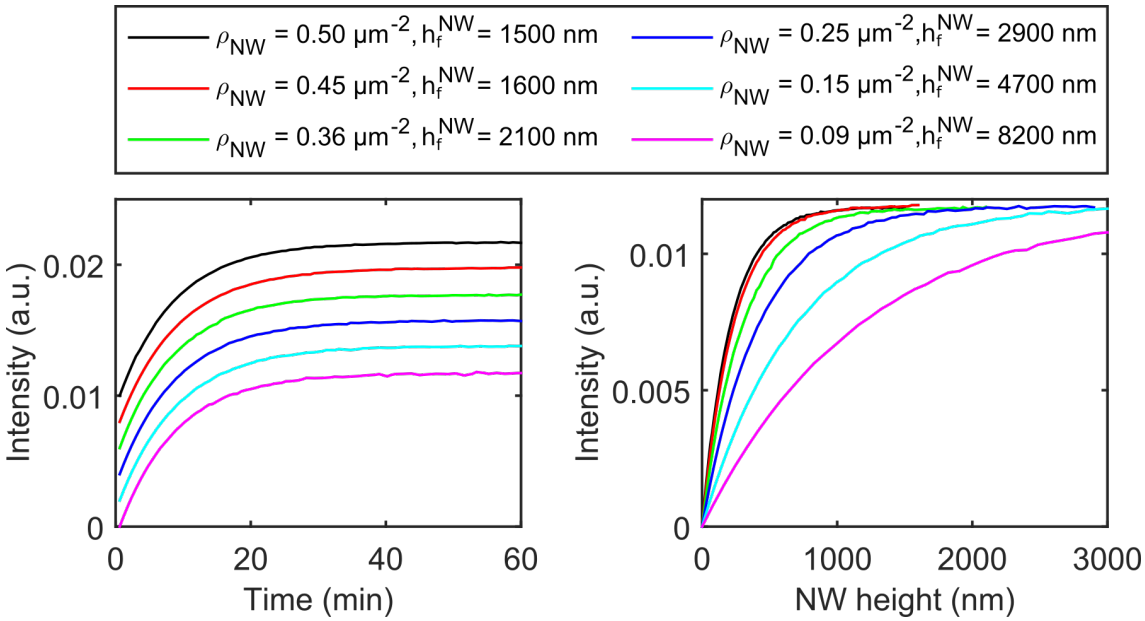

Figure 4.19.: Simulated RHEED intensity evolutions for certain ρ_{NW} and h_f^{NW} combinations. They are chosen such that all curves are identical, while plotted as a function of time (left graph). Each curve is shifted for a better visualisation. In the right graph the same curves are plotted as a function of h_f^{NW}, demonstrating that without knowledge of the axial growth rate or the nanowire number density, misinterpretation of the shadowing conditions and thus of the time-resolved RHEED data is possible.

Table 4.3.: Simulation parameters of RHEED intensity evolutions in figure 4.19.

$t_f = 60\,\text{min}$	$\alpha = 0.6°$	$\Lambda = 15\,\text{nm}$	$r_0^{NW} = r_{f,b}^{NW} = r_{f,t}^{NW} = 25\,\text{nm}$

Moreover, each intensity evolution is not unique and one can find identical shadowing conditions in the parameter space of ρ_{NW}, h_f^{NW} and α. In other words, for each axial growth rate of the nanowires m_{axial}^{NW}, there exists always a ρ_{NW} which results in identical ensemble-shadowing conditions, or vice versa (at fixed α) and thus in identical intensity evolutions. In figure 4.19 we demonstrate this effect for six different axial growth rate m_{axial}^{NW}=$\{25\,\frac{\text{nm}}{\text{min}}, 26.6\,\frac{\text{nm}}{\text{min}}, 35\,\frac{\text{nm}}{\text{min}}, 48.3\,\frac{\text{nm}}{\text{min}}, 78.3\,\frac{\text{nm}}{\text{min}}, 136.65\,\frac{\text{nm}}{\text{min}}\}$, resulting in final nanowire heights of $h_f^{NW} = \{1500\,\text{nm}, 1600\,\text{nm}, 2100\,\text{nm}, 2900\,\text{nm}, 4700\,\text{nm}, 8200\,\text{nm}\}$.
For each axial growth rate, we choose a certain ρ_{NW}, resulting in the identical shape of the time-resolved intensity evolution, as shown in the left graph, where all six curves are shown as a function of the growth time t. For better visualisation, each curve is plotted with an offset. In the right graph, however, each curve is plotted as a function of the nanowire

height $h_f^{NW}(t)$. As expected, the ensemble-shadowing sets in at different $h_f^{NW}(t)$ due to the different ρ_{NW}. Concluding, if one only relies on the time-resolved intensity evolution without detailed knowledge of the growth rates, misinterpretation of the data is possible. We also see that once the ensemble-shadowing dominates the signal formation, RHEED becomes insensitive to changes of the nanowire shape due to the axial growth.

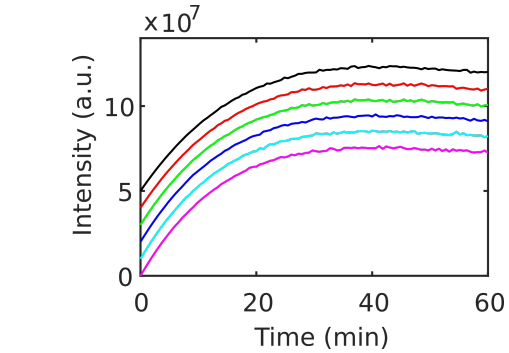

(a) $\rho_{NW} = 0.1\,\mu m^{-2}$.

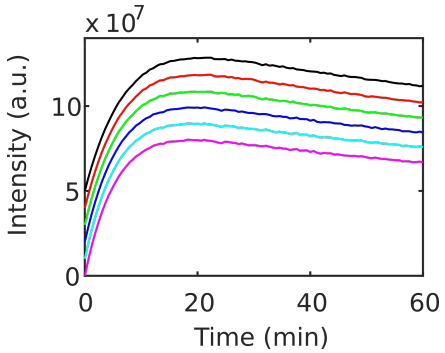

(b) $\rho_{NW} = 0.3\,\mu m^{-2}$.

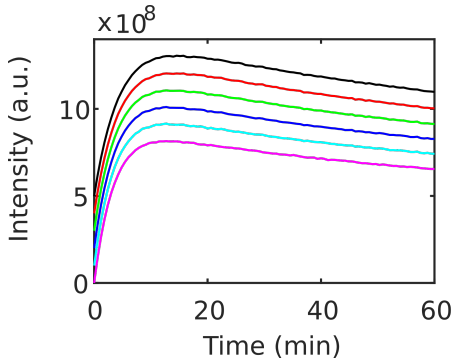

(c) $\rho_{NW} = 0.5\,\mu m^{-2}$.

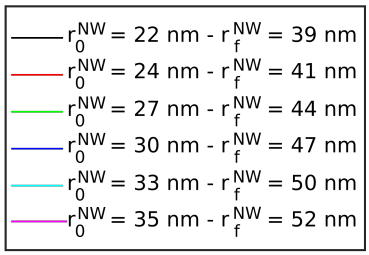

$t_f = 60\,\text{min}$
$\alpha = 0.6°$
$\Lambda = 12\,\text{nm}$
$h_f^{NW} = 3000\,\text{nm}$

Figure 4.20.: Simulated RHEED intensity evolutions for constant radial growth rates m_{radial} starting at different initial radii r_0^{NW}. The plots are vertically shifted for better visualisation. At $\Lambda < r$ RHEED is insensitive towards radial growth. The further parameters are listed in the table.

By investigating the radial growth of the nanowires, we make a comparable observation. In section 4.2.1, we saw that the major contribution of the individual nanowires to the diffraction intensities originates from the edges of their hexagonal cross sections. The absolute values of the radii have a minor influence at small mean free path length Λ. Consequently, at radii larger than Λ *in situ* RHEED becomes more and more insensitive towards radial growth. We study this by simulating time-resolved RHEED intensity evolutions with different radial growth conditions at three different ρ_{NW}. We vary the absolute radii at the onset of growth r_0^{NW} at fixed radial growth rates. The results are illustrated in figure 4.20, where different exemplary intensity evolution are depicted, all

with the same m_{facet} but different absolute values of r_0^{NW}. For better illustration of the results, we plot them again with an offset. We see that although the absolute values of the radii are different, the intensity evolution is the same. From these results, we conclude that RHEED is increasingly insensitive towards radial growth for nanowire radii larger than Λ. As final part of the discussion about the impact of the ensemble properties on the time-resolved RHEED intensity evolutions, we now include the crystallite ensemble in our consideration. In figure 4.21 the crystallite contribution to the diffraction signal is presented for three different ρ_{NW}. In the upper row the overall signals (nanowires and crystallites) are shown as solid lines in each graph with different colour-coded ρ_{NW}/ρ_{cry} ratios. The nanowire contribution is plotted in each graph as a black dashed line. At the bottom row, we plot only the crystallite contribution for the respective ρ_{NW}. By including the crystallites, the obtained intensity curves change their appearance significantly. The additional diffraction contribution of the slower growing crystallites (mainly in axial direction) leads to a stronger rise of intensity at the onset of growth, depending on their relative number density ρ_{NW}/ρ_{cry}. Due to the different axial growth rates of both ensembles, the temporal intensity evolutions can show local maxima, especially at high ρ_{NW}, as shown in figure 4.21. The local maxima occur if firstly the relative diffraction signal of the crystallites is much stronger than that of the nanowires, and if secondly a high ensemble-shadowing is present. The ensemble-shadowing is determined by the higher axial growth rate of the nanowires, which is typically one order of magnitude larger, resulting in earlier shadowing of the crystallites and consequently in a reduction of the overall signal.

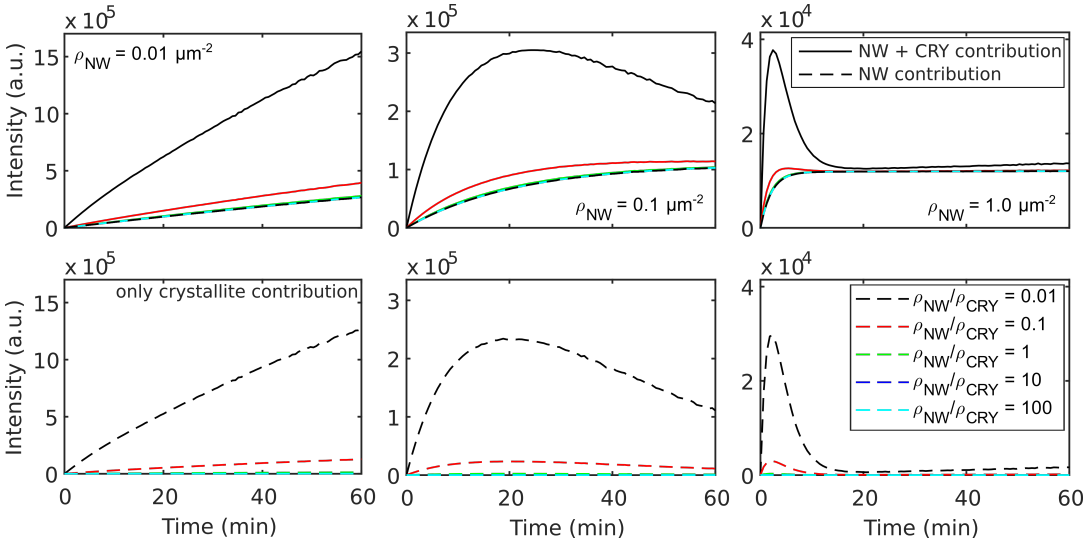

Figure 4.21.: Simulated RHEED intensity evolutions of nanowire and crystallite ensembles for different ρ_{NW}. In the top row the sum of nanowire and crystallite signals is shown as solid lines, the corresponding nanowire contributions as a dashed black line. In the bottom row only the contributions of the crystallite ensemble are depicted. The ρ_{NW}/ρ_{cry} ratios are colour-coded.

Table 4.4.: Simulation parameters of RHEED intensity evolutions in figure 4.21.

$t_f = 60\,\mathrm{min}$	$\alpha = 0.6°$	$\Lambda = 12\,\mathrm{nm}$	$r_0^{NW} = r_{f,b}^{NW} = r_{f,t}^{NW} = 25\,\mathrm{nm}$
$h_f^{NW} = 3000\,\mathrm{nm}$	$r_0^{cry} = 25\,\mathrm{nm}$	$r_f^{cry} = 100\,\mathrm{nm}$	$h_f^{cry} = 200\,\mathrm{nm}$

4.3.3. Crystallographic properties: polytypism

Until now we have restricted the discussion of the RHEED intensity evolutions to phase pure nanowires, meaning we neglect the occurrence of polytypism in the nanowires. In this section, however, we focus now on the impact of polytypism on the intensity evolution with respect to different nanowire number densities. In figure 4.22 the simulated RHEED intensity evolutions for four different ρ_{NW} are shown. Further, we compare the case of phase pure ZB nanowires (in green) to nanowires, which first grow in pure WZ (red) followed by a sharp transition to the ZB crystal structure. In addition, nanowires are simulated which have two sharp transitions, from WZ to ZB to WZ again. Again we neglect the crystallites in our current considerations. The parameters used for the simulation are summarized in table 4.5.

Table 4.5.: Simulation parameters of RHEED intensity evolutions in figure 4.22.

$t_f = 60\,\mathrm{min}$	$\alpha = 0.6°$	$\Lambda = 12\,\mathrm{nm}$	$r_0^{NW} = r_{f,b}^{NW} = r_{f,t}^{NW} = 25\,\mathrm{nm}$	$h_f^{NW} = 3000\,\mathrm{nm}$

In figure 4.22, the nanowire number density is kept constant in each row and the crystal structure is constant column by column. The polytype distribution is depicted at the top of each column. In the first row of figure 4.22, the simulated RHEED intensities of the low nanowire number density with $\rho_{NW} = 0.01\,\mu\mathrm{m}^{-2}$ is shown. Since we simulate the nanowires with only an axial growth contribution, the intensity for the phase pure nanowire ensemble rises linearly. By introducing an abrupt transition of the crystal structure in the nanowires (second column), the formerly rising intensity, belonging to WZ in this case, slightly drops in intensity, which is caused by weak ensemble-shadowing. The intensity belonging to ZB emerges with identical slope as at the onset of growth. The last graph, where two crystal structure transitions are simulated, show the same behaviour by switching to the opposite crystal structure. The intensity belonging to the previous growing phase is moderately decreasing while the other increases with the original slope.

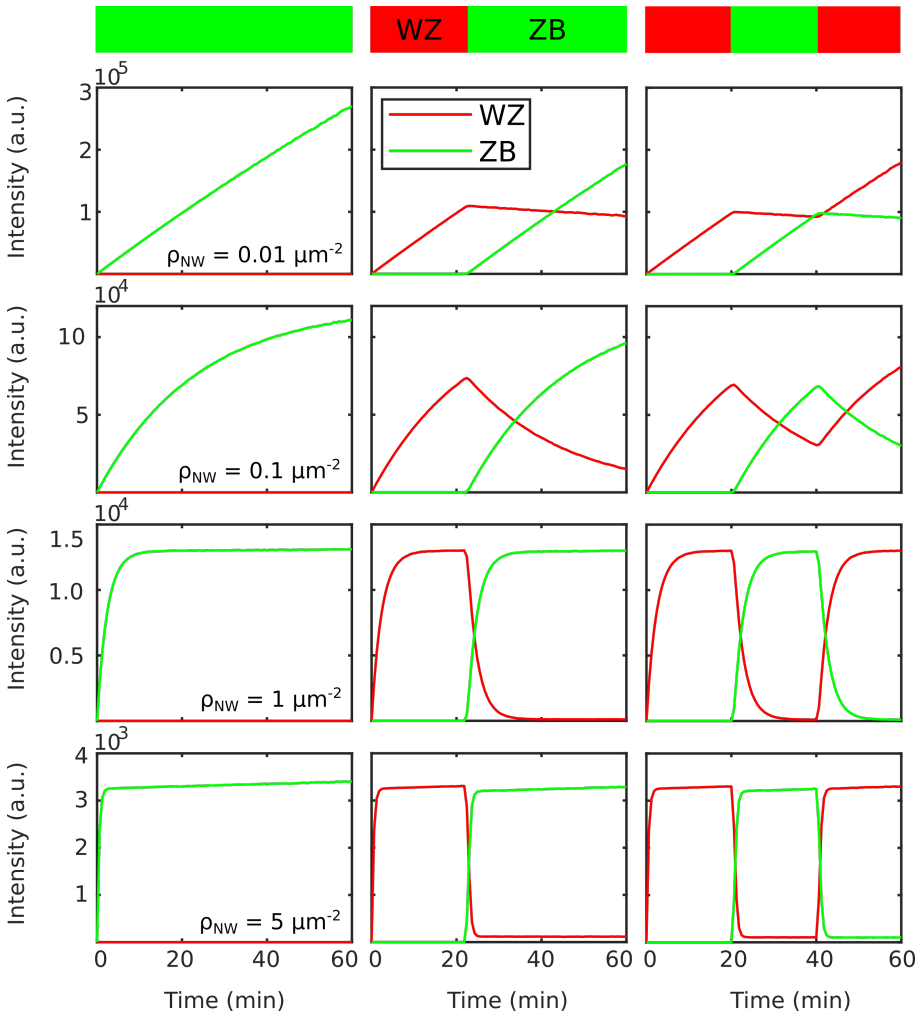

Figure 4.22.: Simulated RHEED intensity evolutions of polytypic nanowires with four different nanowire number densities. In each column the polytype distribution changes according to the figure at the top. Left column: phase pure ZB nanowires (green); middle column: one sharp transition from WZ (red) to ZB; right column: two sharp transitions from WZ to ZB to WZ. By increasing ρ_{NW}, the intensity transition region gets narrower. The further parameters are listed in table 4.5.

The intensity decrease by switching the crystal structure becomes more and more pronounced by increasing ρ_{NW}. This can be directly related to the smaller illumination height $\overline{\lambda}_{crit}$ at higher nanowire number densities. The mean illumination height $\overline{\lambda}_{crit}$ always remains at the top of the nanowires and moves upwards with m_{axial}^{NW}. Consequently, the formerly growing structures quickly move out of the illuminated height window of the nanowires for small $\overline{\lambda}_{crit}$ and RHEED is extremely sensitive to transitions in the crystal structure at high ρ_{NW}. Thus, we conclude that RHEED at high nanowire number density ρ_{NW} is predestined for investigating the crystal structure at the nanowire apex.

4.4. Experimental determination of the parameters given by the setup

The setup properties needed as parameters for the simulations are specific for each RHEED system and thus they need to be determined once. In this section, we present a methodology showing how this can be achieved experimentally for each individual system.

4.4.1. Determination of incidence angle α

The incidence angle α of the electron beam can be determined in the RHEED reflection geometry for a reference substrate with known lattice parameters. Figure 4.23 illustrates on the left side the reflection geometry in side view and in top view with the incidence angle α, the in plane diffraction angle γ, the sample-screen distance L, the distance T of the (00) to (01) truncation rod (TR) on the screen and the distance D between the origin of the reciprocal space, more specifically the direct beam (DB) and the specular reflection (SR). The electrons have the wave vector $\vec{k_0}$ and $g_\perp$ and $g_\parallel$ are the absolute values of the reciprocal lattice vectors perpendicular and parallel to the beam direction. The graph is modified from Ref.,[119] details can be found therein. On the right side of figure 4.23 the RHEED pattern in reflection geometry is shown, which is used to determine α for our setup. We are using a planar GaAs surface.
The following relations can be identified in figure 4.23:

$$\tan\alpha = \frac{D}{2L} \tag{4.18}$$

and

$$\tan\gamma = \frac{T}{L}. \tag{4.19}$$

A third relation is given in Ref.:[119]

$$\tan\gamma = \frac{g_\perp}{k_{0\parallel}} = \frac{2\pi}{ak_0\cos\alpha}, \tag{4.20}$$

with the substrate's lattice constant a. Consequently, the unknown distance L can be replaced and we get as final equation for α:

$$\sin\alpha = \frac{D}{T}\cdot\frac{\pi}{k_0\cdot a_\perp}. \tag{4.21}$$

For our beam energy of 20 keV ± 1 keV in the setup, we get $\alpha = 0.60° \pm 0.01°$. The rather high uncertainty of the beam energy is caused by the controller at our setup, which allows only this rough setting. However, we must emphasize, that the internal rotation of the substrate holder in our MBE wobbles while rotating, meaning that the determined angle is

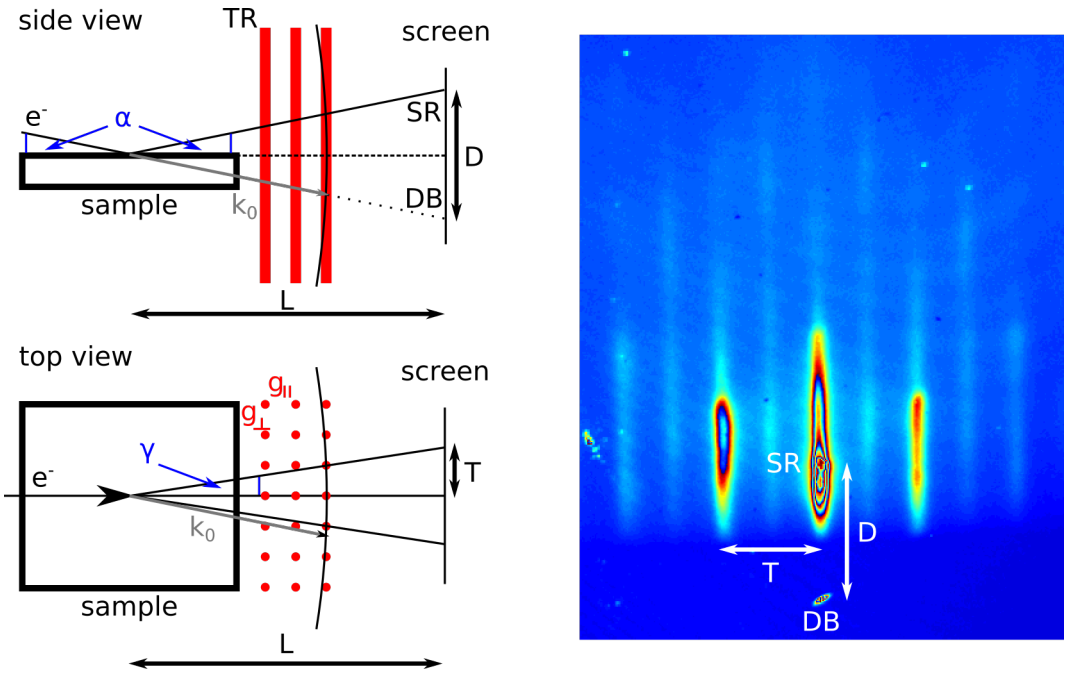

Figure 4.23.: Left image: side view and top view of planar RHEED diffraction geometry with Ewald sphere and reciprocal lattice. The figure is modified from Ref.[119] Right image: RHEED pattern of planar GaAs(100) substrate in the (2x4) reconstruction. This pattern is used to determine α.

only true for a certain azimuthal orientation of the substrate. Consequently, in our later experiments, we take particular care that the azimuthal orientation is always the same and identical to the one here used to determine α.

4.4.2. Experimental refinement of the electron mean free path length Λ

For a realistic estimation of self-shadowing and ensemble-shadowing in our simulation model we need a reliable input value for the electron mean free path length Λ of the electron beam. In the literature, values for Λ show a large variation and uncertainties.[133,134] Therefore, we present an approach to calibrate Λ for our purpose experimentally. By increasing the nanowire thickness in a controlled manner, while all other parameters are kept constant, the detected RHEED intensity should decrease in a well-defined way due to increasing self-shadowing caused by electron absorption. Experimentally, such conditions can be achieved by growing homo-epitaxial shells around nanowire cores.
To determine Λ for our RHEED system and with a beam energy of 20 keV, we grew two such homo-epitaxial GaAs shell samples with different shell growth rates. Each shell was grown for 60 min around nanowire cores with an initial nanowire radius at the apex of $r^{NW}_{reference,f,t} = (31 \pm 2)$ nm. The initial radius was measured for a reference sample by post-growth SEM. During the deposition time RHEED patterns were taken. After growth,

sample A has a final radius of $r^{NW}_{A,f,t} = (47 \pm 7)$ nm and sample B a final radius of $r^{NW}_{B,f,t} = (77 \pm 10)$ nm, which correspond to a mean shell growth rate of $m_{A,shell} = (0.27 \pm 0.03)$ $\frac{nm}{min}$ and $m_{B,shell} = (0.77 \pm 0.18)$ $\frac{nm}{min}$.
In figure 4.24 the integrated intensity of the GaAs(111) peak normalized to the value at $r^{NW}_{reference,f,t}$ is plotted as a function of the nanowire radius for sample A (depicted in blue) and sample B (depicted in green). We simulate the intensity decay for both samples with different $\Lambda \in$ [5,25] nm. To compare the simulations and the experiment, we determine the root-mean-square deviation (RMSD) for each Λ. In agreement for both samples, the lowest RMSD is at $\Lambda = 12$ nm, illustrated by the red curve. The red shaded area depicts the intensity decay for $\Lambda = 12 \pm 3$ nm. In the subsequent analyses, we use $\Lambda = 12$ nm as a value in the simulation model.

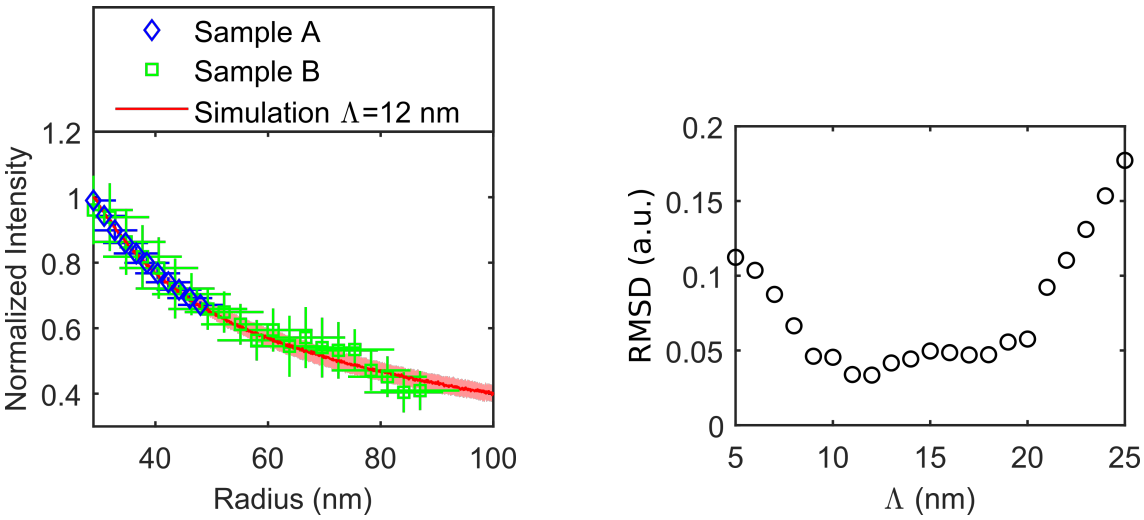

(a) (b)

Figure 4.24.: Determination of the mean free path length Λ: (a) evolution of the normalized integrated intensity of the GaAs(111) peak during radial growth of two different homo-epitaxial shell growth experiments. The intensity decay is plotted as a function of the nanowire radius for sample A in blue and for sample B in green. The intensity decay can be well described by a mean free path of $\Lambda = 12$ nm, the red shaded area gives $\Lambda = 12 \pm 3$ nm. (b) RMSD values of the experiment and simulation for different $\Lambda \in$ [5,25] nm of samples A and B.

Using the example of sample A, we shortly describe the RHEED data processing. To get the integrated intensities of the diffraction spots, we choose an integration interval in the RHEED pattern for each spot separately. We take particular care, that on the one hand the intensity at the border of the interval reaches the background level, and on the other hand we take care that the intensity of only one diffraction spot is inside the integration area. In figure 4.25(a), a RHEED raw frame of sample A is illustrated, additionally the integration interval for the GaAs(111) diffraction spot is visualised as a white frame. The interval for

this reflection is $\Delta\, Q_y = 0.92\,\text{Å}^{-1}$ and $\Delta\, Q_z = 0.56\,\text{Å}^{-1}$. However, in subsequent chapters, the analysis of the phase-sensitive diffraction spots are important, therefore we shortly discuss their processing, too. The typical integration intervals for the phase-sensitive diffraction spots are marked with different colours, the size of the intervals here are $\Delta\, Q_y = 0.60\,\text{Å}^{-1}$ and $\Delta\, Q_z = 0.39\,\text{Å}^{-1}$.

In order to determine and subtract the background from the signals, we integrate in a further step the intensity of equal areas left and right of each particular diffraction spot, normalize all to equal areas and subtract the background from the signal. In figure 4.25(b) the intensity profile of the GaAs(111) diffraction spot inside the integration interval along the Q_y direction is shown, in blue the profile before background correction and in red after background correction. Finally, to be able to compare different diffraction spot intensities, we correct for the structure factors, which were introduced in section 2.4. In the following chapters, we use RHEED intensity as short form for the RHEED integrated intensity.

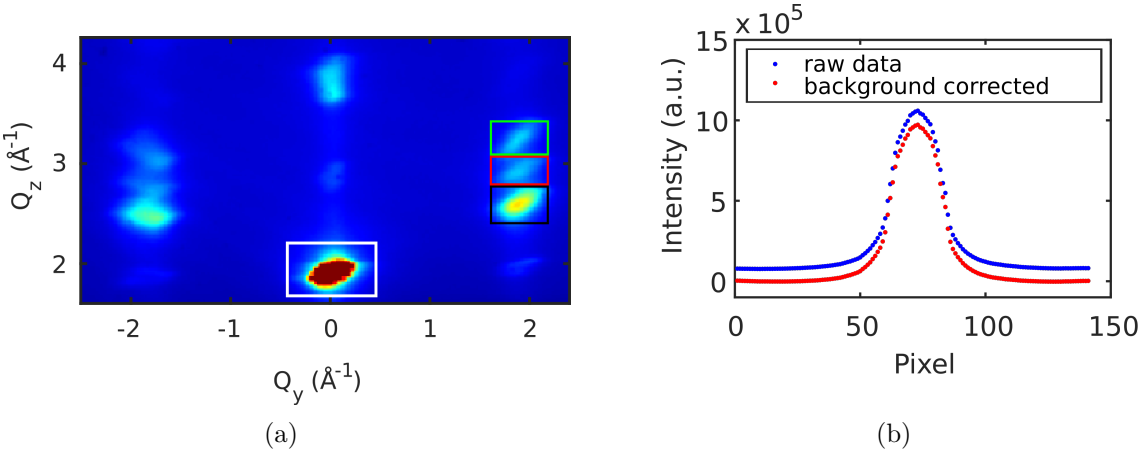

(a) (b)

Figure 4.25.: RHEED frame processing: (a) raw frame of sample A with the integration intervals marked by the coloured lines. The background is removed by subtracting equal integration intervals left and right to each diffraction spot. (b) Q_y-profiles before and after background correction.

4.5. Summary

Summarizing, we have developed a model which allows for the simulation of *in situ* time-resolved integrated intensities of RHEED diffraction spots in transmission geometry during the growth of vertical nanowires. We have estimated the impact of the electron beam interaction with individual nanowire, leading to self-shadowing, and with the whole ensemble leading to mutual shadowing within the nanowire ensemble, so called ensemble-shadowing. The dynamics of both is taken into account by simulating the structure evolution of the nanowire ensemble, including axial growth and radial growth with tapering and facet

growth. The parasitic intergrowth on the substrate is considered as well with different growth rates. Including all contributions enables us to simulate the time-resolved intensity evolutions of phase-sensitive diffraction spots during the growth of polytypic nanowire ensembles.

We have discussed the characteristics, the possibilities and the limitations of *in situ* RHEED and highlighted the impact of different parameters on the evolution of the RHEED signals by case studies employing the simulation programme. We conclude that the strength of the ensemble-shadowing is affected by the diffraction geometry, mainly by the angle of incidence with respect to the mean substrate surface and by the mean number density of nanowires on the substrate. The magnitude of the illumination height $\overline{\lambda}_{crit}$ defines the character of RHEED: at large $\overline{\lambda}_{crit}$ as a volume method for nanowire examination similar to *in situ* XRD, conversely, for decreasing $\overline{\lambda}_{crit}$ RHEED becomes increasingly height-selective. For very small $\overline{\lambda}_{crit}$, the RHEED signals can be attributed to a narrow illuminated part just below the axial growth front. The latter holds for sufficiently large and therefore more efficiently shadowing nanowire number densities, where $\overline{\lambda}_{crit}$ is much smaller than the nanowire height. Concluding, similarly to planar RHEED, also RHEED in transmission geometry can become extremely sensitive towards changes in the crystal structure at the growth front.

By carefully evaluating different axial and radial growth rates, we have deduced that at dominating self-shadowing conditions, the RHEED signal becomes insensitive to radial growth of the nanowires, whereas at dominating ensemble-shadowing conditions, RHEED is insensitive to changes caused by axial growth.

However, as we saw in the study of crystallographic properties, the insensitivity towards axial growth makes RHEED ideal for the characterization of the polytypism. Finally, we have introduced experimental procedures to determine the setup parameters, which are important to run the simulation. Now, we can apply the developed RHEED simulation model to real experiments, which will be presented in the subsequent chapters.

5. Simultaneous *in situ* RHEED and *in situ* XRD during nanowire growth

In situ characterization during nanowire growth is essential in order to understand and optimize the structural properties of the nanowires. A direct feedback enables tailoring the nanowires' structural properties and thus to fulfil specific demands which are needed for any applications in devices. The portfolio of *in situ* techniques capable for structural characterization consists of different representatives: the most prominent one is *in situ* transmission electron microscopy during nanowire growth, which offers unrivalled spatial resolution down to the atomic scale together with high temporal resolution. However, it is restricted to special equipment which is not broadly available.[98,105,136–138] The investigations are typically performed with pre-grown nanowires[98,136] or nanowires without epitaxial connection to any substrate.[105,137,138] Therefore a number of growth effects under standard conditions are excluded, such as the impact of diffusion processes on the substrate. The second well established technique is *in situ* X-ray diffraction during growth,[48,101,108–110] which probes representative structural properties averaged over a large statistical nanowire ensemble. By using micro-focused beams, even individual properties of single nanowires can be examined.[139] In both cases nanowire growth close to standard growth conditions with epitaxial connection to the substrate can be monitored. However, again special growth chambers equipped with X-ray windows are required, as well as access to heavy-duty diffractometers at high-flux synchrotron light sources.

The results presented in chapter 4 will allow us now to include also *in situ* RHEED during nanowire growth as an additional representative in this list. RHEED equipment is usually already integrated into commercial MBE systems and the RHEED characteristics are suitable to complement other techniques, for example XRD experiments.

In this chapter, we will discuss the complementarity of *in situ* RHEED and *in situ* XRD, which are the current available non-destructive structural characterization techniques for nanowire ensembles. In section 5.1, we will start with a theoretical discussion of the information which is contained in each method, as well as the corresponding advantages and disadvantages and their complementarity. These findings will be applied to real experiments in section 5.2, where we will present for the first time experimental results of simultaneous *in situ* RHEED and *in situ* XRD during the growth of self-catalysed GaAs nanowires. The high sensitivity of RHEED towards changes in the crystal structure will be demonstrated

in section 5.2.1, where a nanowire ensemble with a high number density is investigated. At the end of this chapter in section 5.2.2, we will apply our combinative approach to the nanowire nucleation stage, where we will conclude on the impact on the resulting polytypism of different procedures of initiating the nanowire growth of self-catalysed GaAs nanowires. Parts of this chapter will be published in publication II, which is in preparation.

5.1. The complementarity of *in situ* RHEED and *in situ* XRD during nanowire growth

In the following section we discuss and compare the main principles underlying the quantitative analysis of the RHEED and XRD intensities, respectively. We will show that *in situ* XRD during nanowire growth is characterized by a high sensitivity to the temporal evolution of phase-sensitive nanowire volume-growth rates, whereby *in situ* RHEED during nanowire growth is eminently suitable for quantitative determination of the evolution of the phase fraction of the main polytypes near the axial growth front. The well suited properties of RHEED are determined by: (1) the comparable large scattering cross section of electrons in solids, creating a high sensitivity to small volumes, which becomes particularly important for the crystal structure analysis during nanowire nucleation and early growth stages. This characteristic we are employing in section 5.2.2. (2) The high attenuation of the electron beam in the nanowires causes the ensemble-shadowing effect, which results in the height-selectivity of the RHEED signal from nanowire ensembles. The ensemble-shadowing focuses the sensitivity of RHEED on the crystalline properties at the nanowire tips, giving access to temporal evolution of the VLS growth. We exploit the second characteristic in section 5.2.1.

We now compare the diffracted integrated intensity of a certain RLP of both diffraction methods. The integrated RHEED diffraction signal is given in equation (4.16), in analogy we can write the integral form:

$$I^{ED}_{hkl,p}(t) \propto \left|F^{ED}_{hkl,p}\right| \int_0^{h^{NW}(t)} dh f_p(h,t) \cdot \Omega(r(h,t),\Lambda) \cdot (1 - s(h,t)). \tag{5.1}$$

Due to dynamical diffraction, $I^{ED}_{hkl,p}(t)$ is proportional to the structure factor of the corresponding crystal phase, $\left|F^{ED}_{hkl,p}\right|$. The values of the structure factors which are important in this work are given in table 2.2. We see that only the height window defined and weighted by the condition $(1 - s(h,t)) > 0$ contributes to the RHEED signal, which makes RHEED height-selective for this upper part of the nanowires. However, due to the time-dependency of both self-shadowing and ensemble-shadowing, the dynamics of the RHEED signal can be rather complicated, even for simple cases of stationary axial and radial growth conditions and stationary phase fractions, as we saw in section 4.3.

For X-ray diffraction the shadowing (self-shadowing and ensemble-shadowing) is negligible because of the comparably low absorption and larger incidence and diffraction angles. The illumination efficiency is always $(1 - s(h,t)) \approx 1$ and can therefore be omitted:

$$I_{hkl,p}^{XRD}(t) \propto \left|F_{hkl,p}^{XRD}\right|^2 \underbrace{\int_0^{h^{NW}(t)} dh f_p(h,t) \cdot \Omega(r(h,t),\Lambda)}_{\cong f_p^V(t)V^{NW}}, \tag{5.2}$$

where Λ is much larger than the nanowire diameter and thus it can be omitted in $\Omega(r(h,t),\Lambda)$, too. During the whole growth time, the integrated XRD intensity of a phase-sensitive RLP contains information of the selected crystal phase contribution integrated over the whole nanowire length $h^{NW}(t)$. Consequently, in contrast to RHEED being nanowire height-selective, this does not hold for XRD. Within the kinematical diffraction theory and for the low X-ray absorption the integrated XRD intensity signal is directly proportional to the crystal phase volume $V_p^{NW} = f_p^V V^{NW}$ contributing to the phase-sensitive RLP. In contrast to dynamical theory, the intensity is proportional to the square of the structure factor[107] $\left|F_{hkl,p}^{XRD}\right|^2$. A list of the structure factor values can be found in Ref.[83] This difference to RHEED will be essential, when recalibrating intensities of different phase-sensitive Bragg reflections. From the equations (5.1) and (5.2) we can derive the main similarities and differences of the temporal evolution of the XRD and RHEED signals.

5.1.1. X-ray diffraction

The temporal dynamics of a phase-sensitive XRD-signal reflects the dynamics of the related total crystal-phase volume. Compared to the high sensitivity of RHEED, especially towards crystal quality and phase changes at the axial VLS growth front over the whole growth cycle, similar phase changes translate to a substantially reduced XRD signal variation.
At the early growth stage and for small crystal volumes, the XRD signal is weak and the signal-to-noise ratio (SNR) very low. At later stages, the SNR improves, but the impact of newly grown material at the growth front on intensity variations during a given time interval Δt decreases with time proportionally to the increasing crystal phase volume:

$$\frac{\frac{d}{dt} I_{hkl,p}^{XRD}(t)\Delta t}{I_{hkl,p}^{XRD}(t)} \approx \frac{\frac{d}{dt} V_p^{NW}(t)\Delta t}{V_p^{NW}(t)}. \tag{5.3}$$

For the general case of simultaneous radial and axial growth, the sum over the crystallite-corrected and structure factor-recalibrated phase-sensitive reflection intensities $\tilde{I}_{hkl,p}^{XRD}$ is always proportional to the whole nanowire crystal volume,

$$\left(\sum_p \tilde{I}_{hkl,p}^{XRD}(t)\right) \propto V^{NW}(t). \tag{5.4}$$

We now introduce the rate of change of a physical quantity by the "physical quantity rate". The total intensity rate correlates with the total nanowire volume rate $v^{NW}(t)$ by

$$\frac{d}{dt}\left(\sum_p \tilde{I}^{XRD}_{hkl,p}(t)\right) \propto \frac{d}{dt}V^{NW}(t) \propto v^{NW}(t). \tag{5.5}$$

Further we can write $v^{NW}(t) = \sum_p v^{NW}_p(t)$, where the sum is taken over the particular volume rates of all occurring crystal phases. For the total nanowire volume rate we differentiate between the three following cases, where the factor Π depends on the wire shape and is for hexagonal wires $\Pi = (3/2)\sqrt{3}$ and for cylindrical wires $\Pi = \pi$:

$$v^{NW}(t) = \begin{cases} \Pi r_0^2\ m^{NW}_{axial}(t), & \text{for pure axial growth} \\ 2h^{NW}\ \Pi(r_0\ m^{NW}_{rad}\ +\ (m^{NW}_{rad})^2\ t), & \text{for pure radial growth} \\ \Pi r_0^2\ m^{NW}_{axial}\ +\ 4t\ \Pi r_0\ m^{NW}_{axial}\ m^{NW}_{rad} & \\ \qquad +\ 3t^2\ \Pi\ m^{NW}_{axial}\ \left(m^{NW}_{rad}\right)^2, & \text{for constant axial and radial} \\ & \text{growth rates.} \end{cases} \tag{5.6}$$

For *purely axial growth* the total nanowire volume rate is proportional to the mean initial nanowire nucleation diameter and the axial nanowire growth rate at given time m^{NW}_{axial}(t). Assuming temporally constant axial growth the total intensity increases linearly with the nanowire height $h^{NW}(t) = \int_0^t m^{NW}_{axial}(t')dt'$ and for constant axial growth rate linearly with time.

For *purely radial facet growth*, the total intensity and volume rates are a function of the initial nanowire diameter after nucleation and the temporal evolution of the radial growth rate m^{NW}_{rad}(t). If the radial growth rate would be constant over time, the total volume and intensity rates will increase linearly with time and, consequently, the volume and intensity themselves develop quadratically with time.

Supposing simultaneous radial and axial growth, but stationary growth conditions with temporally constant axial and radial growth rates, we obtain the time dependence of the intensity and volume rates given in the third line of equation (5.6), with the initial nanowire base radius r_0 at starting axial growth time.

5.1.2. Reflection high-energy electron diffraction

In chapter 4, we saw that the RHEED signal behaves differently compared to the previously described XRD signal. Due to the self-shadowing and the ensemble-shadowing as a result of the high electron absorption, the resulting sensitivity of RHEED to any nanowire growth rate is more complicated. Roughly speaking, absorption changes the illumination strength of the diffracting volume. To illustrate the differences to XRD, in addition to the

illumination height $\overline{\lambda(t)}$ we introduce an effective weighted illuminated volume $\overline{V^{lum}(t)}$, which essentially shrinks by self-shadowing and ensemble-shadowing:

$$\begin{cases} \overline{V^{lum}(t)} = \int_0^{h^{NW}(t)} dh\Omega(r(h,t)\Lambda) \cdot (1 - s(h,t)) \\ \overline{\lambda(t)} = \int_0^{h^{NW}(t)} dh \cdot (1 - s(h,t)), \end{cases} \tag{5.7}$$

Substituting V^{NW} by $\overline{V^{lum}}$, equation (5.3) holds also for RHEED. The total RHEED intensity rate measures the illuminated volume rate $\upsilon^{lum} \equiv \frac{d}{dt}\overline{V^{lum}}$ instead of υ^{NW}. Therefore, in contrast to equation (5.3), the equations (5.6) cannot be applied to RHEED. But studying carefully the influence of self-shadowing and ensemble-shadowing on the evolution one can immediately derive characteristic features of the RHEED intensities:
In case of *purely axial growth*, at early growth times till a first critical time $0 < t < t_{c1}$, ensemble-shadowing plays no role, and the mean illumination height $\overline{\lambda(t)}$ grows proportionally with $h^{NW}(t)$, as already shown in figure 4.12. Therefore, in this early growth stage the RHEED intensity rate corresponds to the axial growth rate $m^{NW}_{axial}(t)$. For stationary axial growth the RHEED signal would therefore linearly increase, similar to XRD, but with a much better SNR as a result of the high sensitivity to small crystal volumes.
At t_{c1}, the shadow footprint reaches the first nanowire neighbours and the ensemble-shadowing starts. Consequently, the illumination efficiency of the nanowire ensemble at the nanowire base drops from $(1 - s(h = 0,t \leq t_{c1})) = 1$, down to $(1 - s(h = 0,t \geq t_{c2})) = 0$, when at t_{c2} all shadow footprints reach the next nanowire neighbours.
In the time interval $t_{c1} < t < t_{c2}$, the increase of $\overline{\lambda(t)}$ and, accordingly, of the RHEED signal slows down, converging until t_{c2} to the saturation value $\overline{\lambda(t_{c2})} = \overline{\lambda}_{crit}$, and $I^{ED}_{hkl,p}(t_{c2})$ stays constant during further growth $t > t_{c2}$ (compare again to figure 4.12).
Summarizing, if above $t > t_{c1}$ the nanowire volume V^{NW} continues increasing, the shadowed nanowire volume also increases and consequently the increase of $\overline{V^{lum}}$ appears much more moderate and will even come to a halt at $t \geq t_{c2}$.
For the evolution of the volume rates we find

$$\begin{cases} \upsilon^{lum}(t < t_{c1}) & = \upsilon^{NW}(t < t_{c1}) \\ \upsilon^{lum}(t_{c1} < t < t_{c2}) & < \upsilon^{NW}(t_{c1} < t < t_{c2}) \\ \upsilon^{lum}(t > t_{c2}) & = 0. \end{cases} \tag{5.8}$$

Above t_{c2}, the size of the illuminated height window fulfilling the condition (1-$s(h,t > t_{c2})$) > 0 is stationary in time, but the window shifts with the nanowire growth upwards with the speed given by the axial growth rate ($ds/dt = m^{NW}_{axial} ds/dh$). The total RHEED signal becomes completely insensitive to the future evolution of the axial growth rate m^{NW}_{axial}.
The situation is similar in the case of *purely radial growth*: for thin wires ($D_c < \Lambda$)

RHEED is sensitive to m_{rad}^{NW}, but self-shadowing increases nearly exponentially with growing nanowire diameter. Both effects have opposite and therefore competing influences on the dynamics of the RHEED signal. In figure 4.7(a), we showed that initially the diffraction signal increases linearly due to increasing scattering volume. Then the signal increase slows down and passes through a maximum. Finally, sufficiently beyond nanowire diameters $D_c \approx 2\Lambda$ the RHEED signal converges to a stationary intensity value, depending on the azimuthal orientation of the nanowire cross section. This means that during radial growth the RHEED signal becomes increasingly insensitive to the radial growth rates. For certain azimuthal orientations the RHEED signal may nearly disappear, although radial and axial growth may continue.

For simultaneous radial and axial growth, the initial nanowire radius r_0 and the ratio of radial and axial growth determine the dynamics of RHEED, up to the growth stages when the illuminated volume $\overline{V^{lum}}$ converges to a constant value.

Since the total intensity corresponds directly to the illuminated volume $\overline{V^{lum}}$, if the latter becomes stationary the former will be stationary too. However, in contrast to XRD, $\overline{V^{lum}}$ of RHEED can appear to be stationary even in the presence of ongoing growth. Therefore to allow correct interpretation of the RHEED signal and to enable quantitative data evaluation of the whole growth cycle, it is imperative that shadowing effects are taken into account.

For the growth stages where the influence of axial and radial growth on the RHEED signal is negligible, it becomes nearly exclusively sensitive to changes of the polytype fraction within $\overline{V^{lum}}$ of the height $\overline{\lambda}_{crit}$.

However, we emphasize that based on our theoretical approach, also from the beginning of growth, and starting from thin nanowires, the RHEED signal can be quantitatively evaluated by equation (5.1), allowing determination of the time evolution of polytypism.

Concluding, by taking into account the fundamental differences of scattering and absorption of *in situ* RHEED and *in situ* XRD at all stages of nanowire growth, our methodology allows the targeted use of their complementarity: XRD, integrating the diffraction signal over the complete nanowire ensemble, gives representative information about the growth dynamics over the whole nanowire length, whereas RHEED is sensitive to the growth near the axial growth front. Their combination permits comprehensive characterization of the structure evolution during growth, as well as the final state after growth of the nanowire ensemble.

5.2. Simultaneous *in situ* RHEED and *in situ* XRD experiments

Finally, we apply the complementarity of both techniques, firstly to prove that our simulation model of *in situ* RHEED has validity and secondly to exploit the combined approach with additional post-growth SEM analysis for a comprehensive study of the structural evolution of nanowire ensembles.

The simultaneous *in situ* RHEED and *in situ* XRD experiments were performed at the Resonant Scattering and Diffraction Beamline P09[116] at the synchrotron facility PETRA III at DESY in Hamburg, Germany.

The asymmetric skew geometry at fixed incidence angle, introduced in section 3.2, enables access to an equivalent set of phase-sensitive Bragg reflections with both diffraction techniques by avoiding any interference. The *in situ* XRD experiment was performed with a X-ray beam energy of 15 keV and the diffraction signal was collected with a PILATUS 300K detector. During the growth experiment, we subsequently recorded small reciprocal space maps (RSM) in the vicinity of the phase-sensitive zinc blende (311), the twinned zinc blende (220) and the wurtzite (10.3) Bragg reflections of the GaAs. Additionally, in each scanning cycle, the Si (311) Bragg reflection was measured as a reference. The sizes of the small RSMs determine the overall temporal resolution, which is different for each investigated sample: the temporal resolutions are for sample C approximately 3.75 min, for sample D approximately 2.25 min and for sample E approximately 5.3 min. The X-ray beam size of approximately 16(v) x 70(h) μm^2 allowed us to measure a large nanowire ensemble and ensures gaining the mean properties of the nanowire ensemble. The experiments were completed by a post-growth RSM at room temperature with high-resolution.

The RHEED experiment was performed at an electron energy of 20 keV. The diffraction patterns on the fluorescence screen are captured with the low noise 14-bit PCO PixelFly camera with maximal time-resolution of 140 ms. During growth, 5 frames of 140 ms exposure time were recorded every 7 s and integrated to increase the SNR. While RHEED excites the Bragg reflections simultaneously, allowing a high temporal resolution, XRD has a low temporal resolution and a slight time delay between three, subsequently recorded, phase-sensitive reflections. This drawback is compensated by the advantage of a high Q-resolution giving access to the fine structure of the Bragg reflection patterns, allowing, e.g. to distinguish radial from axial volume growth rates.

In the subsequent sections, we first discuss a growth experiment with a high nanowire number density to illustrate the complementarity, afterwards we employ the approach to systematically investigate the polytypism within two further samples having low nanowire density. These last two samples are the basis of an analysis of the impact of differences in the nanowire nucleation procedures on the resulting polytypism.

For the investigation of polytypism it is useful to determine for both RHEED and XRD the respective phase fraction of the intensity $J_p(t)$ of phase sensitive RLPs:

$$J_p(t) = I_p(t) / \sum_p I_p(t). \tag{5.9}$$

In case of XRD, $J_p^{XRD}(t)$ is determined by the intensities $\tilde{I}_p^{NW}(t)$ of the Bragg reflections, corrected by the respective structure factors and by the contribution of parasitic crystallites. For XRD it follows from (5.2) that $J_p^{XRD}(t)$ is a direct measure for the phase volume fraction $f_p^V(t)$. Since the nanowire volume rate of a selected phase is proportional to the intensity rate of the corresponding reflection, we obtain

$$\frac{d}{dt} J_p^{XRD}(t) \approx \frac{d}{dt} f_p^V(t). \tag{5.10}$$

Similarly to XRD, the phase fraction of the RHEED intensity corresponds directly to the phase fraction of the illuminated volume $f_p^{V^{lum}}(t)$, even if the sensitivity of RHEED to any growth rate is more complicated,

$$J_p^{RHEED}(t) \approx f_p^{V^{lum}}(t) \equiv \frac{\int_0^{h^{NW}(t)} dh f_p(h,t) \cdot (1 - s(h,t))}{\int_0^{h^{NW}(t)} dh \cdot (1 - s(h,t))} \tag{5.11}$$

$$\approx \frac{\int_{h^{NW}(t) - \overline{\lambda(t)}}^{h^{NW}(t)} dh f_p(h,t)}{\overline{\lambda(t)}}, \tag{5.12}$$

and consequently,

$$\frac{d}{dt} J_p^{RHEED}(t) = \frac{d}{dt} f_p^{V^{lum}}(t) \approx m_{axial}^{NW}(t) \frac{d}{dh} f_p^{V^{lum}}(h). \tag{5.13}$$

Considering a high nanowire number density resulting in a small illumination height $\overline{\lambda(t)}$, the phase fraction of the intensity corresponds nearly directly to the phase-volume fraction at the nanowire apex and thus to the phase generation probability $f_p(h(t),t)$ ($f_p^{V^{lum}}(t) \approx f_p(h(t),t)$), or alternatively the rate of the phase-sensitive intensity fraction $\frac{d}{dt} J_p^{RHEED}(t)$ corresponds nearly directly to the ensemble averaged phase change at the axial growth front. Knowing the final nanowire height from SEM and assuming a constant axial growth rate, or by determining the axial growth rate from XRD, we can transform the time dependence of $J_p^{RHEED}(t)$ and thus $f_p(h(t),t)$ by equation (5.13) into a height dependence of $f_p(h,t_f)$.

5.2.1. High sensitivity to polytypism over the whole growth at high nanowire number density

The conditions for the nanowire growth experiment were chosen such that we can prove the complementarity of the simultaneous approach and demonstrate the high sensitivity of RHEED to changes in the crystal structure in the nanowire ensemble. This requires a high nanowire number density in order to obtain high ensemble-shadowing conditions for RHEED, thus enabling the investigation of only a small part at the top of the nanowires. In contrast, XRD can probe as well the shadowed part of RHEED and detect changes inside the electron shadow. Therefore, the growth protocol introduced in section 3.3 is adapted as described in the following.

Sample

The GaAs nanowires were grown on a n-type Si(111) substrate covered with native oxide. This was first degassed for 30 min at $T_{sub} = 300\,^{\circ}\mathrm{C}$ before being loaded into the growth chamber of the pMBE. To condition the substrate and to tune the nanowire number density to the desired value, the SMP method was used (see section 3.3), in which the second step was modified to a substrate temperature of $T_{sub} = 510\,^{\circ}\mathrm{C}$ and the deposited amount of Ga to a thickness equivalent to 58 ML of planar GaAs. After Ga desorption at higher substrate temperature and before the actual nanowire growth at $T_{sub} = 580\,^{\circ}\mathrm{C}$, Ga was pre-deposited at $T_{sub} = 580\,^{\circ}\mathrm{C}$ to form droplets on the substrate with an equivalent thickness of 48 ML of planar GaAs. After this pre-deposition step, self-catalysed GaAs nanowires were grown by simultaneous supply of Ga and As_4 with an equivalent Ga-limited 2D layer growth rate of 0.1 ML/s and a V/III - ratio of 3.5. After 30 min of nanowire growth (t_{f1}), first the Ga supply was stopped while the As_4 flux was kept constant to consume the liquid Ga droplet at the tip of the nanowires.
The resulting non-tapered nanowires on sample C have a final height of $h_f^{NW} = (800 \pm 160)$ nm and an identical final radius at the bottom and at the tip of $r_{f,b}^{NW} = r_{f,t}^{NW} = (27 \pm 2)$ nm. The number density of the nanowires is $\rho_{NW} = (8.4 \pm 2.1)\ \mu\mathrm{m}^{-2}$. Scanning electron micrographs of the grown nanowires are depicted in figure 5.1, illustrating the successful consumption of the liquid Ga droplets at the nanowire tips after t_{f1}. Besides vertical nanowires, parasitic growth of bulky GaAs crystallites is observable on the substrate with an object density of $\rho_{cry} = (6.4 \pm 2.0)\ \mu\mathrm{m}^{-2}$.

Results and discussion

We start our discussion with the results of the RHEED experiment. Exemplary raw frames before the structure factor correction for different growth times are shown in figure 5.2(a), where we see a clear separation of the phase-sensitive diffraction spots. The strong variation

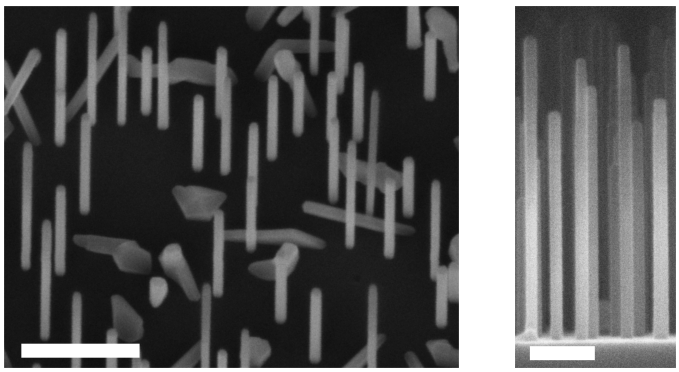

(a) 30° tilt view. (b) Side view.

Figure 5.1.: Representative SEM images of sample C. The nanowire ensemble exhibit a high number density, they are non-tapered and have no droplet at their tips, indicating the successful droplet consumption after t_{f1}. The scale bars equal 500 nm in figure (a) and 200 nm in figure (b).

in the intensity is directly observable, especially the WZ diffraction peak nearly vanishes during the middle part of the growth run. The RHEED frames are processed according to section 4.4.2 to account for the background in the signal and to calibrate the diffracted intensity for the structure factors of the different diffraction spots. The resulting structure factor calibrated intensity evolution is presented in figure 5.2(b). The shaded regions indicate the uncertainties of the signals. Additionally, we plot the sum of both zinc blende reflections Σ ZB = ZB + TZB and the sum of all three phase-sensitive reflections, which we call the overall intensity.

The intensity evolution of the RHEED diffraction spots shows some interesting features, at the beginning of growth until $t \approx 3\,\text{min}$ a dominating WZ intensity rate is observable, which abruptly stops. Immediately afterwards, the WZ intensity rapidly drops between $t = 3\,\text{min}$ and $t = 9\,\text{min}$ until it becomes effectively constant between $t = 20\,\text{min}$ and $t = 30\,\text{min} = t_{f1}$.

The ZB intensity increases already at $t = 0\,\text{min}$ simultaneously with WZ, but before TZB, which increases after a short delay. However after $t = 3\,\text{min}$ the two zinc blende related ZB and TZB intensity curves coincide again and increase together, but with a less strong intensity rate compared to WZ. The intersection of the Σ ZB and WZ intensity curves are at $t \approx 8\,\text{min}$, resulting in domination of the intensity distribution by the zinc blende phases. Around $t \approx 15\,\text{min}$ they reach their maximum value and decrease afterwards slowly until the end of Ga supply at $t_{f1} = 30\,\text{min}$.

During the consumption of the catalyst particles, the WZ intensity begins to increase again, which is known from literature,[127] and almost simultaneously the Σ ZB curves show a short period of increase before rapidly decreasing again. Another remarkable feature in this plot is the abrupt increase of the overall intensity at t_{f1}.

The oscillations in the RHEED signals are typical for the simultaneous *in situ* RHEED and *in situ* XRD growth experiments and are related to the experimental station at the synchrotron beamline. The less shielded infrastructure to magnetic fields there, provoke instabilities in the RHEED flux. Since for the *in situ* XRD experiment, we move the whole chamber on the diffractometer in order to excite different Bragg reflections, its relative position inside the experimental hutch changes. The instabilities of the RHEED signal coincide with these XRD scans. However, the RHEED signals have better quality in the standard laboratory use, as we will show in chapter 6.

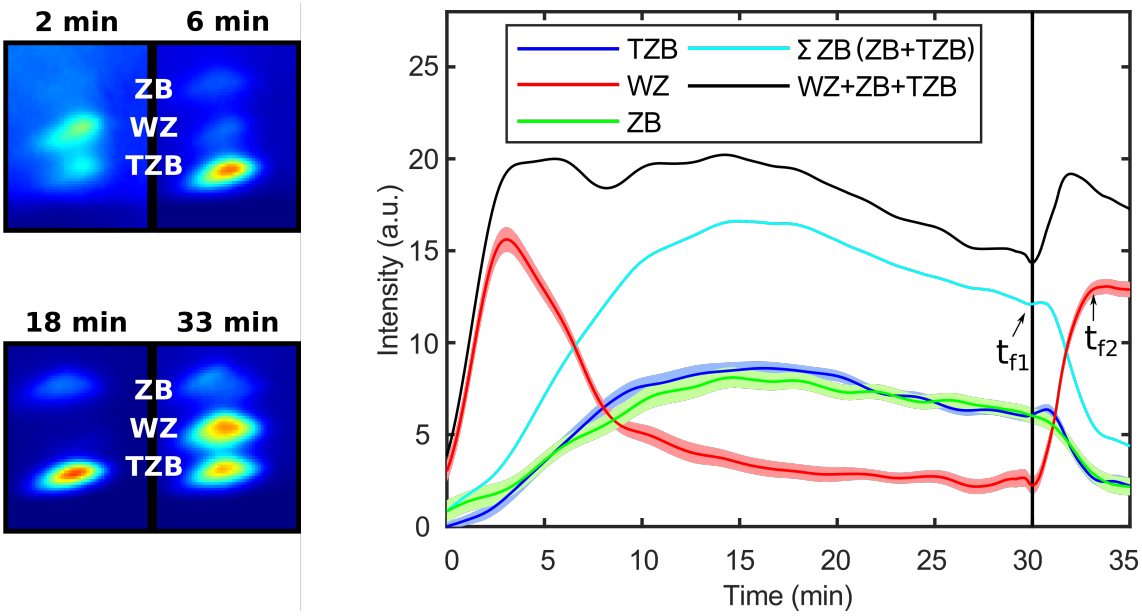

(a) (b)

Figure 5.2.: Experimental result of the RHEED experiment. (a) RHEED camera frames at different growth times show the strong variation of the diffraction spot intensity during the growth. (b) Temporal evolution of the structure factor calibrated phase-sensitive diffraction spot intensities, the Σ ZB intensity and the overall RHEED intensity. At t_{f1} the Ga flux is stopped while the As_4 flux is kept constant leading to a consumption of the catalyst droplets at the nanowire tips until t_{f2}.

Now we proceed with the discussion of the XRD experiment. For the subsequent analysis, the detector raw frames were transformed into reciprocal space. The post-growth RSM at room temperature is shown in figure 5.3(a), where a three dimensional volume of the reciprocal space is integrated along Q_x, resulting a Q_y-Q_z projection. The intensity is colour coded with a logarithmic scale. The Si(311) Bragg reflection is the most intense one, originating from the Si substrate. The phase-sensitive GaAs Bragg reflections are vertically connected, along Q_z by an intensity streak which arises from the diffuse scattering of stacking faults in the nanowires. Additionally, each reflection is elongated along Q_y: these facet streaks originate from the hexagonal cross section of the nanowires. They are

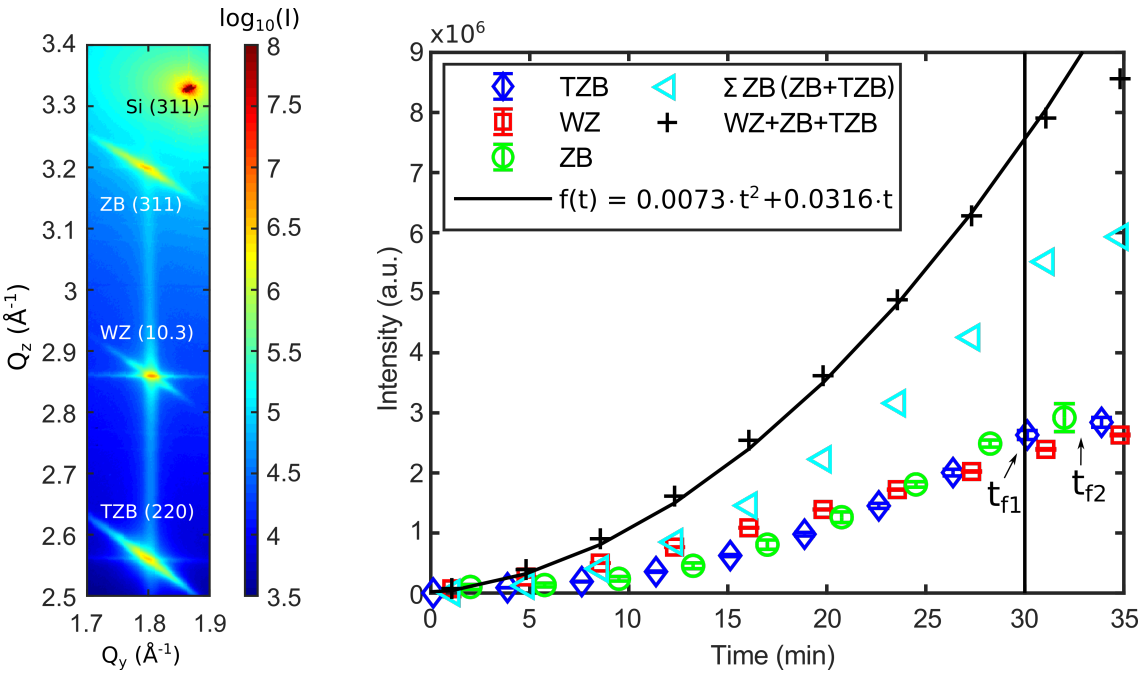

(a) (b)

Figure 5.3.: Experimental result of the XRD experiment. (a) RSM of the asymmetric truncation rod including the Si(311), GaAs(311), GaAs(10.3) and GaAs(220) Bragg reflections. The RSM was measured after growth at room temperature. (b) Temporal evolution of the crystallite and structure factor corrected phase-sensitive Bragg reflection intensities. The Σ ZB intensity and the overall RHEED intensity evolution are a non-linear function as shown by the polynomial fit.

perpendicular to each of the six facets and due to the projection of the reciprocal space on 2D, they are only discernible on two sides of the Bragg reflections. The last prominent features in the RSM are the inclined streaks crossing the Bragg peaks perpendicular to the reciprocal lattice vectors, along the virtual Debye-Scherrer-rings. A slight distribution of the orientation of parasitically grown crystallites and nanowires leads to these streaks. However, this also allows the separation of the intensity contribution arising from the crystallite and nanowire ensemble as described in Ref.[68,101]

The Bragg peak intensity evolution of the time-resolved XRD experiment is plotted in figure 5.3(b), the non-linear increase of the total X-ray intensity (ZB + TZB + WZ depicted in black) during the first 30 min gives clear evidence for simultaneous axial and radial growth, as we discussed in equation (5.6). After $t_{f1} = 30$ min the slope of the total intensity changes but still increases with a reduced rate and comes to an end at $t_{f2} = 33.5$ min. We explain this kink in the intensity evolution by the expiration of radial growth due to the stop of the Ga flux and the remaining axial growth due to the continuing supply of As_4, which maintains the axial VLS growth until complete consumption of the liquid Ga droplets on top of the nanowires. The XRD intensity stagnates beyond t_{f2} proving the stop of any

nanowire growth after the droplet consumption, as has been confirmed by SEM.
Focusing on the phase-sensitive XRD intensities, we see that the WZ phase crystal volume develops approximately linearly, whereas the zinc blende related intensities develop initially slower, but later benefit from a non-linear increase, with progressing rates till t_{f1}. The WZ - ZB intensity crossover is at about $t = 22\,\text{min}$ and the WZ - Σ ZB crossover already at $t = 12\,\text{min}$. The volume increase between $(t_{f1} < t < t_{f2})$ is approximately $\Delta V^{NW}/V^{NW}(t = 30\,\text{min}) \approx 10\,\%$.

Determination of the radial growth by *in situ* XRD

The time-resolved *in situ* XRD experiment with high Q-resolution allows to determine the radial growth rate of the nanowires. As introduced in section 2.3, the intensity distribution of a Bragg reflection contains information on the shape of the scattering object. Consequentially, the temporal evolution of the facet streaks originating from the hexagonal cross section of the nanowires contains information on their radial growth rate. Post-growth SEM inspection has provided evidence that the nanowires are non-tapered, meaning that the radial growth rate averaged over the nanowire height can be independently determined from the temporal change of the positions of the size oscillations of the facet streaks perpendicular to Q_z (details can be found in Ref.[68,101]).

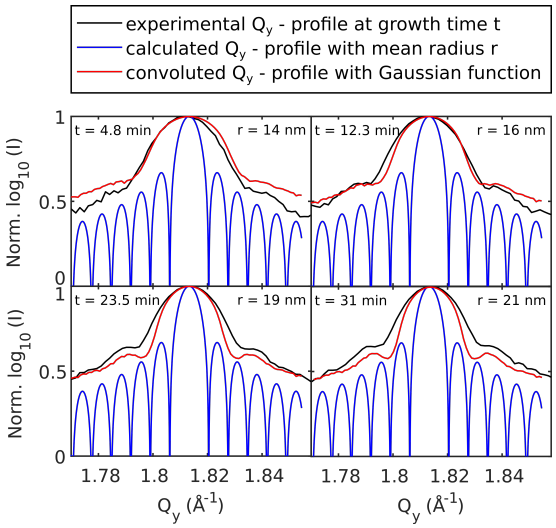

(a) Representative Q_y-profiles at certain growth times in black. The shape function of the hexagonal cross section along Q_y is plotted for none radius distribution in blue and with a Gaussian distribution with standard deviation of 2 nm in red, which is motivated by the SEM results.

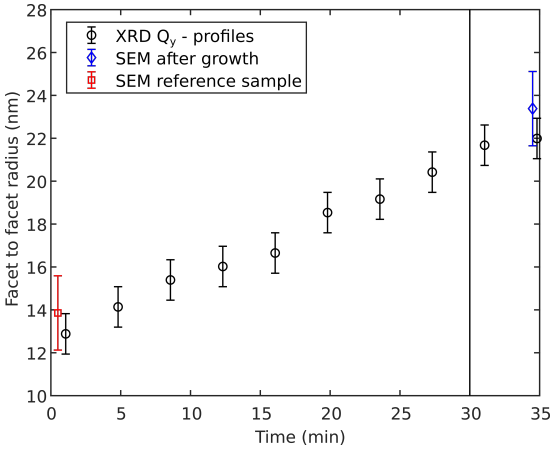

(b) Temporal evolution of the facet to facet radius of the nanowire ensemble (compare figure 4.4) determined by the fine structure of the WZ reflection. Additionally, SEM measurements are shown at the beginning and at the end of growth for comparison.

Figure 5.4.: Determination of the radial growth rate by XRD.

Figure 5.4 illustrates the determination of the radial growth rates. Chosen experimental Q_y-profiles through the WZ reflection at different growth times t are depicted in black in figure 5.4(a). For the determination of the nanowire radius, we consider its distribution function measured after growth by SEM, where we measured a Gaussian distribution with a standard deviation of 2 nm around the mean radius. The measured values can be found in table 5.1. Therefore, we convolute the shape function of the nanowire cross section with a Gaussian distribution having the aforementioned standard deviation of 2 nm. The resulting profiles are presented in red, whereas in blue the shape functions without convolution are shown for comparison. Not considering the radius distribution would lead to different absolute values of the radial growth. However, the convoluted profile functions describe the experiment with good agreement.
All determined mean radii of the time-resolved Q_y-profiles through the WZ reflection are summarized in figure 5.4(b). For comparison we marked the final radius measured by SEM in blue and in red the radius of a reference sample measured by SEM, where we stopped the growth directly after the nucleation. From figure 5.4(b), we can conclude that the radial growth rate is linear.

Characterization of polytypism by means of the developed simulation model

The determination of the radial growth rates by *in situ* XRD together with the post-growth SEM analysis to obtain the values of the final shape of both ensembles and their number density, allow us to set appropriate starting values for the input parameter of the developed simulation model. As further free parameter space, in a second step, we vary the time-dependent polytype fraction during the growth run.
For the RHEED intensity simulation, we additionally require the mean free path length of the electron beam energy at 20 keV, which is $\Lambda = 12$ nm, as was determined in section 4.4.2. The incidence angle of the electron beam α is in this experiment different to the determined value in section 4.4.1. During this experiment, we had to choose a different azimuthal orientation of the sample. Due to the wobbling of the manipulator the incidence angle of the electron beam is in the current case $\alpha = 1°$. According to equation (4.5), the height-selectivity for the RHEED measurements is very small and approximately $\overline{\lambda}_{crit} = 19$ nm which corresponds to 6 GaAs layers.
For the simulation of the X-ray intensity evolution, we neglect self- and ensemble-shadowing, which is conform with the low absorption of 15 keV X-ray photons with $\Lambda \approx 20.27\,\mu$m.[140]
The simulation routines are performed with a temporal resolution of t_i steps with $i \in$ [1,100] for the nanowire growth and for additional t_i steps with $i \in$ [1,12] for the droplet consumption.
In a first simulation procedure, we simulate the intensity evolution without polytypism and compare the resulting curves with the overall intensity evolution. This first step allows us to determine the shape parameters of both ensembles (ρ_{NW}, r_0^{NW}, $r_{f,b}^{NW}$, $r_{f,t}^{NW}$, h_f^{NW},

Table 5.1.: Values of sample C obtained by post-growth SEM analysis and parameters used for the simulation model.

parameter	post-growth SEM	simulation
ρ_{NW} (µm^{-2})	8.4 ± 2.1	8.0
r_0^{NW} (nm)	–	14
$r_{f,b}^{NW}$ (nm)	27 ± 2	27
$r_{f,t}^{NW}$ (nm)	27 ± 2	27
h_f^{NW} (nm)	800 ± 160	800
ρ_{cry} (µm^{-2})	6.4 ± 2.0	6.0
r_0^{cry} (nm)	–	14
r_f^{cry} (nm)	80 ± 30	80
h_0^{cry} (nm)	–	0
h_f^{cry} (nm)	100 ± 30	100
t_{f1} (min)	–	30

ρ_{cry}, r_0^{cry}, r_f^{cry}, h_0^{cry} and h_f^{cry}) and set these in relation to post-growth SEM results. The parameters of the nanowire and crystallite shape evolution for the best fitting simulated curves together with the results of SEM are listed in table 5.1.

Each of these simulated intensity evolution with a different set of shape parameters is compared to the experimental intensity evolution of *in situ* RHEED and *in situ* XRD. The curves of the simulations as well as the obtained experimental data are normalized to equal areas under the curves (equal time-integrated intensities), followed by the determination of the root-mean-square deviation (RMSD). The set of parameters resulting in the intensity evolution with the lowest RMSD value is used in the subsequent steps.

In a second simulation procedure, we now focus on the polytype variation. Therefore, we are using the phase-sensitive reflections and fix the structure parameters to the best obtained set of the previous simulation round. This time, we vary the polytype distribution $f_p(h^{NW}(t),t)$ in the nanowire ensemble over a large parameter space, which is indicated in figure 5.7(a) as a light brown shaded area. Again, we normalize the curves to equal areas under curves (equal time-integrated intensities), followed by the determination of the RMSD for WZ and ZB separately as well as for each diffraction method. Figure 5.5 shows the experimental intensity evolution and best fitting simulated curves.

The simulations are based on the same nanowire growth model with identical parameter sets, the only difference is the the consideration of self- and ensemble-shadowing in RHEED, which result in the different curves of figures 5.5(a) and 5.5(b). The successful simulation

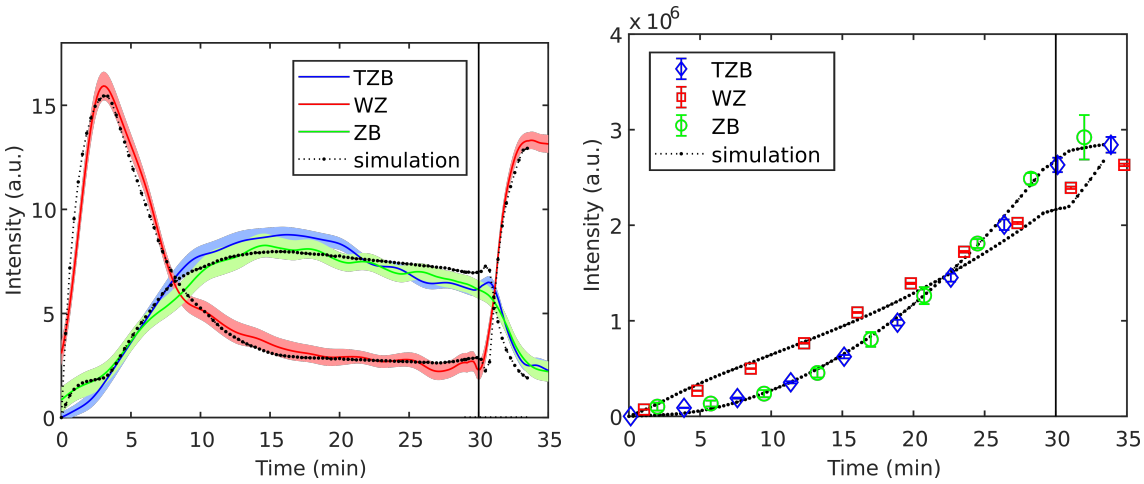

(a) (b)

Figure 5.5.: The experimental intensity evolutions plotted with the results of the simulation model for RHEED (a) and XRD (b). The parameters of the simulation are listed in table 5.1 and are the same for both plots, the only difference is the consideration of self- and ensemble-shadowing in the RHEED simulation.

of the experimental data by our model enables us now to draw some further conclusions. In section 5.1, we saw that the total RHEED intensity is proportional to the illuminated volume $\overline{V^{lum}}$. According to the Monte Carlo simulations, the ensemble-shadowing sets in already at $t_{c1} \approx 1\,\text{min}$ and reaches its maximum two minutes later around $t_{c2} \approx 3\,\text{min}$. Thus, the initially high sensitivity of RHEED to the axial growth rate diminishes already after 1 min and only until then the related volume rate $v^{lum}(t)$ is proportional to the axial growth rate. The phase-sensitive volume rates are additionally weighted by the illuminated volume phase fractions.

At $t_{c2} \approx 3\,\text{min}$, where the illumination height has reached its maximum value $\overline{\lambda(t_{c2})}$, RHEED has lost already its sensitivity to any volume increase generated by the axial growth, which can be identified in figures 5.2(b) and 5.5(a) by the saturation of both the total RHEED intensity and the WZ intensity curves. Thus, from the growth time t_{c2} on, changing ratios of phase-sensitive RHEED signals can be directly attributed to changes of the corresponding growing crystal phases in the nanowire ensemble, located in the now stationary illuminated height $\overline{\lambda(t_{c2})} = \overline{\lambda}_{crit}$ below the nanowire tip.

The decrease of the WZ intensity after $t \approx 3\,\text{min}$ can be explained by the concurrence of two effects: (1) the rise of of the Σ ZB intensity indicates a changing WZ to Σ ZB ratio, which is discernible in both diffraction techniques, XRD and RHEED. (2) the high sensitivity to the axial growth front of RHEED, which is governed by the high number density of nanowires at this sample and the resulting small illumination height of RHEED. The observed change in the Σ ZB phase volume rate can only originate from the axial growth front, where the generation probability changes from WZ rich to Σ ZB rich. The

previously grown WZ segments in the nanowires move outside the illumination height $\overline{\lambda}_{crit}$ and only newly grown ZB and TZB segments contribute to the diffraction signals. The speed of this relative vertical window movement is given by the axial growth rate $m_{axial}^{NW}(t)$ (equation (5.13)).

The slight decrease in the overall RHEED intensity starting from $t \approx 10\,\text{min}$ and lasting until $t \approx 30\,\text{min}$ can be attributed to the radial growth of the nanowires. As described in section 4.3, there exists a competition of the influence on the signal induced by the positive volume rate and by the reduction of the signal due to self-shadowing, which in our case dominates for diameters larger than $D_c \approx 30\,\text{nm}$. We should also mention that a reduction of the RHEED signal could also be induced by other effects, like a change of the droplet height affecting the ensemble-shadowing, or due to variations in the incident electron flux, which are however in the current case unlikely. The XRD total intensity rates and the perfectly fitting simulation confirm the explanation by the radial growth rate.

The variation of the ZB and TZB intensities at the onset of growth is also explained by means of the simulation model and can be related to the additional contribution of the crystallite ensemble at this growth stage and its subsequent shadowing during further growth. In figure 5.6 a magnified region of the onset of growth is shown, in black the simulated ZB intensity of both ensembles, nanowire and crystallites is plotted. In grey, however only the intensity originating from the crystallite ensemble is depicted, which has its maximum around $t = 1\,\text{min}$. The slower growing crystallites rapidly become fully shadowed, resulting in the superposition of ZB and TZB intensities again.

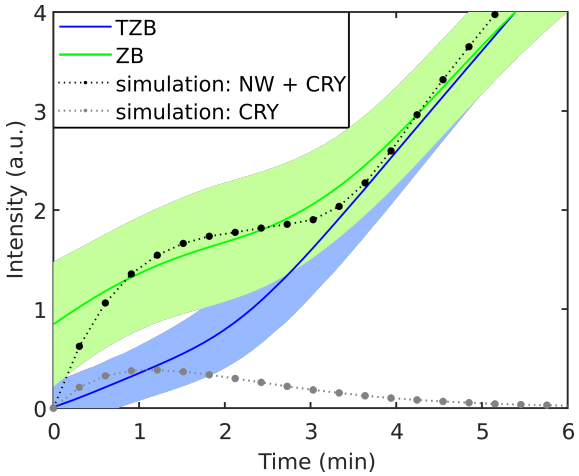

Figure 5.6.: Magnification of the onset of growth of the RHEED experiment. The ZB and TZB intensities show a different magnitude, which is explained by the additional intensity contribution of the crystallite ensemble as shown by the simulation model. In black the simulated ZB intensity of the nanowires and crystallites and in grey only the intensity of the crystallite ensemble is plotted.

A further interesting feature is that at $t_{f1} = 30\,\text{min}$ both the RHEED WZ intensity as well as the total RHEED intensity rise abruptly again. This can only be explained by the increase of the mean illumination height $\overline{\lambda}_{crit}$ of the nanowires below their tips and gives evidence for the consumption of the Ga droplet until $t_{f2} \approx 33.5\,\text{min}$. For stationary VLS conditions, $\overline{\lambda}_{crit}$ should be constant, but after t_{f1} the droplet on top of the nanowires shrinks due to its consumption and leads to an increase of the illumination height.
The remaining As_4 flux and the Ga reservoir in the droplets permit to maintain the axial growth further, the XRD signal enables characterization of the remaining axial growth rate. At t_{f2}, when the Ga reservoir of the droplet has been completely consumed, the overall growth comes to a standstill.

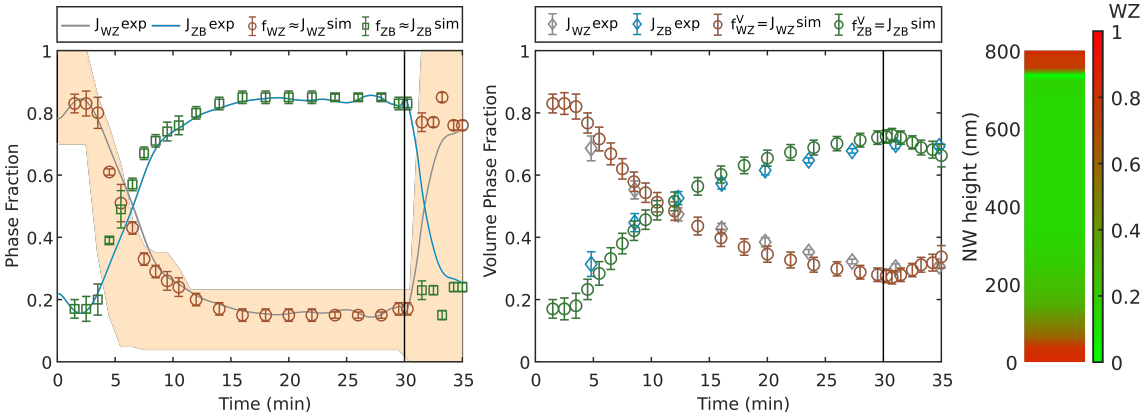

(a) (b) (c)

Figure 5.7.: Phase fractions plotted as a function of time: (a) phase fraction at the axial growth front, $J_p^{RHEED}exp(t)$ are the RHEED intensity fractions, the phase fractions $f_p(h^{NW}(t),t) \approx f_p^{V^{lum}}(t)$ are due to the high nanowire number density equal to $J_p^{RHEED}sim(t)$ of RHEED. (b) volume phase fraction in the nanowires, $J_p^{XRD}exp(t)$ are the XRD intensity fractions, the volume phase fractions $f_p^V(t)$ are equal to $J_p^{XRD}sim(t)$ of XRD. (c) final height profile of the polytypism. High WZ fraction is illustrated in red shifting towards green for high ZB/TZB fraction.

To compare and interpret the quantitative evolution of different crystal phases, we apply the equations (5.1), (5.2), and (5.9) and further use the findings in section 5.1. In figure 5.7(a), the RHEED intensity fractions $J_{WZ}^{RHEED}exp(t)$ and $J_{ZB}^{RHEED}exp(t)$ obtained from the RHEED experiment are plotted. The phase generation probabilities $f_{WZ}(h^{NW}(t),t)$ and $f_{ZB}(h^{NW}(t),t)$ are directly the free parameter in the simulation model, which were fitted during the second simulation iteration. Due to the high number density and the resulting effective ensemble-shadowing, the RHEED intensity fractions $J_{WZ}^{RHEED}(t)$ and $J_{ZB}^{RHEED}(t)$ can be directly interpreted as the generation probability at the axial growth $f_{WZ}(h^{NW}(t),t)$ and $f_{ZB}(h^{NW}(t),t)$. Figure 5.7(b) depicts the XRD intensity fractions $J_{WZ}^{XRD}exp(t)$ and $J_{ZB}^{XRD}exp(t)$ of WZ and Σ ZB obtained from the XRD experiments and

$J_{WZ}^{XRD}sim(t)$ and $J_{ZB}^{XRD}sim(t)$ of the simulated curve, which are according to equation (5.10) equal to the volume phase fractions $f_{WZ}^{V}(t)$ and $f_{ZB}^{V}(t)$. Except at the very beginning of growth, where the XRD intensities are low, the SNR is weak, and possibly insufficient crystallite correction of the signals shows a higher impact, the simulation and experiment fit very well.
The WZ - Σ ZB crossover of the volume phase fraction $f_p^V(t)$ is at $t = 11\,\text{min}$, the Σ ZB - WZ crossover of the phase generation probability at the axial growth front $f_p(h^{NW}(t),t)$ already occurs at $t = 7\,\text{min}$, corresponding to a final height of $h^{NW} = 180\,\text{nm}$. The second crossover (WZ - Σ ZB) takes place at $t = 32\,\text{min}$ and respectively at $h^{NW} = 740\,\text{nm}$.
In principle, any phase volume change observed by XRD or RHEED could be caused (1) by phase transformation within the probed nanowire volume or (2) by changing phase generation probabilities at the growth fronts. Hypothetical phase transformations and changes at the radial growth front should induce comparable changes in the corresponding intensity fractions of the involved Bragg reflections. XRD intensity fractions probe the affected total crystal volume of the nanowire ensemble, their growth rates are therefore sensitive to phase transformations in the whole nanowire and to changes at both the radial and axial growth front. In contrast, due to the large differences of the radial and axial growth rates the RHEED signal is particularly sensitive to the axial phase generation probability and therefore to the VLS growth conditions at the interface of the Ga-droplet and the nanowire top facet. The agreement between simulation and simultaneously recorded XRD and RHEED intensity profiles confirms volume phase transformation and phase changes during radial growth to be highly improbable.
Thanks to the high temporal and height resolution of RHEED, one can directly compare the phase generation rates of the nanowire ensemble with the experimental phase related intensity fractions of RHEED. If the axial growth rate is given via the XRD experiment and confirmed by SEM, and no phase-transformation occurs at the radial facets or in the nanowire volume, as has been confirmed by combining RHEED and XRD, then by equation (5.13) the strong ensemble shadowing allows direct translation of the measured temporal evolution of the phase fraction of the illuminated volume $f_p^{V^{lum}}(t) \approx f_p(h^{NW}(t),t)$ into the final height profile of the corresponding phase fractions, as shown in figure 5.7(c).

Summary

We successfully conduct a simultaneous *in situ* RHEED and *in situ* XRD experiment during the growth of self-catalysed GaAs nanowires. The complementarity of the simultaneous RHEED and XRD experiment are exploited to get comprehensive information on the nanowire growth. The developed simulation model of chapter 4 is successfully applied and proved experimentally by describing both curves with an identical parameter set. The high nanowire number density of sample C reduces the illumination height down to a narrow region at the nanowire apex and enables us to follow the crystal structure at the axial

growth front with high sensitivity. While the RHEED experiment is particularly sensitive to the axial growth front, XRD probes the whole nanowire height. Thus it is sensitive to the changes inside the electron shadow and combined with the suitable Q-resolution, we are able to determine the radial growth rate, which is important as input for the simulation model. The theoretical considerations at the beginning of the chapter and the results of the simulation model allowed us to draw conclusions from the shape of the different intensity evolutions, such as e.g. the saturation of the RHEED signals or the crystallite ensemble contribution. By means of the model, we determine the nucleation probability at the axial growth front during growth, which is equal to the intensity fractions of RHEED in case of high nanowire densities. By supposing the phase fraction of a given height to be stationary over time, we are able to translate the time-dependency of the phase fraction into a final height profile along the nanowire height.

5.2.2. High sensitivity to polytypism during nanowire nucleation at moderate nanowire number density

In this section, we are now applying the approach of simultaneous *in situ* RHEED and *in situ* XRD during nanowire growth to a systematic study, where we focus on the nucleation phase of nanowires. In general, there exist two different ways of initiating the nanowire growth. In the first method, Ga is pre-deposited (PD) before the actual nanowire growth in order to form droplets on the substrate from which afterwards the nanowire nucleates (sample D). The second method omits a PD step and the Ga is supplied after the As, when the As flux is already stabilized. Consequently, the Ga droplets form in an As background pressure (sample E). Both samples are characterized by *in situ* RHEED and *in situ* XRD in order to draw conclusions on the impact of PD on the polytypism.

Samples

The GaAs nanowires were again grown on n-type Si(111) substrates covered with a thin native oxide layer, which were degassed at $T = 300\,°\mathrm{C}$ for 30 min before loading them into the pMBE. The used growth protocol for this experiment deviates from the standard growth protocol presented in section 3.3. Instead, we used a growth scheme developed in our working group and published in Ref.,[78] where an iterative nanowire growth and thermal desorption scenario is used to increase the number density of nanowires.
First the substrate was heated to $T_{sub} = 650\,°\mathrm{C}$ for 30 min to create small openings in the oxide layer.[67] After a reduction of the substrate temperature to $T_{sub} = 590\,°\mathrm{C}$, Ga was deposited equivalent to 40 ML of planar GaAs as a PD step, followed by the nanowire growth at a 2D-layer-growth rate of 0.07 ML/s at a V/III - ratio of ≈ 2. After this procedure, the nanowires were thermally desorbed at $T_{sub} = 650\,°\mathrm{C}$ until no indication of GaAs is discernible in RHEED.

In the second iteration, the growth scheme stayed the same for sample D, meaning that at a substrate temperature of $T_{sub} = 590\,°C$ first an equivalent of 40 ML of Ga was pre-deposited, followed by the nanowire growth, which was performed again with a growth rate equivalent to 2D-layer-growth of 0.07 ML/s at a V/III - ratio of ≈ 2 for $t_f = 60\,\text{min}$. At the end of growth both material fluxes were stopped in parallel and the substrate temperature was immediately ramped down to room temperature. During the whole growth we performed simultaneously XRD and RHEED experiments.
For sample E, we omit the PD step in the second iteration. After the desorption of the nanowires, the substrate temperature T_{sub} was set to 590 °C, however, for this sample we first supply As_4 until the pressure inside the chamber stabilized, followed by initiating the nanowire growth by the supply of Ga with the same growth conditions as for sample D. Again, we stopped both material fluxes simultaneously and ramped down the substrate temperature. Over the whole growth process we perform simultaneously XRD and RHEED experiments. More details about the growth scheme can be found in the corresponding publication.[78]
Scanning electron micrographs of both samples are shown in figure 5.8. The resulting nanowires of sample D and E have comparable shape and are slightly negatively tapered with a final mean nanowire height of $h_{f,D}^{NW} = 1600\,\text{nm}$ and $h_{f,E}^{NW} = 1800\,\text{nm}$. The nanowire number densities are $\rho_{NW,D} = 0.1\,\mu\text{m}^{-2}$ and $\rho_{NW,E} = 0.07\,\mu\text{m}^{-2}$. Further values of the SEM analysis are summarized in table 5.2.

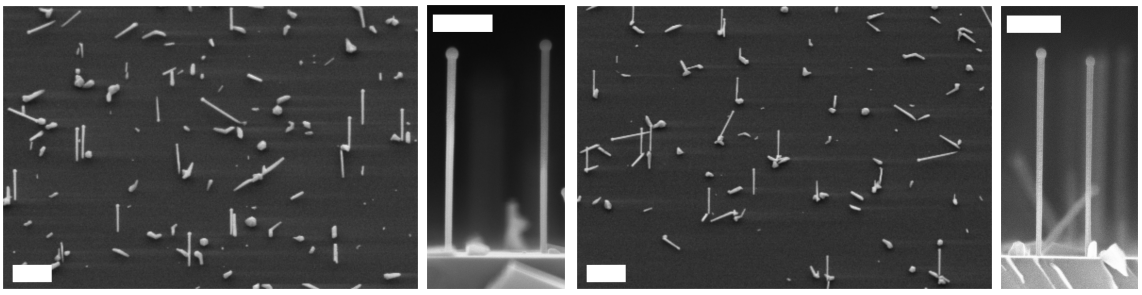

(a) 30° tilt view of sample D. (b) Side view of sample D. (c) 30° tilt view of sample E. (d) Side view of sample E.

Figure 5.8.: Representative SEM images of samples D and E. The nanowires are negatively tapered with a pronounced droplet at the apex. The 30° tilt view images of the nanowire ensembles show the low number density. The scale bars equal 1 µm in figure (a) and (c), and 500 nm in figure (b) and (d).

Results and discussion

The collected datasets are processed according to the description in the previous chapters. We start the discussion with sample D. The structure factor calibrated RHEED intensity evolution of the phase-sensitive diffraction spots is depicted in figure 5.9(a). The intensities

Table 5.2.: Values of sample D and sample E obtained by post-growth SEM analysis and parameters used for the simulation model.

	sample D		sample E	
parameter	SEM	simulation	SEM	simulation
ρ_{NW} (μm^{-2})	0.1 ± 0.02	0.1	0.07 ± 0.03	0.04
r_0^{NW} (nm)	–	11	–	11
$r_{f,b}^{NW}$ (nm)	26 ± 2	26	23 ± 2	23
$r_{f,t}^{NW}$ (nm)	33 ± 2	35	30 ± 2	30
h_f^{NW} (nm)	1585 ± 80	1600	1815 ± 80	1800
ρ_{cry} (μm^{-2})	0.45 ± 0.13	0.2	1.4 ± 1.0	0.5
r_0^{cry} (nm)	–	16	–	16
r_f^{cry} (nm)	105 ± 65	135	140 ± 70	140
h_f^{cry} (nm)	95 ± 15	90	134 ± 30	135
t_f (min)	–	60	–	60

of all three phase-sensitive spots emerge simultaneously at $t = 0\,\text{min}$, the overall intensity, depicted in black, rises linearly until $t_{c1} \approx 23\,\text{min}$, during this time the intensity rate is proportional to $\upsilon^{lum} = \upsilon^{NW}$. The saturation of the overall signal is discernible at $t \approx 50\,\text{min}$, which, however, we are not interpreting as the constant ensemble-shadowing condition, as we will discuss later. At $t = 15\,\text{min}$, the Σ ZB signal changes its slope to a higher rate with a concomitant decrease in the WZ intensity rate, indicating a transition in the WZ - Σ ZB generation probability. Until $t = 10\,\text{min}$, the zinc blende signal is slightly more intense compared to the twinned zinc blende signal.

The time-resolved intensity evolution of the XRD experiment is shown in figure 5.9(b). The intensities are corrected for the contribution of crystallites. The non-linear increase of the overall intensity again gives evidence for parallel axial and radial nanowire growth. The WZ intensity develops nearly linearly over the whole growth time. Around $t \approx 10\,\text{min}$ the phase-sensitive zinc blende signals and the wurtzite signal intersect.

Following equation (4.5), the RHEED ensemble-shadowing reaches constant conditions at $t = 31\,\text{min}$, which is in agreement with the decrease in the WZ intensity occurring at this time. We attribute the further rise in the overall intensity after $t = 31\,\text{min}$ to the radial growth inside the comparably large illumination height of $\overline{\lambda}_{crit} \approx 850\,\text{nm}$. The diameter at the lower border of the illuminated height does not reach the self-shadowing condition yet, which is finally fulfilled around $t = 50\,\text{min}$. This leads to a proceeding rise of the intensities although the ensemble-shadowing is already constant.

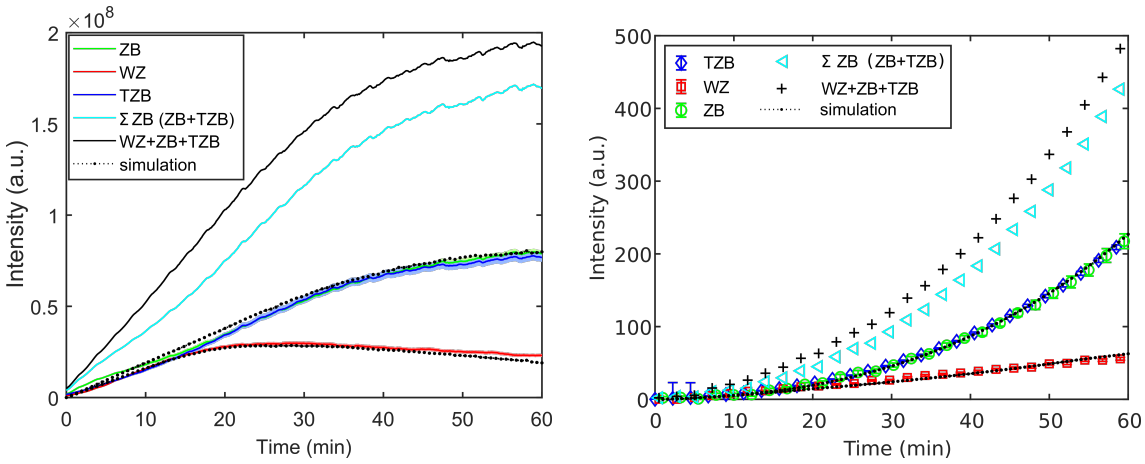

(a) Time-resolved RHEED intensity evolution.

(b) Time-resolved XRD intensity evolution.

Figure 5.9.: Experimental integrated intensity evolutions of the GaAs phase-sensitive ZB(311), WZ(10.3) and TZB(220) reflections plotted with the best fitting result of the simulation model of sample D. The simulation parameters are identical for both diffraction methods and are listed in table 5.2.

The experimental results of the second sample, sample E, are shown in figure 5.10. The overall RHEED intensity shows a comparable shape and develops nearly linearly until $t \approx 40\,\text{min}$. From the onset of growth till $t \approx 20\,\text{min}$, the intensity rate deviates from ideal linear behaviour. This observation, however, we attribute to the impact of magnetic fields in the experimental station of the synchrotron beamline resulting in oscillations of the individual signals. A clear change of the overall intensity rate is observable after $t \approx 40\,\text{min}$, where the signal starts to saturate. Sample E show a much weaker WZ signal over the whole growth run compared to sample D, it is dominated by Σ ZB signal. We interpret the splitting of both ZB related signals until $t \approx 30\,\text{min}$ to the additional contribution of the crystallites, which get shadowed during the subsequent growth time. The mean illumination height $\overline{\lambda}_{crit}$ is approximately 1270 nm as determined by equation (4.5). The missing saturation of the signals is explained by remaining radial growth as discussed for sample D.

The overall intensity evolution of the XRD experiment of sample E shows comparable features as observed at sample D. Similar, we conclude on axial and radial growth contributions at the nanowire ensemble. As observed in the RHEED experiment, the WZ intensity is less, as shown figure 5.10(b).

The GaAs Bragg peaks in the post-growth RSMs of both samples, depicted in figure 5.11, do not exhibit any intensity streaks along Q_y. The low nanowire number density has the effect that the size oscillations of the nanowire ensemble are too weak and cannot be evaluated for these samples. The radial growth nevertheless can be determined by carefully evaluating the non-linear evolution of the overall XRD intensity, which enables us to set

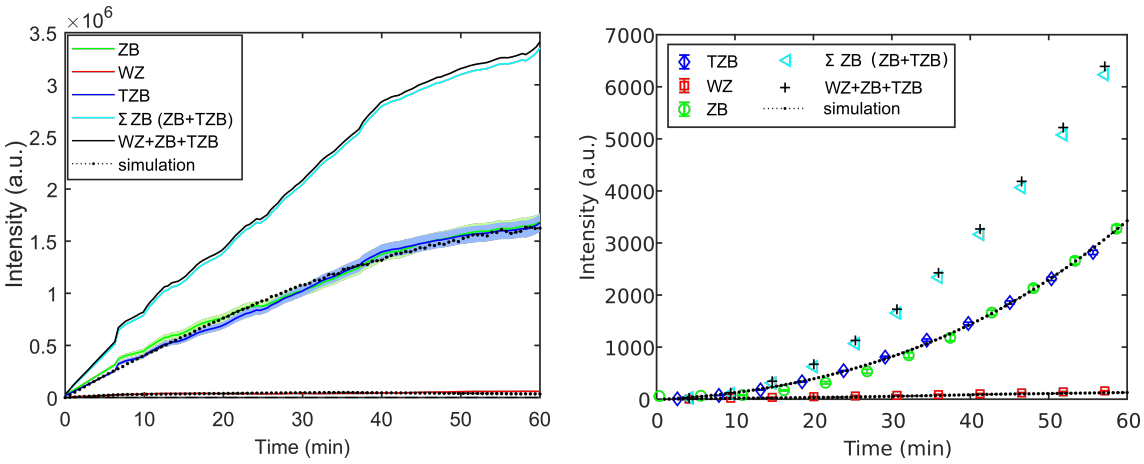

(a) Time-resolved RHEED intensity evolution.

(b) Time-resolved XRD intensity evolution.

Figure 5.10.: Experimental integrated intensity evolutions of the GaAs phase-sensitive ZB(311), WZ(10.3) and TZB(220) reflections plotted with the best fitting result of the simulation model of sample E. The simulation parameters are identical for both diffraction methods and are listed in table 5.2.

appropriate starting parameters for the simulations.

By describing the experimental studies with the simulation model, we can determine the generation rate of the different polytypes $f_p(h^{NW}(t),t)$ with high temporal and height resolution and therefore we are able to conclude on the effect of the different growth schemes on the polytypism. The best fitting simulated intensity evolution is plotted as black dotted lines in figures 5.9 and 5.10, where for clarity, we omit the crystallite contributions and plot only the simulated signals of the nanowires. The temporal resolution of the simulations are t_i, with $i \in [1,100]$.

The agreement of experiment and simulation in case of sample D is remarkable. Sample E shows for the RHEED experiment a higher deviation between experiment and simulation. The overestimation of the simulated ZB curve between $t \approx 20\,\text{min}$ - $30\,\text{min}$ is explained by the uncertainty in the signal oscillations as a result of the magnet fields in the experimental station. The simulation parameters for both samples are summarized in table 5.2. The incidence angle of the electron beam is again $\alpha = 0.6°$ and the mean free path length $\Lambda = 12\,\text{nm}$.

To compare the samples, we plot the RHEED intensity fractions $J_{WZ}^{RHEED}(t)$ and $J_{ZB}^{RHEED}(t)$ and the XRD intensity fractions $J_{WZ}^{XRD}(t)$ and $J_{ZB}^{XRD}(t)$ in figure 5.12(a) for sample D and in figure 5.12(b) for sample E. However, the low nanowire number density changes the interpretation of RHEED: while in section 5.2.1 the RHEED was extremely sensitive to the nanowire tip region, now due to the low nanowire number density, the RHEED provides rather volume information, similar to XRD. Consequently, $J_{WZ}^{RHEED}(t)$ and $J_{WZ}^{XRD}(t)$, respectively $J_{ZB}^{RHEED}(t)$ and $J_{ZB}^{XRD}(t)$ nearly coincide over the whole growth time. The

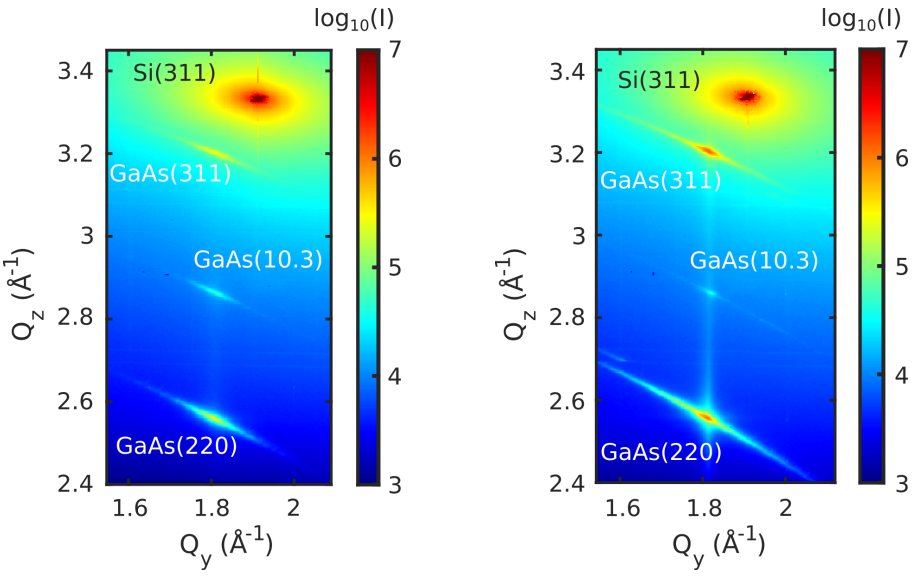

(a) Sample D. (b) Sample E.

Figure 5.11.: RSMs of the asymmetric truncation rod including the Si(311), GaAs(311), GaAs(10.3) and GaAs(220) Bragg reflections. The RSMs are measured after growth at room temperature. The Bragg peaks do not exhibit intensity streaks along Q_y due to the low nanowire number density.

disagreement from the onset of growth is related to the contribution of the crystallites in the RHEED intensities, which reduces $J_{WZ}^{RHEED}(t)$ and increases $J_{ZB}^{RHEED}(t)$. We recall that J^{XRD} is defined as the intensity fraction of the structure factor and crystallite-corrected intensities. At the growth time, when $\overline{\lambda(t)}$ becomes constant and the crystallite

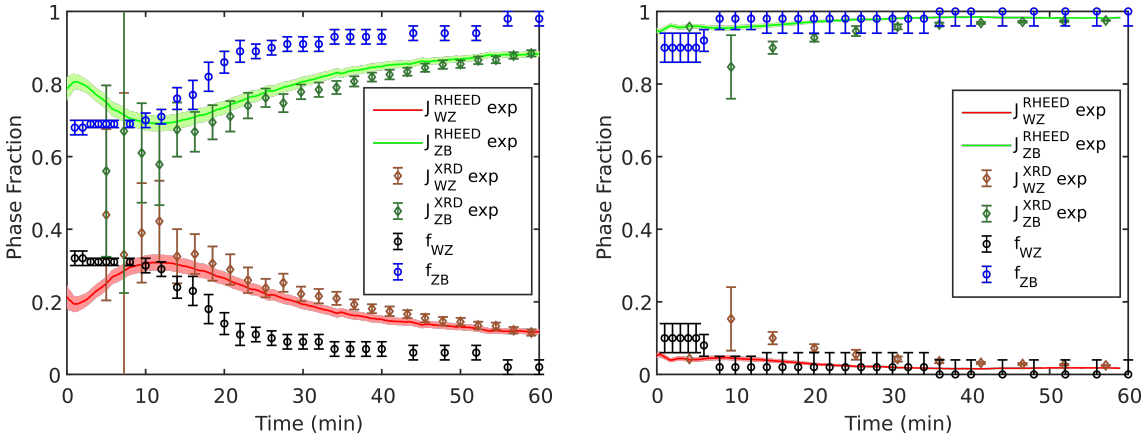

(a) Sample D. (b) Sample E.

Figure 5.12.: RHEED and XRD intensity phase fractions $J_p^{RHEED}(t)$ and $J_p^{XRD}(t)$ and phase fraction at the axial growth front $f_p(h^{NW}(t),t)$ as a function of growth time. Due to the large illumination height $f_p(h^{NW}(t),t)$ is different to $J_p^{RHEED}(t)$.

contribution diminishes, $J^{RHEED}(t)$ and $J^{XRD}(t)$ should coincide. However, we see that $J_{WZ}^{RHEED}(t)$ shows still a lower value compared to $J_{WZ}^{XRD}(t)$, this is again related to the ensemble-shadowing effect. For the current samples the illumination height is quite large, nevertheless it is smaller than the final nanowire height h_f^{NW}, meaning that after t_{c2}, when $\overline{\lambda}_{crit}$ is reached, the contribution of the nanowire base, where in the current samples WZ is located becomes less and thus $J_{WZ}^{RHEED}(t)$ is smaller compared to $J_{WZ}^{XRD}(t)$.
The low SNR of XRD during the nucleation of nanowires makes reliable characterization of the polytypism difficult, which is demonstrated by the high uncertainty indicated by the large error bars of $J_p^{XRD}(t)$. The subsequent improvement of the SNR quickly reduces the uncertainty of $J^{XRD}(t)$ making it even better than that of $J^{RHEED}(t)$. The complementary of the simultaneous *in situ* RHEED and *in situ* XRD experiments during nanowire growth therefore ensures a higher accuracy for the determination of the polytype fraction in the nanowire ensembles over the whole nanowire height.
We also see that the evolution of $J_p^{RHEED}(t)$ is not essentially identical to the evolution of $f_p(h^{NW}(t),t)$ and thus cannot be interpreted as this in all experiments. However, by carefully considering self-shadowing and ensemble-shadowing in RHEED, we are able to determine the generation probability $f_p(h^{NW}(t),t)$ even for low ensemble-shadowing conditions, where it deviates from $J_p^{RHEED}(t)$ as shown in the current cases. The resulting parameter $f_p(h^{NW}(t),t)$, which is optimised in the simulations, allows us to compare the different growth schemes directly in terms of the polytypism during the nucleation phase. In figure 5.13 we transform the time-resolved generation probability $f_p(h^{NW}(t),t)$ according to equation (5.13) to a height-resolved representation $f_p(h,t_f)$.

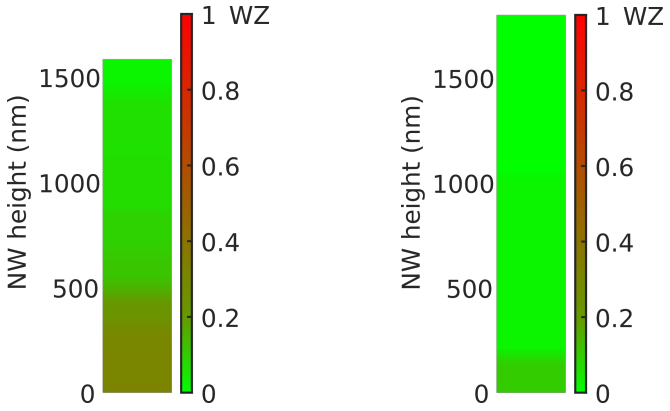

(a) Sample D. (b) Sample E.

Figure 5.13.: Final height profiles of the polytypism translated from $f_p(h^{NW}(t),t)$ into $f_p(h,t_f)$ assuming linear axial growth. High WZ content is illustrated in red shifting towards green for high ZB/TZB content.

Concluding from figure 5.13, sample D, which was grown with a PD step, exhibits a higher WZ fraction at the nanowire base compared to sample E. Moreover, the transition to

mainly Σ ZB nucleation sets in at larger $h^{NW}(t)$, and the transition duration is longer. Afterwards, the growth at constant conditions is dominated by the Σ ZB crystal structure for both samples.
This observation agrees with the negatively tapered appearance measured by SEM, which also indicates an unbalanced Ga flux, meaning that the incoming Ga flux is higher than the incorporation of Ga adatoms into the solid. The zinc blende nucleation and negative tapering is governed by wetting angles larger than 127°, as we introduced in section 2.2. The WZ segments at the nanowire base however, require according to Dubrovskii *et al.*[105,106] wetting angles from 100° - 125°.
Differences in the extent of the polytypism in the different growth schemes, consequently, must be a result of the characteristics of the Ga droplets at the beginning of growth. By omitting the PD step in sample E, the Ga droplets form directly in an As atmosphere. We speculate that during their formation and growth, the nanowires already nucleate at the solid-liquid interface due to the dissolved As in the droplets. The inverse tapering is evidence for an excessive relative Ga supply, and consequently the forming Ga droplets tend to increase continuously in size, resulting in large wetting angles and mainly ZB nucleation. During the PD step in sample D, the droplets form in vacuum with absence of As and their size is determined by the deposition conditions. During the initiation of growth, when both materials are supplied, the wetting angles are most likely in the region which favours WZ nucleation. However, due to the excessive relative Ga supply, the Ga droplets can inflate and depending on the axial growth rate, WZ layers nucleate until the droplets reach the transition angle of $\beta \approx 125°$. During further growth time, the nanowires grow in mainly ZB or TZB crystal structure.

Summary

We studied by means of the simultaneous *in situ* RHEED and *in situ* XRD experiments during nanowire growth the evolution of polytypism during the fabrication of self-catalysed GaAs nanowires. The focus was on the nucleation phase of the nanowire ensemble, where two different scenarios of initiating the growth were compared. We showed the importance of the PD in terms of polytypism during the early growth. The nanowires grown without the PD step exhibit only limited polytypism, with a final fraction of 2 % ± 0.5 % of WZ in the nanowire ensemble, compared to the nanowires grown with PD step with a final WZ fraction in the nanowire ensemble of 11 % ± 1 %. Moreover, the height-resolved profiles of the polytypism in the nanowire ensemble, pinpoint the defective region to the interface with the substrate, meaning that the PD step directly increase the polytypism there.

Our study underlines the importance of carefully tuning the PD conditions to obtain droplets close to the optimal wetting conditions for the subsequent nanowire growth. In the literature, the PD step has significance for increasing the vertical yield for growth on patterned [141–144] and unpatterned [76,145] substrates. For nanowire fabrication on unpatterned substrates however, high vertical yield was also achieved by omitting the PD step, using different growth processing schemes as demonstrated by Tauchnitz *et al.* [77,79] and Balaghi *et al.* [63] On the contrary, these growth schemes are not applicable to growth on patterned substrates, where the PD remains an important parameter to control the vertical yield. Here, the optimization of the PD by tuning the droplet shapes is essential to achieve both high vertical yield with low defect densities.

5.3. Summary

In summary, we applied for the first time the RHEED simulation model to real experiments. During simultaneous *in situ* RHEED and *in situ* XRD growth experiment, we exploit the complementarity of both diffraction techniques to obtain comprehensive information on the evolution of the mean shape and mean crystal structure of the nanowire ensemble.
We briefly discuss the main differences of the information contained in the integrated diffraction peak intensities of RHEED and XRD and make conclusions on the characteristic appearance of the intensity as a function of growth time.
Time-resolved *in situ* XRD in asymmetric geometry always probes the full nanowire volume, giving direct access to the phase-sensitive diffraction spots containing information on the axial and radial growth parameters and the volume fractions of the polytypism in the nanowires, whereas time-resolved *in situ* RHEED can be increasingly sensitive to the polytypism at the axial growth front and thus provide height-dependent information, depending on the nanowire number density.
Their combination allows us to obtain a comprehensive quantitative picture of the evolution of growth rates and polytypism averaged over a large nanowire ensemble.
We verified our simulation model by the measurement of a nanowire ensemble with high number density, demonstrating the complementarity of RHEED and XRD under effective ensemble-shadowing conditions. The high Q-resolution of XRD enabled us to conclude on the radial growth rate, which is in most cases inaccessible by the RHEED experiment. The remarkable agreement of RHEED and XRD simulations with the experiments for an identical parameter set additionally permits us to explain other features in the experimental data, such as the contribution of the crystallite ensemble in the experimental RHEED curves. The final result of the simulation model is the crystal phase generation probability at the axial growth front $f_p(h^{NW}(t),t)$ with high temporal resolution, enabled by RHEED. Using the comprehensive results of the simultaneous experiments we were able to translate

the time-resolved phase fraction $f_p(h^{NW}(t),t)$ into a height-resolved profile of the mean polytypism in the nanowire ensemble $f_p(h^{NW},t_f)$.

Finally, we applied the simultaneous *in situ* RHEED and *in situ* XRD experiments to a study investigating the polytypism at the early growth phase. We compared the effect of the PD step before the actual nanowire growth on the polytypism and conclude that the PD could increase the polytypic segments at the nanowire base. We attributed this observation to changing wetting conditions of the liquid Ga droplets during the early stage. For practical use, our results emphasize that optimization of the PD step during nanowire growth is essential to reduce these polytypic segments at the nanowire base to grow defect free nanowires.

By comparing the samples with high and low nanowire number density, we deduce that for correct interpretation of RHEED patterns careful considerations of the properties of the nanowire ensemble are inevitable to obtain correct information on the polytypism height profiles, since the phase fraction at the axial growth front is not necessarily identical to the RHEED intensity fraction.

6. *In situ* RHEED during nanowire nucleation: Correlation between polytypism and catalyst shape

In this chapter, we apply the developed simulation model again to the growth of self-catalysed GaAs nanowires and demonstrate the laboratory-based possibilities by exploiting the height-sensitivity of *in situ* RHEED to identify specific changes in the nucleation probabilities during growth.

In section 5.2.2 of the previous chapter, we speculated that the higher WZ fraction at the nanowire stem during the growth containing a PD step, results from the changing shape of the liquid Ga droplet at the nanowire apex acting as catalyst for the VLS growth. In the following experiments, we are now investigating this early growth stage more carefully to correlate the nucleation probability of the polytypes with the actual droplet shape measured by post-growth SEM. The results obtained confirm a previous published theoretical model describing the nanowire VLS growth mechanism, by combining polytype nucleation probabilities caused by the wetting conditions of the catalyst droplets, with the self-stabilization process of the nanowire diameters.[106] The theoretical model was already applied to describe *in situ* nanowire growth experiments in an environmental TEM,[105] however our results underline the application of the theoretical model to standard growth conditions in common MBE reactors.

The simultaneous *in situ* RHEED and *in situ* XRD experiments enable the characterization of the whole nanowire growth including shape and crystals structure by their complementarity. However, *in situ* XRD is not broadly available and is restricted to dedicated instruments. Here, we use *in situ* RHEED during nanowire growth as laboratory-based instrument, thus this routine is available at all MBE growth chambers equipped with a common RHEED setup.

The major limitation of RHEED is the insensitivity towards axial and radial growth which could lead to ambiguities in the results. In the previous chapter, these large uncertainties in the required parameter space needed to simulate and evaluate the RHEED intensity evolution, were determined by the complementary *in situ* XRD experiment. Nevertheless, by a careful post-growth SEM analysis and suitable reference samples, the parameters describing the objects' shape can be reduced or even determined. Consequently, with proper

a priori knowledge *in situ* RHEED can also be applied for the quantitative determination of the crystal structure as sole technique.
In section 6.1, the samples for the current nanowire growth experiments will be introduced. In section 6.2 the results of the post-growth SEM analysis will be discussed, followed by the evaluation of the polytypism by *in situ* RHEED. The obtained phase fraction of *in situ* RHEED will be compared with results obtained by *ex situ* XRD experiments in symmetric diffraction geometry to validate the results and demonstrate the significance of RHEED as a laboratory-based characterization technique. Finally in this section, we will set our results in the context of the theoretical model which was published recently,[105,106] where we will compare the time-resolved phase fractions of *in situ* RHEED with the droplet shapes obtained by post-growth SEM. In section 6.3 we summarize our results. Parts of this chapter will be published in publication II.

6.1. Samples

In this study, we focus on the nucleation phase of self-catalysed GaAs nanowires grown with a Ga PD step. Therefore, the study consists in total of five samples, during each growth we perform *in situ* RHEED experiments. The samples were again grown according to our standard growth protocol presented in section 3.3 on n-type Si(111) substrates covered with native oxide. During the first Ga deposition step at $T_{sub} = 570\,°C$, which determines the nanowire number density, the amount of Ga deposited on the substrate equals 48 ML of planar GaAs growth. After the desorption of these deposited droplets at elevated temperature, T_{sub} was set again to 590 °C. At this growth temperature, first a Ga PD step was performed equivalent to 40 ML of planar GaAs growth, followed by the actual nanowire growth performed with a 2D-growth rate of planar GaAs of 0.1 ML/s at a nominal V/III - ratio of 2.1. The growth time t_f was different for each sample, and was determined from distinct characteristics of the intensity evolution of the wurtzite diffraction spot in the RHEED patterns. The characteristics for the sample F - J are: (1) the emergence of the wurtzite intensity I_{WZ}, (2) the maximum of I_{WZ}, (3) the onset of reduction of I_{WZ}, (4) the minimum of I_{WZ} and (5) staying at the minimum of I_{WZ} for some time. The final growth times t_f of the samples are summarized in table 6.1.

Table 6.1.: Final growth times and characteristics of the wurtzite intensity evolution for sample F - J.

sample name	characteristic of I_{WZ}	growth time t_f
Sample F	$I_{WZ} > 0$	1 min
Sample G	$I_{WZ} = \max$	5.7 min
Sample H	$I_{WZ} < \max$	11.2 min
Sample I	$I_{WZ} = \min$	20 min
Sample J	$I_{WZ} = \min$ and stable	30 min

6.2. Results and discussion

After each growth run the corresponding sample was analysed by SEM in order to get information on the final shape of the nanowires and crystallites as well as on the number density of the corresponding ensembles. Exemplary scanning electron micrographs of typical nanowires for the samples F - J are presented in figure 6.1. Besides the expected difference in the final nanowire height h_f^{NW}, we observe a remarkable change of the shape of the Ga droplet at the apex of the nanowires. For the first two samples (F and G) the droplets have a shallow appearance, meaning a low wetting angle β. At the later growth stages, the droplets are pronounced with comparable large wetting angles. Further, for sample I we can identify the occurrence of negative tapering. Additionally, we observe that the axial growth rate is lower for samples G and H resulting in slightly smaller h_f^{NW} than expected. We attribute this to the higher nanowire number densities which are present

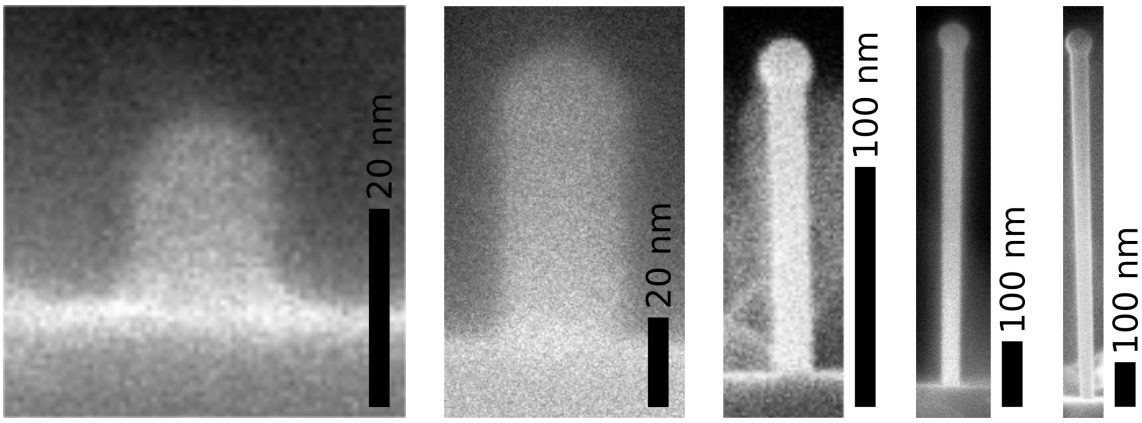

Figure 6.1.: Exemplary SEM images of the different growth stages: (a) sample F, (b) sample G, (c) sample H, (d) sample I, (e) sample J. The variation of the catalyst particle's shape during the growth is remarkable.

Table 6.2.: Mean shape and number density of nanowires and crystallites for samples F - J measured by SEM.

parameter	sample F	sample G	sample H	sample I	sample J
ρ_{NW} (μm^{-2})	0.7 ± 0.2	1.0 ± 0.3	1.1 ± 0.3	0.8 ± 0.3	0.8 ± 0.1
$r_{f,b}^{NW}$ (nm)	16 ± 4	15 ± 2	16 ± 3	21 ± 2	21 ± 3
$r_{f,t}^{NW}$ (nm)	19 ± 4	16 ± 2	16 ± 3	22 ± 1	24 ± 2
h_f^{NW} (nm)	18 ± 4	66 ± 15	139 ± 44	558 ± 123	829 ± 114
ρ_{cry} (μm^{-2})	- -	0.6 ± 0.2	0.9 ± 0.3	0.3 ± 0.1	0.3 ± 0.1
r_f^{cry} (nm)	- -	35 ± 14	53 ± 23	82 ± 41	95 ± 66
h_f^{cry} (nm)	- -	32 ± 9	38 ± 10	77 ± 30	95 ± 41
β (°)	98 ± 19	95 ± 13	121 ± 15	138 ± 3	140 ± 3

at these two samples. In total we measured by SEM more than 200 individual nanowires and crystallites, thus obtaining their mean shape. The number density was determined by evaluating different top view SEM images with a total area of more than 1000 μm^2 for each sample. The results of the SEM analysis are listed in table 6.2.

We exploit the occurring ensemble-shadowing during *in situ* RHEED and the resulting height-sensitivity towards transition of the polytypism, to identify directly any change in the crystal structure during growth. By following the intensity evolution of the unprocessed RHEED frames in real-time (figure 6.2(a)), we immediately stopped the growth at the desired feature in I_{WZ} and ramped down the MBE to maintain the droplet shape as best as possible. The electron beam energy is set again to 20 keV.

For the subsequent data analysis, we integrate every 7 s five frames, each with a exposure time of 140 ms, to achieve a better SNR. While the time-resolution could in principle be increased, we observe that these values are ideal for following the intensity evolution. Further processing of the raw data is performed according to section 4.4.2.

The resulting time-resolved RHEED intensities for the phase-sensitive diffraction spots are depicted in figure 6.3 for each grown sample. The overall intensity evolution of sample J, which is shown in figure 6.2(b), saturates around $t = 15$ min which suggests the steady state conditions of self- and ensemble-shadowing. The time-resolved intensities of the phase-sensitive diffraction spots show a similar shape for samples C and D, both grown with a PD step. At the beginning the signals are dominated by the WZ intensity, which rapidly increases until its maximum around $t = 9$ min. During further growth, the WZ intensity decreases until at around $t = 20$ min a constant level is reached. The ZB and TZB intensities rise moderately, whereas the ZB intensity show a relatively faster rate compared to the TZB signal, which we identify as the contribution of the crystallites, concluding

from the previous results. After the subsequent shadowing of the crystallites, both signals coincide again, which is completed at $t = 8\,\text{min}$. However, this is only observable for samples I and J, due to their longer growth time.

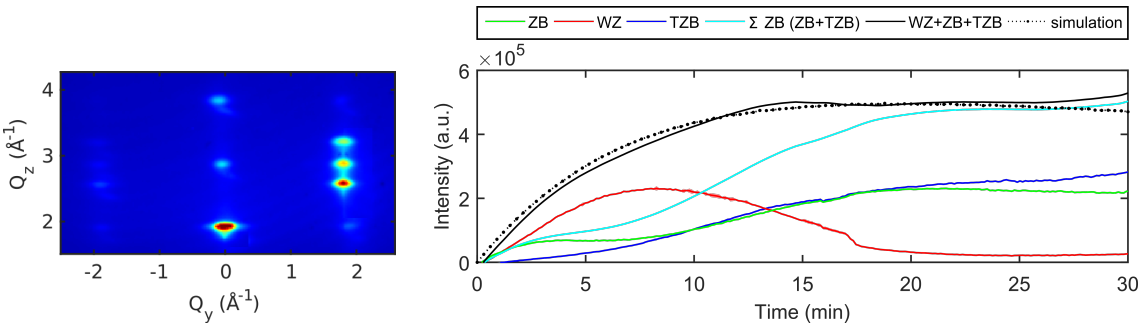

Figure 6.2.: Sample J: (a) RHEED pattern at $t = 13\,\text{min}$. (b) Intensity evolution of phase-sensitive diffraction spots, Σ ZB (ZB+TZB) and the overall intensity (WZ+ZB+TZB). The black dotted line is the result of the overall intensity simulation (omitting the polytypism) to determine the partially uncertain shape parameters.

We aim on the determination of the polytype generation probability at the axial growth front $f_p(h^{NW}(t),t)$ of each sample, especially at the respective end of growth at t_f to compare $f_p(h^{NW}(t_f),t_f)$ with the droplet shape. Therefore, we need to compare the RHEED experiments with simulated curves which will allow us to determined $f_p(h^{NW}(t),t)$.
Since in the current experiment we are using *in situ* RHEED as sole diffraction technique, we need to obtain the growth rates from somewhere else. The results obtained by SEM give a first indication for the growth rates, however these must be refined and so we simulate the evolution of the overall RHEED intensity (ZB+TZB+WZ) by omitting the polytypism. For this first simulation iteration, we choose a parameter space which is orientated on the SEM results but with enough margin to lower and higher values. By comparing the overall RHEED intensity (ZB+TZB+WZ) with the resulting simulated curves, we find a set of parameters describing the overall intensity with good agreement. From this simulated curve, we conclude on the unknown growth rates of the ensembles. The results of chapter 5 justify the assumptions of linear axial and radial growth rates, consequently the unknown parameters, like e.g. r_0^{NW} and r_0^{cry} which cannot be accessed by SEM, are determined by the simulation itself. Besides that, the sample series, which is grown under identical growth conditions, facilitates defining the radial growth rates, since each sample acts as a reference for the others. Namely, we can use the shape of sample F as a reference value for the initial nanowire radius r_0^{NW}.
The simulated intervals containing the safety margins and the parameters of the best description of the experimental data are summarized in table 6.3. In figure 6.2(b), we additionally plot the simulated curve of the best parameter set given in table 6.3. The

setup parameters used for the simulation are again $\Lambda = 12\,\text{nm}$ and $\alpha = 0.6°$. The mean illumination height is $\overline{\lambda}_{crit} \approx 125\,\text{nm}$ according to equation (4.5).

Table 6.3.: Simulated parameter interval and values resulting in the best description of the experiments for samples F - J.

sample		ρ_{NW} (μm^{-2})	r_0^{NW} (nm)	$r_{f,b}^{NW}$ (nm)	$r_{f,t}^{NW}$ (nm)	h_f^{NW} (nm)
F	interval	0.5 - 0.9	12 - 20	12 - 20	12 - 20	10 - 50
	best result	0.7	16	16	16	20
G	interval	0.5 - 0.9	12 - 17	13 - 17	13 - 17	50 - 70
	best result	0.9	14	16	16	65
H	interval	0.5 - 0.9	12 - 20	12 - 20	12 - 20	100 - 180
	best result	0.9	14	16	16	120
I	interval	0.6 - 1.0	12 - 20	17 - 25	18 - 26	450 - 650
	best result	0.6	14	21	26	550
J	interval	0.5 - 0.9	10 - 20	16 - 24	19 - 27	700 -950
	best result	0.7	14	20	23	800

sample		ρ_{cry} (μm^{-2})	r_0^{cry} (nm)	r_f^{cry} (nm)	h_f^{cry} (nm)	# t_i
F	interval	0.4 - 0.9	12 - 20	12 - 20	10 - 50	4
	best result	0.9	16	20	20	4
G	interval	0.3 - 2.2	12 - 20	25 - 45	25 - 45	25
	best result	0.8	14	35	30	25
H	interval	0.01 - 1.5	12 - 20	30 - 65	25 - 55	40
	best result	1.0	14	40	55	40
I	interval	0.1 - 0.5	12 - 20	70 - 95	60 - 95	100
	best result	0.2	14	80	90	100
J	interval	0.1 - 0.5	10 - 16	85 - 110	80 - 110	100
	best result	0.2	10	85	95	100

After the successful determination of the structure parameters of each sample, we now focus on the polytypism. As a free parameter, after fixing the growth rates, we are now varying $f_p(h^{NW}(t),t)$ in the simulations in order to describe the experimental intensity evolutions of the phase-sensitive diffraction spots.

The results of the simulations are indicated in figures 6.3(a) - 6.3(e) as dotted lines. In black the simulated intensities of the nanowire ensemble are depicted, consisting of ZB/TZB and WZ intensities. For the three samples F - H, the experimental ZB signal shows a higher intensity compared to the TZB signal. As previously described, we attribute this difference to the contribution of the crystallites, this assumption being justified by the simulations.

For the first three samples, we additionally plot as grey dotted lines the sum of the ZB signals originating from the nanowires and the crystallites. Interpreting the TZB signal originating only from the nanowire ensemble, shown by the black dotted line, and the ZB signal composed by the additional diffraction contribution of the crystallite ensemble, shown by the grey dotted line, there is remarkable agreement between experiment and simulation.

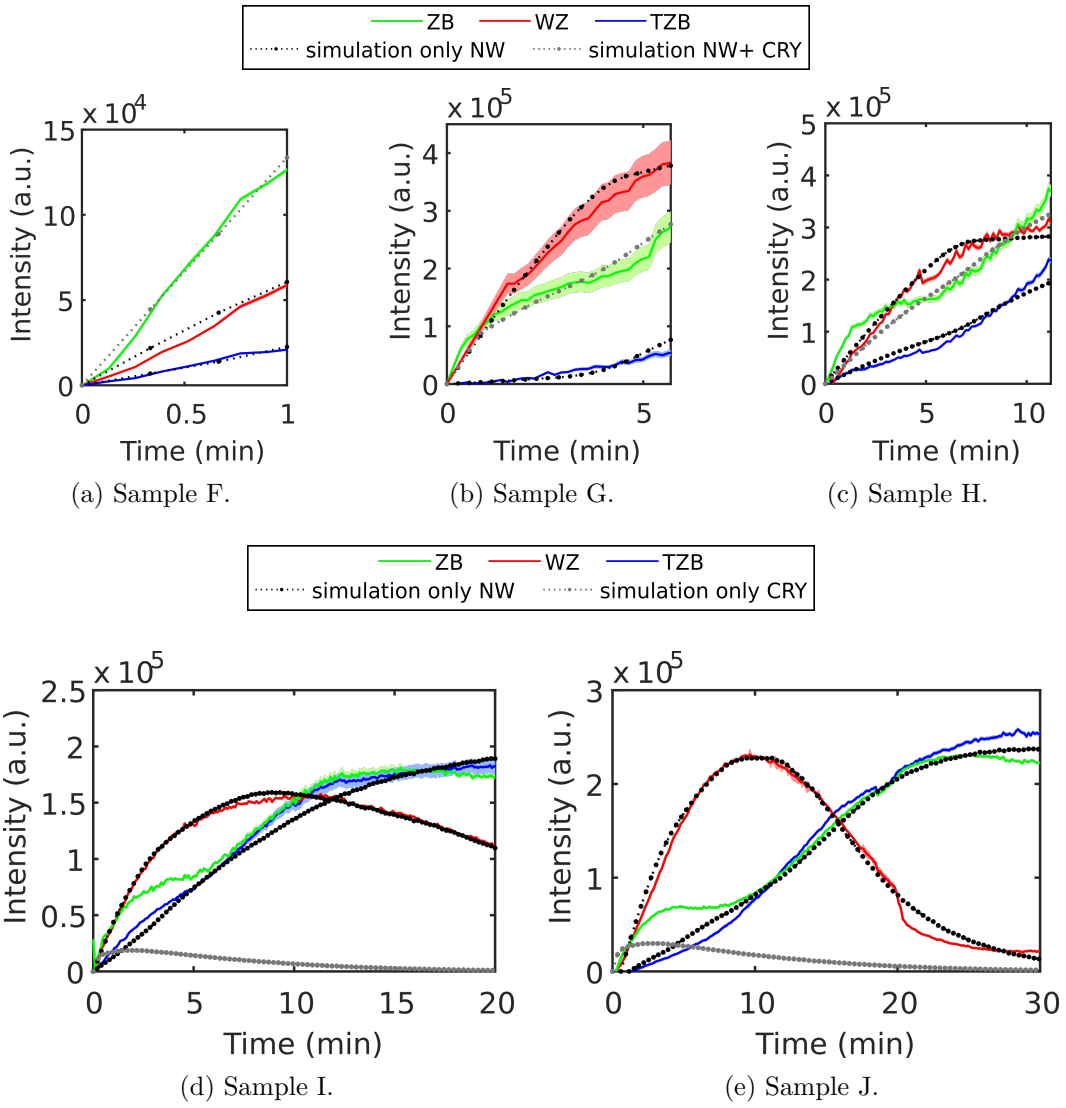

(a) Sample F. (b) Sample G. (c) Sample H.

(d) Sample I. (e) Sample J.

Figure 6.3.: Experimental and simulated temporal evolution of the phase-sensitive RHEED spots of samples F - J. The simulated intensity evolution of the nanowire ensemble is depicted in black. For samples F - H, we depicted the sum of the nanowire and crystallite ZB intensities in grey, they fit well to the experimental ZB intensities. For samples I - J, only the crystallite intensity evolution is depicted in grey for better illustration.

For better illustration of the results of samples I and J, which were grown for a longer time, we illustrate the signals of the crystallite ensemble differently. In the figures 6.3(d) and 6.3(e), in grey only the crystallite ensemble contribution to the signal is shown, emphasizing the gradual shadowing during growth. The ensemble-shadowing leads to a contribution to the signal only during the first few minutes of growth. In black, we plot again the simulated intensity evolution of the nanowire ensemble.
The resulting polytype fractions $f_p(h^{NW}(t),t)$ used to simulate the RHEED intensity evolution in samples F - J in figure 6.3 are summarized and plotted in figure 6.4. The time-resolved wurtzite fractions in the nanowire ensemble $f_{WZ}(h^{NW}(t),t)$ are shown in figure 6.4(a). However, due to the differences in the axial growth rates of the samples G and H, resulting in different ensemble-shadowing conditions, we additionally plot the wurtzite fraction in the nanowire ensemble as a function of the nanowire height $f_{WZ}(h^{NW},t_f)$ in figure 6.4(b). The WZ generation rate dominates during nanowire nucleation and decreases with progressing growth time for all samples. All functions cross the 0.5 level between $t = 3\,\text{min}$ - $7\,\text{min}$ or $h^{NW} = 50\,\text{nm}$ - $170\,\text{nm}$, leading to mainly nucleation of Σ ZB. Samples G and H start at higher WZ nucleation probabilities, which we explain by the higher nanowire number density, as measured by SEM. At higher nanowire number densities, the competition between the nanowires for the incoming Ga flux increases, leading to local higher V/III - ratios, which again promotes smaller wetting angles of the Ga droplets and thus WZ nucleation. This explains as well the opposite trend in sample I.

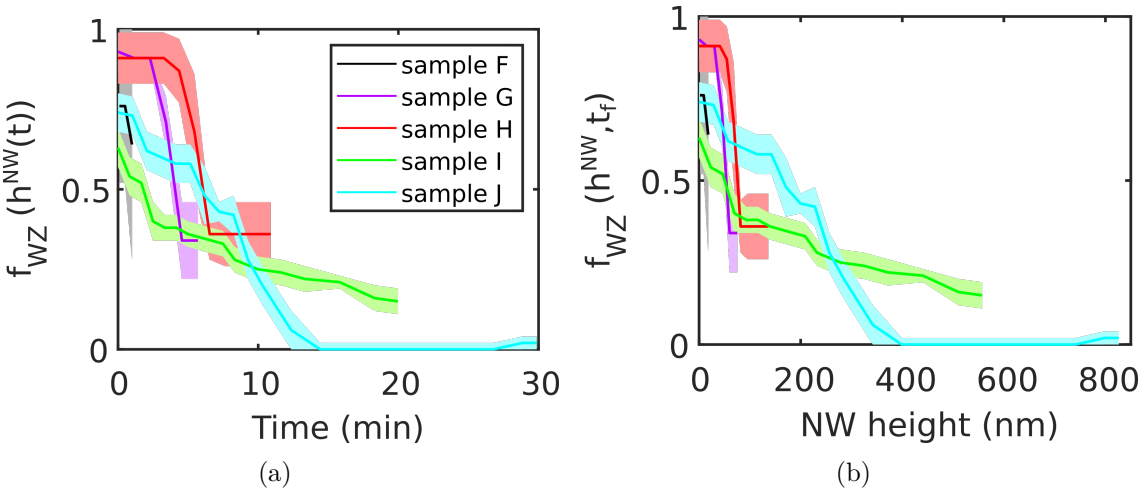

Figure 6.4.: Wurtzite phase generation probabilities at the axial growth front for the samples F - J: (a) $f_p(h^{NW}(t),t)$ as a function of time, and (b) $f_p(h^{NW},t_f)$ as a function of nanowire height.

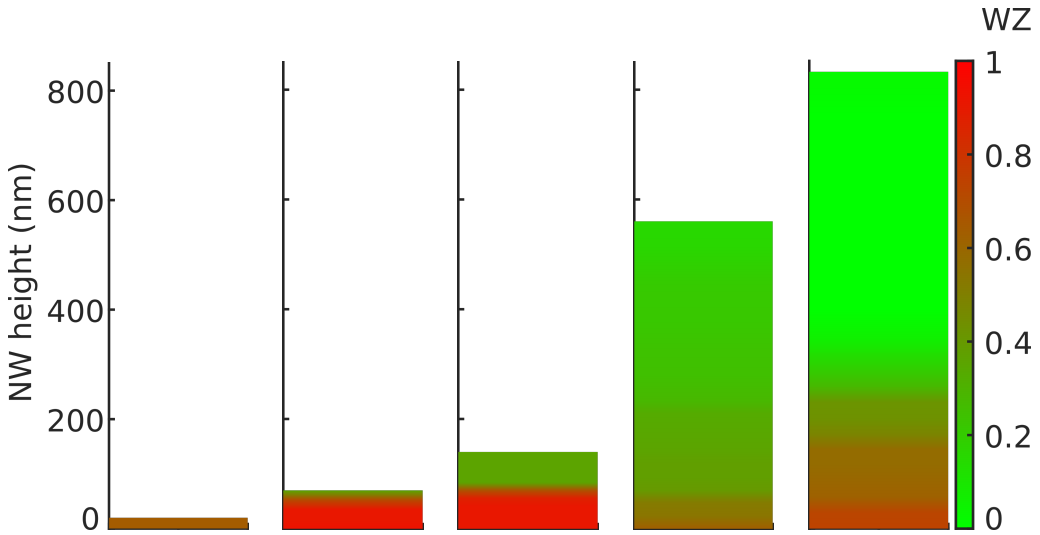

(a) Sample F. (b) Sample G. (c) Sample H. (d) Sample I. (e) Sample J.

Figure 6.5.: Final mean height profiles of the polytypism in the nanowire ensemble translated from $f_p(h^{NW}(t),t)$ to $f_p(h^{NW},t_f)$ assuming linear axial growth for samples F - J. High WZ content is illustrated in red shifting towards green for high ZB/TZB content.

The phase fractions at a certain nanowire height $h^{NW}(t)$ are determined by the polytype generation probability $f_p(h^{NW}(t),t)$. By assuming that the polytype distribution at a certain height h^{NW} is stable during further growth, we can translate the time-resolved generation probability $f_p(h^{NW}(t),t)$ into a height-resolved profile of the mean polytype fraction in the nanowire ensemble $f_p(h^{NW},t_f)$ using m^{NW}_{axial}, according to (5.13). In figures 6.5(a) - 6.5(e) the final height profiles of the mean polytype fraction in the nanowire ensembles of the samples F - J are plotted.

In addition to the *in situ* RHEED analysis during growth, all samples were subsequently characterized by *ex situ* XRD. The characterization after growth allows us to compare the final state of the nanowire ensembles polytype fractions with the results determined by *in situ* RHEED. The XRD experiments were performed at the Resonant Scattering and Diffraction Beamline P09[116] at the synchrotron facility PETRA III at DESY in Hamburg. The X-ray beam with an energy of 15 keV was focused to a beam size of 16 µm (v) x 70 µm (h), which allowed us to investigated several thousands of nanowires at the same time to obtain the mean properties of the nanowire ensembles. The reciprocal space was measured in the vicinity of the GaAs(111) Bragg reflection at the Bragg angle of $\theta^{GaAs}_{B,(111)} = 7.27°$ and for reference in the vicinity of the Si(111) Bragg reflection of the substrate at $\theta^{Si}_{B,(111)} = 7.57°$. The diffraction signal was detected by a PILATUS 300K detector with a pixel size of 172 µm which was placed in a distance of 102.5 cm from the sample. The recorded 3-dimensional intensity distribution is transformed into reciprocal space and by integrating the 3D volume along the Q_y - direction, one obtains a RSM of

the Q_x - Q_z - plane. The RSM of samples F - J are depicted in figures 6.6(a) - 6.6(e). In the RSM of sample F (figure 6.6(a)), we cannot observe any signal in the region between $Q_z = 1.9\,\text{Å}^{-1}$ and $1.95\,\text{Å}^{-1}$. At this early stage of growth, the amount of GaAs on the substrate is below the detection limit of the XRD experiment and thus no signal is visible. In figure 6.6(b) (sample G) a broad reflection around $1.91\,\text{Å}^{-1}$ arises, which is located at the expected position of WZ. For the subsequent samples a second intensity contribution arises at slightly higher Q_z values, which we assign to the ZB structures. The relative contribution from WZ and ZB changes with increasing growth times in favour of ZB. In order to verify this, we integrate the intensity distribution of the RSMs along Q_x and correct for the crystallites (as demonstrated in Ref.[68]). The resulting Q_z - profiles of each sample are shown in figures 6.6(f) - 6.6(i). The normalized Q_z - profiles support the finding that over the growth time the relative intensity distribution changes in favour of the ZB peak, and this now allows a subsequent analysis procedure to determine the mean polytype fraction in the nanowire ensemble of each sample, representing different growth times.
The determination of the mean polytype fraction from symmetric XRD data is not as easy as it is for asymmetric XRD data, where the phase-sensitive Bragg peaks are well separated in reciprocal space, as shown e.g. in figure 5.3(a). Nevertheless, it is possible to distinguish the cubic and hexagonal polytypes by exploiting the small difference in the lattice parameters of ZB and WZ along the [111] - direction of the nanowires, equal to the Q_z - direction in reciprocal space, as introduced in section 2.2. This small difference results in different positions for the respective reflections in reciprocal space, however, the relative intensity contributions of both characteristic peaks do not necessarily reflect the real phase fraction in the nanowires. The occurrence of both crystal phases in the nanowire ensemble result in characteristic shapes of the Q_z - profiles and allow us to derive on the mean polytype fraction in the nanowire ensemble.[68,83,86,110]
We now interpret the Q_z - profiles in the framework of a statistical simulation model based on a Markov chain, developed by Martin Köhl and Philipp Schroth. Details of the model can be found in the Ref.[68,83,86] The model generates a statistical ensemble of nanowires, each nanowire consisting of stacking sequences of ZB and WZ segments. The stacking sequences are created by a given static transition probability p, which determines if the crystal structure changes after each new monolayer, where $p_{ZB\rightarrow WZ}$ gives the probability for changing the stacking from ZB to WZ and $p_{WZ\rightarrow ZB}$ from WZ to ZB. The resulting nanowire ensemble has identical transition probabilities, however each individual nanowire inside the ensemble has a different stacking sequence. The diffraction signals of all individual simulated nanowires are incoherently summed up, resulting in the characteristic Q_z - profiles in the vicinity of the GaAs(111) Bragg reflection.[146]

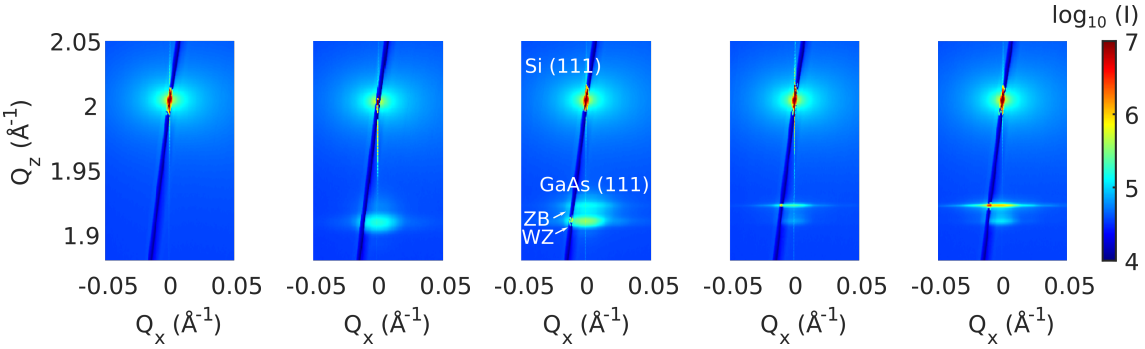

(a) Sample F. (b) Sample G. (c) Sample H. (d) Sample I. (e) Sample J.

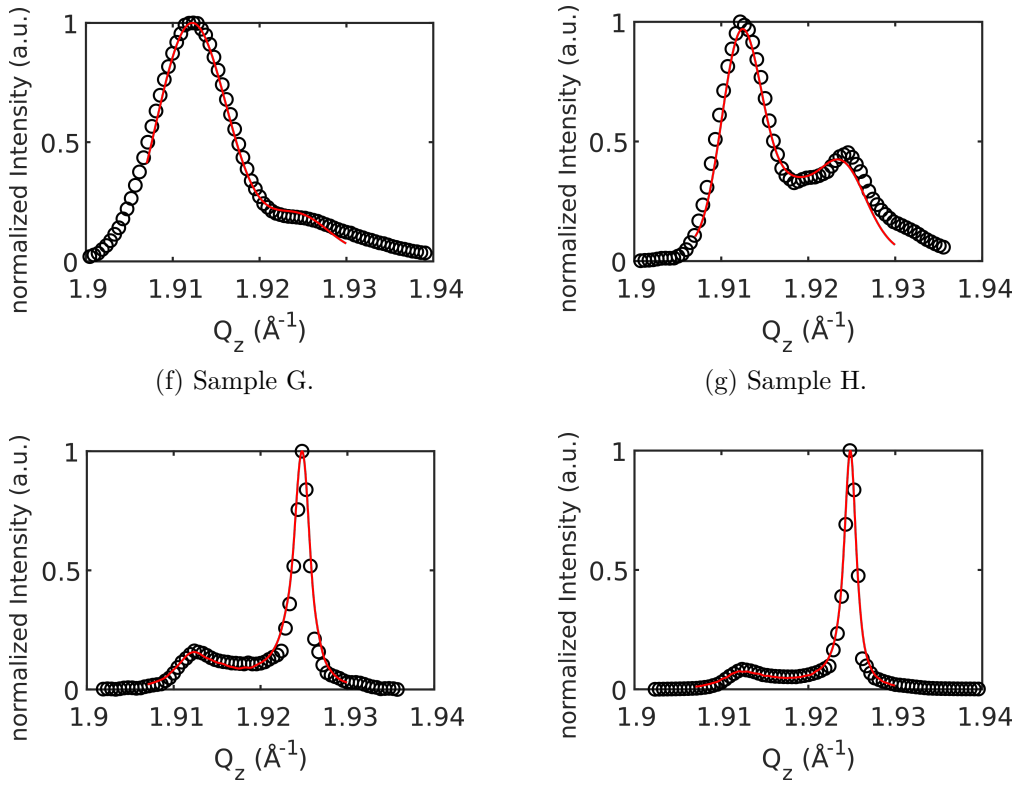

(f) Sample G. (g) Sample H.

(h) Sample I. (i) Sample J.

Figure 6.6.: Experimental results of the *ex situ* XRD experiment: (a) - (e): reciprocal space maps of the Si(111) and GaAs(111) Bragg reflections. (f) - (i): normalized integrated Q_z intensity profiles around the GaAs(111) Bragg reflection. The red line is the simulation of the X-ray profile using the Markov approach.

The Q_z - profiles of the Markov approach, which fit best to the experiments are plotted as red lines in figures 6.6(f) - 6.6(i). The small deviation of simulation and experiment for Q_z values larger than $1.93\,\text{Å}^{-1}$, can be explained by the remaining signal of the Si(111) Bragg reflection after the corresponding background correction due to the low diffraction intensities of the nanowires. By comparing the simulated profiles with the experimental curves, we can conclude on the crystal phase fraction directly from the transition probabilities of the respective simulated curves with the following relation:

$$\tilde{p}_{WZ} = \frac{1}{1 + \frac{p_{WZ \to ZB}}{p_{ZB \to WZ}}} \tag{6.1}$$

or

$$\tilde{p}_{ZB} = \frac{1}{1 + \frac{p_{ZB \to WZ}}{p_{WZ \to ZB}}}. \tag{6.2}$$

In table 6.4 the static transition probabilities and the final phase fractions $\tilde{p}_{WZ}$ and $\tilde{p}_{ZB}$ determined by the Markov model are summarized for each sample. The polytype fraction determined by the Markov approach reflects the situation at the end of growth. Thus, we need to integrate, respectively, the time-resolved and height-resolved polytype fractions of *in situ* RHEED to compare the final state of both diffraction methods.

Table 6.4.: Transition probabilities of Markov chain simulation resulting in Q_z - profiles of figures 6.6(f) - 6.6(i) and final phase fractions in the nanowire ensembles of samples F - J.

parameter	sample F	sample G	sample H	sample I	sample J
$p_{WZ \to ZB}$	–	0.0034	0.0053	0.0084	0.0091
$p_{ZB \to WZ}$	–	0.0080	0.0096	0.0032	0.0023
$\tilde{p}_{WZ}$	–	0.70	0.64	0.27	0.20
$\tilde{p}_{ZB}$	–	0.30	0.36	0.73	0.80

As final step in the discussion, we now merge the previous findings and set them in relation to the VLS growth model published by Panciera *et al.*,[105] introduced and summarized in section 2.2. Correlating the droplet shape of the liquid Ga droplets at the nanowire apex with the nucleation probability at the same time t, respectively nanowire height $h^{NW}(t)$, we are able to confirm the VLS growth model for a large nanowire ensemble grown under standard growth conditions in a common MBE growth chamber. We summarize the droplet shape obtained from SEM, the simulation results of the *in situ* RHEED experiment and additionally, the results of the XRD experiment with information on the final phase fractions in the nanowire ensemble in figure 6.7. In the top panel the phase generation probabilities at the axial growth front $f_{WZ}(h^{NW}(t))$ and $f_{ZB}(h^{NW}(t))$ of sample J are

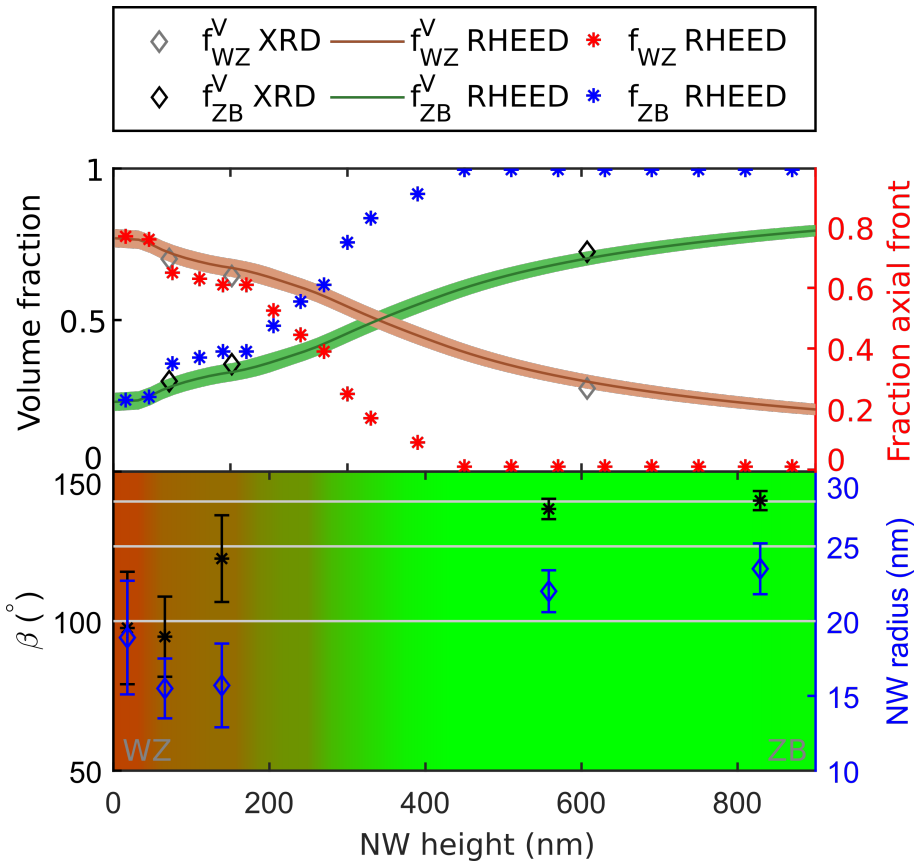

Figure 6.7.: Comparison of wetting angle $\beta(h^{NW})$, nanowire radius $r(h^{NW})$ and nucleation probability at the axial growth front $f_p(h^{NW}(t))$. In the top panel, the phase fraction at the axial growth front f_p $RHEED(h^{NW}(t))$ determined by *in situ* RHEED (which are identical to the nucleation probabilities), the volume phase fractions of *in situ* RHEED f_p^V $RHEED(h^{NW}(t))$ obtained by integrating f_p $RHEED(h^{NW}(t))$ and the results of XRD f_p^V $XRD(h^{NW}(t))$ determined by the Markov approach are depicted as a function of the nanowire height $h^{NW}(t)$. In the bottom panel the wetting angle $\beta(h^{NW})$ and the nanowire radius $r(h^{NW})$ are plotted for the samples F - J at the corresponding nanowire heights $h^{NW}(t)$. The colour code represents the nucleation probability f_{WZ} $RHEED(h^{NW}(t))$.

plotted in red and blue respectively. The volume phase fractions $f^V_{WZ}(t)$ and $f^V_{ZB}(t)$ are obtained by integrating $f_{WZ}(h^{NW}(t))$ and $f_{ZB}(h^{NW}(t))$ in the interval 0 to t, they are shown in brown and green, respectively. The final phase fractions determined by the Markov model which has been applied to the XRD data are illustrated in grey and black for each sample at the corresponding nanowire height h^{NW}. In the bottom panel the results of the SEM evaluation are shown, in black the measured wetting angles β, and in blue the nanowire radii directly below the droplets. Additionally, as a colour code the WZ fraction is included according to figure 6.5(e). At the important wetting angles of the VLS growth model of $\beta = 100°$, $125°$ and $140°$ we draw grey lines as guide for the eyes.

Table 6.5.: Final volume phase fractions determined by *in situ* RHEED and *ex situ* XRD for each sample and determined by sample J at the corresponding nanowire height $h^{NW}(t)$.

parameter	sample F	sample G	sample H	sample I	sample J
$f^V_{WZ}(t)$ at sample J	0.76 ± 0.02	0.74 ± 0.02	0.68 ± 0.02	0.30 ± 0.02	0.20 ± 0.02
f^V_{WZ}	0.64 ± 0.20	0.69 ± 0.03	0.63 ± 0.04	0.29 ± 0.02	0.20 ± 0.02
$\tilde{p}_{WZ}$	–	0.70	0.64	0.27	0.20
$f^V_{ZB}(t)$ at sample J	0.24 ± 0.02	0.26 ± 0.02	0.32 ± 0.02	0.70 ± 0.02	0.80 ± 0.02
f^V_{ZB}	0.36 ± 0.20	0.3 ± 0.03	0.37 ± 0.04	0.71 ± 0.02	0.80 ± 0.02
$\tilde{p}_{ZB}$	–	0.30	0.36	0.73	0.80

At the beginning of growth at $h^{NW} = 18\,\text{nm}$ and $h^{NW} = 66\,\text{nm}$ (samples F and G), the wetting angle β is approximately 100°, however with a large variation indicated by the error bars. During further growth time, β increases, passing $\beta \approx 120°$ at $h^{NW} = 140\,\text{nm}$ (sample H), which is close to 125°, where the theoretical transition from WZ nucleation to ZB nucleation occurs. For the last two samples β is close to 140°. The nanowire radius is constant for the first three samples within the measured radius distribution. The lower radii of sample G and H at $h^{NW} = 66\,\text{nm}$ and $h^{NW} = 140\,\text{nm}$ could also be attributed to their slightly higher nanowire number density resulting in less available Ga for each nanowire. However, we see a clear trend for larger h^{NW} (samples I and J) towards bigger radii, which implies the onset of negative tapering at the nanowires. This is supported by the result in table 6.2, where the exact radii at the nanowire base and at the top are listed. The phase fractions at the axial growth front $f_p(h^{NW}(t))$ of sample J, integrated along $h^{NW}(t)$, giving the functions $f^V_p(h^{NW}(t))$ $RHEED$ in figure 6.7, are in good agreement with the results of XRD obtained by each individual sample and plotted at the corresponding nanowire heights h^{NW}. An overview of the volume phase fractions determined by *in situ* RHEED and *ex situ* XRD for each individual sample, as well as the volume fractions of sample J at the corresponding nanowire height of each individual sample, is presented in table 6.5. The results of RHEED and XRD of each individual sample fit perfectly, though in comparison to sample J the results show some differences caused probably by variations when comparing different growth runs.

The overview presented allows us now to correlate the wetting conditions of the catalyst at the nanowire apex, with the nucleation probabilities of the specific polytypes. We observe a high WZ nucleation probability at contact angles close to 100° in the first 100 nm, during further growth the droplets inflate, which results in increasing β. Close to $h^{NW} = 140\,\text{nm}$

(sample H) $f_p(h^{NW}(t))$ changes from WZ rich to ZB rich, which is in full agreement with the transition angle of $\beta = 125°$ predicted by Panciera *et al.*[105] and Dursap *et al.*[131] During the subsequent growth, we measure the onset of negative tapering, nearly concomitantly with the nucleation of pure ZB. The wetting angle seems to reach the steady-state or equilibrium angle at β =140° for the current growth conditions, indicating the self-stabilization of the nanowire diameter.[99,100]

All our findings fully agree with the proposed VLS growth model published by Panciera *et al.*[105] While those authors confirmed their model of self-catalysed VLS growth for results obtained during nanowire growth in an environmental TEM which allowed *in situ* growth of nanowires by molecular beam-epitaxy, our results emphasize its applicability to standard growth conditions in common growth reactors. Moreover, we demonstrate the application of the model to a large statistical ensemble of nanowires which can only be achieved by techniques probing simultaneously several thousands of nanowires to obtain their mean properties, as in the case for example during *in situ* RHEED.

6.3. Summary

Concluding, we have investigated in detail the nucleation phase of self-catalysed GaAs nanowires grown with a PD step by *in situ* RHEED combined with post-growth SEM analysis. The focus was on the correlation between the properties of the liquid Ga droplets at the apex of the nanowires, mainly the wetting conditions, with the parallel nucleating crystal structures. Therefore, we exploited the shadowing effect of *in situ* RHEED to directly follow the nucleation probability live during growth and to terminate the growth at specific characteristics of the polytype intensity evolution. The immediate ramp down ensures preservation of the droplet shape as best as possible.

Furthermore, in the current experiment we demonstrate the applicability of *in situ* RHEED as a quantitative laboratory-based characterization technique for polytypism in nanowire ensembles. With proper *a priori* knowledge and suitable reference samples, we determine the axial and radial growth rates which are essential for the RHEED simulations and thus we derive the phase fractions at the axial growth front. In addition, we have performed post-growth XRD in symmetric geometry and combined this with the Markov approach, to determine the final volume phase fractions of each sample, to supplement the RHEED results.

All aspects of the present study provide a comprehensive image of nanowire growth in the early growth stage. Furthermore the results were set in relation to a previously published VLS growth model, which was first verified by the growth results of an individual nanowire in an environmental TEM, grown without epitaxial contact to a substrate. In contrast our results demonstrate the validation of the proposed VLS growth model to the nanowire

growth of a large ensemble with epitaxial contact to a substrate under standard growth conditions in a common MBE growth reactor.
The results of this chapter highlight the significance of *in situ* RHEED as a powerful laboratory-based technique for the characterization of the nanowire crystal structure, broadly accessible in most standard MBE chambers.

7. Conclusion and Outlook

In the present work, we developed a quantitative analysis method of *in situ* time-resolved RHEED in transmission geometry during growth of vertical nanowires. We have presented a simulation model which calculates the time-resolved diffraction spot intensities in RHEED patterns of polytypic nanowire ensembles. By investigating the experimental intensity evolution of phase-sensitive RHEED spots during growth and comparing them with results of the simulation model, we can conclude on the evolution of the mean polytype fraction in the nanowire ensemble at the axial growth front. The combination of RHEED simulations and experiments enables us to obtain quantitative information on the final polytypic distribution in nanowires along the growth axis.

The simulation programme considers so-called self-shadowing and ensemble-shadowing. The former is caused by the electron absorption within the nanowires, resulting in the contribution of only a reduced part of the nanowire cross section to the diffracted intensity. The latter is caused by the mutual shadowing within the nanowire ensemble due to the electron absorption. Both make *in situ* RHEED analysis suitable for the detailed characterization of the polytypism in vertical nanowires. The ensemble-shadowing determines the magnitude of the illumination height which defines the height-selectivity of RHEED as a function of the nanowire number density. For small illumination heights, RHEED probes mainly the nanowire axial growth front and is thus particularly interesting for the characterization of the VLS growth. These properties of *in situ* RHEED are suited to complement other techniques and therefore to perform comprehensive growth studies. During simultaneous *in situ* RHEED and *in situ* XRD experiments, we have exploited the small illumination height of *in situ* RHEED at high nanowire number density to obtain the polytype fraction directly at the axial growth front, and the volume information of *in situ* XRD to obtain the growth rates resulting in the shape evolution. Additionally, the high scattering cross section of electrons compared to X-rays enables the detailed characterization of the nucleation phase of nanowires by *in situ* RHEED. The simultaneous experiments further allow us to demonstrate the validity of the model, by describing both, XRD and RHEED experimental intensity evolution by an identical temporal development of nanowire shape and crystal structure.

Moreover, we have shown that *in situ* RHEED can be used as a stand-alone analysis method for the quantitative characterization of polytypism, which is easily accessible in laboratories. We have demonstrated that with suitable reference samples and knowledge

about the growth rates, the developed simulation model can be successfully applied to sole RHEED measurements with the laboratory setup, allowing to perform fundamental growth studies with this quantitative measuring technique. By a combination of *in situ* RHEED to determine the nucleation probabilities of the different polytypes during growth and SEM to determine the wetting conditions of the liquid Ga catalyst droplets at reference samples, we have demonstrated the validity of a recently published theoretical model at large nanowire ensembles, explaining the nucleation probabilities with the wetting conditions of the catalyst particle.

For future studies, quantitative RHEED analysis of the crystal structure can be extended to other materials systems such as InAs nanowires. The characterization of hetero-epitaxial nanowire structures, like core-shell nanowires, would also be attractive. The sensitivity of RHEED to the edges of the hexagonal cross section can be especially suitable for the shell characterization. However, the expected non-uniform strain at the edges might blur the RHEED patterns and makes the interpretation more challenging, as was already observed during growth experiments of GaAs/InGaAs core-shell nanowires.

A remaining open question is the transition of the droplet from wetting of the substrate to wetting of the nanowire stub, and its effect on the crystal structure during the nanowire nucleation. Since the pMBE setup enables RHEED experiments under different, complementary X-ray scattering geometries, we propose future experiments to characterize the morphology of the droplets on substrates during nucleation of the nanowires by X-rays, while RHEED is used to monitor the crystal phases at the onset of growth. In grazing incidence conditions, *in situ* grazing-incidence small-angle X-ray scattering (GISAXS) is directly sensitive to the shape of the scattering objects and thus we may correlate the droplet shape evolution with the crystal structure obtained by RHEED, which would allow the verification and refinement of theoretical models of nanowire nucleation.

Bibliography

[1] Moore, G. *Electronics* **1965**, *38*, 114–117.

[2] Chen, R.; Ng, K. W.; Ko, W. S.; Parekh, D.; Lu, F.; Tran, T.-T. D.; Li, K.; Chang-Hasnain, C. *Nature Communications* **2014**, *5*, 4325.

[3] Thelander, C.; Agarwal, P.; Brongersma, S.; Eymery, J.; Feiner, L.; Forchel, A.; Scheffler, M.; Riess, W.; Ohlsson, B.; Gösele, U.; Samuelson, L. *Materials Today* **2006**, *9*, 28 – 35.

[4] Thelander, C.; Caroff, P.; Plissard, S.; Dey, A. W.; Dick, K. A. *Nano Letters* **2011**, *11*, 2424–2429.

[5] Bussone, G.; Schäfer-Eberwein, H.; Dimakis, E.; Biermanns, A.; Carbone, D.; Tahraoui, A.; Geelhaar, L.; Haring Bolívar, P.; Schülli, T. U.; Pietsch, U. *Nano Letters* **2015**, *15*, 981–989.

[6] Akopian, N.; Patriarche, G.; Liu, L.; Harmand, J.-C.; Zwiller, V. *Nano Letters* **2010**, *10*, 1198–1201.

[7] Knutsson, J. V.; Lehmann, S.; Hjort, M.; Lundgren, E.; Dick, K. A.; Timm, R.; Mikkelsen, A. *ACS Nano* **2017**, *11*, 10519–10528.

[8] Hayden, O.; Agarwal, R.; Lu, W. *Nano Today* **2008**, *3*, 12 – 22.

[9] Ferry, D. K. *Science* **2008**, *319*, 579–580.

[10] Sauer, R. *Halbleiterphysik: Lehrbuch für Physiker und Ingenieure*; Oldenbourg, 2009.

[11] Ashcroft, N.; Mermin, D. *Festkörperphysik*; Oldenbourg Wissenschaftsverlag, 2012.

[12] Lieber, C. M. *MRS Bulletin* **2003**, *28*, 486–491.

[13] Dick Thelander, K. *Progress in Crystal Growth and Characterization of Materials* **2008**, *54*, 138–173.

[14] LaPierre, R. R.; Robson, M.; Azizur-Rahman, K. M.; Kuyanov, P. *Journal of Physics D: Applied Physics* **2017**, *50*, 123001.

[15] Dubrovskii, V. G. *Nucleation Theory and Growth of Nanostructures*; Springer-Verlag Berlin Heidelberg, 2014.

[16] Tomioka, K.; Fukui, T. *Applied Physics Letters* **2011**, *98*, 083114.

[17] Tomioka, K.; Yoshimura, M.; Fukui, T. *Nature* **2012**, *488*, 189.

[18] Kilpi, O.-P.; Svensson, J.; Wu, J.; Persson, A. R.; Wallenberg, R.; Lind, E.; Wernersson, L.-E. *Nano Letters* **2017**, *17*, 6006–6010.

[19] Dimakis, E.; Jahn, U.; Ramsteiner, M.; Tahraoui, A.; Grandal, J.; Kong, X.; Marquardt, O.; Trampert, A.; Riechert, H.; Geelhaar, L. *Nano Letters* **2014**, *14*, 2604–2609.

[20] Berg, A.; Yazdi, S.; Nowzari, A.; Storm, K.; Jain, V.; Vainorius, N.; Samuelson, L.; Wagner, J. B.; Borgström, M. T. *Nano Letters* **2016**, *16*, 656–662.

[21] Sadaf, S. M.; Zhao, S.; Wu, Y.; Ra, Y.-H.; Liu, X.; Vanka, S.; Mi, Z. *Nano Letters* **2017**, *17*, 1212–1218.

[22] Wallentin, J.; Anttu, N.; Asoli, D.; Huffman, M.; Åberg, I.; Magnusson, M. H.; Siefer, G.; Fuss-Kailuweit, P.; Dimroth, F.; Witzigmann, B.; Xu, H. Q.; Samuelson, L.; Deppert, K.; Borgström, M. T. *Science* **2013**, *339*, 1057–1060.

[23] Krogstrup, P.; Jørgensen, H. I.; Heiss, M.; Demichel, O.; Holm, J. V.; Aagesen, M.; Nygard, J.; Fontcuberta i Morral, A. *Nature Photonics* **2013**, *7*, 306.

[24] Yao, M.; Cong, S.; Arab, S.; Huang, N.; Povinelli, M. L.; Cronin, S. B.; Dapkus, P. D.; Zhou, C. *Nano Letters* **2015**, *15*, 7217–7224.

[25] Mayer, B.; Rudolph, D.; Schnell, J.; Morkötter, S.; Winnerl, J.; Treu, J.; Müller, K.; Bracher, G.; Abstreiter, G.; Koblmüller, G.; Finley, J. J. *Nature Communications* **2013**, *4*, 2931.

[26] Kim, H.; Lee, W.-J.; Farrell, A. C.; Morales, J. S. D.; Senanayake, P.; Prikhodko, S. V.; Ochalski, T. J.; Huffaker, D. L. *Nano Letters* **2017**, *17*, 3465–3470.

[27] Xu, W.-Z.; Ren, F.-F.; Jevtics, D.; Hurtado, A.; Li, L.; Gao, Q.; Ye, J.; Wang, F.; Guilhabert, B.; Fu, L.; Lu, H.; Zhang, R.; Tan, H. H.; Dawson, M. D.; Jagadish, C. *Nano Letters* **2018**, *18*, 3414–3420.

[28] Boukai, A. I.; Bunimovich, Y.; Tahir-Kheli, J.; Yu, J.-K.; Goddard III, W. A.; Heath, J. R. *Nature* **2008**, *451*, 168–171.

[29] Mensch, P.; Karg, S.; Schmidt, V.; Gotsmann, B.; Schmid, H.; Riel, H. *Applied Physics Letters* **2015**, *106*, 093101.

[30] Prete, D.; Erdman, P. A.; Demontis, V.; Zannier, V.; Ercolani, D.; Sorba, L.; Beltram, F.; Rossella, F.; Taddei, F.; Roddaro, S. *Nano Letters* **2019**, *19*, 3033–3039.

[31] Ramgir, N. S.; Yang, Y.; Zacharias, M. *Small* **2010**, *6*, 1705–1722.

[32] Madel, M.; Jakob, J.; Huber, F.; Neuschl, B.; Bauer, S.; Xie, Y.; Tischer, I.; Thonke, K. *physica status solidi (a)* **2015**, *212*, 1810–1816.

[33] Hobbs, R. G.; Petkov, N.; Holmes, J. D. *Chemistry of Materials* **2012**, *24*, 1975–1991.

[34] Wagner, R. S.; Ellis, W. C. *Applied Physics Letters* **1964**, *4*, 89–90.

[35] Ragnarsdóttir, K. V. *Nature Geoscience* **2008**, *1*, 720.

[36] Chiba, K.; Yoshida, A.; Tomioka, K.; Motohisa, J. *ACS Photonics* **2019**, *6*, 260–264.

[37] Li, Y.; Xiang, J.; Qian, F.; Gradecak, S.; Wu, Y.; Yan, H.; Blom, D. A.; Lieber, C. M. *Nano Letters* **2006**, *6*, 1468–1473.

[38] Dayeh, S.; Aplin, D. P.; Zhou, X.; Yu, P. K.; Yu, E.; Wang, D. *Small* **2007**, *3*, 326–332.

[39] Morral, A. F. i. *IEEE Journal of Selected Topics in Quantum Electronics* **2011**, *17*, 819–828.

[40] Herr, U.; Riedmueller, B.; Haddad, M.; AbuShgair, K.; Madel, M.; Jakob, J. B.; Thonke, K. *physica status solidi c* **2012**, *9*, 1912–1915.

[41] Yu, B.; Sun, X. H.; Calebotta, G. A.; Dholakia, G. R.; Meyyappan, M. *Journal of Cluster Science* **2006**, *17*, 579–597.

[42] Hao, Y.; Meng, G.; Wang, Z. L.; Ye, C.; Zhang, L. *Nano Letters* **2006**, *6*, 1650–1655.

[43] Di Carlo, V.; Prete, P.; Dubrovskii, V. G.; Berdnikov, Y.; Lovergine, N. *Nano Letters* **2017**, *17*, 4075–4082.

[44] Bullis, W. *Solid-State Electronics* **1966**, *9*, 143 – 168.

[45] Dick, K. A.; Caroff, P. *Nanoscale* **2014**, *6*, 3006–3021.

[46] Oehler, F.; Cattoni, A.; Scaccabarozzi, A.; Patriarche, G.; Glas, F.; Harmand, J.-C. *Nano Letters* **2018**, *18*, 701–708.

[47] Tu, L. W.; Hsiao, C. L.; Chi, T. W.; Lo, I.; Hsieh, K. Y. *Applied Physics Letters* **2003**, *82*, 1601–1603.

[48] Biermanns, A.; Dimakis, E.; Davydok, A.; Sasaki, T.; Geelhaar, L.; Takahasi, M.; Pietsch, U. *Nano Letters* **2014**, *14*, 6878–6883.

[49] Woo, R. L.; Xiao, R.; Kobayashi, Y.; Gao, L.; Goel, N.; Hudait, M. K.; Mallouk, T. E.; Hicks, R. F. *Nano Letters* **2008**, *8*, 4664–4669.

[50] Breuer, S. Molecular Beam Epitaxy of GaAs Nanowires and their Suitability for Optoelectronic Applications. Ph.D. thesis, Humboldt-Universität zu Berlin, 2011.

[51] Cirlin, G. E.; Dubrovskii, V. G.; Soshnikov, I. P.; Sibirev, N. V.; Samsonenko, Y. B.; Bouravleuv, A. D.; Harmand, J. C.; Glas, F. *physica status solidi (RRL) – Rapid Research Letters* **2009**, *3*, 112–114.

[52] Perea, D. E.; Allen, J. E.; May, S. J.; Wessels, B. W.; Seidman, D. N.; Lauhon, L. J. *Nano Letters* **2006**, *6*, 181–185.

[53] Tambe, M. J.; Ren, S.; Gradecak, S. *Nano Letters* **2010**, *10*, 4584–4589.

[54] Breuer, S.; Pfüller, C.; Flissikowski, T.; Brandt, O.; Grahn, H. T.; Geelhaar, L.; Riechert, H. *Nano Letters* **2011**, *11*, 1276–1279.

[55] Bar-Sadan, M.; Barthel, J.; Shtrikman, H.; Houben, L. *Nano Letters* **2012**, *12*, 2352–2356.

[56] Jiang, N.; Parkinson, P.; Gao, Q.; Breuer, S.; Tan, H. H.; Wong-Leung, J.; Jagadish, C. *Applied Physics Letters* **2012**, *101*, 023111.

[57] Jiang, N.; Gao, Q.; Parkinson, P.; Wong-Leung, J.; Mokkapati, S.; Breuer, S.; Tan, H. H.; Zheng, C. L.; Etheridge, J.; Jagadish, C. *Nano Letters* **2013**, *13*, 5135–5140.

[58] Heun, S.; Radha, B.; Ercolani, D.; Kulkarni, G. U.; Rossi, F.; Grillo, V.; Salviati, G.; Beltram, F.; Sorba, L. *Crystal Growth & Design* **2010**, *10*, 4197–4202.

[59] Hillerich, K.; Messing, M. E.; Wallenberg, L. R.; Deppert, K.; Dick, K. A. *Journal of Crystal Growth* **2011**, *315*, 134 – 137, 15th International Conference on Metalorganic Vapor Phase Epitaxy (ICMOVPE-XV).

[60] Vogel, A. T.; de Boor, J.; Becker, M.; Wittemann, J. V.; Mensah, S. L.; Werner, P.; Schmidt, V. *Nanotechnology* **2010**, *22*, 015605.

[61] Tomioka, K.; Ikejiri, K.; Tanaka, T.; Motohisa, J.; Hara, S.; Hiruma, K.; Fukui, T. *Journal of Materials Research* **2011**, *26*, 2127–2141.

[62] Chatillon, C.; Chatain, D. *Journal of Crystal Growth* **1995**, *151*, 91 – 101.

[63] Balaghi, L.; Tauchnitz, T.; Hübner, R.; Bischoff, L.; Schneider, H.; Helm, M.; Dimakis, E. *Nano Letters* **2016**, *16*, 4032–4039.

[64] Colombo, C.; Spirkoska, D.; Frimmer, M.; Abstreiter, G.; Fontcuberta i Morral, A. *Phys. Rev. B* **2008**, *77*, 155326.

[65] Matteini, F.; Tütüncüoğlu, G.; Rüffer, D.; Alarcón-Lladó, E.; i Morral, A. F. *Journal of Crystal Growth* **2014**, *404*, 246 – 255.

[66] Matteini, F.; Tütüncüoglu, G.; Potts, H.; Jabeen, F.; Fontcuberta i Morral, A. *Crystal Growth & Design* **2015**, *15*, 3105–3109.

[67] Matteini, F.; Tütüncüoglu, G.; Mikulik, D.; Vukajlovic-Plestina, J.; Potts, H.; Leran, J.-B.; Carter, W. C.; Fontcuberta i Morral, A. *Crystal Growth & Design* **2016**, *16*, 5781–5786.

[68] Schroth, P. Growth of self-catalyzed GaAs nanowires using molecular-beam-epitaxy and structural characterization by in-situ X-ray diffraction. Ph.D. thesis, Universität Siegen, 2016.

[69] Fontcuberta i Morral, A.; Colombo, C.; Abstreiter, G.; Arbiol, J.; Morante, J. R. *Applied Physics Letters* **2008**, *92*, 063112.

[70] Bastiman, F.; Küpers, H.; Somaschini, C.; Geelhaar, L. *Nanotechnology* **2016**, *27*, 095601.

[71] Tomioka, K.; Motohisa, J.; Hara, S.; Fukui, T. *Nano Letters* **2008**, *8*, 3475–3480.

[72] Bauer, B.; Rudolph, A.; Soda, M.; i Morral, A. F.; Zweck, J.; Schuh, D.; Reiger, E. *Nanotechnology* **2010**, *21*, 435601.

[73] Plissard, S.; Dick, K. A.; Larrieu, G.; Godey, S.; Addad, A.; Wallart, X.; Caroff, P. *Nanotechnology* **2010**, *21*, 385602.

[74] Somaschini, C.; Bietti, S.; Trampert, A.; Jahn, U.; Hauswald, C.; Riechert, H.; Sanguinetti, S.; Geelhaar, L. *Nano Letters* **2013**, *13*, 3607–3613.

[75] Hakkarainen, T. V.; Schramm, A.; Mäkelä, J.; Laukkanen, P.; Guina, M. *Nanotechnology* **2015**, *26*, 275301.

[76] Küpers, H.; Bastiman, F.; Luna, E.; Somaschini, C.; Geelhaar, L. *Journal of Crystal Growth* **2017**, *459*, 43 – 49.

[77] Tauchnitz, T.; Nurmamytov, T.; Hübner, R.; Engler, M.; Facsko, S.; Schneider, H.; Helm, M.; Dimakis, E. *Crystal Growth & Design* **2017**, *17*, 5276–5282.

[78] Schroth, P.; Jakob, J.; Feigl, L.; Kashani, S. M. M.; Pietsch, U.; Baumbach, T. *MRS Communications* **2018**, *8*, 871–877.

[79] Tauchnitz, T.; Berdnikov, Y.; Dubrovskii, V. G.; Schneider, H.; Helm, M.; Dimakis, E. *Nanotechnology* **2018**, *29*, 504004.

[80] Anttu, N.; Lehmann, S.; Storm, K.; Dick, K. A.; Samuelson, L.; Wu, P. M.; Pistol, M.-E. *Nano Letters* **2014**, *14*, 5650–5655.

[81] Dobrovolsky, A.; Persson, P. O.; Sukrittanon, S.; Kuang, Y.; Tu, C. W.; Chen, W. M.; Buyanova, I. A. *Nano Letters* **2015**, *15*, 4052–4058.

[82] Ikejiri, K.; Kitauchi, Y.; Tomioka, K.; Motohisa, J.; Fukui, T. *Nano Letters* **2011**, *11*, 4314–4318.

[83] Köhl, M. Analysis of nanostructures based on diffraction of X-ray radiation. Ph.D. thesis, Karlsruhe Institute of Technology, 2014.

[84] Momma, K.; Izumi, F. *Journal of Applied Crystallography* **2011**, *44*, 1272–1276.

[85] Biermanns, A. X-ray diffraction from single GaAs nanowires. Ph.D. thesis, Universität Siegen, 2012.

[86] Köhl, M.; Schroth, P.; Minkevich, A. A.; Hornung, J.-W.; Dimakis, E.; Somaschini, C.; Geelhaar, L.; Aschenbrenner, T.; Lazarev, S.; Grigoriev, D.; Pietsch, U.; Baumbach, T. *Journal of Synchrotron Radiation* **2015**, *22*, 67–75.

[87] Biermanns, A.; Breuer, S.; Davydok, A.; Geelhaar, L.; Pietsch, U. *physica status solidi (RRL) – Rapid Research Letters* **2011**, *5*, 156–158.

[88] Biermanns, A.; Breuer, S.; Davydok, A.; Geelhaar, L.; Pietsch, U. *Journal of Applied Crystallography* **2012**, *45*, 239–244.

[89] Yeh, C.-Y.; Lu, Z. W.; Froyen, S.; Zunger, A. *Phys. Rev. B* **1992**, *46*, 10086–10097.

[90] Akiyama, T.; Sano, K.; Nakamura, K.; Ito, T. *Japanese Journal of Applied Physics* **2006**, *45*, L275–L278.

[91] Glas, F.; Harmand, J.-C.; Patriarche, G. *Phys. Rev. Lett.* **2007**, *99*, 146101.

[92] Dubrovskii, V. G.; Sibirev, N. V.; Harmand, J. C.; Glas, F. *Phys. Rev. B* **2008**, *78*, 235301.

[93] Johansson, J.; Karlsson, L. S.; Dick, K. A.; Bolinsson, J.; Wacaser, B. A.; Deppert, K.; Samuelson, L. *Crystal Growth & Design* **2009**, *9*, 766–773.

[94] Dubrovskii, V. G. *Applied Physics Letters* **2014**, *104*, 053110.

[95] Krogstrup, P.; Curiotto, S.; Johnson, E.; Aagesen, M.; Nygård, J.; Chatain, D. *Phys. Rev. Lett.* **2011**, *106*, 125505.

[96] Sibirev, N. V.; Koryakin, A. A. *Technical Physics Letters* **2015**, *41*, 1189–1191.

[97] Wen, C.-Y.; Tersoff, J.; Hillerich, K.; Reuter, M. C.; Park, J. H.; Kodambaka, S.; Stach, E. A.; Ross, F. M. *Phys. Rev. Lett.* **2011**, *107*, 025503.

[98] Jacobsson, D.; Panciera, F.; Tersoff, J.; Reuter, M. C.; Lehmann, S.; Hofmann, S.; Dick, K. A.; Ross, F. M. *Nature* **2016**, *531*, 317.

[99] Tersoff, J. *Nano Letters* **2015**, *15*, 6609–6613.

[100] Dubrovskii, V. G.; Xu, T.; Álvarez, A. D.; Plissard, S. R.; Caroff, P.; Glas, F.; Grandidier, B. *Nano Letters* **2015**, *15*, 5580–5584.

[101] Schroth, P.; Jakob, J.; Feigl, L.; Mostafavi Kashani, S. M.; Vogel, J.; Strempfer, J.; Keller, T. F.; Pietsch, U.; Baumbach, T. *Nano Letters* **2018**, *18*, 101–108.

[102] Glas, F.; Ramdani, M. R.; Patriarche, G.; Harmand, J.-C. *Phys. Rev. B* **2013**, *88*, 195304.

[103] Dubrovskii, V. G. *Crystal Growth & Design* **2017**, *17*, 2544–2548.

[104] Kim, W.; Dubrovskii, V. G.; Vukajlovic-Plestina, J.; Tütüncüoglu, G.; Francaviglia, L.; Güniat, L.; Potts, H.; Friedl, M.; Leran, J.-B.; Fontcuberta i Morral, A. *Nano Letters* **2018**, *18*, 49–57.

[105] Panciera, F.; Baraissov, Z.; Patriarche, G.; Dubrovskii, V. G.; Glas, F.; Travers, L.; Mirsaidov, U.; Harmand, J.-C. *Nano Letters* **2020**, *20*, 1669–1675.

[106] Dubrovskii, V. G. *physica status solidi (RRL) – Rapid Research Letters* **2019**, *13*, 1900301.

[107] Pietsch, U.; Holy, V.; Baumbach, T. *High-Resolution X-Ray Scattering: From Thin Films to Lateral Nanostructures*; Advanced Texts in Physics; Springer New York, 2004.

[108] Krogstrup, P.; Hannibal Madsen, M.; Hu, W.; Kozu, M.; Nakata, Y.; Nygård, J.; Takahasi, M.; Feidenhans'l, R. *Applied Physics Letters* **2012**, *100*, 093103.

[109] Takahasi, M.; Kozu, M.; Sasaki, T.; Hu, W. *Crystal Growth & Design* **2015**, *15*, 4979–4985.

[110] Schroth, P.; Köhl, M.; Hornung, J.-W.; Dimakis, E.; Somaschini, C.; Geelhaar, L.; Biermanns, A.; Bauer, S.; Lazarev, S.; Pietsch, U.; Baumbach, T. *Phys. Rev. Lett.* **2015**, *114*, 055504.

[111] IUCr, In *International Tables for Crystallography, Volume C: Mathematical, physical and chemical tables*, 3rd ed.; Prince, E., Ed.; International Tables for Crystallography; Kluwer Academic Publishers, 2004.

[112] Cowley, J. *Diffraction Physics*; North-Holland Personal Library; Elsevier Science, 1995.

[113] Slobodskyy, T.; Schroth, P.; Grigoriev, D.; Minkevich, A. A.; Hu, D. Z.; Schaadt, D. M.; Baumbach, T. *Review of Scientific Instruments* **2012**, *83*, 105112.

[114] Schroth, P.; Slobodskyy, T.; Grigoriev, D.; Minkevich, A.; Riotte, M.; Lazarev, S.; Fohtung, E.; Hu, D.; Schaadt, D.; Baumbach, T. *Materials Science and Engineering: B* **2012**, *177*, 721 – 724.

[115] Schroth, P.; Al Humaidi, M.; Feigl, L.; Jakob, J.; Al Hassan, A.; Davtyan, A.; Küpers, H.; Tahraoui, A.; Geelhaar, L.; Pietsch, U.; Baumbach, T. *Nano Letters* **2019**, *19*, 4263–4271.

[116] Strempfer, J.; Francoual, S.; Reuther, D.; Shukla, D. K.; Skaugen, A.; Schulte-Schrepping, H.; Kracht, T.; Franz, H. *Journal of Synchrotron Radiation* **2013**, *20*, 541–549.

[117] Grigoriev, D.; Lazarev, S.; Schroth, P.; Minkevich, A.; Köhl, M.; Slobodskyy, T.; Helfrich, M.; Schaadt, D.; Aschenbrenner, T.; Hommel, D.; Baumbach, T. *Journal of Applied Crystallography* **2016**, *49*, 961–967.

[118] Jakob, J.; Schroth, P.; Feigl, L.; Hauck, D.; Pietsch, U.; Baumbach, T. *Nanoscale* **2020**, *12*, 5471–5482.

[119] Braun, W. *Applied RHEED: Reflection High-Energy Electron Diffraction During Crystal Growth*; Springer Tracts in Modern Physics; Springer Berlin Heidelberg, 1999.

[120] Wang, G.; Lu, T. *RHEED Transmission Mode and Pole Figures: Thin Film and Nanostructure Texture Analysis*; Springer, 2013.

[121] Consonni, V.; Trampert, A.; Geelhaar, L.; Riechert, H. *Applied Physics Letters* **2011**, *99*.

[122] Consonni, V.; Hanke, M.; Knelangen, M.; Geelhaar, L.; Trampert, A.; Riechert, H. *Phys. Rev. B* **2011**, *83*, 035310.

[123] Hertenberger, S.; Rudolph, D.; Bolte, S.; Döblinger, M.; Bichler, M.; Spirkoska, D.; Finley, J. J.; Abstreiter, G.; Koblmüller, G. *Applied Physics Letters* **2011**, *98*, 123114.

[124] Patella, F.; Arciprete, F.; Fanfoni, M.; Sessi, V.; Balzarotti, A.; Placidi, E. *Applied Physics Letters* **2005**, *87*.

[125] Chèze, C.; Geelhaar, L.; Brandt, O.; Weber, W. M.; Riechert, H.; Münch, S.; Rothemund, R.; Reitzenstein, S.; Forchel, A.; Kehagias, T.; Komninou, P.; Dimitrakopulos, G. P.; Karakostas, T. *Nano Research* **2010**, *3*, 528–536.

[126] Somaschini, C.; Fedorov, A.; Bietti, S.; Scarpellini, D.; Sanguinetti, S. Flat top formation in self-assisted GaAs nanowires. 2015 1st Workshop on Nanotechnology in Instrumentation and Measurement (NANOFIM). 2015; pp 146–149.

[127] Cirlin, G. E.; Dubrovskii, V. G.; Samsonenko, Y. B.; Bouravleuv, A. D.; Durose, K.; Proskuryakov, Y. Y.; Mendes, B.; Bowen, L.; Kaliteevski, M. A.; Abram, R. A.; Zeze, D. *Phys. Rev. B* **2010**, *82*, 035302.

[128] Jo, J.; Tchoe, Y.; Yi, G.-C.; Kim, M. *Scientific Reports* **2018**, *8*, 1694.

[129] Rudolph, D.; Hertenberger, S.; Bolte, S.; Paosangthong, W.; Spirkoska, D.; Döblinger, M.; Bichler, M.; Finley, J. J.; Abstreiter, G.; Koblmüller, G. *Nano Letters* **2011**, *11*, 3848–3854.

[130] Breuer, S.; Hilse, M.; Trampert, A.; Geelhaar, L.; Riechert, H. *Phys. Rev. B* **2010**, *82*, 075406.

[131] Dursap, T.; Vettori, M.; Danescu, A.; Botella, C.; Regreny, P.; Patriarche, G.; Gendry, M.; Penuelas, J. *Nanoscale Adv.* **2020**, *2*, 2127–2134.

[132] Tang, F.; Wang, G.-C.; Lu, T.-M. *Journal of Applied Physics* **2007**, *102*, 014306.

[133] Akkerman, A. F.; Chernov, G. Y. *physica status solidi (b)* **1978**, *89*, 329–333.

[134] Mayol, R.; Salvat, F. *Atomic Data and Nuclear Data Tables* **1997**, *65*, 55 – 154.

[135] Küpers, H.; Lewis, R. B.; Geelhaar, L. *Journal of Crystal Growth* **2020**, *531*, 125320.

[136] Zheng, H.; Wang, J.; Huang, J. Y.; Wang, J.; Zhang, Z.; Mao, S. X. *Nano Letters* **2013**, *13*, 6023–6027.

[137] Lenrick, F.; Ek, M.; Deppert, K.; Samuelson, L.; Reine Wallenberg, L. *Nano Research* **2014**, *7*, 1188–1194.

[138] Zhang, Z.; Liu, N.; Li, L.; Su, J.; Chen, P.-P.; Lu, W.; Gao, Y.; Zou, J. *Nano Letters* **2018**, *18*, 6597–6603.

[139] Mostafavi Kashani, S. M.; Kriegner, D.; Bahrami, D.; Vogel, J.; Davtyan, A.; Feigl, L.; Schroth, P.; Jakob, J.; Baumbach, T.; Pietsch, U. *ACS Applied Nano Materials* **2019**, *2*, 689–699.

[140] Stepanov, S. A. X-ray server: an online resource for simulations of x-ray diffraction and scattering. Advances in Computational Methods for X-Ray and Neutron Optics. 2004; pp 16 – 26.

[141] Plissard, S.; Larrieu, G.; Wallart, X.; Caroff, P. *Nanotechnology* **2011**, *22*, 275602.

[142] Munshi, A. M.; Dheeraj, D. L.; Fauske, V. T.; Kim, D. C.; Huh, J.; Reinertsen, J. F.; Ahtapodov, L.; Lee, K. D.; Heidari, B.; van Helvoort, A. T. J.; Fimland, B. O.; Weman, H. *Nano Letters* **2014**, *14*, 960–966.

[143] Russo-Averchi, E.; Vukajlovic Plestina, J.; Tütüncüoglu, G.; Matteini, F.; Dalmau-Mallorquí, A.; de la Mata, M.; Rüffer, D.; Potts, H. A.; Arbiol, J.; Conesa-Boj, S.; Fontcuberta i Morral, A. *Nano Letters* **2015**, *15*, 2869–2874.

[144] Vukajlovic-Plestina, J.; Kim, W.; Ghisalberti, L.; Varnavides, G.; Tütüncuoglu, G.; Potts, H.; Friedl, M.; Güniat, L.; Carter, W. C.; Dubrovskii, V. G.; Fontcuberta i Morral, A. *Nature Communications* **2019**, *10*, 869.

[145] Bastiman, F.; Küpers, H.; Somaschini, C.; Dubrovskii, V. G.; Geelhaar, L. *Phys. Rev. Materials* **2019**, *3*, 073401.

[146] Köhl, M.; Schroth, P.; Baumbach, T. *Journal of Synchrotron Radiation* **2016**, *23*, 487–500.

A. Publications

Publications in peer-reviewed journals

This dissertation is based on the following articles:

- **Publication I:**
  J. Jakob, P. Schroth, L. Feigl, D. Hauck, U. Pietsch and T. Baumbach, Quantitative analysis of time-resolved RHEED during growth of vertical nanowires, *Nanoscale*, 12, 5471-5482, 2020.

- **Publication II:**
  J. Jakob, P. Schroth, L. Feigl, M. Al Humaidi, A. Al Hassan, A. Davtyan, D. Hauck, U. Pietsch and T. Baumbach, RHEED in comparison to XRD for the quantitative in situ analysis of polytypism during NW growth, *in preparation*, 2020.

Other co-authored articles:

- P. Schroth, **J. Jakob**, L. Feigl, S. M. Mostafavi Kashani, J. Vogel, J. Strempfer, T. Keller, U. Pietsch and T. Baumbach, Radial Growth of Self-Catalyzed GaAs Nanowires and the Evolution of the Liquid Ga-Droplet Studied by Time-Resolved in Situ X-ray Diffraction, *Nano Letters*, 18, 101-108, 2018.

- P. Schroth, **J. Jakob**, L. Feigl, S. M. Mostafavi Kashani, U. Pietsch and T. Baumbach, Lithography-free variation of the number density of self-catalyzed GaAs nanowires and its impact on polytypism, *MRS Communications*, 8, 871-877, 2018.

- S. M. Mostafavi Kashani, D. Kriegner, D. Bahrami, J. Vogel, A. Davtyan, L. Feigl, P. Schroth, **J. Jakob**, T. Baumbach and U. Pietsch, X-ray Diffraction Analysis of the Angular Stability of Self-Catalyzed GaAs Nanowires for Future Applications in Solar Light Harvesting and Light Emission Devices, *ACS Applied Nano Materials*, 2, 689-699, 2019.

- P. Schroth, M. Al Humaidi, L. Feigl, **J. Jakob**, A. Al Hassan, A. Davtyan, H. Küpers, A. Tahraoui, L. Geelhaar, U. Pietsch and T. Baumbach, Impact of the shadowing effect on crystal structure of patterned self-catalyzed GaAs nanowires, *Nano Letters*, 19, 4263-4271, 2019.

Conference contributions

Oral presentations:

- **J. Jakob**, P. Schroth, L. Feigl, D. Hauck, S. M. Mostafavi Kashani, A. Al Hassan, J. Vogel, U. Pietsch and T. Baumbach, Investigation of self-catalysed GaAs NW at the nucleation stage - in-situ XRD and RHEED as complementary probes, *2018 MRS SPRING MEETING & EXHIBIT*, Phoenix, Arizona (USA), April 2 - 6, 2018.
- **J. Jakob**, P. Schroth, L. Feigl, D. Hauck, M. Al Humaidi, A. Al Hassan, U. Pietsch and T. Baumbach, GaAs NW during the nucleation stage studied by simultaneous time-resolved in situ XRD and RHEED, *14th Biennial Conference on High Resolution X-ray Diffraction and Imaging - XTOP 2018*, Bari (Italy), September 3 - 7, 2018.

Poster presentations:

- **J. Jakob**, P. Schroth, S. M. Mostafavi Kashani, U. Pietsch and T. Baumbach, Tailoring growth of GaAs NW for *in situ* X-ray investigations using a portable MBE, *Nanowires Barcelona 2015*, Barcelona (Spain), October 26 - 30, 2015.
- **J. Jakob**, P. Schroth, L. Feigl, S. M. Mostafavi Kashani, J. Vogel, U. Pietsch and T. Baumbach, *In situ* time-resolved XRD and RHEED study of the polytypism in GaAs nanowires, *13th Biennial Conference on High Resolution X-ray Diffraction and Imaging - XTOP 2016*, Brno (Czech Republic), September 4 - 8, 2016.
- **J. Jakob**, P. Schroth, L. Feigl, S. M. Mostafavi Kashani, J. Vogel, U. Pietsch and T. Baumbach, *In situ* time-resolved XRD and RHEED study of the polytypism in GaAs nanowires, *25th Annual Meeting of the German Crystallographic Society*, Karlsruhe (Germany), March 27 - 30, 2017.
- **J. Jakob**, P. Schroth, L. Feigl, S. M. Mostafavi Kashani, J. Vogel, A. Al Hassan, U. Pietsch and T. Baumbach, Simultaneous time-resolved in-situ XRD and RHEED study during growth of GaAs nanowires, *Nanowire Week 2017*, Lund (Sweden), May 29 - June 2, 2017.
- **J. Jakob**, P. Schroth, L. Feigl, M. Al Humaidi, A. Davtyan, A. Al Hassan, U. Pietsch and T. Baumbach , Quantification of in situ RHEED for height-resolved analysis of polytypism in nanowires, *Nanowire Week 2019*, Pisa (Italy), September 23 - 27, 2019.

B. Simulation programme

In this section, we give a short overview over the simulation programme. The source code of the programme is written in Fortran and was realized by Daniel Hauck during his student assistance. The main programme executes a *config file* in the form of *.rshad, in which the necessary information is contained. In the *config file* each parameter consists of two lines with the parameter's name in the first line and the value in the second line. All possible parameters and their respective values are listed in the following, in italic font a short description of each parameter is given:

```
use shadows                 ensemble-shadowing for determination of intensity on/off
     true/false
crystal correction          only for XRD: simulation with/without crystallite ensemble
     true/false
polynom order               degree of polynomial function to interpolate phase fraction between anchor values
     2
weight ZB1                  rel. contribution of ZB for RMSD determination between simulation and experiment
     1.0
weight ZB2                  rel. contribution of TZB for RMSD determination between simulation and experiment
     1.0
normalization length        nanowire length at which the normalization is done,
     -1.0                         negative values are set to normalize on equal area under the curve
growth time                 growth time in min
     60.0
free path                   mean free path length in nm
     12.0
data directory              directory path of the experimental data
     /home
sample prefix               sample name
     Sample1_
name ZB1                    suffix 1 of sample name
     220
name ZB2                    suffix 2 of sample name
     311
name WZ                     suffix 3 of sample name
     103
number of bins              number of slices K
     1000
output directory            directory path for storing the simulated curves
     output_folder
list file                   directory path and name of the listfile.txt with further simulation parameters (see below)
     listfile.txt
integrated fraction         use integrated phase fractions on/off
     true/false
histogram output            export ensemble-shadowing function s(h,t) on/off
     true/false
wireposition output         export (x,y) positions of all simulated nanowires on/off
     true/false
```

In the *config file*, the main information for the data processing of the programme is given. The actual nanowire and crystallite parameters are given in a second file, which can be individually named. The directory path is defined in the *config file*, in the current example it is called *listfile.txt*. The separation of both files allows to vary different parameters and thus simulate the intensity evolution for a large parameter space. The structure of the *listfile* moreover does not limit the number of simulations because each line describes an individual set of simulation parameters. Thus the number of lines determines the amount of simulated curves. Each line has a fixed number of columns, whereas the last one decides if the intensity evolution will be exported into an *intensity file*. A typical *listfile* is presented in the following, where at the top, we numbered the columns and gave a short description of the parameters in the respective column:

1	Size of A parallel to the incident beam in nm.
2	Size of A perpendicular to the incident beam in nm.
3	Grid spacing in A parallel to the incident beam.
4	Grid spacing in A perpendicular to the incident beam.
5	Incident angle α in °.
6	Nanowire number density ρ_{NW} in nm^{-2}.
7	Beam divergence in °.
8	Initial nanowire radius at substrate r_0^{NW} in nm.
9	Final nanowire radius at substrate $r_{f,b}^{NW}$ in nm.
10	Final nanowire radius at tip $r_{f,t}^{NW}$ in nm.
11	Final nanowire height h_f^{NW} in nm.
12	Crystallite number density ρ_{cry} in nm^{-2}.
13	Initial crystallite radius r_0^{cry} in nm.
14	Final crystallite radius r_f^{cry} in nm.
15	Initial crystallite height h_0^{cry} in nm.
16	Final crystallite height h_f^{cry} in nm.
17	Transmittance (factor by which the shadowing is decreased).
18	Minimum nanowire length in nm.
19	Maximum nanowire length in nm.
20	Number of simulation points t_i.
21	Number of simulation repetitions j.
22	Filename of *phase fraction file*.
23	(optional) Filename of *intensity file*.

```
500000 50000 500 50 0.6 1.0e-6 0.0 15 17 25 3000 4.0e-6 15 30 0 100 0.0 0 3000 100 5 PhFr1.dat 1.txt
500000 50000 500 50 0.6 1.0e-6 0.0 15 17 25 3000 4.0e-6 15 30 0 100 0.0 0 3000 100 5 PhFr1.dat 2.txt
500000 50000 500 50 0.6 1.0e-6 0.0 15 17 25 3000 4.0e-6 15 30 0 100 0.0 0 3000 100 5 PhFr2.dat 3.txt
500000 50000 500 50 0.6 1.0e-6 0.0 15 17 25 3000 4.0e-6 15 30 0 100 0.0 0 3000 100 5 PhFr2.dat 4.txt
  .      .     .  .  .     .     .  .  .  .    .     .    .  .  .   .   .  .    .   .  .       .
  .      .     .  .  .     .     .  .  .  .    .     .    .  .  .   .   .  .    .   .  .       .
  .      .     .  .  .     .     .  .  .  .    .     .    .  .  .   .   .  .    .   .  .       .
```

The *listfile* contains the parameter set for each simulated curve. Besides the shape evolution of both ensembles, we can assign each line a different evolution of phase fractions to simulate the intensity evolution. The phase fractions are again given in separate *phase fraction files* with the filenames given in column number 22. The *phase fraction files* have two columns, the first one gives a growth time, which act as the anchor value and the second one gives the phase fraction. These anchor values are interpolated in the programme according to the polynomial function in the *config file* to assign each slice k a certain phase fraction. In the following, we show two examples of the *phase fraction file*:

Example 1

`PhFr1.dat`

```
1.0    0.76
2.0    0.75
3.0    0.64
4.0    0.62
5.0    0.60
6.0    0.55
7.0    0.52
8.0    0.44
9.0    0.38
10.0   0.24
11.0   0.20
13.0   0.19
15.0   0.18
17.0   0.15
19.0   0.10
21.0   0.08
23.0   0.04
25.0   0.02
27.0   0.00
29.0   0.00
30.0   0.00
```

Example 2

`PhFr2.dat`

```
1.0    0.90
4.0    0.85
3.0    0.80
4.0    0.75
5.0    0.70
6.0    0.68
7.0    0.66
8.0    0.64
9.0    0.62
10.0   0.60
11.0   0.50
13.0   0.40
15.0   0.30
17.0   0.20
19.0   0.10
21.0   0.00
23.0   0.00
25.0   0.00
27.0   0.00
29.0   0.00
30.0   0.00
```

As result of the programme a file is generated, which contains the determined RMSD values between the experimental curves and each simulated intensity evolution, given by the parameters of each line. If in column 23 an entry is given, the time-resolved intensity evolution of the WZ intensity, the ZB intensity of the nanowires, the ZB intensity of the crystallites and the overall ZB intensity is additionally saved in the respective *intensity file* with the name given in the column 23.
On the following pages, the source code of the programme is given.

Main programme: rshadlist

```
!> main program.
!!
!! This program parses a configuration file and reads a list of parameters from a list file.
program rshadlist
    use :: types
    use :: config
    use :: analysis
    use :: utils
    implicit none
    integer :: i, u, numpar, ios
    character(len=200) :: conf_file
    character(len=:), allocatable :: list_file
    type(ConfigParameter), allocatable :: conf(:)
    type(AnalysisParameter) :: p
    type(SimulationParameter), allocatable :: parameters(:)
    real(rp), allocatable :: rmsd_wz(:), rmsd_zb(:), &
        rmsd_fraction(:), norm_factors(:)
    real(rp) :: free_path
    type(ConsoleLog) :: console_log
    type(FileLog) :: file_log, debug_log
#ifdef MPI
    !> MPI error code.
    integer :: ierr
    !> MPI rank.
    integer :: num
    !> MPI total size.
    integer :: total, total_recv
    !> MPI status.
    integer :: mpistat(MPI_STATUS_SIZE)
    integer :: mpi_range(2)
    integer :: mpi_step
    integer :: count, c
    logical, allocatable :: finished(:)
    real :: stime, lasttime
#endif
    call init_random()
    console_log%min_level = LOG_LEVEL_INFO
    call add_log_target(console_log)
#ifdef MPI
    call MPI_INIT(ierr)
    call MPI_COMM_RANK(MPI_COMM_WORLD, num, ierr)
    call MPI_COMM_SIZE(MPI_COMM_WORLD, total, ierr)
#endif
    conf_file = 'analysis.rshad'
    if (command_argument_count() > 0) then
        call get_command_argument(1, conf_file)
    end if
    call read_config_file(conf_file, conf)
    p%shadows = .true.
    p%crystal_correction = .true.
    p%polynom_order = 2
    p%weight_zb1 = 1.0
    p%weight_zb2 = 1.0
    p%norm_length = 1600.0
    p%growth_time = 60.0
    p%data_directory = '/home'
    p%sample = 'Si248_'
    p%name_zb1 = '220'
    p%name_zb2 = '311'
    p%name_wz = '103'
    p%nbins = 1000
    p%output_directory = 'output'
    p%absorption = 0
    p%integrated_fraction = .true.
    p%histogram_output = .false.
    p%wireposition_output = .false.
    list_file = 'list.txt'

    do i = 1,size(conf)
        select case (conf(i)%get_name())
        case ('use␣shadows')
            call conf(i)%get_value(p%shadows)
        case ('crystal␣correction')
```

```
            call conf(i)%get_value(p%crystal_correction)
        case ('weight␣ZB1')
            call conf(i)%get_value(p%weight_zb1)
        case ('weight␣ZB2')
            call conf(i)%get_value(p%weight_zb2)
        case ('normalization␣length')
            call conf(i)%get_value(p%norm_length)
        case ('growth␣time')
            call conf(i)%get_value(p%growth_time)
        case ('polynom_order')
            call conf(i)%get_value(p%polynom_order)
        case ('data␣directory')
            call conf(i)%get_value(p%data_directory)
        case ('sample␣prefix')
            call conf(i)%get_value(p%sample)
        case ('name␣ZB1')
            call conf(i)%get_value(p%name_zb1)
        case ('name␣ZB2')
            call conf(i)%get_value(p%name_zb2)
        case ('name␣WZ')
            call conf(i)%get_value(p%name_wz)
        case ('number␣of␣bins')
            call conf(i)%get_value(p%nbins)
        case ('output␣directory')
            call conf(i)%get_value(p%output_directory)
        case ('list␣file')
            call conf(i)%get_value(list_file)
        case ('free␣path')
            call conf(i)%get_value(free_path)
            p%absorption = 1./free_path
        case ('integrated␣fraction')
            call conf(i)%get_value(p%integrated_fraction)
        case ('histogram␣output')
            call conf(i)%get_value(p%histogram_output)
        case ('wireposition␣output')
            call conf(i)%get_value(p%wireposition_output)
        end select
    end do

#ifdef MPI
    if (num == 0) then
#endif
#ifndef RAM_CACHE
#ifndef NO_CACHE
    call system('mkdir␣cache')
#endif
#endif
    call system('mkdir␣'//trim(adjustl(p%output_directory)))
    file_log%filename = trim(adjustl(p%output_directory))//'/rshadlist.log'
    file_log%min_level = LOG_LEVEL_INFO
    call add_log_target(file_log)
    debug_log%filename = trim(adjustl(p%output_directory))//'/rshadlist_debug.log'
    debug_log%min_level = LOG_LEVEL_DEBUG
    call add_log_target(debug_log)
    call save_config(trim(adjustl(p%output_directory))//'/analysis.rshad')
#ifdef MPI
    ! TODO better syncronization
        do i = 1,total-1
            call MPI_Send(total, 1, MPI_INTEGER, i, 0, MPI_COMM_WORLD, ierr)
        end do
    else
        call MPI_Recv(total_recv, 1, MPI_INTEGER, 0, MPI_ANY_TAG, &
            MPI_COMM_WORLD, mpistat, ierr)
    endif
#endif
    open (file=list_file, action='read', newunit=u, status='old', iostat=ios)
    if (ios /= 0) then
        call log_message(LOG_LEVEL_CRITICAL, 'Error␣while␣opening␣list␣file.')
        close (u)
    end if
    numpar = 0
    do
        read (u, *, iostat=ios)
        if (ios /= 0) then
```

```
            exit
        end if
        numpar = numpar + 1
    end do
    if (numpar < 1) then
        call log_message(LOG_LEVEL_CRITICAL, 'No␣parameters␣found.')
    end if
    rewind u
    if (verify_version(u)) then
        numpar = numpar - 1
    end if
    allocate(parameters(numpar))
    do i = 1,numpar
        if (.not. parameters(i)%read_from_line(u)) then
            call log_message(LOG_LEVEL_CRITICAL, 'Error␣while␣parsing␣parameters.')
        end if
    end do
    close (u)
#ifdef MPI
    if (num == 0) then
#endif
    call print_info(trim(adjustl(p%output_directory))//'/info.txt')
#ifdef MPI
    end if
#endif

#ifdef MPI
    if (num == 0) then
        mpi_step = nint(real(numpar)/real(total - 1))
        mpi_range(2) = numpar
        mpi_range(1) = numpar - mpi_step + 1
        do i = total-1,2,-1
            call MPI_Send(mpi_range, 2, MPI_INTEGER, i, 0, MPI_COMM_WORLD, ierr)
            mpi_range = mpi_range - mpi_step
            mpi_range(1) = max(0, mpi_range(1))
            mpi_range(2) = max(0, mpi_range(2))
        end do
        mpi_range(1) = 1
        call MPI_Send(mpi_range, 2, MPI_INTEGER, i, 0, MPI_COMM_WORLD, ierr)
        count = 0
        call cpu_time(stime)
        allocate(finished(total-1))
        finished = .false.
        call sleep(1)
        call print_bar_time(0., bar_width, stime, force=.true.)
        do
            do i = 1,total-1
                if (finished(i)) then
                    cycle
                end if
                call MPI_Probe(i, MPI_ANY_TAG, MPI_COMM_WORLD, mpistat, ierr)
                call MPI_Recv(c, 1, MPI_INTEGER, i, MPI_ANY_TAG, MPI_COMM_WORLD, mpistat, ierr)
                if (c < 0) then
                    finished(i) = .true.
                else
                    count = count + c
                    call print_bar_time(real(count)/real(numpar), bar_width, stime, force=.true.)
                end if
            end do
            if (all(finished)) then
                exit
            end if
        end do
        call print_bar_time(1., bar_width, stime, force=.true.)
        print *
    else
        call MPI_Recv(mpi_range, 2, MPI_INTEGER, 0, MPI_ANY_TAG, MPI_COMM_WORLD, mpistat, ierr)
        print *, num, ':', mpi_range
        call get_rmsd(p, parameters, rmsd_wz, rmsd_zb, rmsd_fraction, norm_factors, &
            start=mpi_range(1), end=mpi_range(2), bar=.false.)
    end if
#else
    call get_rmsd(p, parameters, rmsd_wz, rmsd_zb, rmsd_fraction, norm_factors)
#endif
```

```
#ifdef MPI
    if (num == 0) then
        allocate(rmsd_wz(1:numpar), rmsd_zb(1:numpar), rmsd_fraction(1:numpar), norm_factors(1:numpar))
        do i = 1,total-1
            call MPI_Send(total, 1, MPI_INTEGER, i, 0, MPI_COMM_WORLD, ierr)
            call MPI_Recv(mpi_range, 2, MPI_INTEGER, i, MPI_ANY_TAG, MPI_COMM_WORLD, mpistat, ierr)
            call MPI_Recv(rmsd_wz(mpi_range(1):mpi_range(2)), mpi_range(2) - mpi_range(1) + 1, &
                MPI_RP, i, MPI_ANY_TAG, MPI_COMM_WORLD, mpistat, ierr)
            call MPI_Recv(rmsd_zb(mpi_range(1):mpi_range(2)), mpi_range(2) - mpi_range(1) + 1, &
                MPI_RP, i, MPI_ANY_TAG, MPI_COMM_WORLD, mpistat, ierr)
            call MPI_Recv(rmsd_fraction(mpi_range(1):mpi_range(2)), mpi_range(2) - mpi_range(1) + 1, &
                MPI_RP, i, MPI_ANY_TAG, MPI_COMM_WORLD, mpistat, ierr)
            call MPI_Recv(norm_factors(mpi_range(1):mpi_range(2)), mpi_range(2) - mpi_range(1) + 1, &
                MPI_RP, i, MPI_ANY_TAG, MPI_COMM_WORLD, mpistat, ierr)
        end do
    else
        call MPI_Recv(total_recv, 1, MPI_INTEGER, 0, MPI_ANY_TAG, MPI_COMM_WORLD, mpistat, ierr)
        call MPI_Send(mpi_range, 2, MPI_INTEGER, 0, 0, MPI_COMM_WORLD, ierr)
        call MPI_Send(rmsd_wz(mpi_range(1):mpi_range(2)), mpi_range(2) - mpi_range(1) + 1, &
            MPI_RP, 0, 0, MPI_COMM_WORLD, ierr)
        call MPI_Send(rmsd_zb(mpi_range(1):mpi_range(2)), mpi_range(2) - mpi_range(1) + 1, &
            MPI_RP, 0, 0, MPI_COMM_WORLD, ierr)
        call MPI_Send(rmsd_fraction(mpi_range(1):mpi_range(2)), mpi_range(2) - mpi_range(1) + 1, &
            MPI_RP, 0, 0, MPI_COMM_WORLD, ierr)
        call MPI_Send(norm_factors(mpi_range(1):mpi_range(2)), mpi_range(2) - mpi_range(1) + 1, &
            MPI_RP, 0, 0, MPI_COMM_WORLD, ierr)
    end if
    if (num == 0) then
#endif
    open (newunit=u, file=trim(adjustl(p%output_directory))//'/rmsd.txt')
    do i = 1,numpar
        write (u, *) parameters(i)%grid%sx, parameters(i)%grid%sy, parameters(i)%grid%dx, &
            parameters(i)%grid%dy, parameters(i)%alpha/deg, parameters(i)%density, &
            parameters(i)%divergence/deg, parameters(i)%r0, parameters(i)%rb, parameters(i)%rt, parameters(i)%
                Lf, &
            parameters(i)%cry_density, parameters(i)%cry_ri, parameters(i)%cry_rf, parameters(i)%cry_hi, &
            parameters(i)%cry_hf, parameters(i)%transm, parameters(i)%lengths%min_val, parameters(i)%lengths%
                max_val, &
            parameters(i)%lengths%n_val, parameters(i)%nrep, trim(adjustl(parameters(i)%fraction)), &
            rmsd_wz(i), rmsd_zb(i), rmsd_fraction(i), norm_factors(i)
    end do
    close (u)
    call write_endtime(trim(adjustl(p%output_directory))//'/info.txt')
#ifdef KEEP_OPEN
    print *, 'Finished. Press return to close ...'
    read *
#endif
#ifdef MPI
    end if
    call MPI_FINALIZE(ierr)
#endif
contains
    !> Save configuration to a text file.
    !! This routine uses the variables used in the main program.
    subroutine save_config(filename)
        !> Filename of configuration file.
        character(len=*), intent(in) :: filename
        type(ConfigParameter) :: par
        integer :: u
        open (file=filename, newunit=u)
        call par%init('use shadows', p%shadows)
        call par%write(u)
        call par%init('crystal correction', p%crystal_correction)
        call par%write(u)
        call par%init('polynom order', p%polynom_order)
        call par%write(u)
        call par%init('weight ZB1', p%weight_zb1)
        call par%write(u)
        call par%init('weight ZB2', p%weight_zb2)
        call par%write(u)
        call par%init('normalization length', p%norm_length)
        call par%write(u)
        call par%init('growth time', p%growth_time)
```

```
        call par%write(u)
        call par%init('free path', 1./p%absorption)
        call par%write(u)
        call par%init('data directory', p%data_directory)
        call par%write(u)
        call par%init('sample prefix', p%sample)
        call par%write(u)
        call par%init('name ZB1', p%name_zb1)
        call par%write(u)
        call par%init('name ZB2', p%name_zb2)
        call par%write(u)
        call par%init('name WZ', p%name_wz)
        call par%write(u)
        call par%init('number of bins', p%nbins)
        call par%write(u)
        call par%init('output directory', p%output_directory)
        call par%write(u)
        call par%init('list file', list_file)
        call par%write(u)
        call par%init('integrated fraction', p%integrated_fraction)
        call par%write(u)
        call par%init('histogram output', p%histogram_output)
        call par%write(u)
        call par%init('wireposition output', p%wireposition_output)
        call par%write(u)
        close(u)
    end subroutine save_config
end program rshadlist
```

Module: analysis

```
!> Module for analysis functions.
module analysis
    use :: const
    use :: utils
    use :: shadow
    use :: types
    use, intrinsic :: iso_fortran_env
    implicit none
    private
    public :: get_hist, get_intensities, interpolate
    public :: polynom_fit, get_experimental_data, get_rmsd
    logical :: frac_neg_warning_shown = .false.
    logical :: frac_big_warning_shown = .false.
#ifdef RAM_CACHE
    !> List of hashs of parameters in cache.
    type(ParameterHash), allocatable :: hash_list(:)
    !> Element in cache list.
    !! This is needed for a list of histograms of different lengths.
    type :: CacheElement
        !> Histogram.
        real(rp), allocatable :: histogram(:)
    end type

    !> List of cached histograms.
    type(CacheElement), allocatable :: cache_list(:)
#endif
contains
    !> Calculate histogram from shadow height list.
    !! This function calculates a shadowing histogram from a list of shadow heigts as it is generated by shadow
        ::calc_height. The histogram is integrated as it contains the fraction or number (depending on the
        normalize parameter) of wires which are shadowed at a certain height.
    !! \see shadow::calc_height
    subroutine get_hist(data, bin_edges, res, normalize)
        !> Shadow height list.
        real(rp), allocatable, intent(in) :: data(:)
        !> Bin edges for histogram.
        type(RealRange), intent(in) :: bin_edges
        !> Resulting histogram.
        real(rp), allocatable, intent(out) :: res(:)
        !> Normalize histogram.
        !! If this is set, the histogram is divided by the number of wires,
        !! otherwise it contains raw numbers.
        logical, optional, intent(in) :: normalize
```

```
    integer :: i, j
    logical :: norm
    norm = .false.
    if (present(normalize)) then
        norm = normalize
    end if
    allocate(res(bin_edges%n_val - 1))
    res = 0
    do i = 1,size(data)
        do j = 1,bin_edges%n_val-1
            if (data(i) > 0) then
                ! Look for wires for which the shadow ends higher that the
                ! current bin.
                if (data(i) > bin_edges%index(j)) then
                    res(j) = res(j) + 1
                end if
            end if
        end do
    end do
    if (norm) then
        res = res/size(data)
    end if
end subroutine get_hist

!> Fit polynom on list of data points.
function polynom_fit(x, y, order) result(res)
    !> x values of points.
    real(rp), intent(in) :: x(:)
    !> y values of points.
    real(rp), intent(in) :: y(:)
    !> Order of polynom.
    integer, intent(in) :: order
    !> Resulting coefficients.
    real(rp), allocatable :: res(:)
    integer :: n, i, info
    ! M is matrix for linear system, V is Vandermonde matrix, b is the inhomogenity
    real(rp), allocatable :: M(:,:), V(:,:), b(:)
    integer, allocatable :: ipiv(:)
    if (size(x) /= size(y)) then
        call log_message(LOG_LEVEL_CRITICAL, "Fit error: input arrays have to be of same size.")
    end if
    n = size(x)
    allocate(V(n, order + 1))
    do i = 0,order
        V(:,i + 1) = x**i
    end do
    M = matmul(transpose(V), V)
    allocate(b(order + 1))
    do i = 0,order
        b(i + 1) = sum(x**i * y)
    end do
    allocate(ipiv(order + 1))
    if (rp == real64) then
        call dgesv(order + 1, 1, M, order + 1, ipiv, b, order + 1, info)
    elseif (rp == real32) then
        call sgesv(order + 1, 1, M, order + 1, ipiv, b, order + 1, info)
    else
        call log_message(LOG_LEVEL_CRITICAL, 'Unsupported real kind. Only 32 and 64 bit are supported for
            fitting.')
    end if
    if (info /= 0) then
        call log_message(LOG_LEVEL_CRITICAL, "Fit error: Parameters could not be computed.")
    end if
    allocate(res(order + 1))
    res = b
end function polynom_fit

!> Evaluate polynomial at given points.
!! \return Value of polynomial at points x.
function polynom(x, coeff) result(y)
    !> x values.
    real(rp), intent(in) :: x(:)
    !> Coefficients.
    real(rp), intent(in) :: coeff(:)
```

```
    integer :: i
    real(rp), allocatable :: y(:)
    allocate(y(size(x)))
    y = 0
    do i = 0,size(coeff) - 1
        y = y + coeff(i + 1)*x**i
    end do
end function polynom

!> Calculate the gradient of points given by x and y values.
!! For the calculation first order centered finite differences are used:
!! \f[ \nabla y(x)\big|_{x=x_i} \approx \frac{y_{i+1} - y_{i-1}}{x_{i+1} - x_{i-1}} \f]
!! For the first and last value one sided differences are used:
!! \f{eqnarray*}{
!!      \nabla y(x)\big|_{x=x_1} &\approx& \frac{y_2 - y_1}{x_2 - x_1} \\
!!      \nabla y(x)\big|_{x=x_n} &\approx& \frac{y_n - y_{n-1}}{x_n - x_{n-1}}
!! \f}
function gradient(x, y) result(res)
    !> x values.
    real(rp), intent(in) :: x(:)
    !> y values.
    real(rp), intent(in) :: y(:)
    !> Gradient.
    real(rp), allocatable :: res(:)
    integer :: i, n
    if (size(x) /= size(y)) then
        call log_message(LOG_LEVEL_CRITICAL, "Gradient error: input arrays have to be of same size.")
    end if
    n = size(x)
    allocate(res(n))
    res(1) = (y(2) - y(1))/(x(2) - x(1))
    do i = 2,n - 1
        res(i) = (y(i + 1) - y(i - 1))/(x(i + 1) - x(i - 1))
    end do
    res(n) = (y(n) - y(n - 1))/(x(n) - x(n - 1))
end function gradient

!> Calculate differential fraction from integrated fraction.
!! This is given by (see also the algorithm part in the manual):
!! \f{eqnarray*}{
!!    f_\mathrm{WZ}(l,L) &=& \frac{1}{\pi r(l,L)^2}\frac{\partial}{\partial l} \left(
!!            V(l,L) F_\mathrm{WZ,exp}(l) \right) \\
!!    r(l,L) &=& r_0 + (r_\mathrm{t} - r_\mathrm{b})\frac{l}{L_\mathrm{f}} + (r_\mathrm{b} - r_0)\frac{L}{
     L_\mathrm{f}} \\
!!    V(l,L) &=& \frac{\pi L_\mathrm{f}}{3(r_\mathrm{t} - r_\mathrm{b})}\left( r(l,L)^3 - r(0,L)^3 \right)
!!\f}
function get_differential_fraction(x, L, fraction, anaparam, param) result(res)
    !> Height values.
    real(rp), intent(in) :: x(:)
    !> Integrated WZ fraction.
    real(rp), intent(in) :: fraction(:,:)
    !> Length of the wire.
    real(rp), intent(in) :: L
    !> Analysis parameters.
    class(AnalysisParameter), intent(in) :: anaparam
    !> Simulation parameters.
    class(SimulationParameter), intent(in) :: param
    !> Differential WZ fraction.
    real(rp), allocatable :: res(:)
    real(rp), allocatable :: coeff(:), fracint(:), rtap(:), V(:)
    real(rp) :: r0
    if (anaparam%polynom_order >= 0) then
        coeff = polynom_fit(fraction(:,1), fraction(:,2), anaparam%polynom_order)
        fracint = polynom(x, coeff)
    else
        fracint = interpolate(x, fraction(:,1), fraction(:,2))
    end if
    rtap = radius(x, L, param%r0, param%rb, param%rt, param%Lf)
    r0 = radius(0._rp, L, param%r0, param%rb, param%rt, param%Lf)
    V = pi*(param%Lf/(3._rp*(param%rt - param%rb)))*(rtap**3 - r0**3)
    allocate(res(size(x)))
    res = 0
    where (fracint*V /= 0)
        res = gradient(x, fracint*V)/(pi*rtap**2)
```

```
        end where
    end function get_differential_fraction
    elemental function eff_area(r, f) result(res)
        real(rp), intent(in) :: r, f
        real(rp) :: res, a
        if (f == 0) then
            res = 0.5_rp*pi*r**2
        else
            a = r
            res = (sqrt(3._rp) + (-sqrt(3._rp) + 3._rp*a*f*(-1._rp + sqrt(3._rp)*a*f))/exp(sqrt(3._rp)*a*f))
                /(3._rp*f**2)
        end if
    end function eff_area

    !> Calculate intentsities for given parameters.
    !! Those are given by (see also the algorithm section in the manual):
    !! \f{eqnarray*}{
    !! I_\mathrm{WZ}^\mathrm{RHEED}(L) &=& \int\limits_0^L\!\mathrm{d}l\,A(l,L)f_\mathrm{WZ}(l,L)s(l,L) \\
    !! I_\mathrm{ZB}^\mathrm{RHEED}(L) &=& \int\limits_0^L\!\mathrm{d}l\,(A(l,L)+A_\mathrm{cry}(l))(1-f_\mathrm
        {WZ}(l,L))s(l,L)\\
    !! I_\mathrm{WZ,sim}^\mathrm{XRAY}(L) &=& \int\limits_0^L\!\mathrm{d}l\,A(l,L)f_\mathrm{WZ}(l,L)\\
    !! I_\mathrm{ZB,sim}^\mathrm{XRAY}(L) &=& \int\limits_0^L\!\mathrm{d}l\,(A(l,L)+A_\mathrm{cry}(l))(1-f_\
        mathrm{WZ}(l,L))\\
    !! I_\mathrm{WZ,sim}^\mathrm{XRAY,CC}(L) &=& \int\limits_0^L\!\mathrm{d}l\,A(l,L)f_\mathrm{WZ}(l,L)\\
    !! I_\mathrm{ZB,sim}^\mathrm{XRAY,CC}(L) &=& \int\limits_0^L\!\mathrm{d}l\,A(l,L)(1-f_\mathrm{WZ}(l,L))\\
    !! A(l,L) &=& \pi r(l,L)^2
    !! \f}
    subroutine get_intensities(fraction, simparam, anaparam, wz, zb, bar, zb_wire, zb_cry)
        !> Integrated experimental WZ fraction.
        real(rp), intent(in) :: fraction(:,:)
        !> Simulation parameters.
        type(SimulationParameter), intent(in) :: simparam
        !> Analysis parameters.
        type(AnalysisParameter), intent(in) :: anaparam
        !> WZ intensity.
        real(rp), allocatable, intent(out) :: wz(:)
        !> ZB intensity.
        real(rp), allocatable, intent(out) :: zb(:)
        !> Display progressbar.
        logical, optional, intent(in) :: bar
        !> ZB intensity of wires.
        real(rp), optional, allocatable, intent(out) :: zb_wire(:)
        !> ZB intensity of crystallites.
        real(rp), optional, allocatable, intent(out) :: zb_cry(:)
        real(rp), allocatable :: result(:), single_histogram(:), histogram(:)
        real(rp) :: cry_r, cry_h, l, mean_radius
        integer :: nbins, num_lengths
        real(rp), allocatable :: frac(:), lbins(:), A(:), A_crys(:)
        type(RealRange) :: bin_edges
        type(monowire) :: r
        integer :: i, j
        real :: stime
        integer :: cache_index, ios, u
        character(len=200) :: iomsg
        logical :: showbar, cache_exists
        type(ParameterHash) :: hash
        character(len=20) :: hash_string
        character(len=1000) :: histogram_folder, histogram_file
        character(len=1000) :: wireposition_folder, wireposition_file
        real(rp), allocatable :: outputwire(:,:)
#ifdef RAM_CACHE
        type(CacheElement), allocatable :: tmp_cache_list(:)
        type(ParameterHash), allocatable :: tmp_hash_list(:)
#endif
        if (size(fraction, 2) /= 2) then
            call log_message(LOG_LEVEL_CRITICAL, 'Wrong␣number␣of␣columns␣of␣fraction␣parameter.')
        end if
        showbar = .true.
        if (present(bar)) then
            showbar = bar
        end if
        num_lengths = simparam%lengths%n_val
        cache_index = 0
        iomsg = ''
```

```
        call cpu_time(stime)
        allocate(wz(num_lengths), zb(num_lengths))
        if (present(zb_wire)) then
            allocate(zb_wire(num_lengths))
        end if
        if (present(zb_cry)) then
            allocate(zb_cry(num_lengths))
        end if
        ! Output histogram.
        if (anaparam%shadows) then
            if (allocated(simparam%filename)) then
                if (len(simparam%filename) > 0) then
                    if (anaparam%histogram_output) then
                        histogram_folder = trim(adjustl(anaparam%output_directory))//'/' &
                            //trim(adjustl(simparam%filename))//'_histogram'
                        call system('mkdir␣'//trim(adjustl(histogram_folder)))
                    end if
                    if (anaparam%wireposition_output) then
                        wireposition_folder = trim(adjustl(anaparam%output_directory))//'/' &
                            //trim(adjustl(simparam%filename))//'_wireposition'
                        call system('mkdir␣'//trim(adjustl(wireposition_folder)))
                    end if
                end if
            end if
        end if
#ifdef RAM_CACHE
!$omp parallel do private(l,hash,hash_string,bin_edges,nbins,lbins,mean_radius,histogram, &
!$omp& single_histogram,frac,u,ios,iomsg,A,A_crys,cry_r,cry_h,cache_exists, &
!$omp& result, tmp_cache_list,tmp_hash_list,j,cache_index,r,num_lengths,outputwire)
#else
!$omp parallel do private(l,hash,hash_string,bin_edges,nbins,lbins,mean_radius,histogram, &
!$omp& single_histogram,frac,u,ios,iomsg,A,A_crys,cry_r,cry_h,cache_exists,result,j, &
!$omp& cache_opened, cache_index,r,num_lengths,outputwire)
#endif
        do i = 1,num_lengths
            if (showbar) then
                call print_bar_time(real(i-1)/real(num_lengths), bar_width, stime)
            end if
            l = simparam%lengths%index(i)

            ! Get hash of current parameter set.
            hash = simparam%hist_hash()
            call hash%add(l)
            hash_string = hash%get_string()
#ifndef NO_CACHE
#ifdef RAM_CACHE
!$omp critical
            if (allocated(cache_list)) then
                cache_exists = .false.
                do cache_index = 1,size(cache_list)
                    if (all(hash%data == hash_list(cache_index)%data)) then
                        cache_exists = .true.
                        exit
                    end if
                end do
            else
                allocate(cache_list(1))
                allocate(hash_list(1))
                cache_exists = .false.
            end if
!$omp end critical
#else
            inquire(file='cache/'//hash_string//'.txt', exist=cache_exists)
#endif
#else
            cache_exists = .false.
#endif
            ! Get fraction and prepare variables.
            bin_edges%min_val = 0._rp
            bin_edges%max_val = 1
            bin_edges%n_val = anaparam%nbins
            nbins = bin_edges%n_val - 1
            lbins = bin_edges%get_center_list()
            if (anaparam%integrated_fraction) then
```

```
                frac = get_differential_fraction(lbins, l, fraction, anaparam, simparam)
            else
                frac = interpolate(lbins, fraction(:, 1), fraction(:, 2))
            end if
            if (.not. frac_neg_warning_shown) then
                if (any(frac < 0)) then
                    call log_message(LOG_LEVEL_WARNING, 'WZ␣fraction␣negative.')
                    frac_neg_warning_shown = .true.
                end if
            end if
            if (.not. frac_big_warning_shown) then
                if (any(frac > 1)) then
                    call log_message(LOG_LEVEL_WARNING, 'WZ␣fraction␣too␣big.')
                    frac_big_warning_shown = .true.
                end if
            end if
            mean_radius = 0.5_rp*( &
                    radius(l, l, simparam%r0, simparam%rb, simparam%rt, simparam%Lf) &
                    + radius(0._rp, l, simparam%r0, simparam%rb, simparam%rt, simparam%Lf) &
                )
            call r%init(l, 2._rp*mean_radius)
            ! Calculate histogram only for RHEED and use cached histogram if available.
            if (anaparam%shadows) then
                if (allocated(histogram)) then
                    deallocate(histogram)
                end if
                allocate(histogram(bin_edges%n_val - 1))
                if (cache_exists) then
#ifdef RAM_CACHE
                    histogram = cache_list(cache_index)%histogram
#else
                    open (newunit=u, file='cache/'//hash_string//'.txt', iostat=ios, iomsg=iomsg)
                    if (ios /= 0) then
                        call log_message(LOG_LEVEL_CRITICAL, 'Error␣while␣opening␣cache␣file.␣'//trim(adjustl(
                            iomsg)))
                    end if
                    read (u, *, iostat=ios, iomsg=iomsg) histogram
                    if (ios /= 0) then
                        call log_message(LOG_LEVEL_CRITICAL, 'Error␣while␣reading␣cache␣file.␣'//trim(adjustl(
                            iomsg)))
                    end if
                    close (u)
#endif
                else
                    histogram = 0
                    do j = 1,simparam%nrep
                        if (anaparam%wireposition_output) then
                            if (allocated(simparam%filename)) then
                                if (len(simparam%filename) > 0) then
                                    call calc_height(simparam%alpha, simparam%density, r, simparam%grid, result
                                        , simparam%divergence, outputwire)
                                else
                                    call calc_height(simparam%alpha, simparam%density, r, simparam%grid, result
                                        , simparam%divergence)
                                end if
                            end if
                        else
                            call calc_height(simparam%alpha, simparam%density, r, simparam%grid, result,
                                simparam%divergence)
                        end if
                        call get_hist(result, bin_edges, single_histogram, normalize=.true.)
                        histogram = histogram + single_histogram
                    end do
                    histogram = histogram/real(simparam%nrep)
#ifndef NO_CACHE
#ifdef RAM_CACHE
!$omp critical
                    allocate(tmp_cache_list(size(cache_list) + 1))
                    allocate(tmp_hash_list(size(hash_list) + 1))
                    tmp_cache_list(1:size(cache_list)) = cache_list
                    tmp_hash_list(1:size(hash_list)) = hash_list
                    deallocate(hash_list, cache_list)
                    tmp_cache_list(size(tmp_cache_list))%histogram = histogram
                    tmp_hash_list(size(tmp_hash_list)) = hash
```

```
                    cache_list = tmp_cache_list
                    hash_list = tmp_hash_list
                    deallocate(tmp_cache_list, tmp_hash_list)
!$omp end critical
#else
                    open (newunit=u, file='cache/'//hash_string//'.txt', iostat=ios, iomsg=iomsg)
                    if (ios /= 0) then
                        call log_message(LOG_LEVEL_CRITICAL, 'Error while opening cache file. '//trim(adjustl(
                            iomsg)))
                    end if
                    write (u, *) histogram
                    close (u)
                    open (newunit=u, file='cache/'//hash_string//'.txt', iostat=ios, iomsg=iomsg)
                    read (u, *, iostat=ios, iomsg=iomsg) histogram
                    close(u)
#endif
#endif
                end if
                if (allocated(simparam%filename)) then
                    if (len(simparam%filename) > 0) then
                        if (anaparam%histogram_output) then
                            write (histogram_file, '(A,I8.8,A)') trim(adjustl(histogram_folder))//'/', &
                                nint(1000*l), '.txt'
                            open (newunit=u, file=trim(adjustl(histogram_file)), iostat=ios, iomsg=iomsg)
                            if (ios /= 0) then
                                call log_message(LOG_LEVEL_CRITICAL, 'Error while opening histogram file. '//
                                    trim(adjustl(iomsg)))
                            end if
                            do j = 1,nbins
                                write (u, *) bin_edges%index(j), histogram(j)
                            end do
                            close (u)
                        end if
                        if (anaparam%wireposition_output) then
                            write (wireposition_file, '(A,I8.8,A)') trim(adjustl(wireposition_folder))//'/', &
                                nint(1000*l), '.txt'
                            open (newunit=u, file=trim(adjustl(wireposition_file)), iostat=ios, iomsg=iomsg)
                            if (ios /= 0) then
                                call log_message(LOG_LEVEL_CRITICAL, 'Error while opening wire position file. '
                                    &
                                    //trim(adjustl(iomsg)))
                            end if
                            do j = 1,size(outputwire,2)
                                write (u, *) outputwire(:,j)
                            end do
                            close (u)
                        end if

                    end if
                end if
            end if

            ! Current crystallite dimensions.
            cry_r = simparam%cry_ri + l*(simparam%cry_rf - simparam%cry_ri)/simparam%Lf
            cry_h = simparam%cry_hi + l*(simparam%cry_hf - simparam%cry_hi)/simparam%Lf
            allocate(A_crys(nbins))
            A_crys = 0
            where (lbins <= cry_h)
                A_crys = (simparam%cry_density/simparam%density) * &
                    eff_area(cry_r, anaparam%absorption)
            end where
            A = eff_area(radius(lbins, l, simparam%r0, simparam%rb, simparam%rt, simparam%Lf), anaparam%
                absorption)

            ! Calculate intensities.
            if (anaparam%shadows) then
                wz(i) = (l/real(nbins))*sum(A*frac*(1 - (1 - simparam%transm)*histogram))
                zb(i) = (l/real(nbins))*sum((A*(1 - frac) + A_crys)*(1 - (1 - simparam%transm)*histogram))
                if (present(zb_wire)) then
                    zb_wire(i) = (l/real(nbins))*sum(A*(1 - frac)*(1 - (1 - simparam%transm)*histogram))
                end if
                if (present(zb_cry)) then
                    zb_cry(i) = (l/real(nbins))*sum(A_crys*(1 - (1 - simparam%transm)*histogram))
                end if
```

```
            else
                wz(i) = (1/real(nbins))*sum(A*frac)
                if (anaparam%crystal_correction) then
                    zb(i) = (1/real(nbins))*sum(A*(1 - frac))
                else
                    zb(i) = (1/real(nbins))*sum(A*(1 - frac) + A_crys)
                end if
                if (present(zb_wire)) then
                    zb_wire(i) = (1/real(nbins))*sum(A*(1 - frac))
                end if
                if (present(zb_cry)) then
                    zb_cry(i) = (1/real(nbins))*sum(A_crys)
                end if
            end if
            deallocate(A_crys)
        end do
        if (showbar) then
            call print_bar_time(1., bar_width, stime, force=.true.)
            print *
        end if
    end subroutine get_intensities

    !> Calculate RMSD for given parameters.
    !! For the intensity calculation \link get_intensities \endlink is called. The experimental intensities are
        interpolated and the weighted sum is used to calculate the RMSD values (see also the algorithm
        section in the manual):
    !! \f{eqnarray*}{
    !! d_\mathrm{WZ} &=& \frac{1}{N_{L,\mathrm{sim}}} \sqrt{\sum\limits_{L\in\{L_\mathrm{sim}\}} \left(I_\
        mathrm{WZ,sim}(L) - f_\mathrm{norm}I_\mathrm{WZ,exp}^\mathrm{interp}(L)\right)^2}\\
    !! d_\mathrm{ZB} &=& \frac{1}{N_{L,\mathrm{sim}}} \sqrt{\sum\limits_{L\in\{L_\mathrm{sim}\}} \left(I_\
        mathrm{ZB,sim}(L) - f_\mathrm{norm}I_\mathrm{ZB,exp}^\mathrm{interp}(L) \right)^2}\\
    !! d_\mathrm{frac} &=& \frac{1}{N_{L,\mathrm{sim}}} \sqrt{\sum\limits_{L\in\{L_\mathrm{sim}\}} \left(F_\
        mathrm{WZ,sim}(L) - F_\mathrm{WZ,exp}^\mathrm{interp}(L) \right)^2}\\
    !! I_\mathrm{ZB,exp} &=&
    !! \widetilde{w}_{\mathrm{ZB},1}I_{\mathrm{ZB},1,\mathrm{exp}} + \widetilde{w}_{\mathrm{ZB},2}I_{\mathrm{ZB
        },2,\mathrm{exp}}\\
    !! \widetilde{w}_{\mathrm{ZB},i} &=& 2\frac{w_{\mathrm{ZB},i}}{w_{\mathrm{ZB},1} + w_{\mathrm{ZB},2} }\,.
    !! \f}
    !! Also the calculation can be restricted to a range of indices. This is used by the MPI version to
        distribute the calculation.
    subroutine get_rmsd(anaparam, simparams, rmsd_wz, rmsd_zb, &
        rmsd_fraction, norm_factors, start, end, bar)
        !> Analysis parameters.
        class(AnalysisParameter), intent(in) :: anaparam
        !> List of simulation parameters.
        class(SimulationParameter), intent(in) :: simparams(:)
        !> RMSD value for WZ.
        real(rp), allocatable, intent(out) :: rmsd_wz(:)
        !> RMSD value for ZB.
        real(rp), allocatable, intent(out) :: rmsd_zb(:)
        !> RMSD value for WZ fraction.
        real(rp), allocatable, intent(out) :: rmsd_fraction(:)
        !> Normalization factors.
        real(rp), allocatable, intent(out) :: norm_factors(:)
        !> Start index in list.
        integer, intent(in), optional :: start
        !> End index in list.
        integer, intent(in), optional :: end
        !> Progressbar.
        logical, intent(in), optional :: bar
        real(rp), allocatable :: zb(:), wz(:), fraction(:), zb_inter(:), wz_inter(:), fraction_inter(:)
        real(rp), allocatable :: zb_exp(:,:), zb1_exp(:,:), zb2_exp(:,:), wz_exp(:,:), fraction_exp(:,:)
        real(rp), allocatable :: zb_wire(:), zb_cry(:), input_fraction(:,:)
        integer :: i, numpar, j, u, parcount, start_local, end_local
        real(rp) :: weight_zb1, weight_zb2, factor
        real(rp), allocatable :: lengths(:)
        real :: stime
        logical :: showbar
#ifdef MPI
        integer :: num, ierr, c, total
        real :: lasttime, now
        integer :: mpistat(MPI_STATUS_SIZE)
        call MPI_COMM_RANK(MPI_COMM_WORLD, num, ierr)
        call MPI_COMM_SIZE(MPI_COMM_WORLD, total, ierr)
```

```
        c = 0
        lasttime = 0
#endif
        showbar = .true.
        if (present(bar)) then
            showbar = bar
        end if
        ! Normalize weights.
        weight_zb1 = 2.*anaparam%weight_zb1/(anaparam%weight_zb1 + anaparam%weight_zb2)
        weight_zb2 = 2.*anaparam%weight_zb2/(anaparam%weight_zb1 + anaparam%weight_zb2)
        call cpu_time(stime)
        numpar = size(simparams)
        allocate(rmsd_zb(numpar), rmsd_wz(numpar), rmsd_fraction(numpar), norm_factors(numpar))
        parcount = 0
        start_local = 1
        end_local = numpar
        if (present(start)) then
            start_local = start
        end if
        if (present(end)) then
            end_local = end
        end if
        do i = start_local, end_local
#ifdef MPI
            call cpu_time(now)
            if (now > lasttime + 1) then
                call MPI_Send(c, 1, MPI_INTEGER, 0, 0, MPI_COMM_WORLD, ierr)
                c = 0
                lasttime = now
            end if
#endif
            call get_experimental_data(anaparam%data_directory, anaparam%sample, &
                anaparam%name_zb1, anaparam%name_zb2, anaparam%name_wz, anaparam%shadows, &
                anaparam%crystal_correction, simparams(i)%Lf/anaparam%growth_time, fraction_exp, zb1_exp,
                     zb2_exp, wz_exp)
            input_fraction = get_wz_fraction(simparams(i)%Lf/anaparam%growth_time, simparams(i)%fraction)
            if (showbar) then
                call print_bar_time(real(parcount)/real(numpar), bar_width, stime)
            end if
            allocate(zb_exp(size(zb1_exp, 1), 2))
            zb_exp(:,1) = zb1_exp(:,1)
            zb_exp(:,2) = weight_zb1*zb1_exp(:,2) + weight_zb2*interpolate(zb1_exp(:,1), zb2_exp(:,1), zb2_exp
                 (:,2))
            lengths = simparams(i)%lengths%get_list()
            call get_intensities(input_fraction, simparams(i), anaparam, wz, zb, bar=.false., zb_wire=zb_wire,
                 zb_cry=zb_cry)
            fraction = wz/(zb + wz)
            where (isnan(fraction))
                fraction = 0
            end where
            wz_inter = interpolate(lengths, wz_exp(:,1), wz_exp(:,2))
            zb_inter = interpolate(lengths, zb_exp(:,1), zb_exp(:,2))
            fraction_inter = wz_inter/(wz_inter + zb_inter)
            where (isnan(fraction_inter))
                fraction_inter = 0
            end where
            factor = norm_factor(anaparam%norm_length, wz_exp(:,1), wz_exp(:,2), lengths, wz)
            if (allocated(simparams(i)%filename)) then
                if (len(simparams(i)%filename) > 0) then
                    open (newunit=u, file=trim(adjustl(anaparam%output_directory))//'/'//trim(adjustl(simparams
                         (i)%filename)))
                    do j = 1,size(lengths)
                        write (u,*) lengths(j), factor*wz(j), factor*zb(j), fraction(j), factor*zb_wire(j),
                             factor*zb_cry(j)
                    end do
                    close (u)
                end if
            end if
            rmsd_wz(i) = sqrt(sum((wz_inter - factor*wz)**2)/size(wz_inter))
            rmsd_zb(i) = sqrt(sum((zb_inter - factor*zb)**2)/size(zb_inter))
            rmsd_fraction(i) = sqrt(sum((fraction_inter - fraction)**2)/size(fraction_inter))
            norm_factors(i) = factor
            parcount = parcount + 1
            deallocate(zb_exp)
```

```
#ifdef MPI
            c = c + 1
#endif
        end do
#ifdef MPI
        call MPI_Send(c, 1, MPI_INTEGER, 0, 0, MPI_COMM_WORLD, ierr)
        c = -1
        call MPI_Send(c, 1, MPI_INTEGER, 0, 0, MPI_COMM_WORLD, ierr)
#endif
        if (showbar) then
            call print_bar_time(1., bar_width, stime, force=.true.)
            print *
        end if
    end subroutine get_rmsd

    !> Calculate the Normalization factor. If a value less than zero is given for the reference x value, the
         Normalization is done for means of the data sets
    function norm_factor(x0, x1, y1, x2, y2) result(res)
        !> Reference x value.
        real(rp), intent(in) :: x0
        !> x values of first data set.
        real(rp), intent(in) :: x1(:)
        !> y values of first data set.
        real(rp), intent(in) :: y1(:)
        !> x values of second data set.
        real(rp), intent(in) :: x2(:)
        !> y values of second data set.
        real(rp), intent(in) :: y2(:)
        !> Normalization factor.
        real(rp) :: res
        real(rp) :: y01(1), y02(1)
        if ((size(x1) /= size(y1)) .or. (size(x2) /= size(y2))) then
            call log_message(LOG_LEVEL_ERROR, 'Normalization error: x and y must have identical lengths.')
        end if
        if (x0 < 0) then
            y01 = sum(y1)/real(size(x1))
            y02 = sum(y2)/real(size(x2))
        else
            y01 = interpolate([x0], x1, y1)
            y02 = interpolate([x0], x2, y2)
        end if
        res = y01(1)/y02(1)
    end function norm_factor

    !> Interpolate a set of x and y values.
    function interpolate(x, x0, y0) result(res)
        !> Evaluation points.
        real(rp), intent(in) :: x(:)
        !> x values.
        real(rp), intent(in) :: x0(:)
        !> y values.
        real(rp), intent(in) :: y0(:)
        !> Interpolated y values.
        real(rp), allocatable :: res(:)
        integer :: i, j
        if (size(x0) /= size(y0)) then
            call log_message(LOG_LEVEL_CRITICAL, 'Interpolation error: x0 and y0 must have identical lengths.')
        end if
        allocate(res(size(x)))
        outer: do i = 1,size(x)
            if (x0(1) > x(i)) then
                res(i) = y0(1)
                cycle
            end if
            j = 1
            do
                if (j == size(x0)) then
                    res(i) = y0(size(x0))
                    cycle outer
                end if
                if ((x0(j) <= x(i)) .and. (x0(j + 1) > x(i))) then
                    res(i) = y0(j) + (y0(j + 1) - y0(j))*(x(i) - x0(j))/(x0(j + 1) - x0(j))
                    cycle outer
                end if
```

```
            j = j + 1
        end do
    end do outer
end function interpolate

!> Tapered radius.
elemental real(rp) function radius(x, L, r0, rb, rt, Lf) result(res)
    !> Height.
    real(rp), intent(in) :: x
    !> Length of wire.
    real(rp), intent(in) :: L
    !> Initial radius.
    real(rp), intent(in) :: r0
    !> Final radius at the bottom
    real(rp), intent(in) :: rb
    !> Final radius at the top.
    real(rp), intent(in) :: rt
    !> Final length of the wire.
    real(rp), intent(in) :: Lf
    res = r0 + x*(rt - rb)/Lf + L*(rb - r0)/Lf
end function radius

!> Read experimental data from files.
subroutine get_experimental_data(directory, sample, name_zb1, name_zb2, name_wz, rheed, &
    crystal_correction, growth_rate, fraction, zb1, zb2, wz)
    !> Directory of data files.
    character(len=*), intent(in) :: directory
    !> Sample name.
    character(len=*), intent(in) :: sample
    !> Name of first ZB peak.
    character(len=*), intent(in) :: name_zb1
    !> Name of second ZB peak.
    character(len=*), intent(in) :: name_zb2
    !> Name of WZ peak.
    character(len=*), intent(in) :: name_wz
    !> True for RHEED data, false for XRD.
    logical, intent(in) :: rheed
    !> Get crystallite corrected data.
    logical, intent(in) :: crystal_correction
    !> Length growth per time.
    real(rp), intent(in) :: growth_rate
    !> WZ fraction.
    real(rp), allocatable, intent(out) :: fraction(:,:)
    !> Intensity of first ZB peak.
    real(rp), allocatable, intent(out) :: zb1(:,:)
    !> Intensity of second ZB peak.
    real(rp), allocatable, intent(out) :: zb2(:,:)
    !> Intensity of WB peak.
    real(rp), allocatable, intent(out) :: wz(:,:)
    character(len=20) :: data_type, data_suffix
    character(len=200) :: data_prefix, data_prefix_raw, data_prefix_x
    if (rheed) then
        data_type = 'RHEED'
        data_suffix = '.dat'
    else
        data_type = 'XRD'
        if (crystal_correction) then
            data_suffix = '_CC.dat'
        else
            data_suffix = '.dat'
        end if
    end if
    data_prefix = trim(adjustl(directory))//'/'//trim(adjustl(sample))//trim(data_type)
    data_prefix_raw = trim(adjustl(directory))//'/'//trim(adjustl(sample))
    data_prefix_x = trim(adjustl(directory))//'/'//trim(adjustl(sample))//'x'//trim(data_type)
    if (rheed) then
        zb1 = read_data(data_prefix, data_prefix_x, growth_rate, 'ZB'//trim(name_zb1)//data_suffix)
        zb2 = read_data(data_prefix, data_prefix_x, growth_rate, 'ZB'//trim(name_zb2)//data_suffix)
        wz = read_data(data_prefix, data_prefix_x, growth_rate, 'WZ'//trim(name_wz)//data_suffix)
    else
        zb1 = read_data(data_prefix, data_prefix_x, growth_rate, trim(name_zb1)//data_suffix)
        zb2 = read_data(data_prefix, data_prefix_x, growth_rate, trim(name_zb2)//data_suffix)
        wz = read_data(data_prefix, data_prefix_x, growth_rate, trim(name_wz)//data_suffix)
    end if
```

```
    fraction = read_data(data_prefix, data_prefix_x, growth_rate, 'WZFraction'//trim(data_suffix))
end subroutine get_experimental_data

!> Convert data from time based to length based.
function read_data(data_prefix, data_prefix_x, growth_rate, filename) result(res)
    !> Prefix for y values.
    character(len=*), intent(in) :: data_prefix
    !> Prefix for x values.
    character(len=*), intent(in) :: data_prefix_x
    !> Filename for data (without prefix).
    character(len=*), intent(in) :: filename
    !> Length growth per time.
    real(rp), intent(in) :: growth_rate
    !> Converted data.
    real(rp), allocatable :: res(:,:)
    real(rp), allocatable :: tmp(:), tmpx(:)
    tmpx = growth_rate*read_txt(trim(data_prefix_x)//trim(filename))
    tmp = read_txt(trim(data_prefix)//trim(filename))
    if (size(tmpx) /= size(tmp)) then
        call log_message(LOG_LEVEL_CRITICAL, 'Error while reading input data. x and y have to be of same
            length.')
    end if
    allocate(res(size(tmp), 2))
    res(:,1) = tmpx
    res(:,2) = tmp
end function read_data

!> Read integrated WZ fraction from file.
function get_wz_fraction(growth_rate, filename) result(res)
    real(rp), intent(in) :: growth_rate
    character(len=*), intent(in) :: filename
    real(rp), allocatable :: res(:, :)
    integer :: u, n, ios, i
    character(len=200) :: msg
    open (file=filename, action='read', newunit=u, status='old', iostat=ios)
    if (ios /= 0) then
        close (u)
        call log_message(LOG_LEVEL_CRITICAL, 'Error while opening file: '//trim(filename))
    end if
    n = 0
    do
        read (u, *, iostat=ios)
        if (ios /= 0) then
            exit
        end if
        n = n + 1
    end do
    rewind u
    ! If file has only a single line, try CSV format.
    write (msg, '(A,IO,A)') 'Got ', n, ' values for file '//trim(filename)
    call log_message(LOG_LEVEL_DEBUG, msg)
    allocate(res(n, 2))
    do i = 1,n
        read (u,*) res(i, :)
    end do
    res(:, 1) = res(:, 1) * growth_rate
    close (u)
end function get_wz_fraction

!> Read data from text file. This works both with a single value per line or a single line with comma
    separated values.
function read_txt(filename) result(array)
    !> Filename (complete with prefix).
    character(len=*), intent(in) :: filename
    !> Resulting data.
    real(rp), allocatable :: array(:)
    integer :: u, n, ios, i
    character(len=:), allocatable :: line
    character(len=200) :: msg
    open (file=filename, action='read', newunit=u, status='old', iostat=ios)
    if (ios /= 0) then
        close (u)
        call log_message(LOG_LEVEL_CRITICAL, 'Error while opening file: '//trim(filename))
    end if
```

```
        n = 0
        do
            read (u, *, iostat=ios)
            if (ios /= 0) then
                exit
            end if
            n = n + 1
        end do
        rewind u
        ! If file has only a single line, try CSV format.
        if (n == 1) then
            call log_message(LOG_LEVEL_DEBUG, 'Trying␣CSV␣format␣for␣file␣'//trim(filename))
            allocate(character(len=100000) :: line)
            read (u,'(A)') line
            n = 1
            do i = 1,len(line)
                if (line(i:i) == ',') then
                    n = n + 1
                end if
            end do
            write (msg, '(A,I0,A)') 'Got␣', n, '␣values␣for␣file␣'//trim(filename)
            call log_message(LOG_LEVEL_DEBUG, msg)
            allocate(array(n))
            rewind u
            read (u, *) array
        else
            write (msg, '(A,I0,A)') 'Got␣', n, '␣values␣for␣file␣'//trim(filename)
            call log_message(LOG_LEVEL_DEBUG, msg)
            allocate(array(n))
            do i = 1,n
                read (u,*) array(i)
            end do
        end if
        close (u)
    end function read_txt
end module analysis
```

Module: shadow

```
!> Module for shadow calculation routines.
module shadow
    use :: const
    use :: types
    use :: utils
    !use, intrinsic :: iso_fortran_env
    implicit none
    private
    public :: calc_height
    !> Warning about grid already shown.
    !! This prevents multithreaded programs from showing the warning multiple times.
    logical :: warning_shown = .false.

contains
    !> Calculate shadow height at a test set of wires.
    !! For a better description of the shadow areas consult the algorithm section in the manual.
    subroutine calc_height(alpha, den, r, g, res, divergence, outputwire)
        !> Incident angle.
        real(rp), intent(in) :: alpha
        !> Wire density.
        real(rp), intent(in) :: den
        !> Wire generator.
        class(wire), intent(in) :: r
        !> Grid.
        class(grid), intent(in) :: g
        !> List of shadow height at wires.
        real(rp), allocatable, intent(out) :: res(:)
        !> Divergence.
        !! If no value is given, the divergence is set to 0.
        real(rp), optional, intent(in) :: divergence
        real(rp), optional, intent(out), allocatable :: outputwire(:,:)
        integer :: nx, ny, nwire, i, x1, x2, y1, y2, y_div, x, y, wirex, wirey
        real(rp), allocatable :: array(:,:)
        real(rp) :: xmin, rand(2), max_rand, length, diameter, shadow_length, div, shadow_height
        integer, allocatable :: wire_positions(:,:)
```

```
div = 0._rp
if (present(divergence)) then
    div = divergence
end if
! Calculate number of wires and number range.
nx = nint(g%sx/g%dx)
ny = nint(g%sy/g%dy)
xmin = -r%max_l/tan(alpha)
!nwire = nint((g%sx-xmin)*g%sy*den)
nwire = nint(g%sx*g%sy*den)
max_rand = max(abs(xmin), g%sx, g%sy)
if ((.not. warning_shown) .and. (abs(xmin) > g%sx)) then
    write (error_unit, *) 'WARNING: grid is smaller than largest shadow: ', g%sx, '<', abs(xmin)
    warning_shown = .true.
end if
! Prepare arrays.
allocate(array(0:nx,0:ny))
allocate(wire_positions(2,nwire))
if (allocated(res)) then
    deallocate(res)
end if
allocate(res(nwire))
if (present(outputwire)) then
    if (allocated(outputwire)) then
        deallocate(outputwire)
    end if
    allocate(outputwire(2,nwire))
end if
array = 0
i = 0
do
    ! Generate random position by rejecting results outside the test area and extension.
    do
        call random_number(rand)
        rand = -max_rand + 2*max_rand*rand
        if ((rand(1) >= xmin) .and. (rand(1) <= g%sx) .and. &
            (rand(2) >= 0) .and. (rand(2) <= g%sy)) then
            exit
        end if
    end do

    ! Get next wire.
    length = r%length()
    shadow_length = length/tan(alpha)
    diameter = r%diameter()

    ! Get shadow range directly behind wire (indices on grid).
    x1 = min(nx,max(0,nint(rand(1)/g%dx)))
    x2 = min(nx,max(0,nint((rand(1) + shadow_length)/g%dx)))
    y1 = min(ny,max(0,nint((rand(2) - 0.5_rp*diameter)/g%dy)))
    y2 = min(ny,max(0,nint((rand(2) + 0.5_rp*diameter)/g%dy)))

    ! Save wire position for later analysis. If wire is in test area increase counter.
    wirex = nint(rand(1)/g%dx)
    wirey = nint(rand(2)/g%dy)
    if ((wirex >= 0) .and. (wirex <= nx) .and. &
        (wirey >= 0) .and. (wirey <= ny)) then
        i = i + 1
        wire_positions(1,i) = wirex
        wire_positions(2,i) = wirey
        if (present(outputwire)) then
            outputwire(:,i) = rand
        end if
    end if

    ! Save shadow height in rectangular area behind wire. x1+1 is necessary to exclude the place of the
          wire itself.
    do y = y1,y2
        do x = x1+1,x2
            array(x,y) = max(array(x,y), length*(rand(1)+shadow_length-real(x)*g%dx)/shadow_length)
        end do
    end do

    ! Save shadow height in arcs due to divergence.
```

```
            if (div > 0) then
                do x = x1+1,x2
                    ! Maximum size of shadow in y direction.
                    y_div = nint(tan(div/2) * real(x - x1))
                    do y = y1-y_div,y1-1
                        ! Exlude points outside of shadow.
                        if ((y < 0) .or. (y > ny)) then
                            cycle
                        end if
                        ! Shadow height is proportional to distance to corner or wire.
                        shadow_height = length * (1._rp - &
                            sqrt((rand(1) - real(x)*g%dx)**2 + &
                            (rand(2) - 0.5*diameter - real(y)*g%dy)**2)/shadow_length)
                        if (shadow_height < 0) then
                            cycle
                        end if
                        array(x,y) = max(array(x,y), shadow_height)
                    end do
                    do y = y2+1,y2+y_div
                        ! Exlude points outside of shadow.
                        if ((y < 0) .or. (y > ny)) then
                            cycle
                        end if
                        ! Shadow height is proportional to distance to corner or wire.
                        shadow_height = length * (1._rp - &
                            sqrt((rand(1) - real(x)*g%dx)**2 + &
                            (rand(2) + 0.5*diameter - real(y)*g%dy)**2)/shadow_length)
                        if (shadow_height < 0) then
                            cycle
                        end if
                        array(x,y) = max(array(x,y), shadow_height)
                    end do
                end do
            end if

            ! Test if enough wires were generated.
            if (i == nwire) then
                exit
            elseif (i > nwire) then
                write (error_unit, '(A)') 'ERROR: Too much wires generated'
                stop 2
            end if
        end do

        ! Walk through wire positions and evaluate shadow height at that point.
        do i = 1,nwire
            x = wire_positions(1,i)
            y = wire_positions(2,i)
            if ((x >= 0) .and. (x <= nx) .and. &
                (y >= 0) .and. (y <= ny)) then
                res(i) = array(x,y)
            else
                res(i) = -1._rp
            end if
        end do
    end subroutine calc_height
end module shadow
```

Module: config

```
> Module for reading configuration files.
!! This module contains functions and types for reading configuration files. The configuration files consist of
      two lines per parameter. The first line contains the name of the parameter, the second one the value.

module config
    use :: const
    use :: types
    use :: utils
    implicit none
    private
    public :: ConfigParameter, read_config_file
    !> Type for configuation parameters containing values of different types.
    type :: ConfigParameter
        private
```

```
            character(len=50) :: name
            character(len=200) :: value
        contains
            !> Initialize variable.
            generic :: init => init_integer, init_real, init_grid, &
                init_string, init_range, init_logical
            !> Return value.
            generic :: get_value => get_integer, get_real, get_grid, &
                get_string, get_range, get_logical
            !> Return integer.
            procedure :: get_integer
            !> Return real.
            procedure :: get_real
            !> Return grid.
            procedure :: get_grid
            !> Return string.
            procedure :: get_string
            !> Return RealRange.
            procedure :: get_range
            !> Return name of parameter.
            procedure :: get_name
            !> Return logical.
            procedure :: get_logical
            !> Initialize with integer.
            procedure :: init_integer
            !> Initialize with integer.
            procedure :: init_real
            !> Initialize with real.
            procedure :: init_grid
            !> Initialize with grid.
            procedure :: init_string
            !> Initialize with string.
            procedure :: init_range
            !> Initialize with RealRange.
            procedure :: init_logical
            !> Write parameter to file or console output.
            procedure :: write => par_write
    end type ConfigParameter
contains
    !> Return parameter name.
    function get_name(this) result(res)
        !> Parameter.
        class(ConfigParameter), intent(in) :: this
        !> Output value.
        character(len=:), allocatable :: res
        res = trim(adjustl(this%name))
    end function get_name

    !> Return integer.
    subroutine get_integer(this, res)
        !> Parameter.
        class(ConfigParameter), intent(in) :: this
        !> Output value.
        integer, intent(out) :: res
        read (this%value, *) res
    end subroutine get_integer

    !> Return grid.
    subroutine get_grid(this, res)
        !> Parameter.
        class(ConfigParameter), intent(in) :: this
        !> Output value.
        class(grid), intent(out) :: res
        read (this%value, *) res%sx, res%sy, res%dx, res%dy
    end subroutine get_grid

    !> Return range.
    subroutine get_range(this, res)
        !> Parameter.
        class(ConfigParameter), intent(in) :: this
        !> Output value.
        class(RealRange), intent(out) :: res
        read (this%value, *) res%min_val, res%max_val, res%n_val
    end subroutine get_range
```

```
!> Return real.
subroutine get_real(this, res)
    !> Parameter.
    class(ConfigParameter), intent(in) :: this
    !> Output value.
    real(rp), intent(out) :: res
    read (this%value, *) res
end subroutine get_real

!> Return string.
subroutine get_string(this, res)
    !> Parameter.
    class(ConfigParameter), intent(in) :: this
    !> Output value.
    character(len=:), allocatable, intent(out) :: res
    res = this%value
end subroutine get_string

!> Return logical.
subroutine get_logical(this, res)
    !> Parameter.
    class(ConfigParameter), intent(in) :: this
    !> Output value.
    logical, intent(out) :: res
    if (trim(adjustl(this%value)) == 'true') then
        res = .true.
    elseif (trim(adjustl(this%value)) == 'false') then
        res = .false.
    else
        res = .false.
        call log_message(LOG_LEVEL_WARNING, 'Unable to parse logical value, using FALSE. Got "' &
            //trim(adjustl(this%value))//'".')
    end if
end subroutine get_logical

!> Read configuration file.
!! This routine parses a configuration file and returns a list of parameters.
subroutine read_config_file(filename, res)
    !> Filename of configuration file.
    character(len=*), intent(in) :: filename
    !> List of parameters.
    type(ConfigParameter), allocatable, intent(out) :: res(:)
    integer :: u, stat, n_lines, i
    character(len=500) :: line
    open (file=filename, newunit=u)
    n_lines = 0
    do
        read (u, '(A)', iostat=stat) line
        if (stat < 0) then
            exit
        elseif (stat > 0) then
            stop "Error while reading config file."
        else
            n_lines = n_lines + 1
        end if
    end do
    allocate(res(n_lines/2))
    rewind (u)
    do i = 1, n_lines/2
        read (u, '(A)') line
        res(i)%name = trim(adjustl(line))
        call log_message(LOG_LEVEL_DEBUG, "Got parameter "//res(i)%name//".")
        read (u, '(A)') line
        res(i)%value = trim(adjustl(line))
    end do
    close (u)
end subroutine read_config_file

!> Write parameter to file or console.
subroutine par_write(this, u)
    !> Parameter.
    class(ConfigParameter), intent(in) :: this
    !> Unit number of file or console.
```

```
    integer, intent(in) :: u
    write (u, '(A)') trim(adjustl(this%name))
    write (u, '(2A)') '␣␣␣␣␣␣␣␣', trim(adjustl(this%value))
end subroutine par_write

!> Init with integer.
subroutine init_integer(this, n, v)
    !> Parameter.
    class(ConfigParameter), intent(out) :: this
    !> Name.
    character(len=*), intent(in) :: n
    !> Value.
    integer, intent(in) :: v
    this%name = n
    write (this%value, *) v
    this%value = adjustl(this%value)
end subroutine init_integer

!> Init with real.
subroutine init_real(this, n, v)
    !> Parameter.
    class(ConfigParameter), intent(out) :: this
    !> Name.
    character(len=*), intent(in) :: n
    !> Value.
    real(rp), intent(in) :: v
    this%name = n
    write (this%value, *) v
    this%value = adjustl(this%value)
end subroutine init_real

!> Init with grid.
subroutine init_grid(this, n, v)
    !> Parameter.
    class(ConfigParameter), intent(out) :: this
    !> Name.
    character(len=*), intent(in) :: n
    !> Value.
    class(Grid), intent(in) :: v
    this%name = n
    write (this%value, *) v%sx, v%sy, v%dx, v%dy
    this%value = adjustl(this%value)
end subroutine init_grid

!> Init with string.
subroutine init_string(this, n, v)
    !> Parameter.
    class(ConfigParameter), intent(out) :: this
    !> Name.
    character(len=*), intent(in) :: n
    !> Value.
    character(len=*), intent(in) :: v
    this%name = n
    this%value = v
end subroutine init_string

!> Init with RealRange.
subroutine init_range(this, n, v)
    !> Parameter.
    class(ConfigParameter), intent(out) :: this
    !> Name.
    character(len=*), intent(in) :: n
    !> Value.
    class(RealRange), intent(in) :: v
    this%name = n
    write (this%value, *) v%min_val, v%max_val, v%n_val
    this%value = adjustl(this%value)
end subroutine init_range

!> Init with logical.
subroutine init_logical(this, n, v)
    !> Parameter.
    class(ConfigParameter), intent(out) :: this
    !> Name.
```

```
        character(len=*), intent(in) :: n
        !> Value.
        logical, intent(in) :: v
        this%name = n
        if (v) then
            this%value = 'true'
        else
            this%value = 'false'
        end if
    end subroutine init_logical
end module config
```

Module: types

```
!> Module for some custom defined types.
module types
    use :: const
    use :: utils
    use :: iso_c_binding
    implicit none

    !> Base type for wires.
    !! The type functions as a generator for wires. At each call of length and diameter a new wire is generated
         . The length function is called before the diameter function.
    type, abstract :: wire
        !> Maximum length.
        !! This is required for the shadow calculation, as the maximum occuring length has to be available.
        real(rp) :: max_l
    contains
        !> Get the length of the next wire.
        procedure(wire_length), deferred :: length
        !> Get the diameter of the next wire.
        procedure(wire_diameter), deferred :: diameter
    end type wire
    abstract interface
        !> Get the length of the next wire.
        function wire_length(this)
            use :: const
            import wire
            class(wire), intent(in) :: this
            real(rp) :: wire_length
        end function wire_length
        !> Get the diameter of the next wire.
        function wire_diameter(this)
            use :: const
            import wire
            class(wire), intent(in) :: this
            real(rp) :: wire_diameter
        end function wire_diameter
    end interface

    !> Rod with uniform height and diameter.
    type, extends(wire) :: monowire
        !> Length.
        real(rp) :: l
        !> Diameter.
        real(rp) :: d
    contains
        !> Initialize wire.
        procedure :: init => monowire_init
        !> Get length of next wire.
        procedure :: length => monowire_length
        !> Get diameter of next wire.
        procedure :: diameter => monowire_diameter
    end type

    !> Rod with radius growth linear to the length.
    type, extends(wire) :: relativewire
        !> Length.
        real(rp) :: l
        !> Initial radius (at \f$l = 0\f$).
        real(rp) :: radius_start
        !> Radius growth per unit length.
        real(rp) :: radius_growth
```

```
contains
    !> Initialize wire.
    procedure :: init => relativewire_init
    !> Get length of next wire.
    procedure :: length => relativewire_length
    !> Get diameter of next wire.
    procedure :: diameter => relativewire_diameter
end type

!> Range of read values.
!! This type produces a behaviour similiar to the linspace of Matlab or NumPy (index, get_list).
     Additionally it is possitble to get the values in the middle of a step (index_center, get_center_list)
     .
type :: RealRange
    !> Minimum value.
    real(rp) :: min_val
    !> Maximum value.
    real(rp) :: max_val
    !> Number of values.
    integer :: n_val
contains
    !> Get value at index.
    procedure :: index => range_index
    !> Get value in middle of the indexth space.
    procedure :: index_center => range_index_center
    !> Get list of values.
    procedure :: get_list => range_list
    !> Get list of values in the middle of the steps.
    procedure :: get_center_list => range_center_list
end type RealRange

!> Equality operators for some user defined types.
interface operator(==)
    !> Equality operator for grid.
    module procedure :: grid_equal
    !> Equality operator for RealRange.
    module procedure :: range_equal
end interface

!> Type for a rectangular grid.
type grid
    !> Resulution parallel to the beam.
    real(rp) :: dx
    !> Resulution perpendicular to the beam.
    real(rp) :: dy
    !> Size parallel to the beam.
    real(rp) :: sx
    !> Size perpendicular to the beam.
    real(rp) :: sy
end type grid

!> Type for parameter set for a simulation run.
!! These parameters are specified in the list file.
type SimulationParameter
    !> Grid for simulation.
    type(grid) :: grid
    !> Incident angle in radian.
    real(rp) :: alpha
    !> Density of wires.
    real(rp) :: density
    !> Beam divergence in radian.
    real(rp) :: divergence
    !> Initial radius of the wires.
    real(rp) :: r0
    !> Finial radius of the wires at the bottom.
    real(rp) :: rb
    !> Final radius of the wires at the top.
    real(rp) :: rt
    !> Final length of the wires.
    real(rp) :: Lf
    !> Density of crystallites.
    real(rp) :: cry_density
    !> Initial radius of the crystallites.
    real(rp) :: cry_ri
```

```
        !> Final radius of the crystallites.
        real(rp) :: cry_rf
        !> Initial height of the crystallites.
        real(rp) :: cry_hi
        !> Final height of the crystallites.
        real(rp) :: cry_hf
        !> Transmittivity (factor by which the shadowing is reduced).
        real(rp) :: transm
        !> Lenghts of wires.
        type(RealRange) :: lengths
        !> Number of repetitions (increases both accuracy and runtime).
        integer :: nrep
        !> Filename for fraction file.
        character(len=:), allocatable :: fraction
        !> Optional filename for intentsity profiles.
        character(len=:), allocatable :: filename
    contains
        !> Read parameter from line in a file.
        procedure :: read_from_line => parameter_read_line
        !> Print parameter in human readable form.
        procedure :: print => parameter_print
        !> Test if another parameter produces the same histogram.
        !! This is used in the caching algorithm.
        procedure, pass :: same_hist => parameter_same_hist
        !> Calculate hash, which returns the same value if the histograms are the same.
        !! This is used in the caching algorithm.
        procedure, pass :: hist_hash => parameter_hist_hash
    end type SimulationParameter

    !> Parameters common to all simulation runs.
    type AnalysisParameter
        !> Use shadowing.
        !! This also switches to RHEED data for the RMSD calculation.
        logical :: shadows
        !> Use crytallity corrected data.
        !! This has only an effect for simulations without shadowing. If enabled, no crystallite intensities
            are considered and
        logical :: crystal_correction
        !> Order of polynom fit on experimental fraction.
        integer :: polynom_order
        !> Weight of first experimental ZB peak.
        real(rp) :: weight_zb1
        !> Weight of second experimental ZB peak.
        real(rp) :: weight_zb2
        !> Length on with the signals are normalized using the WZ intensities.
        real(rp) :: norm_length
        !> Absorption coefficient (inverse of the free path).
        real(rp) :: absorption
        !> Use integrated fraction.
        !! This parameter specifies, if the input fraction is given as integrated fraction.
        logical :: integrated_fraction
        !> Total growth time.
        !! This is important to calculate the height from the time given in the experimental data files.
        real(rp) :: growth_time
        !> Directory with experimental data.
        character(len=:), allocatable :: data_directory
        !> Sample name.
        character(len=:), allocatable :: sample
        !> Name of first ZB peak.
        character(len=:), allocatable :: name_zb1
        !> Name of second ZB peak.
        character(len=:), allocatable :: name_zb2
        !> Name of WZ peak.
        character(len=:), allocatable :: name_wz
        !> Directory for output files.
        character(len=:), allocatable :: output_directory
        !> Number of bins for the histogram calculation.
        integer :: nbins
        !> Output histogram to text file.
        logical :: histogram_output
        !> Output wire Positions to text file.
        logical :: wireposition_output
    end type AnalysisParameter
```

```
    !> Hash of simulation parameter set.
    !! This hash is designed to deliver the same result for parameters which result in the same shadowing
         histogram. Therefore parameters with different parameters are not guaranteed to get different hashes.
         The hashing algorithm starts with a list of 10 zeros. At each hashing step first a circular shift is
         applied to the hash array and then the result of a xor operation with the byte representation of the
         paramater is used as a new hash value.
    type ParameterHash
        !> Hash value.
        integer(c_int8_t) :: data(10) = (/0_1, 0_1, 0_1, 0_1, 0_1, 0_1, 0_1, 0_1, 0_1, 0_1/)
    contains
        !> Add parameter to hash.
        generic :: add => hash_real, hash_int
        !> Get hash as string.
        !! This is for example used to generate filenames for caching on disk.
        procedure, pass :: get_string => hash_to_string
        !> Add real parameter to hash.
        procedure :: hash_real
        !> Add integer parameter to hash.
        procedure :: hash_int
    end type ParameterHash
contains
    !> Initialize monowire.
    subroutine monowire_init(this, l, d)
        !> Wire.
        class(monowire), intent(out) :: this
        !> Length of wire.
        real(rp), intent(in) :: l
        !> Diameter of wire.
        real(rp), intent(in) :: d
        this%l = l
        this%d = d
        this%max_l = l
    end subroutine monowire_init

    !> Get length of next wire.
    function monowire_length(this) result(res)
        !> Wire.
        class(monowire), intent(in) :: this
        !> Length.
        real(rp) :: res
        res = this%l
    end function monowire_length

    !> Get diameter of next wire.
    function monowire_diameter(this) result(res)
        !> Wire.
        class(monowire), intent(in) :: this
        !> Diameter.
        real(rp) :: res
        res = this%d
    end function monowire_diameter

    !> Initialize relativewire.
    subroutine relativewire_init(this, l, start, growth)
        !> Wire.
        class(relativewire), intent(out) :: this
        !> Length of wire.
        real(rp), intent(in) :: l
        !> Initial wire radius (for length 0).
        real(rp), intent(in) :: start
        !> Radius growth per length growth.
        real(rp), intent(in) :: growth
        this%l = l
        this%radius_start = start
        this%radius_growth = growth
        this%max_l = l
    end subroutine relativewire_init

    !> Get length of next wire.
    function relativewire_length(this) result(res)
        !> Wire.
        class(relativewire), intent(in) :: this
        !> Length.
        real(rp) :: res
```

```
    res = this%l
end function relativewire_length

!> Get diameter of next wire.
function relativewire_diameter(this) result(res)
    !> Wire.
    class(relativewire), intent(in) :: this
    !> Diameter.
    real(rp) :: res
    res = 2._rp*(this%radius_start + this%radius_growth*this%l)
end function relativewire_diameter

!> Get value at certain index.
!! The index counts from 1 for realrange.min_val to realrange.n_val for realrange.max_val
function range_index(this, i) result(res)
    !> Range.
    class(RealRange), intent(in) :: this
    !> Index.
    integer, intent(in) :: i
    !> Value.
    real(rp) :: res
    res = this%min_val + (this%max_val-this%min_val)*real(i-1)/real(this%n_val-1)
end function range_index

!> Return list of values in range.
function range_list(this) result(res)
    !> Range.
    class(RealRange), intent(in) :: this
    !> List with realrange.n_val values evenly spaced from realrange.min_val to realrange.max_val.
    real(rp) :: res(this%n_val)
    integer :: i
    do i = 1,this%n_val
        res(i) = this%index(i)
    end do
end function range_list

!> Return a list of values in the center of the intervals.
!! This returns a list with values centered in the bins which edges are given by the indexed values
     returned by realrange.get_list or realrange.index.
function range_center_list(this) result(res)
    !> Range.
    class(RealRange), intent(in) :: this
    !> List with values at bin centers.
    real(rp) :: res(this%n_val - 1)
    integer :: i
    do i = 1,this%n_val-1
        res(i) = 0.5*(this%index(i) + this%index(i + 1))
    end do
end function range_center_list

!> Returns the value of a bin center.
!! For a index i the value between the indexed values i and i + 1 (see realrange.index) is return.
function range_index_center(this, i) result(res)
    !> Range.
    class(RealRange), intent(in) :: this
    !> Bin index.
    integer, intent(in) :: i
    !> Value at bin center.
    real(rp) :: res
    res = 0.5*(this%index(i) + this%index(i + 1))
end function range_index_center

!> Checks if two ranges are equal.
!! The ranges are treated as equal if lower boundary, upper boundary and the number of values are the same.
function range_equal(a, b) result(res)
    !> First range.
    type(RealRange), intent(in) :: a
    !> Second range.
    type(RealRange), intent(in) :: b
    !> True if the ranges are equal, false otherwise.
    logical :: res
    res = (a%min_val == b%min_val) &
        .and. (a%max_val == b%max_val) &
        .and. (a%n_val == b%n_val)
```

```
end function range_equal

!> Checks if two grids are equal.
!! The grids are treated to be equal, it both dimension and step size match.
function grid_equal(a, b) result(res)
    !> First grid.
    type(Grid), intent(in) :: a
    !> Second grid.
    type(Grid), intent(in) :: b
    !> True if the grids are equal, false otherwise.
    logical :: res
    res = (a%sx == b%sx) &
        .and. (a%sy == b%sy) &
        .and. (a%dx == b%dx) &
        .and. (a%dy == b%dy)
end function grid_equal

!> Read parameter from line in stream.
!! The line is first attempted to be parsed without a filename for the intensity output. If this failes, is
      is parsed with this parameter.
!! \return False on failure, true otherwise.
logical function parameter_read_line(this, unit) result(res)
    !> Parameter.
    class(SimulationParameter), intent(inout) :: this
    !> Unit to read from.
    integer, intent(in) :: unit
    real(rp) :: gdx, gdy, gsx, gsy, alpha, density, divergence, r0, rb, rt, &
        Lf, cry_density, cry_ri, cry_rf, cry_hi, cry_hf, transm, length_min, length_max
    integer :: nrep, n_length, ios
    character(len=200) :: iomsg
    character(len=1000) :: line, fraction, filename

    ! Parse line.
    res = .true.
    read (unit, '(A)') line
    read (line, *, iostat=ios, iomsg=iomsg) gsx, gsy, gdx, gdy, alpha, density, divergence, &
        r0, rb, rt, Lf, cry_density, cry_ri, cry_rf, cry_hi, cry_hf, transm, length_min, &
        length_max, n_length, nrep, fraction, filename
    if (ios /= 0) then
        call log_message(LOG_LEVEL_DEBUG, 'Could not read parameter, trying again without filename. ')
        read (line, *, iostat=ios) gsx, gsy, gdx, gdy, alpha, density, divergence, &
            r0, rb, rt, Lf, cry_density, cry_ri, cry_rf, cry_hi, cry_hf, transm, length_min, &
            length_max, n_length, nrep, fraction
        filename = ''
        if (ios /= 0) then
            call log_message(LOG_LEVEL_ERROR, 'Error while reading parameter. '//iomsg)
            res = .false.
        end if
    end if

    ! Set values in parameter variable.
    this%grid%dx = gdx
    this%grid%dy = gdy
    this%grid%sx = gsx
    this%grid%sy = gsy
    this%alpha = alpha*deg
    this%density = density
    this%divergence = divergence*deg
    this%r0 = r0
    this%rb = rb
    this%rt = rt
    this%Lf = Lf
    this%cry_density = cry_density
    this%cry_ri = cry_ri
    this%cry_rf = cry_rf
    this%cry_hi = cry_hi
    this%cry_hf = cry_hf
    this%lengths%min_val = length_min
    this%lengths%max_val = length_max
    this%lengths%n_val = n_length
    this%fraction = trim(adjustl(fraction))
    this%filename = trim(adjustl(filename))
    this%transm = transm
    this%nrep = nrep
```

```
end function parameter_read_line

!> Print parameter to unit.
subroutine parameter_print(this, unit)
    !> Parameter.
    class(SimulationParameter), intent(in) :: this
    !> Unit to write to. If not present, standard output is used.
    integer, intent(in), optional :: unit
    integer :: u
    if (present(unit)) then
        u = unit
    else
        u = output_unit
    end if
    associate (g => this%grid)
        write (u, '(A)') 'Grid:'
        write (u, '(A,F20.3,A,F20.3)')  '␣␣␣␣Resolution␣␣', g%dx, 'x', g%dy
        write (u, '(A,F20.3,A,F20.3)')  '␣␣␣␣Size␣␣␣␣␣␣␣␣', g%sx, 'x', g%sy
        write (u, '(A)')                'Incident␣Angle:␣'
        write (u, '(A,F20.3)')          '␣␣␣␣Degrees␣␣␣␣␣', this%alpha/deg
        write (u, '(A,F20.3,A)')        '␣␣␣␣Radian␣␣␣␣␣␣', 1000._rp*this%alpha, 'e-3'
        write (u, '(A,E20.3)')          'Density:␣␣␣␣␣␣␣␣', this%density
        write (u, '(A)')                'Divergence:'
        write (u, '(A,F20.3)')          '␣␣␣␣Degrees␣␣␣␣␣', this%divergence/deg
        write (u, '(A,F20.3,A)')        '␣␣␣␣Radian␣␣␣␣␣␣', 1000._rp*this%divergence, 'e-3'
        write (u, '(A)')                'Wire:'
        write (u, '(A,F20.3)')          '␣␣␣␣Length␣(min)', this%lengths%min_val
        write (u, '(A,F20.3)')          '␣␣␣␣Length␣(max)', this%lengths%max_val
        write (u, '(A,I20)')            '␣␣␣␣Length␣(num)', this%lengths%n_val
        write (u, '(A,F20.3)')          '␣␣␣␣Length␣(fin)', this%Lf
        write (u, '(A,F20.3)')          '␣␣␣␣Radius␣(ini)', this%r0
        write (u, '(A,F20.3)')          '␣␣␣␣Radius␣(bot)', this%rb
        write (u, '(A,F20.3)')          '␣␣␣␣Radius␣(top)', this%rt
        write (u, '(A)')                'Crystallites:'
        write (u, '(A,E20.3)')          '␣␣␣␣Density␣␣␣␣␣', this%density
        write (u, '(A,F20.3)')          '␣␣␣␣Radius␣(ini)', this%cry_ri
        write (u, '(A,F20.3)')          '␣␣␣␣Radius␣(fin)', this%cry_rf
        write (u, '(A,F20.3)')          '␣␣␣␣Height␣(ini)', this%cry_hi
        write (u, '(A,F20.3)')          '␣␣␣␣Height␣(fin)', this%cry_hf
        write (u, '(A,F20.3)')          'Transmission:␣␣␣', this%transm
        write (u, '(A,I20)')            'Repetitions:␣␣␣␣', this%nrep
    end associate
end subroutine parameter_print

!> Check if two parameters produce the same histogram.
function parameter_same_hist(a, b) result(res)
    !> First histogram.
    class(SimulationParameter), intent(in) :: a
    !> Second histogram.
    class(SimulationParameter), intent(in) :: b
    !> True if the parameters produce the same histogram, false otherwise.
    logical :: res

    res = (a%grid == b%grid) &
        .and. (a%alpha == b%alpha) &
        .and. (a%density == b%density) &
        .and. (a%divergence == b%divergence) &
        .and. (a%r0 == b%r0) &
        .and. (a%rb == b%rb) &
        .and. (a%rt == b%rt) &
        .and. (a%Lf == b%Lf) &
        .and. (a%lengths == b%lengths) &
        .and. (a%nrep == b%nrep)
end function parameter_same_hist

!> Add integer to hash.
subroutine hash_int(this, object)
    !> Hash.
    class(ParameterHash), intent(inout) :: this
    !> Value.
    integer, intent(in) :: object
    integer(c_int8_t), allocatable :: tmp(:)
    integer :: i, n
    n = size(this%data)
```

```
        tmp = transfer(object, tmp)
        this%data = cshift(this%data, 1)
        do i = 1,min(size(tmp),n)
            this%data(i) = xor(this%data(i), tmp(i))
        end do
    end subroutine hash_int

    !> Add real to hash.
    subroutine hash_real(this, object)
        !> Hash.
        class(ParameterHash), intent(inout) :: this
        !> Value.
        real(rp), intent(in) :: object
        integer(c_int8_t), allocatable :: tmp(:)
        integer :: i, n
        n = size(this%data)
        tmp = transfer(object, tmp)
        this%data = cshift(this%data, 1)
        do i = 1,min(size(tmp),n)
            this%data(i) = xor(this%data(i), tmp(i))
        end do
    end subroutine hash_real

    !> Return hash as string.
    !! This is done by printing the values as two digital hexadecimal numbers.
    function hash_to_string(this) result(res)
        !> Hash.
        class(ParameterHash), intent(in) :: this
        !> Hash as string.
        character(len=20) :: res
        write (res, '(10Z0.2)') this%data
    end function hash_to_string

    !> Calculate hash of parameter.
    !! The hash is calculated over all variables in the parameter which affect the histogram.
    function parameter_hist_hash(this) result(res)
        class(SimulationParameter), intent(in) :: this
        type(ParameterHash) :: res
        res%data = 0
        call res%add(this%grid%dx)
        call res%add(this%grid%dy)
        call res%add(this%grid%sx)
        call res%add(this%grid%sy)
        call res%add(this%alpha)
        call res%add(this%density)
        call res%add(this%divergence)
        call res%add(this%r0)
        call res%add(this%rb)
        call res%add(this%rt)
        call res%add(this%Lf)
        call res%add(this%lengths%min_val)
        call res%add(this%lengths%max_val)
        call res%add(this%lengths%n_val)
        call res%add(this%nrep)
    end function parameter_hist_hash
end module types
```

Module: const

```
!> Module containing constants.
module const
    use, intrinsic :: iso_fortran_env, rp => real64, ip => int64
    implicit none
    !> Definition of \f$\pi\f$ with highest available accuracy.
    real(rp), parameter :: pi = 4._rp*atan(1._rp)
    !> Conversion factor between radian and degrees.
    real(rp), parameter :: deg = pi/180._rp !<
#ifdef MPI
    include 'mpif.h'
    integer, parameter :: MPI_RP = MPI_REAL8
#endif
#ifdef BAR_WIDTH
    !> Width of progress bars.
    integer, parameter :: bar_width = BAR_WIDTH
```

```
#else
    !> Width of progress bars.
    integer, parameter :: bar_width = 100
#endif
end module const
```

Module: utils

```
!> Module containing some helper functions.
module utils
    use, intrinsic :: iso_fortran_env
    implicit none
    private
    public :: LOG_LEVEL_DEBUG, LOG_LEVEL_INFO, LOG_LEVEL_WARNING, LOG_LEVEL_ERROR, LOG_LEVEL_CRITICAL
    public :: LogTarget, ConsoleLog, FileLog
    public :: print_bar_time, init_random, log_message, add_log_target, print_log_targets
    public :: print_info, write_endtime, verify_version
    integer, parameter :: LOG_LEVEL_DEBUG = 4
    integer, parameter :: LOG_LEVEL_INFO = 3
    integer, parameter :: LOG_LEVEL_WARNING = 2
    integer, parameter :: LOG_LEVEL_ERROR = 1
    integer, parameter :: LOG_LEVEL_CRITICAL = 0

    !> Type for defining a log target.
    type, abstract :: LogTarget
        !> Minimum level of message written to this target.
        integer :: min_level
    contains
        !> Write message to target.
        procedure(log_write_message), deferred, pass :: write_message
        !> Get name of target.
        procedure(log_get_name), deferred, pass :: get_name
    end type LogTarget
    abstract interface
        !> Write message to target.
        subroutine log_write_message(this, level, msg)
            import :: LogTarget
            !> Target to write to.
            class(LogTarget), intent(inout) :: this
            !> Log level of the message.
            integer, intent(in) :: level
            !> Message.
            character(len=*), intent(in) :: msg
        end subroutine log_write_message

        !> Get name of target.
        function log_get_name(this) result(res)
            import :: LogTarget
            !> Target.
            class(LogTarget), intent(in) :: this
            character(len=:), allocatable :: res
        end function log_get_name
    end interface

    !> Log target for logging to the console.
    type, extends(LogTarget) :: ConsoleLog
    contains
        !> Write message to console.
        procedure, pass :: write_message => console_write_message
        !> Get name of target.
        procedure, pass :: get_name => console_get_name
    end type

    !> Log target for logging to a text file.
    type, extends(LogTarget) :: FileLog
        !> Filename of log file.
        character(len=:), allocatable :: filename
    contains
        !> Write message to file.
        procedure, pass :: write_message => file_write_message
        !> Get name of target.
        procedure, pass :: get_name => file_get_name
    end type
```

```
    !> Container for different log target types.
    type :: LogTargetContainter
        !> Target.
        class(LogTarget), pointer :: target => null()
    end type

    !> List of active log targets.
    type(LogTargetContainter), allocatable :: log_targets(:)
contains
    !> Initialize random seed.
    !! This routine initializes the random seed by utilizing the current time.
    subroutine init_random()
        integer :: i, n, clock
        integer, allocatable :: seed(:)
        call random_seed(size=n)
        allocate(seed(n))
        call system_clock(count=clock)
        seed = clock + 37*(/ (i-1, i=1, n) /)
        call random_seed(put=seed)
    end subroutine init_random

    !> Print progress bar with linear time estimation.
    !! This routine prints a progess bar. The UNICODE flag decides, whether UTF-8 block characters or pure
         ASCII is used. If the force argument is not specified or false, the bar is only updated about every 50
         ms to prevent throtteling the program due to a slow console output.
    subroutine print_bar_time(p,n,stime,dat,force)
        !> Percentage.
        real, intent(in) :: p
        !> Progress bar width.
        integer, intent(in) :: n
        !> Starting time.
        real, intent(in) :: stime
        !> Additional data to display.
        real, intent(in), optional :: dat
        !> Force update.
        logical, intent(in), optional :: force
        real :: prog, time
        integer :: i
        logical :: output
        real, save :: lasttime = -1
        prog = min(1.,abs(p))
        output = .false.
        if (present(force)) then
            output = force
        end if
        call cpu_time(time)
        if (output .or. (time - lasttime > 0.05)) then
            lasttime = time
            time = time-stime
            write (output_unit, '(A)', advance='no') achar(13)
            write (output_unit, '(F9.2,A,F9.2,A)', advance='no') time,'s␣/␣',time/prog,'s␣'
            do i = 1,(n-32)
                if (real(i) <= real(n-32)*prog) then
#ifdef UNICODE
                    write (output_unit,'(1A)',advance='no') ''
#else
                    write (output_unit,'(1A)',advance='no') '#'
#endif
                else
#ifdef UNICODE
                    write (output_unit,'(1A)',advance='no') ''
#else
                    write (output_unit,'(1A)',advance='no') '_'
#endif
                end if
            end do
            write (output_unit, '(F10.2,1A)', advance='no') 100.*prog,'%'
            if (present(dat)) then
                write (output_unit, '(E15.7)', advance='no') dat
            end if
        end if
    end subroutine print_bar_time

    !> Log message to all active targets.
```

```
    !! This routine logs a message to all log targets. If the level is CRITICAL, the execution is stopped and a
          backlog is printed, if DEBUG is enabled.
    subroutine log_message(level, msg, exit)
        !> Log level of message.
        integer, intent(in) :: level
        !> Message.
        character(len=*), intent(in) :: msg
        !> Exit the program after logging the message.
        logical, optional, intent(in) :: exit
        integer :: i
        if ( .not. ((size(log_targets) == 0) .or. .not. allocated(log_targets))) then
            do i = 1,size(log_targets)
                if (level <= log_targets(i)%target%min_level) then
                    call log_targets(i)%target%write_message(level, msg)
                end if
            end do
        end if
        if (present(exit)) then
            if (exit) then
                stop 1
            end if
        end if
        if (level == LOG_LEVEL_CRITICAL) then
#ifdef DEBUG
            call backtrace()
#endif
            stop 100
        end if
    end subroutine log_message

    !> Write message to console.
    subroutine console_write_message(this, level, msg)
        !> Target.
        class(ConsoleLog), intent(inout) :: this
        !> Log level of message.
        integer, intent(in) :: level
        !> Message.
        character(len=*), intent(in) :: msg
        if (level > this%min_level) then
            return
        end if
        if (level == LOG_LEVEL_INFO) then
            write (output_unit, '(3A)') msg
        else
            write (output_unit, '(3A)') get_level_name(level), '␣', msg
        end if
    end subroutine console_write_message

    !> Get name of target.
    function console_get_name(this) result(res)
        !> Target.
        class(ConsoleLog), intent(in) :: this
        !> Name of target.
        character(len=:), allocatable :: res
        res = 'ConsoleLog'
    end function console_get_name

    !> Write message to file.
    subroutine file_write_message(this, level, msg)
        !> Target.
        class(FileLog), intent(inout) :: this
        !> Log level of message.
        integer, intent(in) :: level
        !> Message.
        character(len=*), intent(in) :: msg
        logical :: exists, opened
        integer :: u

!$omp critical
        inquire(file=this%filename, opened=opened)
        do while (opened)
            inquire(file=this%filename, opened=opened)
        end do
        inquire(file=this%filename, exist=exists)
```

```
        if (exists) then
            open (file=this%filename, status='old', position='append', action='write', newunit=u)
        else
            open (file=this%filename, status='new', action='write', newunit=u)
        end if
        write (u,'(A,X,A,X,A)') get_time_stamp(), get_level_name(level), msg
        close (u)
!$omp end critical
    end subroutine file_write_message

    !> Get name of target.
    !! This also includes the filename.
    function file_get_name(this) result(res)
        !> Target.
        class(FileLog), intent(in) :: this
        !> Name of target.
        character(len=:), allocatable :: res
        allocate(character(len=9+len(this%filename)) :: res)
        write (res, '(2A)') 'FileLog: ', this%filename
    end function file_get_name

    !> Add log target.
    !! This routine adds a log target to the list of active targets.
    subroutine add_log_target(target)
        !> Target.
        class(LogTarget), target, intent(in) :: target
        type(LogTargetContainter), allocatable :: tmp(:)
        integer :: n
        if (allocated(log_targets)) then
            n = size(log_targets)
            allocate(tmp(n + 1))
            tmp(1:n) = log_targets
            tmp(n + 1)%target => target
            log_targets = tmp
        else
            allocate(log_targets(1))
            log_targets(1)%target => target
        end if
    end subroutine add_log_target

    !> Print active log targets to console.
    subroutine print_log_targets()
        integer :: i
        do i = 1,size(log_targets)
            write (output_unit, '(I5,4X,A)') i, log_targets(i)%target%get_name()
        end do
    end subroutine print_log_targets

    !> Get name of log level.
    function get_level_name(level) result(res)
        !> Log level.
        integer, intent(in) :: level
        !> Name of target.
        character(len=:), allocatable :: res
        select case(level)
        case(LOG_LEVEL_DEBUG)
            res = '[DEBUG   ]'
        case(LOG_LEVEL_INFO)
            res = '[INFO    ]'
        case(LOG_LEVEL_WARNING)
            res = '[WARNING ]'
        case(LOG_LEVEL_ERROR)
            res = '[ERROR   ]'
        case(LOG_LEVEL_CRITICAL)
            res = '[CRITICAL]'
        end select
    end function get_level_name

    !> Get current time stamp.
    function get_time_stamp() result(res)
        !> Timestamp.
        character(len=19) :: res
        integer :: values(8)
        call date_and_time(values=values)
```

```
        write (res, '(I4.4,A,I2.2,A,I2.2,A,I2.2,A,I2.2,A,I2.2)') &
            values(1), '-', values(2), '-', values(3), &
            ' ', values(5), ':', values(6), ':', values(7)
    end function get_time_stamp

    !> Verifies target version of list file.
    !! \return Version string found.
    logical function verify_version(u) result(res)
        integer, intent(in) :: u
        character(len=200) :: line
        character(len=9) :: start
        read (u, '(A)') line
        start = line(1:9)
        res = .false.
        if (start /= '#version ') then
            call log_message(LOG_LEVEL_WARNING, &
                'Target version of list not specified. '// &
                'Please make sure that the syntax is up to date.')
            rewind u
        else
            res = .true.
            if (trim(adjustl(line)) /= '#version '//VERSION_SHORT) then
                call log_message(LOG_LEVEL_WARNING, &
                    'Target version of list file different than program version ('// &
                    trim(adjustl(line(10:)))//' targeted, but version is '//VERSION_SHORT//'). '// &
                    'Please make sure that the syntax is up to date.')
            end if
        end if
    end function verify_version

    !> Print version information and time to file.
    subroutine print_info(filename)
        !> Filename.
        character(len=*), optional, intent(in) :: filename
        integer :: u, time(8)
#ifdef VERSION
        write (output_unit, '(4A)') 'rshad ', VERSION, ' ', BUILD_DATE
        write (output_unit, *)
#endif
        if (present(filename)) then
            open (newunit=u, file=filename)
#ifdef VERSION
            write (u, '(4A)') 'Version: ', VERSION, ' ', BUILD_DATE
#endif
            call date_and_time(values=time)
            write (u,'(A,I4,6(A,I2.2))') 'Start:    ', &
                time(1), '-', time(2), '-', time(3), ' ', &
                time(5), ':', time(6), ':', time(7)
            close (u)
        end if
    end subroutine print_info

    !> Write time to file.
    subroutine write_endtime(filename)
        character(len=*), intent(in) :: filename
        integer :: u, time(8)

        open (newunit=u, file=filename, status='old', position='append')
        call date_and_time(values=time)
        write (u,'(A,I4,6(A,I2.2))') 'End:      ', &
            time(1), '-', time(2), '-', time(3), ' ', &
            time(5), ':', time(6), ':', time(7)
        close (u)
    end subroutine write_endtime
end module utils
```

List of Figures

List of Tables

Acknowledgements

Zum Abschluss möchte ich mich bei allen Bedanken, die zum Gelingen dieser Arbeit beigetragen haben:

Allen voran danke ich Prof. Dr. Tilo Baumbach für die Möglichkeit meine Doktorarbeit in seinem Institut anzufertigen, sowie für das Vertrauen und die Freiheit meinen eigenen Ideen nachzugehen und für die Unterstützung diese umzusetzen.
Prof. Dr. Ullrich Pietsch möchte ich für die kontinuierliche Unterstützung während der gesamten Promotionszeit, für das immer offene Ohr, sowie für die Übernahme des Korreferats danken.

Ein großer Dank gilt meinen ehemaligen Kollegen Dr. Philipp Schroth und Dr. Ludwig Feigl für die stetige Bereitschaft Fragen und Probleme offen zu diskutieren. Die freundschaftliche Arbeitsatmosphäre machten die vielen Wochen Strahlzeit in Hamburg angenehmer.
Ihnen, Dr. Svetoslav Stankov und Dr. Stephen Doyle danke ich für das kritische Durchlesen meiner Doktorarbeit.
Dr. Bärbel Krause und Annette Weißhardt danke ich für die Unterstützung bei allen Angelegenheiten rund um das UHV Labor.
Daniel Hauck danke ich für die Unterstützung bei der Realisierung der Simulationssoftware, sowie die damit verbunden konstruktiven Diskussionen.
Den aktuellen und ehemaligen Kollegen aus Siegen, Dr. Arman Davtyan, Dr. Ali Al Hassan und Mahmoud Al Humaidi, möchte ich für die Unterstützung während der Strahlzeiten in Hamburg danken.
Desweiteren geht ein Dank an die Mitarbeiter des Strahlrohrs P09 am Synchrotron PETRA III in Hamburg, Dr. Sonia Francoual und David Reuther, die mich bei der technischen Umsetzung der durchgeführten Experimente unterstützt haben.

Zu guter Letzt möchte ich mich bei meiner Familie, insbesondere bei meinen Eltern bedanken, die mich immer in meinen Zukunftsplänen unterstützt und ermutigt haben. Ohne sie wäre all das nicht möglich gewesen. Ein ganz besonderer Dank geht an Silke, die nicht gezögert hat mit mir nach Karlsruhe zu kommen und die mich in all den Höhen und Tiefen, welche mit einer solchen Arbeit verbunden sind, unterstützt hat.